High-Power Varactors for Fast Adaptive Impedance Matching at 13.56 MHz

Dem Fachbereich Elektrotechnik und Informationstechnik
der Technischen Universität Darmstadt
zur Erlangung der Würde eines
Doktor-Ingenieurs (Dr.-Ing.)
genehmigte

Dissertation

von

Dipl.-Ing.
Daniel Markus Kienemund
geboren am 18.11.1985
in Stuttgart, Deutschland

Referent:	Prof. Dr.-Ing. Rolf Jakoby
Korreferent:	Prof. Dr.-Ing. habil. Alexander Kölpin
Tag der Einreichung:	03.05.2019
Tag der mündlichen Prüfung:	09.07.2019

Darmstadt 2019

Kienemund, Daniel Markus: High-Power Varactors for Fast Adaptive Impedance Matching at 13.56 MHz
Darmstadt, Technische Universität Darmstadt
Jahr der Veröffentlichung der Dissertation auf TUprints: 2019
URN: urn:nbn:de:tuda-tuprints-88601
Tag der mündlichen Prüfung: 09.07.2019

Erklärungen laut Promotionsordnung

§ 8 Abs. 1 lit. c PromO

Ich versichere hiermit, dass die elektronische Version meiner Disstertation mit der schriftlichen Version übereinstimmt

§ 8 Abs. 1 lit. d PromO

Ich versichere hiermit, dass zu einem vorherigen Zeitpunkt noch keine Promotion versucht wurde. In diesem Fall sind nähere Angaben über Zeitpunkt, Hochschule, Dissertationsthema und Ergebnis dieses Versuches mitzuteilen.

§ 9 Abs. 1 PromO

Ich versichere hiermit, dass die vorliegende Dissertation selbstständig und nur unter Verwendung der angegebenen Quellen verfasst wurde.

§ 9 Abs. 2 PromO

Die Arbeit hat bisher noch nicht zu Prüfungszwecken gedient.

Darmstadt, 03.05.2019 _____

Vorwort

Im Rahmen meiner Zeit als wissenschaftlicher Mitarbeiter am Institut für Mikrowellentechnik und Photonik (IMP) der Technischen Universität Darmstadt ist diese Dissertation entstanden. Beinhaltet sind Erkenntnisse, die in enger interdisziplinärer Kooperation mit der COMET AG, Schweiz und dem Karlsruher Institut für Technologie (KIT) gewonnen wurden. An dieser Stelle möchte ich daher allen Personen danken, die zum Gelingen der Arbeit beigetragen haben.

Allen voran möchte ich Herrn Prof. Dr.-Ing. Rolf Jakoby danken für die Übernahme des Referats meiner Promotion. Ich danke ihm für sein Vertrauen, die konstruktiven Gespräche, die Förderung einer selbständigen Arbeitsweise und die Unterstützung bei kritischen Fragestellungen, wodurch sich stets die Möglichkeit bot die eigene Perspektive auf ein Problem zu erweitern.

Herrn Prof. Dr.-Ing. Alexander Kölpin, Brandenburgische Technische Universität Cottbus, möchte ich danken für die Übernahme des Korreferats dieser Arbeit und die interessanten Gespräche, die dadurch möglich wurden.

Dr. Thomas Fink, Dr. Mike Abrecht und Walter Bigler von der COMET AG, Schweiz danke ich herzlich für ihre in höchstem Maße engagierte Zusammenarbeit während der vergangenen fünf Jahre. Die wertvollen Fachgespräche und das Streben nach einem gemeinsamen Ziel habe ich stets als wertvolle Motivation empfunden. Die gegenseitige Gastfreundschaft werde ich in bester Erinnerung behalten!

Mein besonderer Dank gilt auch Dr. Joachim R. Binder, Nicole Bohn, Kevin Häuser und Dr.-Ing. Christian Kohler vom Institut für Angewandte Materialien (Keramische Werkstoffe und Technologien) des KIT für die durchweg exzellente Zusammenarbeit. Gerade bei Materialfragen bezüglich der verwendeten technischen Keramiken und Prozessierungen empfand ich die Fachgespräche stets als äußerst bereichernd.

Den Kollegen, ehemaligen Kollegen und insbesondere Dr.-Ing. Holger Maune, Dr.-Ing. Alex Wiens, Dominik Walk, Christian Schuster und Prannoy Agrawal danke ich für die zahlreichen fachlichen Diskussionen, gemeinsam erarbeiteten Problemlösungen und konstruktiven Fragestellungen in einem angenehmen Arbeitsumfeld am Institut für Mikrowellentechnik und Photonik. Ein besonderer Dank gilt den technischen Mitarbeitern des Instituts, Andreas Semrad und Peter Kießlich, ohne deren exzellente Mitarbeit die Realisierung der entwickelten Ideen nicht möglich gewesen wäre.

Schlussendlich möchte ich meiner Familie danken, meiner Schwester Janina und meinen Eltern Silvia und Markus, die mir das Studium und damit die Promotion erst ermöglicht

haben. Inbesondere meiner geliebten Weggefährtin Silke danke ich in doppelter Weise für ihre technische Expertise bei der Implementierung der in dieser Arbeit vorgestellten Ideen und für die Geduld, Ruhe und Liebe während der Zeit des Schreibens der Disseration. Unserem Sohn Tillmann danke ich für die unendliche Lebensfreude, den Trubel und das Glück abseits der Promotion.

Klein-Gerau, im Juli 2019 Daniel Markus Kienemund

Kurzfassung

In dieser Arbeit werden Varaktoren entwickelt, die als steuerbare Komponenten in schnellen Hochleistungs-Anpassnetzwerken bei 13.56 MHz eingesetzt werden sollen. Steuerbare Anpassnetzwerke finden ihre Anwendung vor allem in der Prozessierung mikro- und nanoelektrischer Schaltungen und gewinnen an Bedeutung durch deren steigende Integration. In diesem Zusammenhang werden die limitierten Steuerzeiten der eingesetzten Vakuum-Varaktoren von mehr als 1 ms zunehmend zu einem Problem. Bisher war die Substitution der Vakuum-Varaktoren durch Feststoffvaraktoren vor allem durch die höheren dielektrischen Verluste Letztgenannter erschwert. Aufgrund der steigenden Anforderungen an die Varaktorsteuerzeiten, wird jedoch ein Austausch der vakuumbasierten Varaktoren unumgänglich. Feststoffe, die sich als Dielektrikum in Hochleistungsvaraktoren einsetzen lassen, finden sich vor allem in der Gruppe der Ferroelektrika. Hier nimmt Barium Strontium Titanat (BST) als hochsteuerbares, niedrigverlustbehaftetes Mischkristallsystem eine spezielle Rolle ein. Die Kapazität eines BST basierten Varaktors wird durch Anpassung der Permittivität unter Belastung eines DC Steuerfeldes eingestellt. Die dadurch induzierte Piezoelektrizität stellt ein maßgebliches Problem für den Einsatz unter Hochleistung dar. Als Folge entstehen akustische Schwingungen im Material, die lokal den elektrischen Gütefaktor vermindern. In dieser Arbeit werden sowohl neuartige, vollgedruckte BST Dickschicht-, als auch Vollkeramikvaraktoren entwickelt und in Bezug auf ihre Hochleistungseignung in steuerbaren Anpassnetzwerken bewertet. Es zeigt sich, dass der Einsatz dickschichtbasierter Varaktoren unter Hochleistung bis mindestens 1 kW grundsätzlich möglich ist. Durch akustische Optimierung der Varaktoren kann bei Eingangsleistungen von bis zu 1 kW eine Verminderung der Verlustleistung um 63 % von 37.1 W auf 13.5 W erzielt werden, bei gleichzeitiger elektrischer Steuerbarkeit von 18 %. Die hergestellten Varaktoren werden hinsichtlich ihrer Steuerzeit charakterisiert und mit weniger als 1.5 µs für den Kapazitätsbereich C(0 V) bis C(120 V) gemessen. Vollkeramiken werden in Form zylindrischer Pellets, integriert mit Platinenmaterial zu Varaktormodulen, für den Hochleistungseinsatz vorgestellt. Ein Komposit, bestehend aus BST und einem verlustarmen, nicht steuerbaren, magnesiumbasierten Metalloxiddielektrikum stellt sich als besonders geeignet heraus, durch seine Eigenschaft akustisch nur bis in den einstelligen MHz Bereich aktiv zu sein. Die Machbarkeit wird jedoch an einem temperaturstabilisierten Varaktormodulprototyp auf Basis eines kommerziellen Dielektrikums gezeigt. Bei einer Eingangsleistung von 700 W wird eine Steuerbarkeit von 12 % gemessen und ein relativer Verlust von 1.8 %, unabhängig von Eingangsleistung und Steuerspannung. Darüber hinaus wird eine minimale Steuerzeit von weniger als 1.2 µs für den Bereich C(0 V) bis C(1.1 kV) gemessen.

Abstract

Solid state varactors, applicable in rapidly adjustable high-power impedance matching circuits at 13.56 MHz are presented in this work. Tunable impedance matching networks are necessary for RF based plasma processes in the semiconductor industry. With increasing integration level, the speed at which the matching circuit can be adjusted gains impact as constant power transfer is pivotal during ignition and extinction of the plasma. State-of-the-art mechanical vacuum varactors have a limited tuning time of minimum 1 ms but are hardly replaceable, as they introduce lower losses and higher linearity compared to solid state varactors. However, as tuning speed gains impact, the substitution with fast but lossy solid state varactors becomes feasible. Within the group of tunable high-power compatible solids, barium strontium titanate (BST) is a possible candidate, due to its high tunability and low dielectric losses in the desired frequency range. The material gains its tunability from an electric field dependent permittivity, which can be adjusted with a DC biasing voltage. When biased, BST exhibits piezoelectricity, resulting in acoustical excitation with an applied RF voltage. As a result, the electrical Q-factor locally decreases and additional losses are introduced. At high-power operation, this property represents a significant problem. In this work, novel fully-printed BST thick film and bulk ceramic disk varactors are presented and evaluated in regard to their compatibility in high-power impedance matching networks. The general applicability of thick film based varactors under high-power conditions up to 1 kW is shown. At this power level, an acoustically optimized varactor design achieves a 63 % dissipated power reduction from 37.1 W to 13.5 W, while remaining electrically tunable with 18 %. By transient characterization, a response time for thick film varactors of less than 1.5 µs is demonstrated in the range of C(0 V) to C(120 V). Bulk ceramic disk varactors are presented, employed on a printed circuit board for high-power operation. For that, a composite material comprised of BST and a non-tunable, low loss, magnesium based metal oxide dielectric shows favorable properties, with a significantly reduced acoustic activity above the single digit MHz region. The feasibility, however, is shown with a thermally stabilized varactor module, employing bulk ceramic pellets based on a commercially available dielectric. At 700 W input power a tunability of 12 % is obtained with an input power and biasing voltage independent relative loss of 1.8 %. A transient response time of less than 1.2 µs is measured for a tuning range of C(0 V) to C(1.1 kV).

Contents

1 Introduction

During the past decades an increasing demand for low power, high performance, mobile and low priced electronics arose. Not only in consumer driven fields such as computer, communication and entertainment, but also industrial dominated areas i.e. space and automotive electronics or system control a rapid demand for further developed microdevices is existent. The main factor progressing our modern electronics in all key areas is the possible integration level given from the minimal structure size a manufacturing process is capable of providing. Since the 1960s, these integrated circuit chips progressed following Moore's law, stating a doubling of the number of components per integrated circuit every 18 months [1]. While in 1971, the Intel 4004 4-bit microprocessor processed in PMOS technology with a minimal structure size of 10 µm provided for 2300 transistors occupying 12 mm^2 of space, in 2011 the Intel Xeon Westmere-EX processor provided for 2.6 billion transistors in a 32 nm process on 512 mm^2. Current state of the art CMOS processes such as for the Qualcomm Centriq system on chip (SOC) utilize minimal structure sizes of 10 nm, providing for 18 billion transistors on a 398 mm^2 area.

In communication technology a similar trend is visible. Current modems for mobile applications capable of 5G standard, 256-QAM, 5x carrier aggregation and 4 x 4 downlink MIMO are manufactured in a 14 nm process resulting in less current consumption due to reduced leakage current. The HF transceiver is operating in 35 LTE frequency bands up to 5 GHz resulting in a maximum data rate of 1 Gbit s^{-1} [2]. The main obstacle for higher integration levels in this field, however is the predominantly analog circuitry in the frontend of communication devices. Mobile frontends are usually optimized to operate in predefined frequency bands, which also define certain aspects of the geometry and size of the circuitry due to line and impedance matching but also phase correlated reasons. Therefore, even with a process available providing for smaller structure sizes they may not be applicable.

Today, with structure sizes in the 10 nm range and below, technology is leaving the nanoelectronics scale and entering the atomic-scale era. In the next 10 years acceptable feature size variability is expected to be on the order of 3-4 atoms of silicon. As a result, imperfections of the surface atomic layer will contribute to the devices performance significantly [3]. Therefore, increasing requirements to established manufacturing processes such as plasma etching and plasma depositioning arise. These include improved process stability, reproducibility, control and even new features such as pulsed operation with cycling frequencies in the range of 0.1 kHz to 1000 kHz [3]. A key process discussed in literature for several decades is atomic layer etching (ALE) utilizing two separate processes to accurately remove single atomic layers [3]. In a first step, the top surface layer is modified to a reactive layer

followed by the removal step taking off only the modified layer. By using the accelerated ions of a plasma for the removal of the modified layer a highly directional etching process is established. In general, a plasma process can be subdivided into the plasma ignition phase, the working cycle with ignited plasma and the plasma extinction phase. As the working cycle is mainly affected by the reduced process timings, the ignition and extinction phase gain impact [3, 4, 5, 6, 7]. Plasma for technical applications can be generated with different methods. They can be divided into static electric field based plasma and plasmas generated by AC or RF electrical fields. All of these methods have in common, that a critical field strength needs to be provided in a gas, so that free electrons accelerated in the electric field ionize gas molecules by impact ionization. On the other hand, the field strength needs to be insufficient to create an avalanche process which would result in electrical breakdown of the gas volume. The point of operation is defined on the gas discharge curve, depicted in figure 2.16, in the glow discharge region. DC excited plasmas fail to work on insulators, as ions are trapped on the insulator, creating an electric field opposing the DC excitation field. As a result, the plasma is not sustainable. Commonly, RF based plasmas are used when an insulating material needs to be processed. For RF generated plasma, in the moment of ignition, the impedance of the plasma changes drastically. Stable RF power transfer requires a matched impedance condition between generator and load. As a result, the change in plasma impedance during ignition results in an unmatched condition and the electric field strength in the igniting plasma decays. The ignition process is unsuccessful. Exemplary, an inductively coupled plasma (ICP) chamber is depicted in figure 1.1. Common frequencies for RF plasmas are located in the ISM frequency range from 13.56 MHz to 40.68 MHz [8].

To account for that, a tunable matching circuit is required, dynamically matching the generator impedance to the plasma impedance. The circuits require high-power handling capabilities of up to 10 kW as they need to transfer the full process energy to the plasma. Tunable matching circuits for plasma processes are based on mechanically tunable, parallel-plate vacuum capacitors, so-called varactors, utilizing stepper motors to alter the electrode surface and thereby changing their capacitance. Vacuum as a dielectric is almost loss free and highly linear, therefore only the metalization losses of the electrodes and dielectric losses of the housing contribute to the overall losses of the varactors. The main drawback is the limited tuning speed of minimum 1 ms of the varactors, caused by the utilized mechanical stepper motors. Until today, mechanically tunable vacuum varactors were unrivaled in their application as tunable components in high-power matching circuits due to their unmatched advantages in regard to losses, linearity, tunability and power handling capabilities compared to other technologies. However, as process times decrease, tuning speed becomes not only a pivotal but the most critical parameter required to establish ALE capable plasma processes.

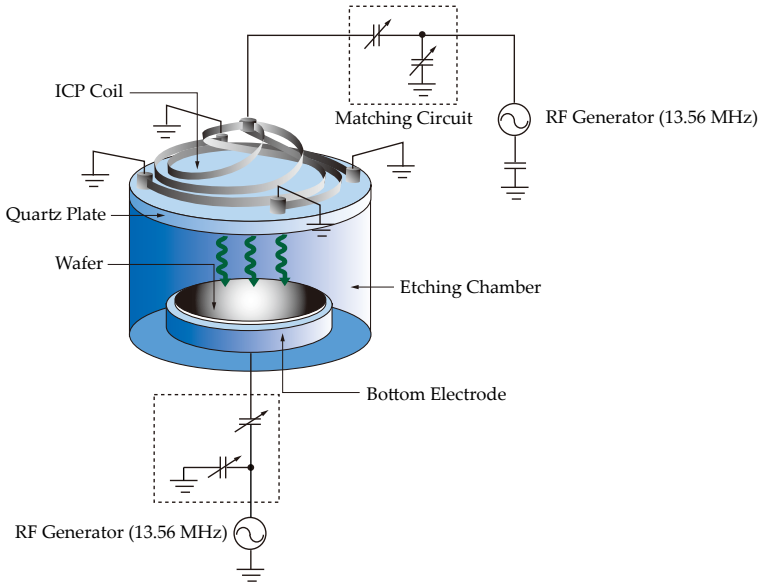

Figure 1.1: Design schematic of a Panasonic ICP dry etching system. A quartz plate with an ICP source is located above an aluminum vacuum chamber. Two RF sources at 13.56 MHz are applied to the ICP source and the lower electrode through a matching network. The sample carrier wafer is held to the lower electrode by an electrostatic chuck [9].

Motivation

Beside mechanically tunable vacuum varactors, varactors based on semiconductors, micromechanical electrical systems (MEMS) and ferroelectrics are known. All of them provide for individual advantages towards each other in regard to tunability, linearity, power handling capability, losses, tuning speed etc. For the given application, only ferroelectric based varactors appear to be a reasonable substitution of vacuum varactors, due to their exclusive property of handling high power levels properly and their very fast tunability [10, 11]. As a solid, ferroelectrics introduce dielectric losses, commonly higher than the metalization dominated losses in a vacuum varactor. Up to this point in time, this major drawback prevented the substitution of vacuum varactors in high-power matching circuits by solid state ceramic varactors. However, as the processing times decrease with integration level in the semiconductor industry, the need for faster matching outweighs the drawbacks of higher losses in the matching circuit. In the material group of ferroelectrics, barium strontium titanate (BST) is a well known candidate as a dielectric in tunable varactors for RF applications [12]. Dependent on the frequency, it is applied in epitaxically grown thin-films (GHz range), high and low temperature sintered thick films (MHz to GHz range) and bulk ceramics (DC to low MHz range) [10, 12, 13]. Commonly, BST features a high tunability, power handling capability, tuning speed and linearity in combination with low dielectric losses [11]. On the other hand, it is thermally tunable and when exposed to high electric

field strengths piezoelectric, resulting in acoustic excitation. For the intended application in the MHz range, the implementation of the varactors based on BST is limited to a thick film and a bulk ceramic approach, as the required capacitance values are not fabricable in thin film technology. In regard to a thick film implementation, the commonly applied planar interdigital shape is not applicable, as again the obtainable capacitance values are too small. Recently, screen-printed components attracted attention, as the required sintering temperature of commonly around 1200 °C was reduced to 850 °C fulfilling Low Temperature Cofired Ceramics (LTCC) technology standard and therefore enabling the possibility of implementing metal-insulator-metal (MIM) based varactor structures [14]. Main advantages of MIM based varactors compared to common planar structures is the thin dielectric filled electrode gap and high electrode overlap region, resulting in high electric breakdown field strength and single varactor capacitance values. Thereby, the power distribution technique of serial stacking becomes viable, as reasonably high overall capacitance values can still be obtained, in the range of the intended matching application. Additionally, the electrode setup shows a favorable field utilization in regard to the DC biasing field compared to planar structures, resulting in increased material utilization and therefore tunability [13, 10]. Small scale varactors based on the novel MIM setup have been implemented in mobile communication frontends to provide adaptive matching capabilities for frequencies up to 3 GHz and power levels up to 41.5 dBm [13, 10]. A significant disadvantage of MIM based thick film varactors, obtained in [10], is their low quality factor of 25 at the operational frequency of 3 GHz compared to commonly used planar structures, originating from the low sintering temperature of BST [14]. For of this reason, their applicability in mobile communication frontends is doubted. However, for reduced frequency, high-power applications, the suitability has yet to be evaluated, as the quality factor of capacitive components is proportional to the inverse of the frequency. A different ferroelectric based approach in this work to implement high-power varactors utilizes bulk ceramics. Bulk ceramics are commonly used in commercially available ceramic capacitors for low frequency grid filter applications. They are divided among other classes into thermally and electrically stable class 1 dielectrics and thermally and electrically unstable class 2 dielectrics. Usually, class 2 dielectrics are based on ferroelectrics, providing for high capacitance values, electrical breakdown field strength but also high nominal value fluctuation. High frequency applications for which electrical but not thermal tunability is desired, with accurate nominal capacitance values over a large production quantity are completely out of the scope of these capacitors. However, the material itself offers the possibility of fulfilling most of these requirements, due to the option of engineering the material in the appropriate fashion with different compositions, additives and dopants. This approach is taken in this work, with a significant focus on not only the electrical properties of the bulk ceramic but also its parasitic acoustical behavior. Compared to thick film varactors, bulk ceramic based varactors introduce a significantly higher permittivity and therefore electrical tunability. However, this higher electrical tunability is also reflected in a higher thermal tunability, which is problematic within the scope of high-power applications, due to the power dissipation in the varactors. Effective temperature monitoring and cooling solutions become highly important for rendering bulk ceramic based varactors applicable in capacitance sensitive matching circuits. In general, bulk ceramic

based varactors feature a significantly larger electrode gap, resulting in higher required biasing voltages to provide for similar electric field strengths in the dielectric. However, the high permittivity of the ceramic results in significantly larger electric field displacement into adjacent materials compared to thick films, making it necessary to encapsulate bulk ceramic varactors in a material with high electric breakdown field strength. As a result, not only the correct material composition is highly important for the application, but also the correct implementation of a varactor module capable of operating under high-power conditions. For both varactor implementations, the corresponding small and large-signal, as well as the transient characterization circuitry has to be developed and set up. Beside that, to provide the required fast tunability, filter based biasing networks have to be designed, as commonly used resistive or simple inductive solutions do not provide for the required tuning speed or selective isolation quality.

2 Tunable Microwave Dielectrics for High-Power Applications

In this chapter, fundamental properties of non-linear dielectric material are presented with particular attention on its key parameters rendering it suitable for high-power RF applications. The electrostrictive induced piezoelectricity and the resulting acoustical behavior of the material is explained. Subsequently, two possible implementation technologies, screen-printed thick films and bulk ceramics, are discussed with their respective advantages to implement tunable high-power RF components.

2.1 Fundamental Properties of Non-linear Dielectrics

Dielectrics are electrical insulators, which can be polarized when exposed to an externally applied electric field. The polarization is defined by the permanent and induced dipoles from an externally applied electric field. Stationary bound charges are deflected from their equilibrium positions creating an internal electrical field that is in opposite direction of the external electrical field, compensating it partially. The displacement field of a polarizable material can be written as [15, 16]:

$$\begin{aligned} \vec{D} &= \varepsilon_0 \vec{E} + \varepsilon_0 \chi_e \vec{E} \qquad (2.1) \\ &= \varepsilon_0 (1 + \chi_e) \vec{E} \\ \vec{D} &= \varepsilon_0 \varepsilon_r \vec{E} \qquad (2.2) \end{aligned}$$

with the vacuum permittivity ε_0, the relative permittivity ε_r, the susceptibility χ_e and the externally applied electric field $\vec{E}$. For a linear, isotropic dielectric the polarization in this term is [15, 16]:

$$\vec{P} = \varepsilon_0 \chi_e \vec{E} \qquad (2.3)$$

The polarization process of a solid material fulfills the claim for causality. The materials polarization does not change instantaneously when an electric field is applied. A phase difference between excitation field and polarization arises. Therefore, the permittivity of a

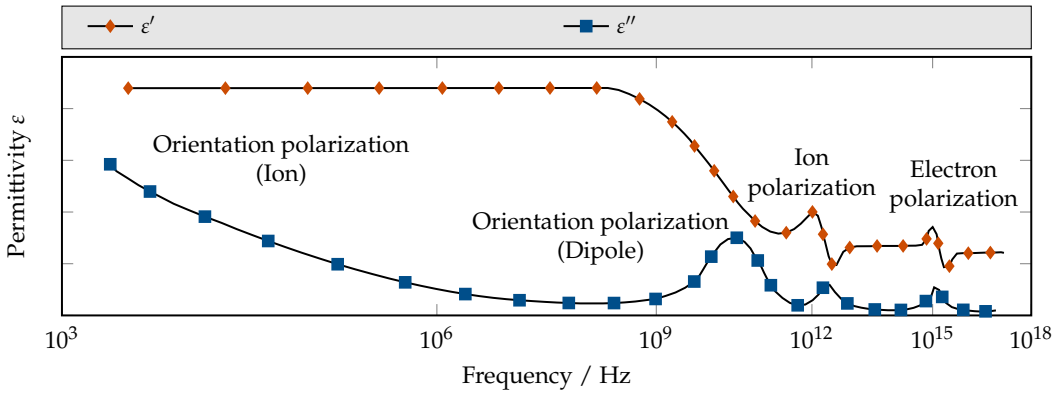

Figure 2.1: Complex permittivity over a wide frequency range. The respective polarization mechanism for the corresponding frequency range is marked.

material, when exposed to an alternating electric field, is treated as a complex function of the frequency of the applied field [16, 17]:

$$\underline{\varepsilon}(\omega) = \varepsilon'(\omega) - j\varepsilon''(\omega) \tag{2.4}$$

In a solid material two main loss mechanisms occur:

- Ohmic losses or conduction losses.
- Dielectric losses or polarization losses.

The conduction losses are based on collisions of free moving charge carriers with stationary particles of the conductive material. Due to the absence of free charge carriers in a dielectric material these losses can be neglected for alternating excitation fields. Dielectric losses originate from the collisions of bound but oscillating molecules, ions and electrons with stationary particles of the surrounding solid material when exposed to an alternating electric field. Several different polarization mechanisms exist. Of main interest for microwave applications are the following polarization mechanisms [17]:

- Orientation polarization. Ions and molecules with permanent dipoles are displaced from or rotated at their equilibrium positions with the external field.
- Ion polarization. Ions in the lattice of the dielectric are shifted from their equilibrium positions.
- Electron polarization. Electrons in their shell around an ion are displaced inducing a dipole moment.

Figure 2.1 depicts the dominating polarization mechanism over frequency and its impact on the complex permittivity of the material. The frequency dependency arises from the time constant of each polarization type. For orientation polarization, large molecules with a permanent dipole moment have to rotate and/or displace with the external field. Their mass is increased while their mobility is decreased compared to ion and electron polarization. Such a system can be described with the mechanical motion equation and harmonic excitation [15, 18]:

$$\vec{F}(t) = m \cdot \frac{d^2\vec{r}(t)}{dt^2} + b \cdot \frac{d\vec{r}(t)}{dt} + B \cdot \vec{r}(t)$$

$$\vec{F}(\omega) = -m\omega^2 \cdot \vec{r}(\omega) + j\omega b \cdot \vec{r}(\omega) + B \cdot \vec{r}(\omega) \tag{2.5}$$

with the displacement $\vec{r}$, friction constant b, mass m, spring constant $B = -m\omega_0^2$ and excitation force $\vec{F}$. Here, the excitation force is equal to the excitation field strength times the exposed charge $\vec{F}(\omega) = q \cdot \vec{E}(\omega)$. The solution to this differential equation is a harmonic vibration with the amplitude term:

$$\vec{r}(\omega) = \frac{q}{m} \frac{\vec{E}(\omega)}{\sqrt{(\omega_0^2 - \omega^2)^2 + (\frac{j\omega b}{m})^2}} \tag{2.6}$$

with the self-resonance ω_0 of the spring mass system and the excitation frequency ω. The shifted resonance frequency ω_{Res} of the damped spring mass system can be written as:

$$\omega_{\mathrm{Res}} = \sqrt{\omega_0^2 - \frac{b^2}{4m^2}} \tag{2.7}$$

Three cases arise for the frequency behavior of the system:

- For $\omega \ll \omega_{\mathrm{Res}}$ the phase difference between the excitation field and the polarization is almost 0°. For this case, energy is stored in the system in form of the electric field created by the polarization of the material over half a period and released over the other half. The amplitude of the deflection is reduced by $\vec{r}(\omega) = q \cdot \vec{E}(\omega)/(m\omega_{\mathrm{Res}}^2)$ and for small friction values b independent from friction losses [19, 20].
- For $\omega = \omega_{\mathrm{Res}}$ the polarization lags the excitation field by 90°. No energy is stored in the system. The amplitude is dominated by the friction losses of the system. For $b \to 0$ the amplitude diverges towards $\vec{r}(\omega) \to \infty$ [19, 20].

- For $\omega \gg \omega_{\mathrm{Res}}$ the polarization lags the excitation field by 180°. Again, energy is stored in the system over half a period and released over the other half. The amplitude is dominated by the excitation frequency: $\vec{r}(\omega) = q \cdot \vec{E}(\omega)/(m\omega^2)$ [19, 20].

Due to the increased amplitude of the deflection in the vicinity of the resonance frequency, losses originating from collisions with stationary particles in the lattice increase, see ε'' in figure 2.1. In order to qualify a material, the ratio between stored energy and dissipated energy over one cycle duration can be utilized:

$$\tan\delta = \frac{\varepsilon''}{\varepsilon'} = \frac{1}{Q} \tag{2.8}$$

In this equation, $\tan\delta$ is the so called loss factor, while Q is the quality factor. From earlier considerations it can be concluded, that this ratio is frequency dependent and at the resonance frequency of the polarization type at its maximum.

2.1.1 Dielectric Properties of Ferroelectrics

In the group of non-linear dielectrics, ferroelectrics assume a special role. Due to their crystalline structure, a polar axis is introduced in the material, rendering it anisotropic. In addition it allows for the preservation of an internal polarization even without an external electric field. Several characteristic traits arise compared to a non-ferroelectric material:

- The permittivity and polarization of a ferroelectric is suszeptible to change with temperature and externally applied electric field.
- The material is piezoelectric, therefore mechanical strain leads to an induced electric voltage and vice versa.
- Above the Curie temperature T_C, the tetragonal crystal structure is changed into a cubic one. As a result, the ferroelectric material becomes paraelectric, losing its piezoelectricity.
- Above the Curie temperature, i.e. in paraelectric phase, piezoelectricity reoccurs, if the material is exposed to an externally applied electric field. This is a result of the electrostriction in the material.

The key attribute rendering ferroelectric material useful for RF applications is the voltage dependent permittivity, enabling the production of tunable components. In particular the perovskite crystal systems are considered in the following due to their favourable properties in the microwave frequency range.

Based on equation (2.3), χ_e is substituted for a non-linear dielectric with a field dependent susceptibility according to:

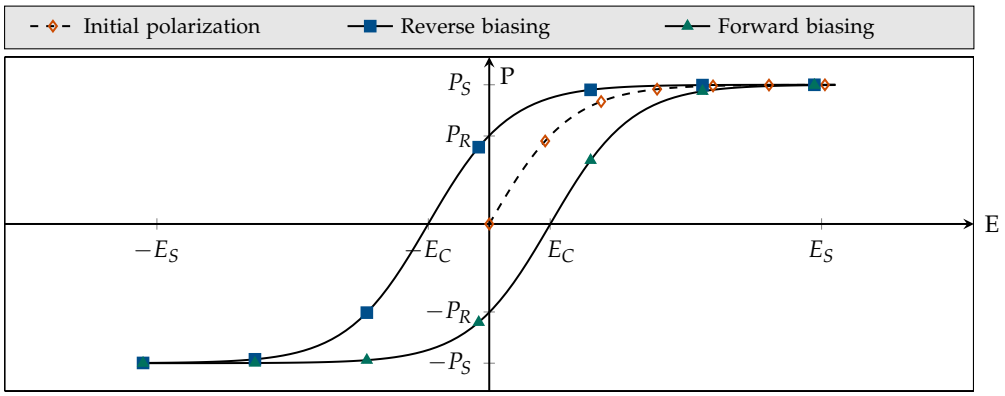

Figure 2.2: Hysteresis curve of the polarization over electric field.

$$\chi_e(\vec{E}) = \frac{1}{\varepsilon_0} \cdot \frac{\partial \vec{P}(\vec{E})}{\partial \vec{E}} \tag{2.9}$$

With $\varepsilon_r(\vec{E}) = (1 + \chi_e(\vec{E}))$, see equation (2.1), an electric field dependent permittivity is introduced, which can be used to tune an RF component.

Figure 2.2 depicts the polarization curve of a ferroelectric material over electric field strength. Once polarized by an external field, a ferroelectric material maintains a macroscopic reminiscent polarization $\vec{P}_\mathrm{R}$ until the oppositely directed coercive field strength $-\vec{E}_\mathrm{C}$ is applied. This effect is called a hysteresis. Important to note are the increased losses in a ferroelectric material undergoing the hysteresis loop in an alternating electric field. The main reason for this is the rearrangement of domains with equal polarization magnitude and direction, while the electric field strength varies. In a single ferroelectric crystal, domains of uniformly oriented spontaneous polarization are adjacent to each other. The region between two domains is called a domain wall. In a perovskite crystal, three directions of spontaneous polarization are favorable: $\pm x$, $\pm y$ and $\pm z$ direction. Therefore, only 90° and 180° domain walls exist, which indicate the direction of spontaneous polarization of adjacent domains. Within a domain wall the polarization direction changes continuously but steeply. The key factor for how the domain walls are oriented to each other is the minimization of potential energy in the crystal. When applying an external electric field, these domains start to rearrange in order to keep a minimum energy configuration with the superimposed external electric field. Domain walls are displaced, vanish or appear newly. The rearrangement itself causes losses due to collisions in the lattice. Heat generation is the consequence.

In commercial ceramic based capacitors, ferroelectrics are commonly used as dielectrics when high capacitance values and high electrical breakdown field strength are required, as well as low to medium frequency or impulse voltage stresses are applied to it. Due to their thermal and voltage dependence they are qualified as class 2 dielectrics by industrial standard. Commonly, class 1 dielectrics comprise thermally and electrically stable ceramics

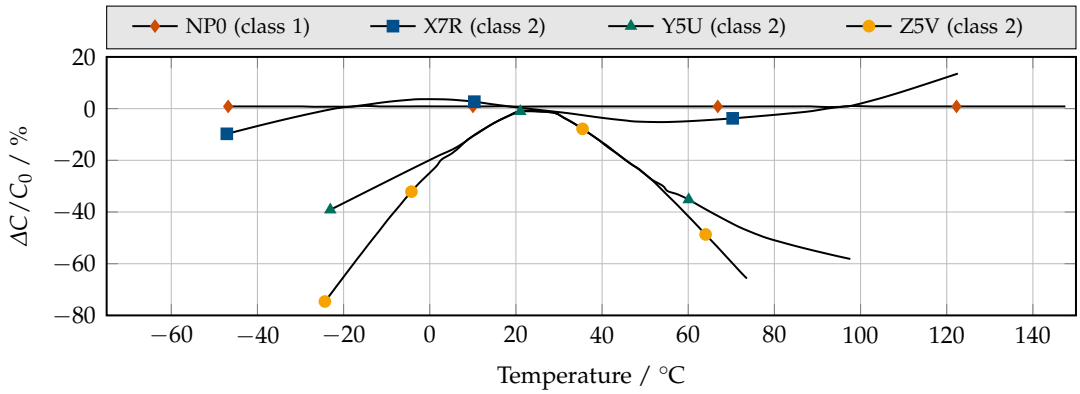

Figure 2.3: Characteristic adaption range of the capacitance over temperature for different dielectrics in commercial ceramic capacitors.

[21, 22]. Due to its industrial applicability as a class 2 dielectric, barium titanate ($BaTiO_3$) is one of the most studied perovskite ferroelectrics. $BaTiO_3$ provides for a high permittivity and therefore enables the production of capacitors with a high volumetric efficiency, meaning high capacitive values with small geometric dimensions. Drawbacks are the reduced stability and accuracy of the permittivity compared to class 1 dielectrics as a result of the temperature and voltage dependency, see equation (2.9). $BaTiO_3$ is a Y5U dielectric, specifying the change of capacitance over a given temperature range in regard to code system EIA RS-198. Y specifies the lower temperature ($-30\,°C$), 5 gives the upper temperature ($85\,°C$) and U the maximum positive and negative change of capacitance ($22\,\%$,$-33\,\%$). The behavior of some class 1 and class 2 dielectrics over temperature are depicted in figure 2.3.

Perovskite based ferroelectrics share the general molecular formula ABO_3, describing the setup of atoms in a single rectangular lattice cell. The corner positions are taken by A-Ions, while the center of the rectangles surfaces is occupied by the smaller O_3-Ions. In the center of the cuboid is the central B-Ion. The exact dimensions of the cuboid are temperature dependent. Below the so called Curie temperature, the unit cell is in a tetragonal form. Above the Curie temperature, the crystal lattice of the unit cell becomes cubic. The phase transition between both arrangements comes along with a permittivity maximum at the Curie temperature point. In case of $BaTiO_3$, the molecular structure of a single lattice cell in ferroelectric- and paraelectric phase is depicted in figure 2.4 on the left and right side, respectively.

In the ferroelectric phase, a general asymmetry in the lattice arises. Not only the central titan ion has two stable equilibrium states with a potential energy minimum, but also the corner and surface positioned ions are displaced from their electrically neutral positions. As a result, the hysteresis effect of a ferroelectric with reminiscent polarization and increased losses occur. In paraelectric phase, the arrangement of the ions is cubic and symmetric. Consequently, the spontaneous polarization, the hysteresis of the polarization and the

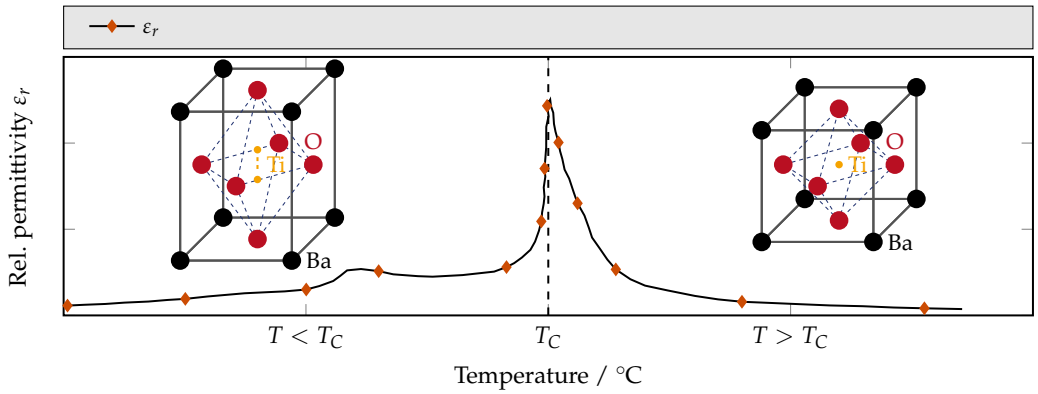

Figure 2.4: Permittivity over temperature for a ferroelectric material with the characteristic permittivity maximum at the Curie temperature.

correlated losses vanish. Usually, for high frequency applications exploiting the materials tunability, it is operated close to the Curie temperature T_C in the paraelectric phase. A detailed explanation of the solid-state physics, deriving the origin for the experienced hysteresis in the ferroelectric phase and the ferroelectric to paraelectric phase transition is given in appendix A.1.

For a parallel plate capacitor filled with a tunable dielectric, the capacitance can be calculated according to $C = \varepsilon_0 \varepsilon_r(E) \frac{A}{l}$. In case of a good electric field penetration of the dielectric material, as it is achieved for a parallel plate capacitor, an ideally linear correlation between permittivity $\varepsilon_r(E)$ and capacitance C can be assumed and the tunability of the capacitor is analogous to the tunability of the dielectric material [13]:

$$\tau = \frac{\varepsilon_r(E=0) - \varepsilon_r(E=E_{\text{bias}})}{\varepsilon_r(E=0)} = \frac{C(E=0) - C(E=E_{\text{bias}})}{C(E=0)} \tag{2.10}$$

The qualitative progression of $\varepsilon_r(E)$ over biasing field is depicted in figure 2.9 a).

2.1.2 Piezoelectricity and Electrostriction

Ferroelectric materials exhibit piezoelectricity in the ferroelectric phase. Due to the non-centrosymmetric crystal unit cell of perovskites, a non-zero charge exists in each cell, creating a dipole moment. In other words, preferred directions of spontaneous polarization in the unit cell exist, rendering the material anisotropic. In a single crystal consisting of several unit cells, the dipole moments of all unit cells are randomly directed and therefore cancel out largely. Almost no charge is measured on the materials surface, required to compensate the resulting macroscopic dipole moment. Mechanical stress applied to the crystal will change the geometric dimensions of the unit cells, and therefore, the strength of the dipole

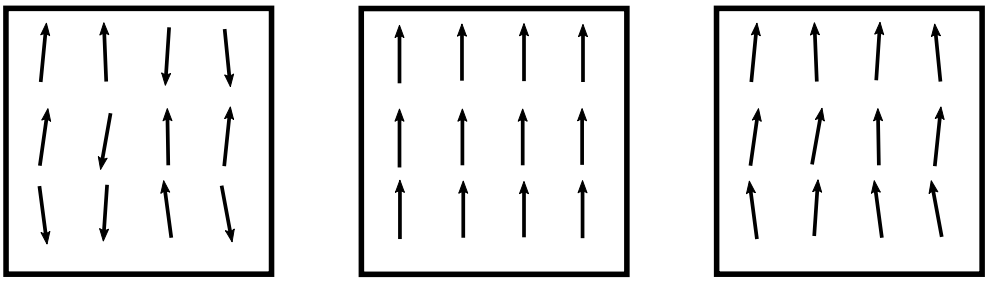

Figure 2.5: Domain orientation in a $Ba_xSr_{1-x}TiO_3$ crystal before, during and after application of DC biasing field in the ferroelectric phase below the Curie temperature.

moment of each cell. This is the source for the direct piezoelectric effect. If all the dipoles are initially randomly oriented, their rotation may not significantly change the macroscopic net polarization of the material, hence the piezoelectric effect exhibited will be negligible. This changes when the material is poled prior to the application of mechanical stress. During poling, the material is subject to an electric field strong enough to induce a polarization $|P| > |P_R|$, see figure 2.2. The randomly oriented dipoles are aligned along the poling axis, dependent on the applied electric field direction. After switching off the electric field, most dipoles will not return into their original orientation due to the preferred direction of spontaneous polarization and the pinning effect produced by microscopic defects in the crystal lattice. Surface charges will appear on the ends of the crystal, compensating the remaining macroscopic dipole moment. These charges are created by lattice distortions leading to an elongation of the material in poling direction. This effect is called the indirect piezoelectric effect [23, 24]. In figure 2.5 the poling process can be seen. The material can be depoled by applying the coercively electric field or heating the material above the Curie temperature, removing the asymmetry from the crystal unit cell.

Piezoelectricity is utilized in highly efficient microwave filters based on the acoustic vibration created by the inverse piezoelectric effect (bulk/surface acoustic wave filter (SAW, BAW)). High voltage and high frequency generation can be implemented as well as high precision servomotors using the direct or indirect piezoelectric effect. In a high-power impedance matching application, utilizing the tunability of a ferroelectric material as it is considered within the scope of this work, the direct and indirect piezoelectric effect is considered as a parasitic phenomenon.

Simulation and modelling of the piezoelectric effect

The indirect and direct piezoelectric effect are modeled with their linear constitutive equations. They are derived from the thermodynamic Gibbs free energy in appendix A.2, which as the Helmholtz free energy is one of four thermodynamic potentials and can be written as [11]:

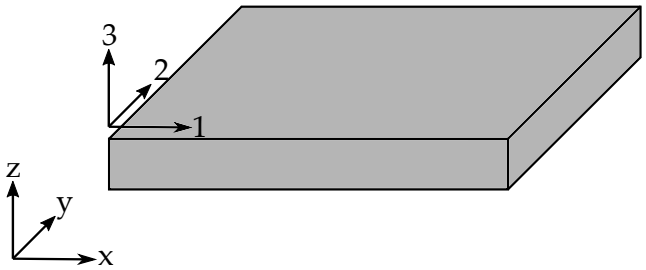

Figure 2.6: Crystal lattice orientation vs. macroscopic orientation of the crystal in the characteristic coordinate system.

$$\varepsilon^{(m)} = s^{E,T}\sigma^{(m)} + d^T E \tag{2.11}$$

$$D = d^T\sigma^{(m)} + \varepsilon_r^{\sigma,T} E \tag{2.12}$$

For the indirect piezoelectric effect, a mechanic strain $\varepsilon^{(m)}$ is generated by an external mechanic stress $sigma^{(m)}$ and the materials elastic compliance s obtained at constant temperature T and electric field strength E. The piezoelectric based component is added as the product of external electric field E and piezoelectric coupling factor d obtained at constant temperature T. For the direct piezoelectric effect, the electric displacement D is calculated from an external electric field E and permittivity ε_r. The piezoelectric component is given by the piezoelectric coupling factor d and the mechanic stress $sigma^{(m)}$. Before utilizing equation (2.11) and equation (2.12) to calculate a certain piezoelectric problem, the direction of the participating quantities have to be considered. In figure 2.6, a hexagonal volume of piezoelectric matter is depicted. The outer coordinate system has the directions x, y and z aligned with the inner coordinates 1, 2 and 3. The outer coordinate system describes the orientation of the model in regard to geometry and excitation sources. The inner system is bound to the crystal lattice with conventionally direction 3 aligned with the vector for preferred polarization. A piezoelectric coupling factor d_{31} describes the strain in direction 1 induced by an electric field in direction z. An exact explanation of the tensor notations for mechanical strain, stress, elasticity and piezoelectric coupling are given in appendix A.3.

In praxis, piezoelectric discs are cut from a single crystal, with the cutting plane rarely aligned with the surfaces of the tetragonal lattice. As a result, the inner coordinate system has to be rotated in order to meet the convention and acquire a viable simulation result [16]. In this work, sintered ceramics with a polycrystalline structure and randomly aligned single crystals are of main interest. Therefore, the material is considered isotropic with a single elastic compliance s_{33}, a piezoelectric coupling factor d_{33} and an electric permittivity $\varepsilon_{r,33}$. Direction 3 is chosen due to convention and the alignment of the electrical excitation field in the model along the z axis in the outer coordinate system, see figure 2.6. Therefore, there is no transversal impact in equation (2.11) and equation (2.12), and the tensors E and

σ, are reduced to their z/3-component. Taking into account the described simplification, the constitutive equations can be written as:

$$\varepsilon_3^{(m)} = s_{33}^{E,T}\sigma_3^{(m)} + d_{33}^T E_3 \tag{2.13}$$

$$D_3 = d_{33}^T\sigma_3^{(m)} + \varepsilon_{r,33}^{\sigma,T} E_3 \tag{2.14}$$

Electrostriction

In contrast to the piezoelectric effect, electrostriction is a property of all dielectric materials. Under the influence of an external electric field, the material changes its shape due to the displacement of ions in the lattice [25, 26]. An inverse effect, for which an electric field is induced by mechanical distortion, is unknown, as a mechanical distortion of a non-piezoelectric material does not induce polarization [27]. Usually, the piezoelectric effect is much larger than electrostriction. Therefore, for ferroelectric materials in the ferroelectric phase, it can be neglected [26]. In paraelectric phase, however, electrostriction is the dominating coupling effect between electrical and mechanical quantities. The electrostrictive coupling factor a can be derived from Gibbs free energy in regard to electric field and electric polarization, see equations (A.12) and (A.17) to (A.19). For linear dielectrics, both formulations are equivalent. For non-linear dielectrics, the coefficient becomes polarization- and therefore electric field-dependent [28]. The field dependent electrostrictive coefficient is given by:

$$a(E) = \left(\frac{\partial^3 G}{\partial\sigma^{(m)}\partial E^2}\right)_T \tag{2.15}$$

Higher order electrostrictive coefficients can also be derived from the change in Gibbs free energy [29, 30, 31]. A detailed explanation is omitted, however, due to a missing option of considering them in the performed piezoelectric simulations within the scope of this work. The constitutive equation for the indirect piezoelectric effect with electrostriction, which describes the behavior of the material in the ferroelectric phase with the aforementioned simplifications, can be expressed as [16, 32]:

$$\varepsilon_3^{(m)} = s_{33}^{E,T}\sigma_3^{(m)} + d_{33}^T E_3 + a_{33}^T(E)E_3^2 \tag{2.16}$$

To derive the equation for the paraelectric phase, the material is now assumed with no piezoelectricity $d_{33} = 0$ and no mechanical stress applied to it ($\sigma_3^{(m)} = 0$). Furthermore, a superimposed electric field with the static DC component $\hat{E}_{DC}$ and the alternating RF component $E_{RF} = \hat{E}_{RF}\sin(\omega_{RF}t)$ is applied to the material. The mechanic strain $\varepsilon_3^{(m)}$ can be written with equation (2.16) [27]:

$$\begin{aligned}\varepsilon_3^{(m)} &= a_{33}(\hat{E}_{DC} + E_{RF})^2 \\ &= a_{33}\hat{E}_{DC}^2 + 2a_{33}E_{RF}\hat{E}_{DC} + a_{33}E_{RF}^2 \\ &= \underbrace{a_{33}(\hat{E}_{DC}^2 + \frac{1}{2}\hat{E}_{RF}^2)}_{static} + \underbrace{2a_{33}\hat{E}_{DC}\hat{E}_{RF}\sin(\omega_{RF}t)}_{piezoelectric} - \underbrace{\frac{1}{2}a_{33}\hat{E}_{RF}^2\sin(2\omega_{RF}t + \frac{\pi}{2})}_{electrostrictive}\end{aligned} \tag{2.17}$$

In equation (2.17), three major terms can be identified, having impact on the mechanical strain of the material:

- A static term, which is not exclusively dependent on the DC component of the external electrical field. In most applications, however, E_{DC} is chosen much larger than E_{RF}.
- A term, with linear dependence on the alternating component of the external electric field. This term describes an induced, reoccurring piezoelectric effect in the material, even though it does not exhibit piezoelectricity in the paraelectric phase. The apparent piezoelectric coupling factor is called $e_{33} = 2a_{33}\hat{E}_{DC}$. In contrast to the piezoelectric coupling factor d, e is not constant but increasing with the DC component of the external electric field [27]. Usually, the electrostrictive coupling factor a is much smaller than the piezoelectric coupling factor d [26]. Due to the amplification of a with E_{DC}, however, the apparent piezoelectric coupling factor e is in the range of d [27]. Descriptively, the amplification of a can be described as a distortion of the cubic lattice up the degree it becomes tetragonal and therefore ferroelectric again [11].
- A second order term, representing the electrostrictive component of the induced mechanic strain. The frequency of this strain component is twice the excitation frequency.

2.1.3 Acoustic Properties of Ferroelectrics

Acoustic waves are based on particle movements in a material independent of its aggregate state. In solids, they can be separated into longitudinal and shear waves. In longitudinal waves, the particle motion is parallel aligned to the propagation direction of the wave, while in shear waves the particle motion is perpendicular to the propagation direction. The relation between particle motion and propagation of the wave is depicted in figure 2.7 [16].

In isotropic material it can be shown, that due to the symmetry of material constants, the acoustic wave contains particle motion only strictly parallel or perpendicular to the direction of wave propagation [16]. For a plane acoustic wave, there is one pure longitudinal mode and two degenerate shear modes, which are coupled by Poisson's ratio [18]. In an anisotropic material, the propagation of acoustic waves is more complicated. Quasilongitudinal and

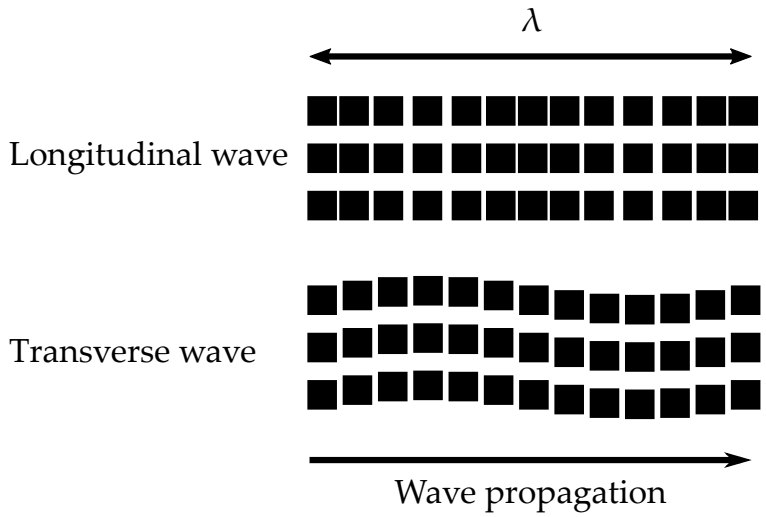

Figure 2.7: Longitudinal and transversal particle movement vs. propagation direction of the acoustic wave.

quasitransversal modes occur, due to the direction dependent material constants [16]. In this work, however, main focus is laid on polycrystalline material, which can be assumed isotropic.

In a piezoelectric material, the origin of acoustic waves lies in the coupling between electrical and mechanical parameters. As described in section 2.1.2, an electrical field induces mechanical strain in the material either by means of the indirect piezoelectric effect (ferroelectric phase) or electrostrictive induced piezoelectricity (paraelectric phase), see equation (2.16) and equation (2.17). For a material exhibiting piezoelectricity, it is important to note, that an excited acoustic wave again induces an electromagnetic wave, that superimposes the electric excitation field. In a piezoelectric solid, the acoustic wave equation can be derived from Newton's second law for an elementary volume dx, dy, dz with r, the displacement of a particle in direction x, y, z or 1, 2, 3, see figure 2.7 [33, 16]:

$$\begin{aligned} \rho\frac{\partial^2 r}{\partial t^2} &= \nabla\sigma^{(m)} \\ &= E^{(m)}\nabla\varepsilon^{(m)} - g\nabla E \end{aligned} \tag{2.18}$$

with the Young's modulus $E^{(m)}$ and the piezoelectric stress g. By substituting $\varepsilon^{(m)} = \nabla r$ and $E = -\nabla\varphi$, with φ being the electrical potential, in equation (2.18), the acoustic wave equation is obtained [33, 16]:

$$\rho\frac{\partial^2 r}{\partial t^2} = E^{(m)}\Delta r + g\Delta\varphi \tag{2.19}$$

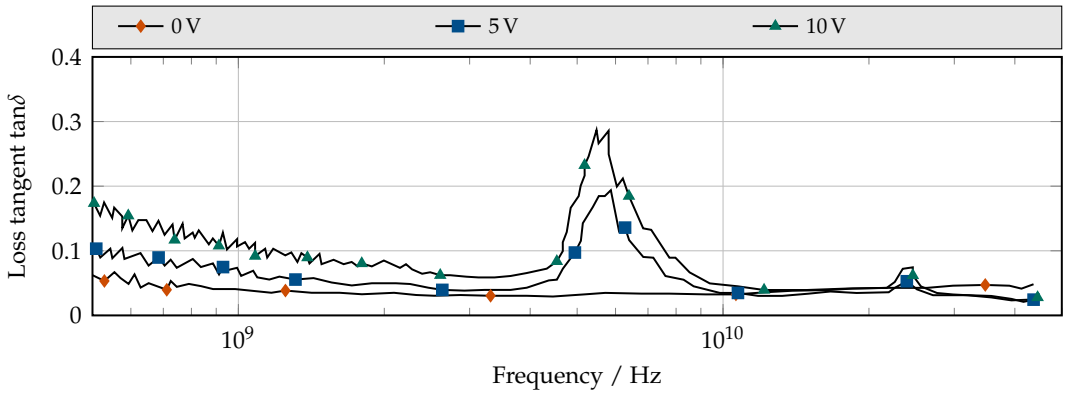

Figure 2.8: Acoustic resonance phenomenon in a $Ba_xSr_{1-x}TiO_3$ single crystal for various DC biasing voltages vs. frequency.

The accompanying backcoupled electromagnetic wave can be expressed as [33, 16]:

$$0 = g\Delta r + \varepsilon_r \Delta\varphi \tag{2.20}$$

The solution to these differential equations are the well known wave functions:

$$\underline{r_k} = R_0 e^{j(\omega t - k[x,y,z])} \tag{2.21}$$

$$\underline{\varphi} = \varphi_0 e^{j(\omega t - k[x,y,z])} \tag{2.22}$$

with the wave vector $|k| = 2\pi/\lambda$. Now, the propagation/phase velocity dependent on the mechanical properties of the material, can be described as [16, 18]:

$$v = \sqrt{\frac{E^{(m)}}{\rho}} = \frac{\omega}{k} \tag{2.23}$$

The result of the excitation of acoustic waves in a ferroelectric material is the periodic occurance of spikes in the frequency spectrum of the loss tangent (see figure 2.8) [34]. At these frequencies, a standing bulk acoustic wave is excited between the electrodes of the parallel plate capacitor. Electric power is transferred into kinetic energy and heat in the dielectric. The kinetic energy is coupled to adjacent layers and mainly lost due to absorption and radiation to air. For the electric excitation both transferred energy types occur as losses.

2.2 Barium Strontium Titanate

This section covers the barium strontium titanate (BST) mixed crystal theory and their application. In regard to varactor processing, the BST powder preparation is presented and the subsequent steps for obtaining either a screen-printable paste or a compressible green body compatible bulk ceramic powder. Subsequently, the actual screen-printing process is presented together with the required drying and sintering steps to obtain a functional MIM thick film varactor. For bulk ceramic pellets, the compression and sintering steps are presented. The Curie temperature of the aforementioned $BaTiO_3$ is at $\sim$105 °C. The operation temperature for most industrial and commercial devices even in the high-power branch is limited to 50 °C. Consequently, the Curie temperature of the tunable material should ideally be 10 °C to 15 °C below the desired operational temperature of the circuit to ensure operation in the paraelectric phase but at the same time maximize the tunability of the material. In the mentioned temperature range no material is known with a matching Curie temperature. It is possible, however, to synthesize a mixed crystal system by substituting barium ions in the $BaTiO_3$ lattice with strontium ions. Barium and strontium are both alkaline earth metals in the second group of the periodic table with a full outer s-electron shell. Both are prone to losing these electrons to become 2+ cations and fulfill noble gas configuration with 8 outer electrons (octet rule). $SrTiO_3$ has its Curie temperature at about -240 °C. Therefore, by substituting Ba with Sr, the Curie temperature of the synthesized $Ba_xSr_{1-x}TiO_3$ can be altered to values optimal for operation in devices at room temperature. The stoichiometric factor x describes the mixing ratio of Ba and Sr and can be chosen arbitrarily in the range between 0 and 1. The Curie point can be approximated with mixing factor x by [35]:

$$T_C(x) = (42 + 439.37x - 95.95x^2)K \tag{2.24}$$

The shift in Curie temperature with mixing ration x is depicted in figure 2.9 on the right side [36, 37].

To obtain the aforementioned goals, mixing ratios with $x = 0.6$ and $x = 0.7$ are chosen, resulting in a Curie temperature of 0 °C and 25 °C respectively. The operational temperature of tunable devices based on a material with these mixing ratios is between 20 °C to 60 °C [36].

BST based ceramics shows a strong grain size effect [38, 39]. This effect correlates the electrical permittivity, tunability and Curie temperature of the material with the size of the grains included in the texture. In general, the permittivity and tunability decreases with grain size, while the Curie temperature slightly increases [38, 40]. The effect is responsible for the significantly different electrical parameters of BST thick film and BST bulk ceramics. BST thick film usually contains smaller grains, due to limitations of the mesh size in the printing screen, see section 2.2.2. As a result, thick films provide much smaller permittivity and tunability compared to bulk ceramics. For the component, however, only the reduced

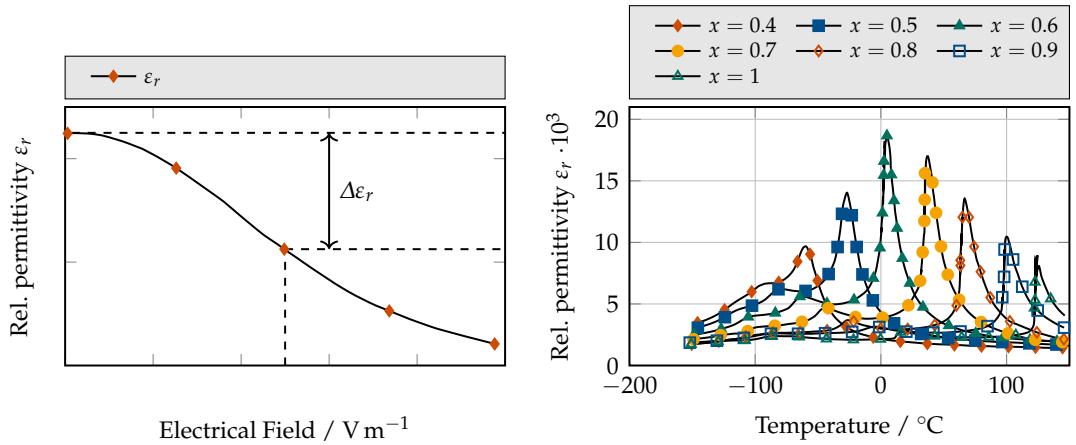

(a) Permittivity vs. eletrical DC field strength.

(b) Permittivity for mixed crystal $Ba_xSr_{1-x}TiO_3$ and various mixing ratios x vs. temperature.

Figure 2.9: Tunability and Curie point adjustment of mixed crystal $Ba_xSr_{1-x}TiO_3$.

tunability is considered a disadvantage. This is mostly due to the highly reduced distance between electrodes in stacked metal-insulator-metal (MIM) thick film varactors, resulting in comparable capacitance values. The impact of the grain size effect on the permittivity of a BST thick film and bulk material is depicted in figure 2.10.

2.2.1 Powder Preparation

Exemplary the preparation of undoped $Ba_xSr_{1-x}TiO_3$ powder is presented. For this, barium- and strontium-acetate are dissolved in acetic acid at room temperature in a nitrogen cleaned

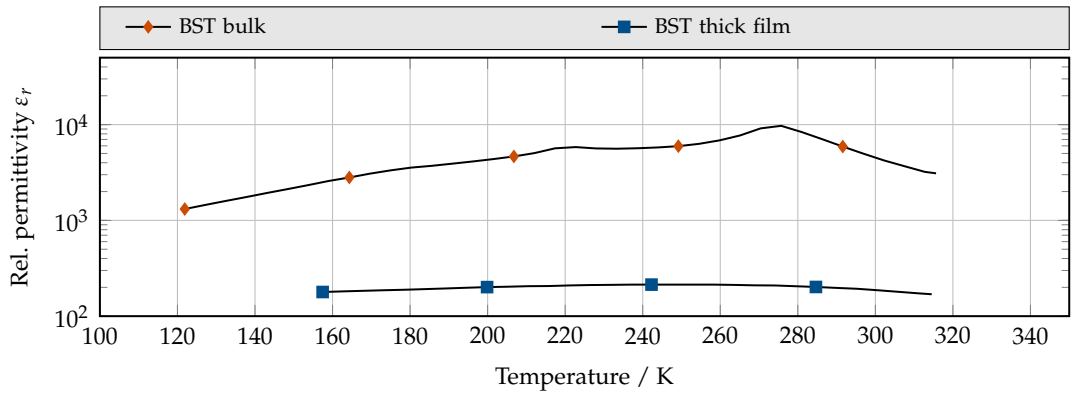

Figure 2.10: Permittivity of bulk and thick film BST over temperature.

Table 2.1: Reactants for the BST powder preparation excluding supplements to ensure low sintering capabilities [14].

Reactant	Sum formula	Manufacturer
Barium acetate	$Ba(CH_3COO)_2$	Merck
Strontium acetate	$Sr(CH_3COO)_2 \cdot {}^1/_2H_2O$	Alfa Aesar
Titan isopropanolate	$Ti(OCH(CH_3)_2)_4$	Sigma Aldrich
Acetic acid	CH_3COOH	Merck
Deionized water	H_2O	-
Trifluoroacetic	CF_3COOH	Merck

glass reactor. Trifluoroacetic is added with glacial acetic acid. The sol is left in the reactor for 16 hours while stirring constantly, to ensure the complete decomposition of the acetate. Subsequently, titanium isopropanolate is added, resulting in a slightly exothermic reaction. After adding de-ionized water, a clear sol with a volume of 5.2 L is obtained. Before spray drying, the sol is filtered through a screen with a mesh size of 1 µm to account for remaining solids. The spray drying process is performed between 245 °C to 260 °C with an output temperature of the resulting precursor of 105 °C to 120 °C. Afterwards, the filtered precursor (mesh size 250 µm) is calcined at 900 °C for 1 h. Now, the further use of the powder has to be considered in the preparation process. To obtain a low sintering temperature, LTCC compatible BST powder, the premilled BST powder has to be supplemented with ZnO and H_3BO_3, to ensure a low onset and offset temperature for the sintering process, see figure 2.12 [14]. A powder for bulk ceramic purposes does not need to be supplemented. The BST is premilled in isopropanol alcohol to avoid washout and therefore reduction of barium, which would occur by milling in water. The powder preparation processed is depicted in a flow diagram in figure 2.11.

2.2.2 Screen-Printed Thick Films

Screen-printing is a low cost fabrication method for microwave components. It is capable of producing material layer thicknesses in the range of several 10 µm and geometries with a minimum edge length of 50 µm. A printed thick film consists of grains that have to be sintered in order to create a dense texture. Usually, sintering temperatures are found above 1100 °C for functional ceramic thick films, such as pure barium strontium titanate [41, 42, 43]. Therefore, due to the lower melting temperature of the metal electrodes, the implementation of microwave components is limited to planar structures such as interdigital capacitors, for which the patterning of the metal electrodes can be done after the sintering process. For high-power applications, planar structures have several disadvantages compared to stacked ones:

- In order to avoid self-tuning of a varactor with the applied RF voltage, the DC

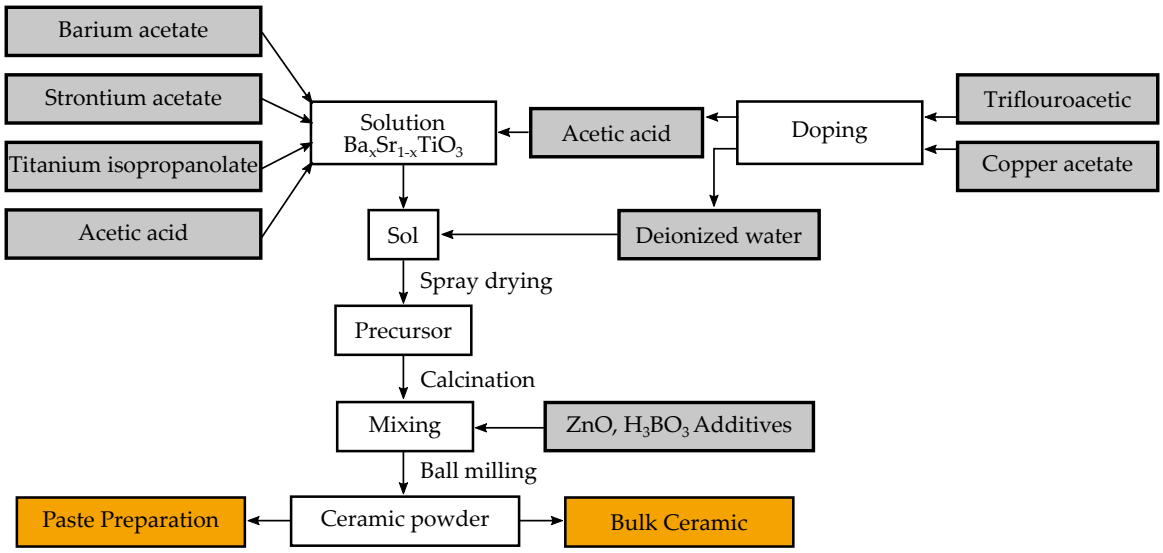

Figure 2.11: Processing of the ceramic powder for the green bodies of bulk ceramic disks or paste preparation for screen-printing purposes.

biasing voltage is chosen to be approximately 10 times the RF voltage amplitude. In circuits exposed to high-power, the RF voltage itself can be of significant amplitude, demanding for DC biasing voltages above the electrical breakdown field strength of air.

- A metal-insulator-metal (MIM) stacked structure produces a more homogeneous electrical field distribution. As a result, the overall breakdown field strength of such a structure exceeds the electrical breakdown field strength of a planar structure even when its infused [44].

To allow the use of common electrode materials such as silver, several approaches have been investigated to reduce the sintering temperature of BST down to 850 °C to 900 °C. Such a reduction not only introduces the possibility of implementing MIM structures, but also enables the fabrication of low temperature cofired ceramic (LTCC) integrated passive tunable microwave devices. As a result, a lot of effort has been put up to achieve this goal [45, 46, 47]. In 2013, composite thick film based on BST, zinc oxide (ZnO) and boron trioxide (B_2O_3) is presented, which shows characteristic starting of the sintering shrinkage, the so called onset temperature, at 880 °C [48]. A reduction in shrinkage (offset temperature) starts at 1100 °C, rendering the composite still infeasible for stacked microwave components. By doping and substituting B_2O_3 with boric acid (H_3BO_3) in the aforementioned composite, however, the sintering process is completely shifted in the temperature window suitable for the application of metal electrodes [49], figure 2.12.

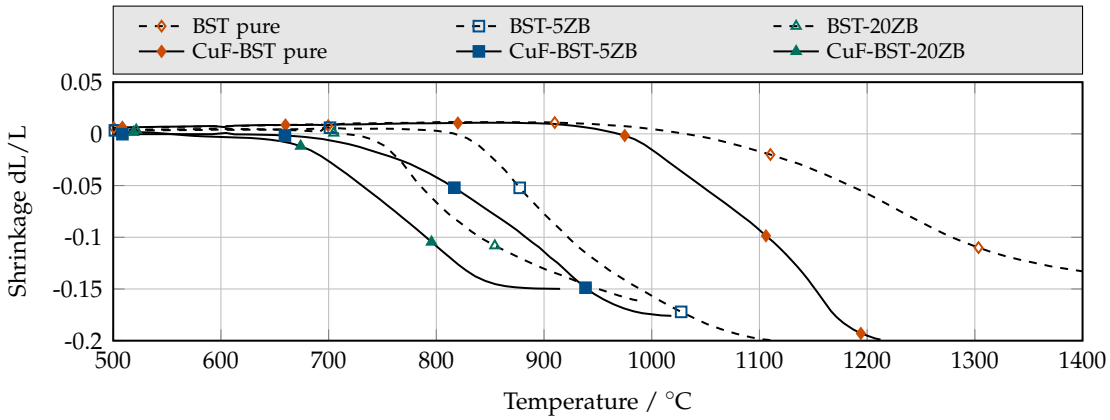

Figure 2.12: Shrinkage of the green body over temperature for different BST compositions and dopants [49].

Table 2.2: Reactants for the thick film paste preparation [14].

Reactant	Function	Manufacturer
Powder mixture	Solid	-
Terpineol	Dispersing medium	Sigma Aldrich
Hypermer HD 1	Dispersant	Uniquema
Ethyl cellulose	Binder	Sigma Aldrich

Paste Preparation for Screen-Printing

In a first step, the premilled powder is fine milled and supplemented with Terpineol as the dispersing medium and Hypermer HD 1 as the dispersant in a three rolling mill for 1 h. The used dissolver is Dispermat CA (VMA-Getzmann GmbH, Reichshof). The binder (ethyl cellulose) is added and the mixture is stirred for 30 min. Subsequently, the paste is further homogenized with Al_2O_3 milling balls, which are known for their abrasion not influencing the mechanical or electrical behavior of the BST. The exact volumetric composition of the paste is depicted in table 2.2.

Screen-Printing Process

Patterned screens with certain mesh sizes are aligned with the carrier substrate. Usually, for screen printing purposes of electric circuitry, alumina (Al_2O_3) or aluminium nitride (AlN) is used as the substrate, due to its mechanical stiffness which prevents delamination of the printed layers and its temperature stability needed for the sintering process. In this work, only alumina carrier substrates are used with the dimensions

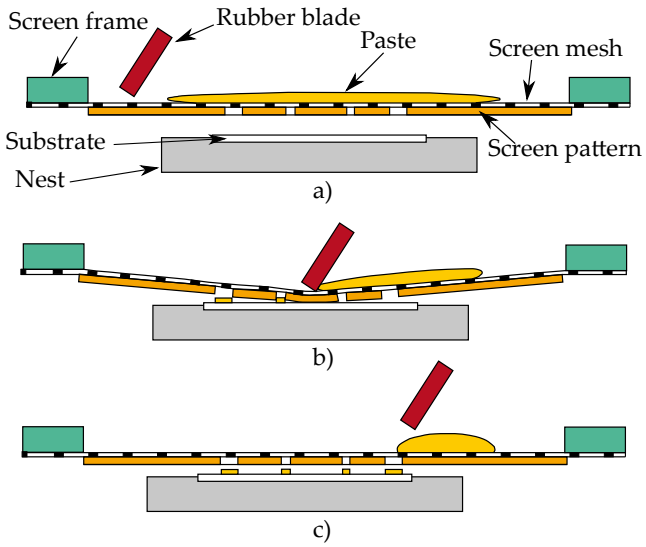

Figure 2.13: Screen-printing process.

51 mm × 51 mm × 0.63 mm. Compared to AlN based substrates, alumina has a lower thermal conductivity of 18 $W\,m^{-1}\,K^{-1}$ compared to 120 $W\,m^{-1}\,K^{-1}$ to 140 $W\,m^{-1}\,K^{-1}$ [50, 51]. The material pastes are pressed through the screen with a rubber blade, printing the pattern of the screen on the carrier substrate. The printing image (layer thickness, layer accuracy) can be adjusted with the mesh size of the screen, the stiffness of the rubber blade and several machine parameters of the printer (printing speed, blade pressure, exit pressure) [14]. In this work, meshes of 200 and 325 with wire diameters of 40 µm and 30 µm are used, resulting in a maximum accuracy of 90 µm and 50 µm in lateral dimensions. With both screen types it is possible to print the dielectric BST layer as well as the silver electrodes. In general, a coarser mesh leads to an increased layer thickness. The screens are provided by Koenen GmbH. The electrode paste is a C1076SD (LPA 609-022) low cost silver/platinum (Ag/Pt), REACH, RoHS and LTCC compliant conductor material from Heraeus, providing good adhesion to alumina substrates and printed BST layers. Figure 2.13 depicts the screen-printing process. In a first step (a) the patterned screen is aligned to the substrate material and the printing paste is distributed on the screen. Subsequently, the rubber blade is pulled over the screen, pressing it on the substrate (b). Due to the pressure, the paste is pushed through the uncovered mesh in the screen and the inverse pattern is transferred to the substrate. Upon lifting the rubber blade, the screen separates from the substrate (c). A stacked structure can be implemented by repeating the steps with a differently patterned screen aligned to the already printed layer. Two different sintering processes are applied in this work:

- Each layer is dried and sintered individually. For this case, a higher BST layer stability is achieved. Organic solvents are vaporized during sintering and leave the printed BST layer unimpeded, due to the reduced single BST layer thickness. The sintering process, however, has to be repeated for each layer, resulting in inhomogeneous

material properties, due to the unequal sintering times for each layer.

- Each layer is dried but not sintered. The entire structure is set up and then sintered in a single process step. The obtained BST layer has a lower electrical breakdown field strength, due to holes from vaporized organic solvents leaving the layer. The material parameters, mechanical as well as electrical, can be assumed homogeneous.

The sintering process of one BST layer is performed in a tube furnace at 850 °C for 10 min in purified air. The final sintering step is expanded to meet a total sintering time of 1 h. Consequently, for the structure exposed to a single sintering process, a sintering time of 1 h is used.

2.2.3 Bulk Ceramics

Bulk ceramics are commonly used as dielectrics in capacitors, due to their high volumetric efficiency, electrical breakdown field strength, low cost fabrication and stability in regard to ageing and radiation [52]. Dependent on the application, the chosen ceramic dielectric is taken from one of three classes, summarizing different ceramic formulations with equal electric properties, see EN 60384-1:2016 and section 2.1.1. Class 1 includes temperature and voltage stable materials with low dielectric losses for applications requiring a high frequency stability such as filters and measurement circuits. Class 2 dielectrics provide for a high volumetric efficiency, due to their high permittivity. They are base on ferroelectrics and therefore introduce a low temperature and voltage stability. Class 3 dielectrics have an even higher volumetric efficiency with increased non-linear behavior in regard to voltage and temperature. In this class, all materials are included that do not suffice the requirements for a class 2 dielectric. The dielectric properties of bulk ceramics are dependent on several factors during the manufacturing process. They can be divided into:

- Powder dependent factors such as: mixing ratio of the reactants, doping, additives, milling time, etc.
- Shaping of the ceramic: pressure, time.
- Sintering process: sintering temperature, sintering time, sintering environment.

Usually, all of these factors affect all properties of the manufactured bulk ceramic, therefore it is highly important to ensure repeatability of the process to guarantee a consistent outcome. In this work, cylindrical BST bulk ceramic pellets with diameter L in the range of 8 mm to 16 mm and a thickness l in the range of 0.6 mm to 1 mm are processed. For this, the prepared powder (see section 2.2.1) is filled in an uniaxial manual laboratory press (P/O/Weber) and compressed see figure 2.14a). A cylindrical green body is obtained with a diameter in the range of 9.1 mm to 17.3 mm as depicted in figure 2.14b).

The thickness of the pellet is adjusted by lapping the sample to a desired height in the range of 0.6 mm to 1 mm for the in house produced pellets. For industrially manufactured

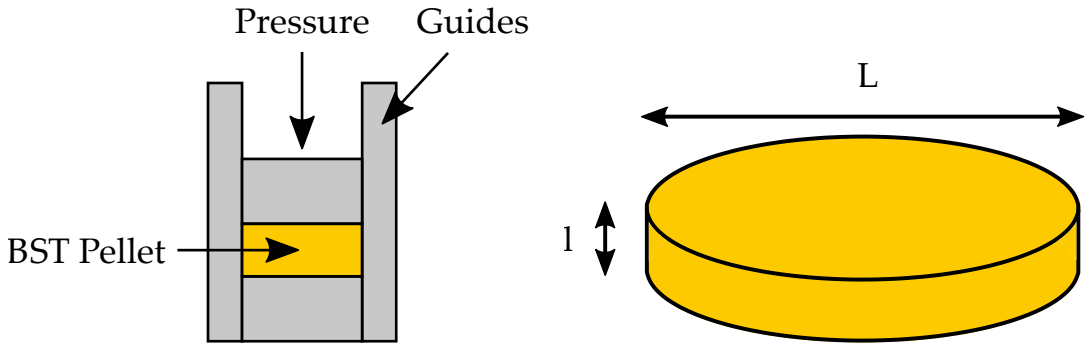

(a) Uniaxial manual press. **(b)** Obtained cylindric BST bulk ceramic pellet.

Figure 2.14: Bulk ceramic pellet manufacturing.

pellets the green body is compressed to geometric dimensions that result in the desired final dimensions of the pellet after shrinkage due to the sintering process. The green bodies are experimentally sintered at temperatures between 1050 °C to 1360 °C for various durations to alter the properties of the bulk ceramic to meet the requirements of the application. In a final step, two circular electrodes are coated to the adjacent sides of the pellet. The electrode diameter is varied between 4 mm to 12 mm.

2.3 High-Voltage Breakdown Processes

This chapter describes the electrical breakdown mechanics in vacuum, gas and solids. For AC and DC stressed mediums, the electrical breakdown marks the end of a sequence of physical discharge mechanisms that dependent on the electric field strength, partial pressure, homogeneity, time constant, humidity and temperature [44]. Even though, a field arrangement might partially exceed the electrical breakdown field strength of the present medium, a complete breakdown does not necessarily occur. The so called partial discharge, however, is in most cases an unwanted phenomenon, as it significantly reduces the electrical strength of a medium over time. Partial discharges occur when the electrical field strength locally exceeds the electrical breakdown field strength of the medium but not across the whole length between the electrodes. Irregularities on the electrodes create highly inhomogeneous field distributions in their vicinity, resulting in locally increased field strengths. Partial discharges starting on the irregularity of an electrode are called outer partial discharges. Irregularities such as inclusions, pores and gas bubbles generate inhomogeneous field distributions within an isolating medium and cause inner discharges [53, 44]. In solids, partial discharges lead to thermal erosion, while gas filled arrangements may recover from partial discharges after unplugging the voltage source. The electrode material, however, suffers from the electrical discharges especially at the arc focus point on the surface [54]. For a breakdown, the electrical strength of the stressed volume needs to be

exceeded across the whole length between the electrodes. Avalanche processes create an ionized conducting channel between the electrodes, which represents a heavy load scenario as the arc resistance is in the range of just a few Ω [55]. As the voltage source is now heavily loaded, the voltage drop across the electrodes usually decreases below the point, where the avalanche processes create enough electrons to sustain the ionizing channel. The arc collapses, removing the heavy load scenario between the electrodes. In case of a gas filled arrangement, the electrical breakdown field strength of the medium recovers. A solid material is usually irretrievably damaged.

Vacuum Breakdown and Conditioning

The vacuum breakdown mechanism fundamentally differs from that of the gas and solid one. Main starting point of a breakdown in a gas and solid, is the presence of a starting electron, that is accelerated in the electrical field. The starting electron is generated from the absorption of cosmic radiation in the volume between the electrodes. Then, avalanche processes based on collisions of the starting electron with molecules of the surrounding media cause the generation of more electrons contributing to the discharge current. An ionized channel is created. In a vacuum, the occurrence of a starting electron is highly improbable as media that absorbs cosmic radiation and thereby generates a starting electron is missing. Therefore, the electrical breakdown process is based on parasitic effects caused by the manufacturing process of the vacuum device. For small electrode gaps, the cathode and anode initiated breakdown process as well as surface based processes are dominant caused by a contamination of the electrodes surface by an alien layer. For larger electrode gaps, contamination of the vacuum with micro particles and the isolator discharge become dominant. In this work, electrode gaps in the µm range are implemented exclusively, therefore the anode and cathode initiated breakdown are explained in more detail [56, 57, 58]:

- Irregularities on the electrodes, where the electrical field is highly increased, cause a field emission current high enough to vaporize the irregularities. Then, the ionized metal is accelerated in the electrical field towards the anode causing a continuously increasing current. This breakdown mechanism is called cathode initiated discharge [44].
- The anode initiated discharge starts with field emission by electrons from the cathode. The electrons are accelerated in the electric field and impact on the surface of the anode, generating a significant temperature increase. Then, irregularities vaporize which, similar to the cathode initiated discharge create a continuously increasing current [44].

Usually, both mechanisms occur in a global electric breakdown of a vacuum device.

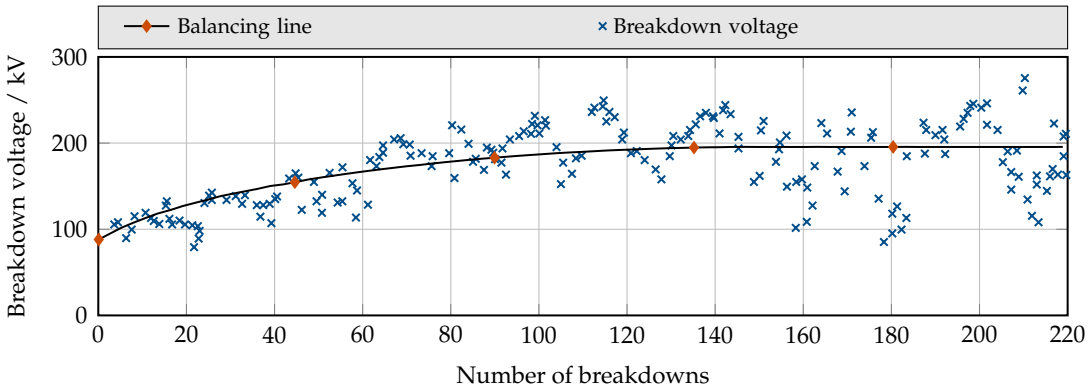

Figure 2.15: Typical impulse conditioning process of a vacuum switch with 3 mm gap. The balancing line marks an ideal conditioning process [56].

By conditioning the electrodes surfaces, the electrical breakdown field strength of a high voltage device can be significantly increased. Conditioning is not exclusively connected to high voltage vacuum devices but also gas filled systems and even insulators. Several different conditioning techniques exist such as DC, AC, impulse and RF conditioning [56, 59, 60]. They all have in common, that not only the wanted increase in electrical breakdown field strength may occur by conditioning, but also a deconditioning effect that reduces the electrical breakdown field strength. Main reason for this, is a too violent vaporization of irregularities on the electrodes surface, creating new and sometimes even larger irregularities [56, 44]. A typical impulse conditioning process is depicted in figure 2.15.

The electrical breakdown field strength of the device is increased by 100 % from 100 kV to 200 kV in the course of the conditioning process. Conditioning of insulators, is performed to remove impurities and trapped charge carrier from the insulator surface and interface between insulator and electrode [61, 58]. As a result, the generation of secondary electrons is prevented, which describe electrons generated as a result of the impact by primary electrons.

Gas Breakdown, Paschen's Law and Triple Points

The discharge process in gas covers the physical background that leads to the electrical breakdown of a gas filled volume. Main criteria for the initiation of gas discharge is the presence of a free start electron, that is accelerated in the electric field according to Coulomb's law. During acceleration, the electron unimpededly surpasses a path until it collides with a gas molecule. This path is called the mean free path. If the mean free path length is sufficient for the electron to accumulate enough kinetic energy to ionize the gas molecule it collides with, an avalanche process is initiated [44]. The characteristic gas discharge curve with unheated electrodes below atmospheric pressure is depicted in figure 2.16.

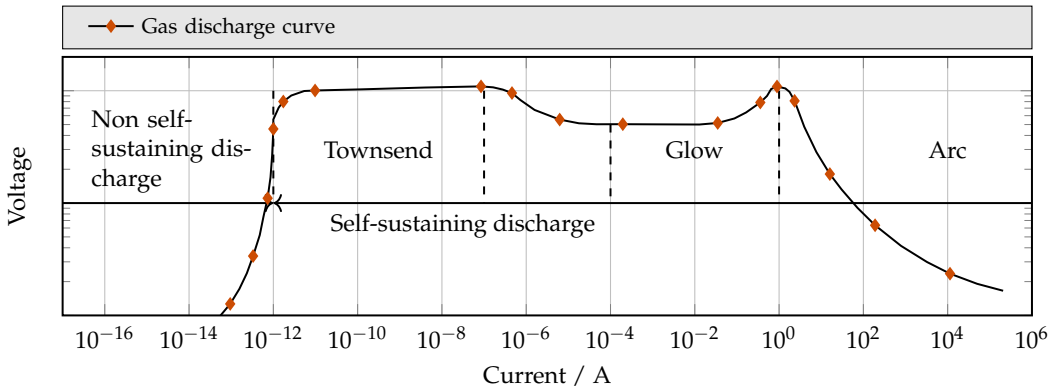

Figure 2.16: Gas discharge curve with division into the characteristic sections [44].

At current levels below the pA region, free electrons contributing to the current flow are generated by background radiation. The discharge is invisible and unable to generate electrons by itself. With increasing voltage and kinetic energy of the accelerated free electrons, impact ionization with gas molecules is introduced. Here, the remaining positively charged ions serve as start electron suppliers as they drift towards the negative electrode and create new start electrons as they collide with the electrode surface. This so called Townsend avalanche mechanism creates a self-sustaining discharge. With increasing current up to 50 mA, the discharge starts to glow as enough photons are generated by:

- recombination of electrons and ions and
- electrons with insufficient kinetic energy to impact ionize gas molecules.

As these collisions are inelastic, the electrons keep most of their kinetic energy, further contributing to impact ionization. The gas molecules remain in an excited state until they emit the absorbed energy by photoemission. The decrease in required voltage for the discharge is caused by a positive ion cloud in front of the cathode. As a result, the electric field in front of the cathode is artificially amplified, stabilizing the discharge. To further increase the current, the voltage needs to be increased. The reason is the ion cloud, fully shielding the cathode. The ion cloud is compressed and heats up until thermal ionization is possible. At this point, thermal ionization is the main driving factor of the discharge, providing for high discharge currents as an arc is created [44].

Paschen's law describes the gas discharge mechanism dependent on the atmospheric gas pressure p and gap g between the electrodes. Both parameters impact the required voltage for the gas discharge by influencing the average free path of discharge contributing electrons. Paschen's law is expressed by a curve over $p \cdot g$ on the abscissa and breakdown voltage U_{bd} on the ordinate. A gas type dependent minimum separates the breakdown for small gaps from large gaps. For small gaps, the Paschen curve transitions into the vacuum discharge mechanism [44]. A characteristic Paschen curve is depicted in figure 2.17.

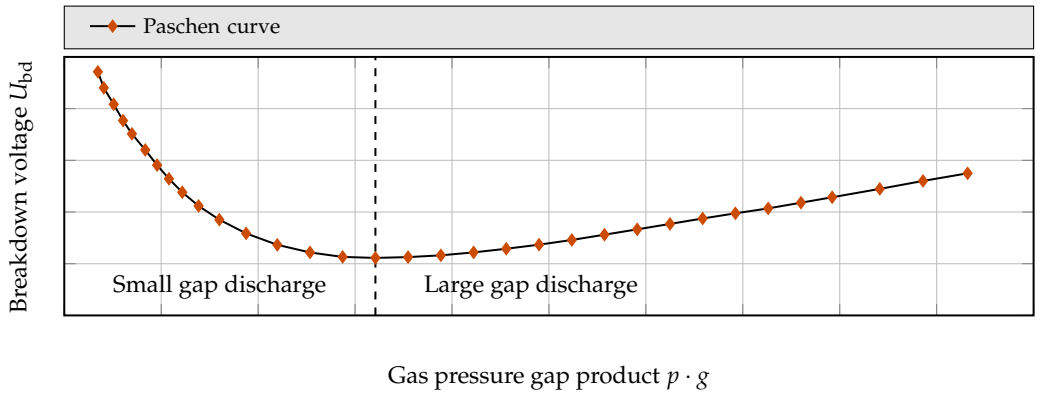

Figure 2.17: Paschen curve with characteristic minimum [62].

Analytically, the Paschen law can be written as [44]:

$$U_{bd} = \frac{B \cdot p \cdot g}{\ln\left(\frac{A \cdot p \cdot g}{\ln\left(1+\frac{1}{\gamma}\right)}\right)} \tag{2.25}$$

with the gas specific constants A and B containing impact and ionization probabilities and γ the 3rd Townsend coefficient. For the small and large gap discharge region the following cases are distinguishable:

- With constant pressure p and decreasing values of g, the probability decreases that an accelerated electron collides with a gas molecule, due to a decreasing presence probability of a gas molecule. The same applies, if g is kept constant and p decreases.
- With constant pressure and increasing electrode gap, the electrical field strength decreases. Therefore, the required electrical breakdown voltage increases. For constant electrode gap and increasing pressure, the average free path length for accelerated electrons decreases. Thereby, the required electrical breakdown voltage increases.

Triple points in a high voltage stressed environment occur when three materials with different electrical permittivities intersect in one point. Then, for frequencies below the resonance frequency of the setup, the electrical field is displaced into the material with the lowest permittivity. The reason for this is the tangential continuity condition of the electrical field. Usually, the material with the lowest permittivity is a gas with the lowest electrical breakdown field strength [44]. A triple point simulation at 250 kHz with 100 V applied to an electrode distance of 1 mm is depicted in section 2.3.

In the left half of the structure, the main voltage drop is applied across the material in the top half with a permittivity of $\varepsilon_r = 4.5$. The high permittivity material ($\varepsilon_r = 3000$) in the bottom left barely carries any voltage drop and electric field. On the right side, the

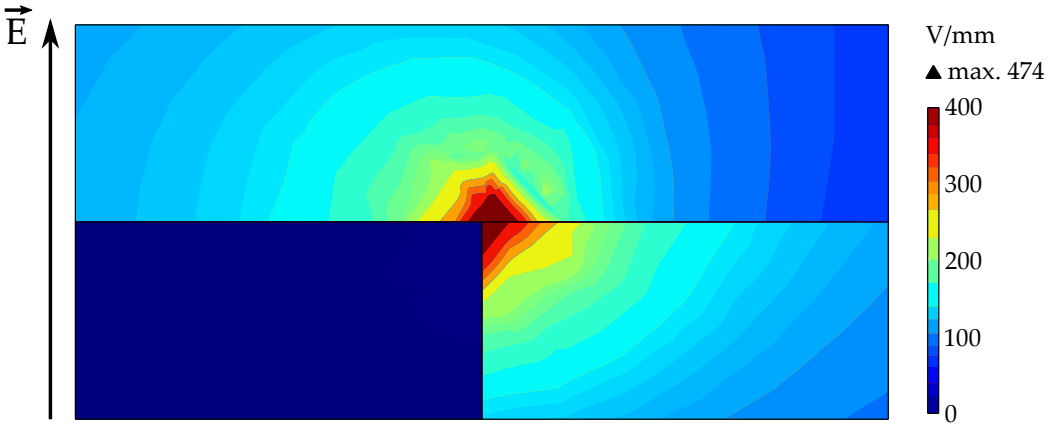

Figure 2.18: Simulation of a triple point consisting of a material in the top half with a permittivity of $\varepsilon_r = 4.5$, bottom left $\varepsilon_r = 3000$ and bottom right $\varepsilon_r = 1$. The RF voltage is 100 V over 1 mm electrode distance and the excitation frequency is 250 kHz.

field distribution is more homogeneous, as the permittivity of the material in the bottom right ($\varepsilon_r = 1$) is in the range of the permittivity of the material in the top half ($\varepsilon_r = 4.5$). However, a displacement of electrical field into the material with the lower permittivity is clearly visible. At the intersection point of the three materials, the electric field is massively displaced out of the material with the highest permittivity. An electrical field strength far beyond the average electrical field strength of a homogeneous setup of 100 V mm^{-1} is created in the materials with the lower permittivities. The highest stress values and largest stressed volume is visible in the material with the lowest permittivity.

Solid Breakdown

The breakdown process in solids is attributed to three different mechanisms. The electrical breakdown (ns to s range), thermal breakdown (min to several h range) and erosion (day to years range) [44]. The occurrence of each breakdown mechanism is characterized by the electrical field magnitude and duration the stress is applied to the material. The characteristic aging curve for the electric breakdown field strength of a solid is depicted in figure 2.19.

The electrical breakdown is of main interest in the ns to s range. Free charge carriers are generated by field emission from the electrodes or in irregularities in the stressed material. The field strength needs to be high enough for the electrons to surpass the valence band to the conduction band. Then, an avalanche process similar to the Townsend mechanism is initiated. Free electrons are accelerated in the electric field and by impact ionization generate further electrons. In practice, breakdown does not occur by the formation of a single avalanche itself, but occurs as a result of many avalanches formed within the dielectric and extending step by step through the entire thickness of the material. This is

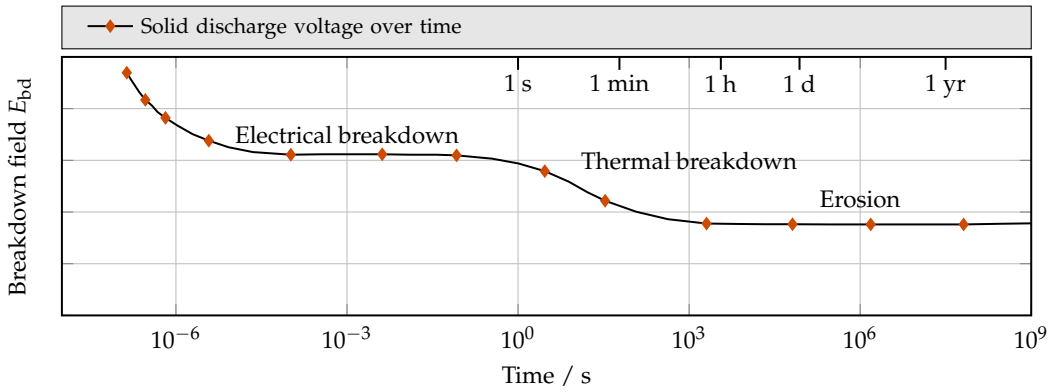

Figure 2.19: Characteristic aging curve of a solid insulation over time [44].

called the Streamer breakdown [44]. A thermal breakdown occurs mainly in dielectrics with disadvantageous dimensions. In particular a large thickness to surface ratio is problematic, as it determines the cooling capabilities of a dielectric [63]. The theory states, by increasing temperature due to conduction and dielectric losses the conduction capabilities and dielectric losses further increase. Thermal runaway is the consequence [64]. With increasing temperature, the activation energy of bound electrons decreases, therefore field emission becomes more probable [64]. By this, the electrical strength of the solid is significantly deteriorated. Now, the breakdown follows the theory of the electric discharge mechanism. The breakdown mechanism of erosion presumes a chemical or physical change of the stressed solid. Chemical or inner erosion includes, among others, oxidation and hydrolysis [44]. A physical change in the stressed solid designates the treeing mechanism. Impurities, interfaces between materials, mechanical defects, voids and gas bubbles cause locally increased electric field components, exceeding the electric strength of the solid or gas over a certain length. Then, partial discharges occur, further damaging the solid thermally, by ultraviolet light and ozone. Carbonization is also possible, resulting in a short-circuited path in the solid material. As a result, the electric field stress in other locations of the solid increases, resulting in reoccurring partial discharges. At some point, the electrical breakdown field strength of the remaining insulation volume is lower than the voltage applied to it. Then, the breakdown follows the mechanism of the electric breakdown [44].

3 Varactor Characterization Methodology

The varactors presented in this work are characterized in regard to their small-signal, large-signal and transient electrical behavior. Main parameters extracted from the small-signal characterization measurements of the varactors are their capacitance, quality factor ($Q = \Im\{\underline{Z}\} / \Re\{\underline{Z}\}$), equivalent series resistance (ESR) and tunability in the frequency range from 5 MHz to 25 MHz and with biasing voltages up to 1.1 kV. Large-signal characterization is performed at 13.56 MHz with biasing voltages up to 6 kV and power levels up to 1 kW. To extract the transient capacitance response behavior of the varactors over time while applying a biasing voltage, a measurement circuit is developed. This circuit utilizes a 13.56 MHz RF voltage as a sampling quantity, being applied to a tunable resonant circuit. The amplitude of the RF envelope is measured and the exact capacitance value of the device under test in the resonant circuit is extracted from the measurements by circuit simulation and analytical approaches.

3.1 Small-Signal Characterization

For characterization purposes of the developed thick film and bulk ceramic varactor pellets as well as acoustically optimized thick film varactor modules and circuit board integrated bulk ceramic varactor modules several measurement fixtures for small-signal measurements are implemented. For thick film varactors with on-substrate biasing circuitry, the fixtures are based on the SMA connector type connected by the fixture to the printed electrodes of the varactor. The main focus is laid upon the minimization of parasitics in the fixture and reliable correction of remaining parasitics, utilizing custom made short/open correction standards. For the acoustically optimized thick film varactors, which do not include on-substrate biasing circuitry, a universal characterization fixture is developed, suitable for measurement setups of large PCB based RF components. The measurement fixture is also used for characterizing the circuit board integrated bulk ceramic varactors (CBIVM). Bulk ceramic pellets are characterized in an APC7 based, temperature controlled fixture.

3.1.1 V/I Measurement Principle and Setup

All presented varactor types are characterized in regard to their small-signal behavior with the V/I measurement method. The measurement method is implemented in the impedance

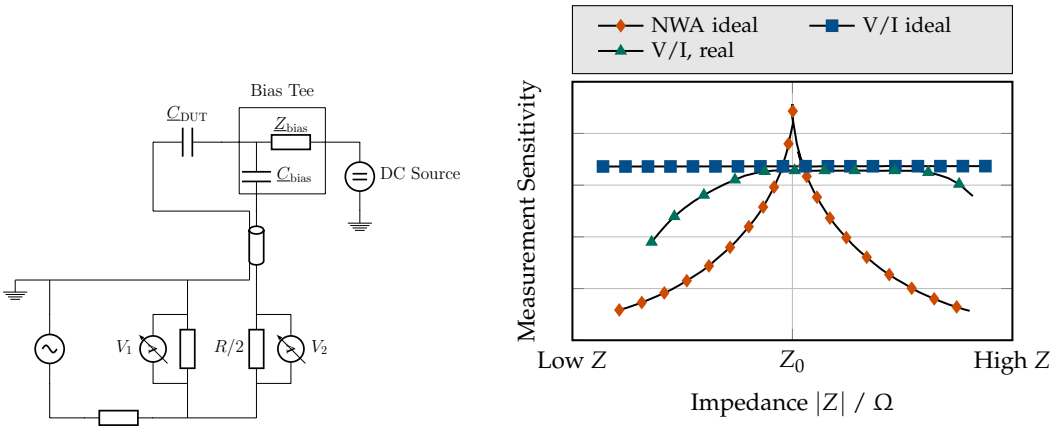

(a) V/I measurement circuit.

(b) Sensitivity of the V/I measurement method vs. VNA reflection method.

Figure 3.1: V/I measurement circuit and theoretical sensitivity of the reflection coefficient vector network analysis and V/I method for various DUT impedances [65].

analyzer Keysight E4991B. The device extracts the reflection coefficient Γ from the complex impedance by performing a voltage and current (V/I) measurement in regard to magnitude and phase. Vector network analysis (VNA) based methods, as well as the impedance analyzer feature a 50 Ω wave impedance output. Main advantage of the V/I principle is the independence of the measurement accuracy from the wave impedance of the setup in contrast to the VNA based method. The impedance of the capacitive DUTs presented in this work, show a small real part in the range of 0.1 Ω to 2 Ω and a larger frequency dependent imaginary part in the range of −2 Ω to −25 Ω at 13.56 MHz. However, the characteristic wave impedance of 50 Ω of the circuit is never met with the capacitive DUTs. Main challenge is the accurate acquisition of the small real part of the impedance, as it is closely located at the lower limitation of the measurement circuit. The internal measurement circuit and the theoretical measurement accuracy of the V/I and network analysis method are depicted in figure 3.1 [65].

The impedance of the DUT is calculated from the measurement of the voltages V_1 and V_2 by [65]:

$$\underline{Z}_{\mathrm{DUT}} = \frac{R}{2}\left(\frac{\underline{V}_1}{\underline{V}_2} - 1\right) \tag{3.1}$$

The device measurement accuracy for C, Q and ESR on the measurement parameters, such as frequency, output power and averaging factor. The DUT impedance also plays a role in the exact measurement tolerances of the device [66]. In this work, the small-signal measurement range for thick film varactors is set to 5 MHz to 25 MHz. An oscillator power level of 0 dBm

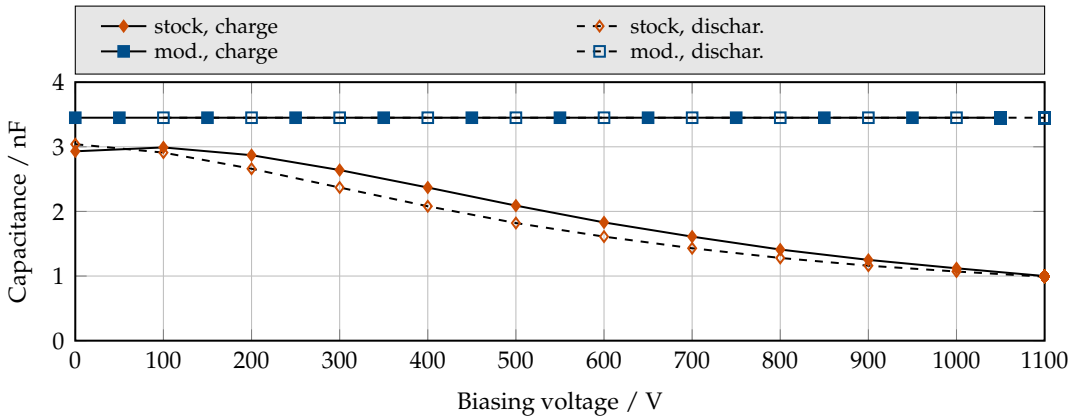

Figure 3.2: Comparison of the stock and modified biasing tee in regard to blocking capacitance over biasing voltage.

with an point averaging factor of 4 is chosen as a compromise in measurement accuracy and time. With these settings at 5 MHz and for impedances $|\underline{Z}|$ up to 300 Ω, the relative C, Q and ESR error is ± 0.01 %, ± 2.23 %, ± 2.23 % respectively. At 25 MHz the relative errors for C, Q and ESR are ± 0.01 %, ± 2.42 %, ± 2.42 % respectively. Bulk ceramic pellets are characterized in a larger frequency range from 1 MHz to 45 MHz, as the characterization fixture provides for a significantly decreased parasitics, due to the advantageous geometry of the pellets. All other settings are retained. For the changed frequency range, the device provides for a relative measurement accuracy for C, Q and ESR of ± 0.01 %, ± 2.19 %, ± 2.19 % at 1 MHz and ± 0.01 %, ± 2.61 %, ± 2.61 % at 45 MHz. For protection purposes of the impedance analyzer, for all measurements that include the application of DC biasing voltages, a modified Tektronix PSPL 5531 DC biasing tee is connected in series to the DUT. The biasing tee features an operational frequency range from 750 kHz to 10 GHz with a maximum DC biasing voltage of 1.5 kV. The 2.2 nF stock blocking capacitor in the bias tee is based on the ferroelectric material Y5U with a temperature dependence of −20 % to 80 %, see figure 2.3. Additionally, a voltage dependence of the capacitor is observed. As a result, the bias tee in its stock condition is not capable of serving in a high precision measurement circuit, as the calibration would only be valid for static components. Therefore, it is exchanged with a 2.2 nF NP0 based capacitor from Knowles. The capacitor features a 2 kV DC voltage rating. The measurement data of the stock and modified DC biasing tee, in regard to the exchanged DC block capacitor is depicted in figure 3.2. The 3-port S-parameter measurement data before and after exchanging the DC block capacitor are depicted in figure 3.3 with port 1 on RF in, port 2 on RF+DC out and port 3 on DC in.

The S-parameter measurement data indicates a fully functional modified biasing tee with marginal deviation from its stock properties in regard to reflection, transmission and isolation. Capacitance over voltage characterization shows a fully removed voltage dependency of the modified DC block capacitor compared to the stock one. As a result, the modi-

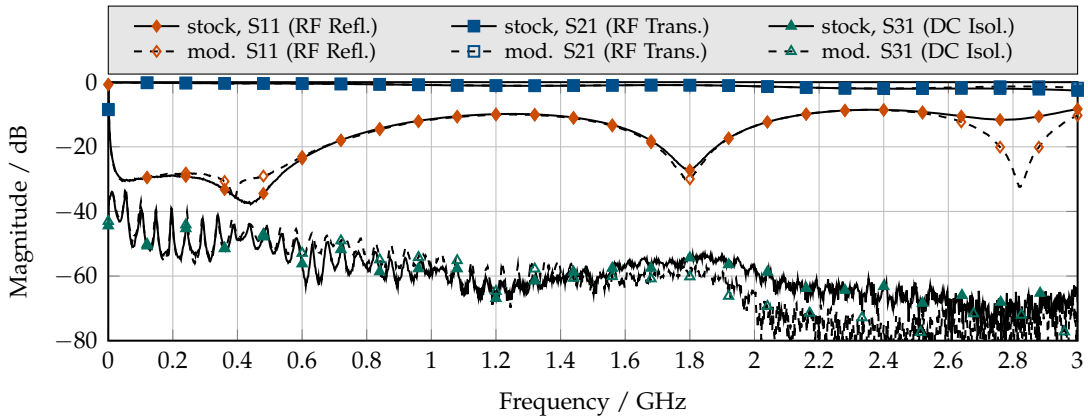

Figure 3.3: Comparison of the stock and modified biasing tee in regard to reflection, transmission and isolation.

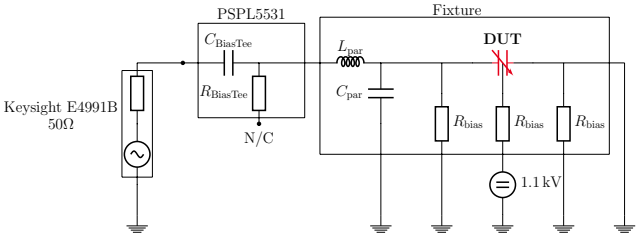

Figure 3.4: Equivalent circuit model of the characterization scheme for a BST thick film varactor with on-substrate DC biasing mounted in a characterization fixture introducing parasitics (see figure 3.5).

fied biasing tee is considered compatible with the intended small-signal characterization measurements.

3.1.2 Thick Film Varactor Characterization with On-Substrate Biasing

To characterize thick film varactors, two different connection methods are implemented, which will be explained in the following. For varactors with on-substrate biasing, characterization fixtures are manufactured, connecting a 3.5 mm SMA port to the electrodes of the varactor. The characterization equivalent circuit with the corresponding fixture parasitics is depicted in figure 3.4.

To characterize varactors with on substrate biasing, a measurement fixture is designed which provides connectors to the RF pads of the varactor as well as to the RF decoupled DC biasing pads, see figure 3.5. All connectors are made of copper to minimize ohmic losses and parasitic capacitances are reduced by avoiding opposing faces of different potential or

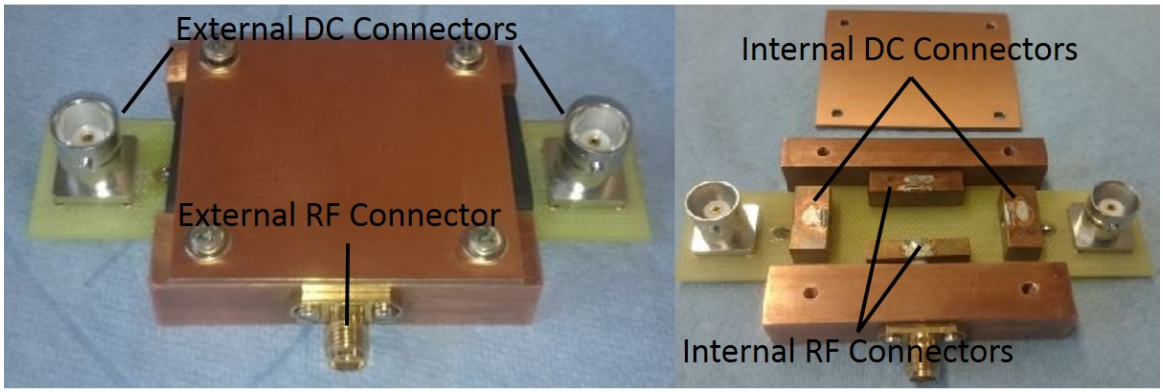

Figure 3.5: Characterization fixture for thick film varactors with on-substrate biasing. On the left side the fixture is closed with a metalized cover plate. On the right side, the internal RF and DC connectors are visible. ©2016 IEEE.

increasing the distance between them. The fixture consists of a non-metalized FR4 ground plate, which is mounted in recesses of two copper blocks. These blocks are externally connectable to the RF by an SMA connector. On the ground plate, four internal copper blocks are mounted, which connect to the varactor. Two opposite internal copper blocks each provide for the RF and DC connection. The external RF connector blocks are electrically connected to the corresponding two internal RF copper blocks with screws providing for the electrical connection, as well as mechanical stabilization. DC biasing voltage is applied to the fixture with two standard BNC connectors on the ground plate. The ground plate provides for the connection of the BNC connectors to the corresponding internal two DC connector blocks. In order to mount the varactor, it is placed in the fixture and pressed against the internal connector blocks with an FR4 cover plate. One side of the FR4 cover plate is metalized providing for the return path of the electric circuit. Connection problems occur when the internal blocks of the fixture do not share the same height. Therefore, copper screws in these connector blocks are implemented to compensate for the unequal elevation.

The fixture is connected to the E4991B impedance analyzer from Keysight using a 3.5 mm SMA standard connector. The impedance analyzer is calibrated using a 3.5 mm SOL calibration kit. First, the fixture is characterized to obtain its parasitic short inductance L_{par} and open capacitance C_{par}, see figure 3.4. For this, one shorted varactor dummy with no BST layer and one opened varactor dummy with no BST layer and no top electrode are placed in the fixture. With these values, a fixture correction on all measurements with varactors installed in the fixture is performed. The measurement results are depicted in figure 3.6.

The fixture compensation parameters are determined as 16.8 pF open parasitic capacitance and 6 nH parasitic short inductance at 13.56 MHz.

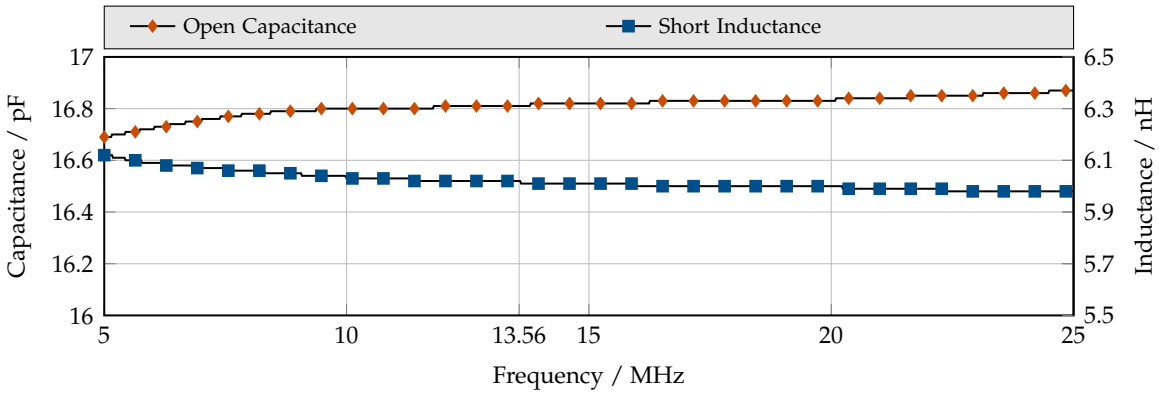

Figure 3.6: Parasitic inductance L_{par} and capacitance C_{par} obtained from the characterization measurements of the fixture.

3.1.3 Bulk Ceramic Pellet Characterization

In this work, bulk ceramic disk varactors with a diameter of 16 mm and thicknesses from 0.6 mm to 1 mm are processed to achieve the desired capacitance range as well as compatibility with FR4 based PCB material. Furthermore, the acoustical behavior of the disk varactors is mainly dependent on the thickness, therefore several different thicknesses are evaluated in this regard. The processing of the disk varactors includes the application of a top and bottom electrode metalization. The metalized surface of the disk varactors is limited to a maximum diameter of 11 mm, leaving a 2.5 mm unmetalized strip on the pellets edge. The reduced diameter of the electrode compared to the diameter of the pellet introduces several advantages. The creepage distance along the edge of the pellet is increased, reducing the probability for surface discharges. Electric stray fields in the adjacent air around the pellet are reduced and a misalignment of the top electrode does not necessarily result in a short circuit along the pellet edge. The other electrode is applied with an even smaller diameter to prevent fluctuating capacitance values due to misaligned issues. A diameter range from 6 mm to 10 mm is evaluated. Commonly, the metalization is applied by screen-printing technology. A variety of different metalizations are investigated in regard to their suitability for high-power RF application such as silver palladium, silver platinum and copper. In some cases, the metalization is applied by hand, using a brush and a stencil or galvanically on a printed seed layer. The small-signal characterization fixture is limited to one device, providing for spring loaded contacts connecting to the metalization on both sides of the pellet without having impact on the measured electrical data due to the geometry of the fixture contacts. The fixture is based on the coaxial RF standard connector type APC-7. The inner connector of the fixture is spring-loaded and centrally connecting to the smaller electrode of the pellet. The unmetalized strip around the pellet touches the grounded metallic housing of the fixture in a length of 1 mm. The connection is needed to stabilize

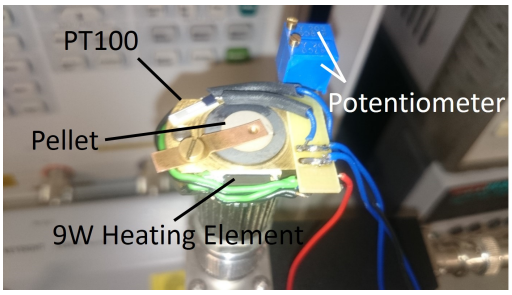

(a) Pellet characterization.

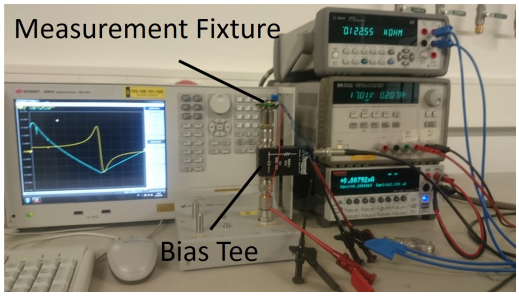

(b) Measurement setup.

Figure 3.7: APC-7 based bulk ceramic pellet characterization fixture and the complete measurement setup.

the pellet in the fixture and to transfer heat from the fixture to the pellet, when temperature dependent measurements are performed. A metal bracket from the grounded housing of the fixture connects to the larger top electrode of the pellet. The fixture introduces a parasitic series inductance of 16 nH, being accounted for in the evaluation of the characterization data. The fixture is depicted in figure 3.7.

The bulk ceramic BST composition chosen for the application in high-power matching circuits is optimized for an operational temperature of 50 °C. To adjust the operational temperature, a mixing ratio of barium to strontium of 70 % to 30 % is chosen, resulting in a Curie temperature of ~ 25 °C, see figure 2.9. To provide for small-signal characterization data in the paraelectric phase of the material, it needs to be heated up to the intended operational temperature. Therefore, the characterization fixture is equipped with two DAWN DN505 9 W self-regulating subminiature heating elements and a PT100 thermal resistor providing for a temperature measurement accuracy of $\pm$ 0.2 K at 50 °C. The heating elements include a control circuit regulating their input current. The manipulative variable is a resistance in the range between 0.7 kΩ to 200 kΩ which is correlated to a temperature. Main advantage is the compensation of small temperature fluctuations during the measurement. However, the temperature is always monitored with the PT100 resistor and stored in the measurement files to account for irregularities caused by larger temperature fluctuations. The pellet is heated via the unmetalized ring, which is thermally connected to the measurement fixture. However, due to the suboptimal thermal connection between pellet and fixture and the resulting temperature difference of 7 °C, the fixture is heated to 57 °C.

3.1.4 Varactor Module Characterization

For thick film varactors mounted on a PCB holding the DC biasing network (varactor module), a generalized fixture is developed, which is also used to characterize circuit integrated bulk ceramic varactor modules. The fixture consists of a metal ground plate with

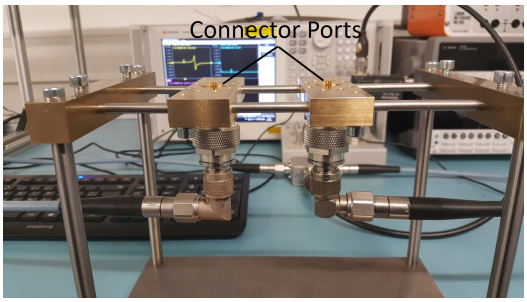

(a) Side view of the module characterization fixture with the spring loaded inner conductors slightly standing out of the two ports.

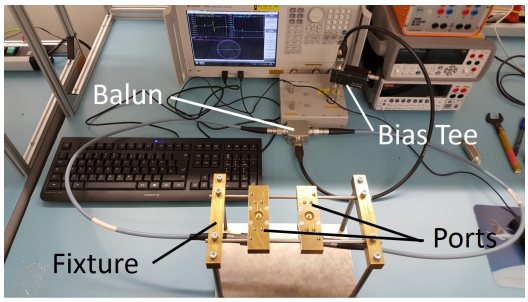

(b) Top view of the whole measurement setup with the impedance analyzer in the back, the protective bias tee, the balun and the fixture in the front.

Figure 3.8: Designed varactor module characterization fixture and setup.

a size of 250 mm × 150 mm and a framework with a height of 170 mm attached to it, holding two custom spring loaded contact connection ports based on the 7/16 HF coaxial standard. The two ports are fed from the single measurement port of the impedance analyzer and hold a signal-ground (SG) configuration on one port and a ground-ground (GG) setup on the other port. The separation of the single port to the two port setup is accomplished with a custom made balun based on coaxial standard type N. To characterize a varactor module, it is mounted on the fixture and pressed against the spring-loaded inner connectors of the two ports of the fixture. Main advantage of the setup is the shielded environment of the signal path up to the connection point to the varactor module. The two ports of the fixture are guided on metal shafts, therefore it is possible to adjust the distance between the ports to characterize PCBs with different sizes. The metal shafts also provide for a low inductance short circuit between the outer ground connectors of both ports, ensuring identical ground potentials on both outer port connectors. Between the ports, mostly free space is available, therefore electric components on the mounted PCB such as DC/RF decoupling resistors or filters do not interfere with the connection scheme. The measurement fixture and whole characterization setup are depicted in figure 3.8

Main drawback of the fixture is the necessity for custom made calibration standards to eliminate parasitics introduced by the connection cables, the balun and the fixture itself, which are only viable for a certain distance between the ports. For every other distance, a new standard or at least a new set of raw calibration parameters has to be obtained. The required calibration standard short, open, load (SOL) is determined by the impedance analyzer. The standards are connected to the inner conductors of the ports, establishing a connection between the ports. Before using the standards for calibration, their raw electrical parameters have to be obtained. Two different methods are presented in this work. One is based on a full-wave simulation of the standards in CST and the other utilizes a partially calibrated 2-port setup to characterize the standards, extracting the raw electrical data from the measurement with a symmetrical 2-port model. Subsequently, the part of the setup

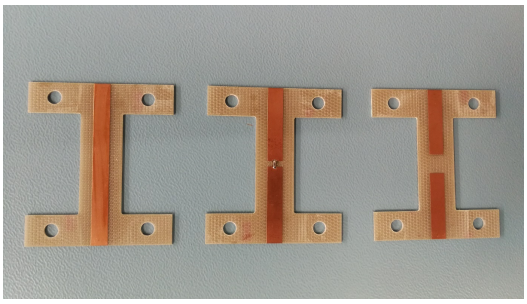

(a) From left: short, load, open.

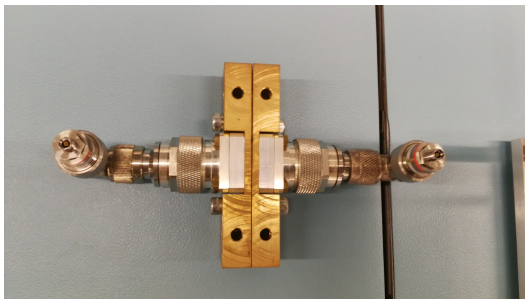

(b) Back-to-back arrangement of the two ports of the measurement fixture with SMA adapters.

Figure 3.9: Module fixture calibration standards and de-embedding characterization setup of the two measurement ports.

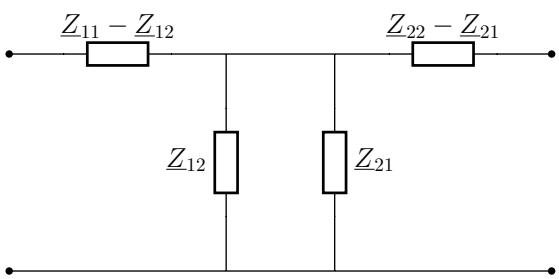

(a) 2-port impedance matrix equivalent circuit model.

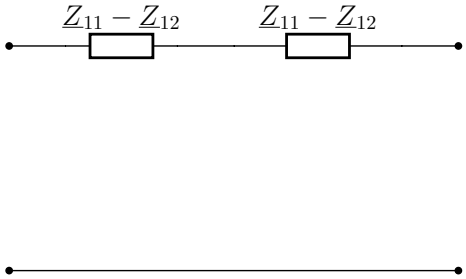

(b) Reciprocal 2-port impedance model for setups with missing ground plane.

Figure 3.10: Calibration standards and back-to-back setup of the two measurement ports of the fixture.

which was excluded from the calibration is measured in back-to-back configuration and utilized for de-embedding the measured data. The designed calibration standards short, open and load, as well as the back-to-back setup of the two characterization fixture ports, are depicted in figure 3.9.

The fixture is extended by a temperature control unit, to guarantee a measurement temperature of 50 °C. This is necessary, as the circuit board integrated bulk ceramic varactors have a Curie temperature of 20 °C and should be operated in the paraelectric phase at 50 °C, see section 2.1.1. The implemented control unit is presented in detail in appendix B.2. For the measurement approach, the equivalent circuit for Z-parameters of a reciprocal two-port network serve as the extraction model. The basic two port equivalent circuit model and the derived reciprocal one for calibration substrates is depicted in figure 3.10. The shunt connection of $\underline{Z}_{12}$ and $\underline{Z}_{21}$ to ground is not considered in the final model, as the calibration substrates do not carry a grounded metalization.

After obtaining the two port S-parameter data from the measurement, it is transformed into two port Z-parameters in Keysights ADS. With the model, the one port complex input impedance of the calibration substrate is calculated according to:

$$\underline{Z} = \frac{2(\underline{Z}_{11} - \underline{Z}_{12}) + 2(\underline{Z}_{22} - \underline{Z}_{21})}{2} \tag{3.2}$$

The same approach is used to characterize the remaining part of the fixture connectors in back-to-back configuration. The obtained raw data sets of the short, open and load calibration substrates from the CST simulation and the measurement with and without de-embedding of the fixture connectors are depicted in figure 3.11.

Overall, the obtained simulated and de-embedded data sets of the implemented custom calibration standard match. For the open and load standard, the de-embedding of the fixture connectors impacts less, compared to the short standard. Here, the fixture connector accounts for 55 % error in the obtained inductance raw data compared to the simulated inductance. For the ESR, the error determined by the fixture connectors is even larger with 89 %. The reason for this, are the spring loaded connectors, which are not optimized for high frequency conduction. To evaluate the impact of erroneous calibration data on a C, Q, ESR measurement, a $\pm$ 1 % parameter variation of the de-embedded calibration data L_{short}, R_{short}, L_{load}, R_{load}, C_{open}, R_{open} is performed and applied to a measurement of a circuit board integrated bulk ceramic varactor module. The detailed equations are given in appendix B.1. The results of the evaluation are depicted in figure 3.12.

At 13.56 MHz the resulting error is less than 1.5 % for the capacitance. For ESR and Q-factor a $\pm$ 1 % variation in calibration data leads to erroneous measurement data smaller than 22 % of the real value. The results show a less significant impact of an erroneous calibration data set on capacitance compared to ESR and Q-factor.

3.2 Large-Signal Characterization

Large-signal characterizations of thick film varactors in general and circuit board integrated bulk ceramic varactor modules are performed in a L-match circuit at COMET AG Switzerland. The circuit is monitored in regard to input power, output power, power loss, tuning state of the mechanical vacuum varactors. The measurement of the DUT quantities is performed indirectly, as a controlled mechanically tunable vacuum varactor compensates for changes of the interconnected DUT varactor. Only the temperature is measured directly at the DUT during high-power operation. The extraction of the characteristic DUT properties, such as voltage and current stresses, capacitance, Q-factor, ESR and power loss are done subsequent to the measurement with an implemented model of the L-match circuit in Keysights ADS. To extract the data of the DUT, a reference measurement of the circuit without a DUT is performed and compared to the same measurement with a DUT included.

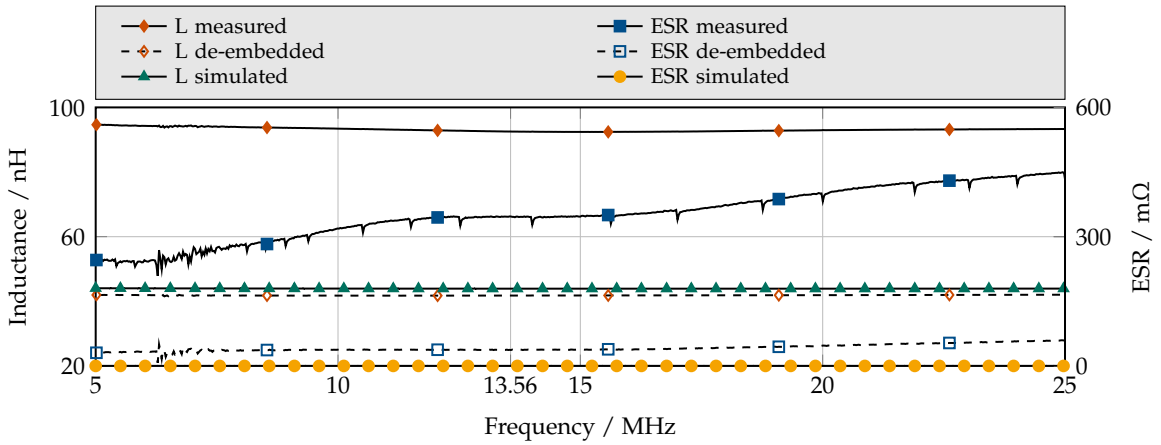

(a) Short.

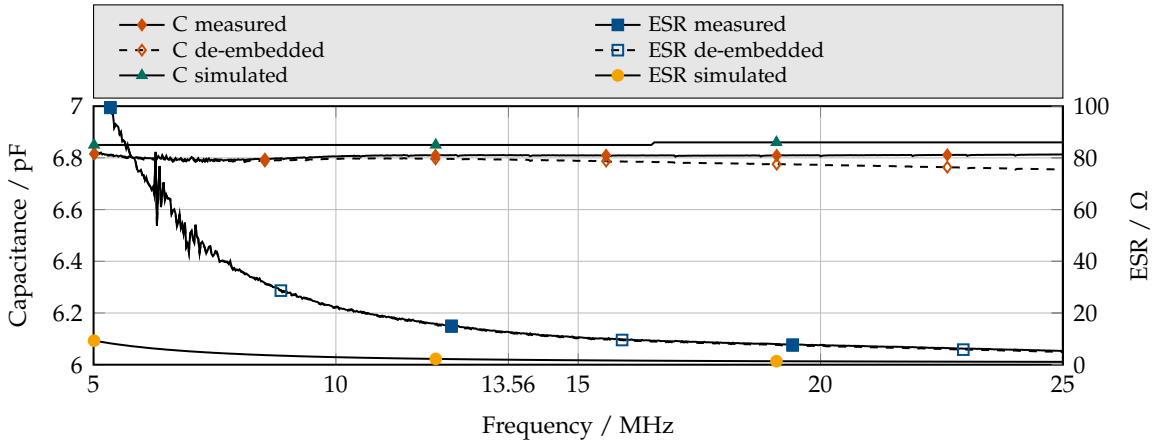

(b) Open.

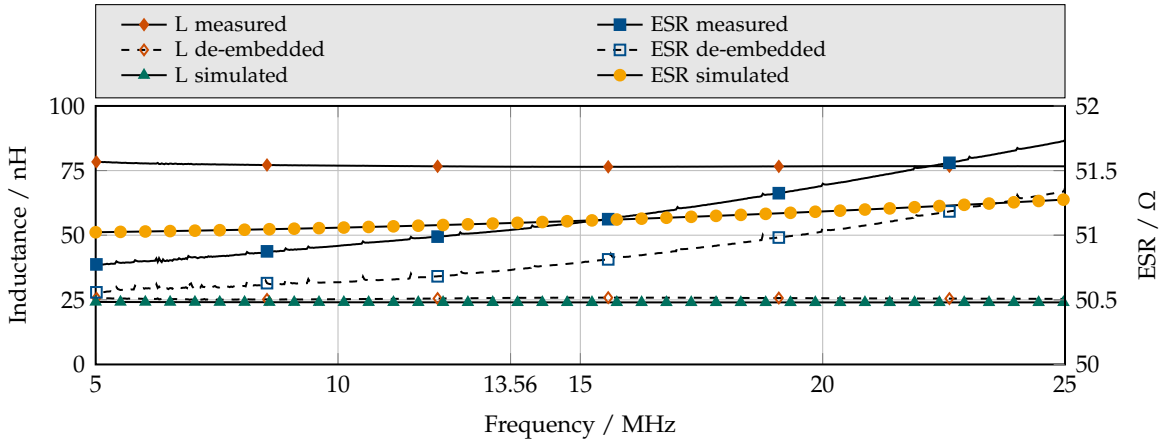

(c) Load.

Figure 3.11: Simulated and raw/de-embedded calibration data for the implemented custom SOL standards.

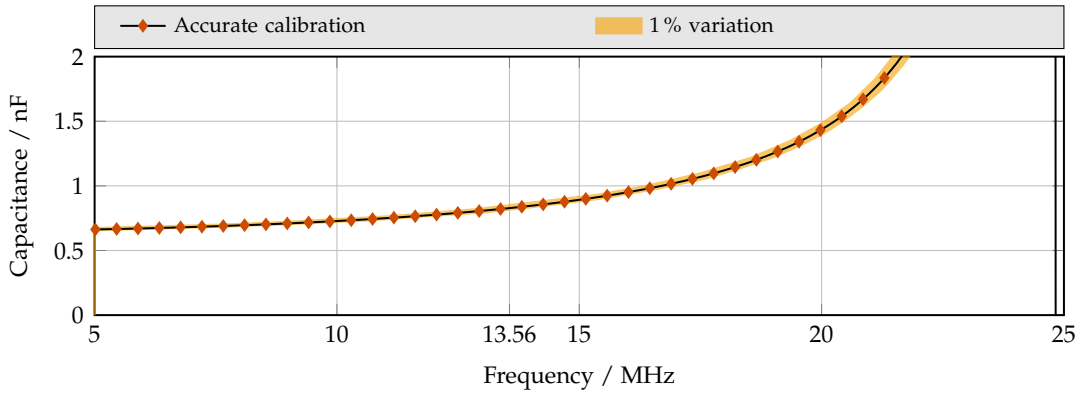

(a) Evaluation in regard to capacitance.

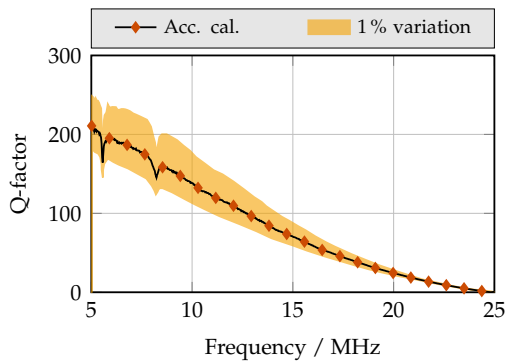

(b) Evaluation in regard to Q-factor.

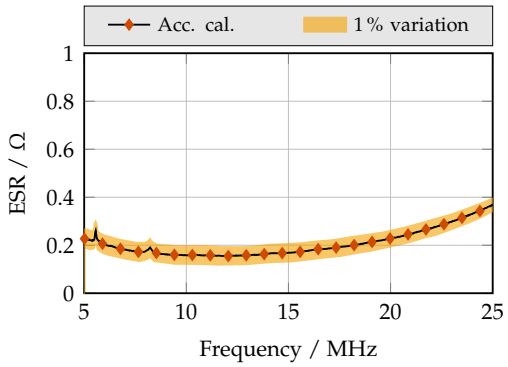

(c) Evaluation in regard to ESR.

Figure 3.12: Impact of a ± 1 % error in compensated calibration data on the capacitance measurement of a circuit board integrated bulk ceramic varactor module.

This is a valid approach, as all electrical components in the L-match circuit are highly linear vacuum varactors and air coils.

Measurement Principle and Setup

The large-signal characterization measurements are carried out in a 50 Ω setup with two L-match circuits in back-to-back configuration and a 10 kW-rated 50 Ω load. The L-match circuits provide for a 6 kW power rating, while the RF generator has a maximum output power of 1 kW. The setup monitors the input power from the generator and the output power of the back-to-back matching system to the 50 Ω load. The monitoring systems are two Bird Model 4421 RF Power Meter provided by COMET. Due to the high RF power, a voltage or current monitoring system is not installed. The voltages and currents are extracted from an exact model of the L-match circuits. The circuit diagram, including parasitics of the measurement setup with the installed DUT varactor is depicted in figure 3.13, where P_{in} is a 50 Ω power source providing up to 1 kW of RF power at 13.56 MHz. The tunable load impedance Z_{M}^{*} is adjustable but set to a fixed impedance for the large-signal characterization measurement. A change of $\underline{Z}_{\text{M}}^{*}$ during the measurement process would alter the loading of every component in the measurement circuit and therefore heavily influence the outcome of the measurement. In general, small values of $\underline{Z}_{\text{M}}^{*}$ result in increased voltage and current stresses of the components in the measurement circuit, while larger values especially reduce the current stresses. The tunable L-match circuit at the input of the RF power source consists in the shunt branch of a mechanically tunable vacuum varactor C_{Vac1} which is in series connection to the DUT thick film varactor. C_{Vac1} is mechanically tunable in the range of 150 pF to 1500 pF. The thick film varactor is placed in a fixture similar to the characterization fixture and connected to the L-match circuit using copper stripes. Varactor modules are installed in the circuit without an additional fixture with copper stripes soldered to the RF pads of the module. C_{Vac1} is controlled using a phase/mag detector and a steepest decent algorithm. Its capacitance value can be acquired with an accuracy of 0.084 pF. A capacitance change of the DUT due to thermal deviation or voltage tuning is compensated by C_{Vac1} due to the fact that the overall capacitance in the shunt branch may not change in order to maintain the matching requirement with the fixed $\underline{Z}_{\text{M}}^{*}$. As a result, the capacitance of the DUT can be extracted from the tuning position of C_{Vac1} and the required overall capacitance in the shunt branch for the matched state. In the series branch of the L-match, a second mechanically tunable vacuum varactor C_{Vac2} is installed. The capacitance range of C_{Vac2} is 50 pF to 500 pF. The varactor is controlled in the same way as C_{Vac1}. An air core inductance L with an ohmic resistance of 0.056 mΩ and an inductance of 280 nH is in series connection to C_{Vac2}. Parasitics of the circuit include series inductances and resistances in each branch, introduced by the internal copper connections. The output of the measurement L-match is loaded with a parasitic capacitance introduced by the coaxial output port.

The measured values of the components and parasitics of the circuit are given in table 3.1.

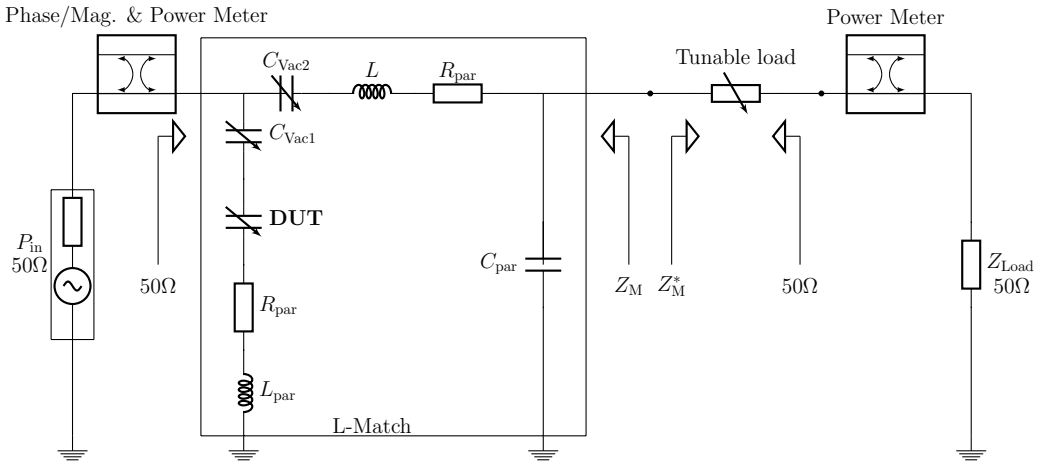

Figure 3.13: High-power characterization circuit with parasitics.

Table 3.1: Measured component and parasitics values of the L-Match circuit.

C_{Vac1} pF	C_{Vac2} pF	L µH	L_{par} µH	C_{par} pF	R_{par} Ω
150..1500	50..500	0.28	0.02	5	0.05

For parameter extraction, in a first step, a 1-port AC/S-parameter simulation model is setup to the reference measurements. For every power level, the same setup is sufficient as the temperature does not impact the impedance of the circuit. However, the absolute losses of the reference circuit increase linearly with the input power level. The relative losses are 1.6 % of the input power, independent of the input power level. The circuits parasitic elements in the simulation are adjusted in a way, that measured input, output and reflected power match the measured ones. Then, in a second step, the DUT is added to the circuit. Here, for every power level an individual circuit has to be set up, as temperature influences the DUTs capacitance and losses significantly. For this, C_{Vac1} and C_{Vac2} values are adjusted from the reference values measured without the DUT to the measured values during large-signal characterization with the DUT included. The DUT is set up as a capacitance with a series resistance. First, the DUT capacitance and resistance is adjusted roughly by tuning C and ESR until a matching $|\underline{S11}| \leq -20\mathrm{dB}$ is achieved. In a second step, C and ESR are fine-tuned until the simulated input, output and reflected power match their corresponding values in the measurement. Typical extracted large-signal characterization parameters of the DUT are capacitance, quality factor, ESR, tunability, temperature, dissipated power as well as voltage and current stresses. The implemented setup with an installed thick film varactor in the shunt branch of the circuit is depicted in figure 3.14.

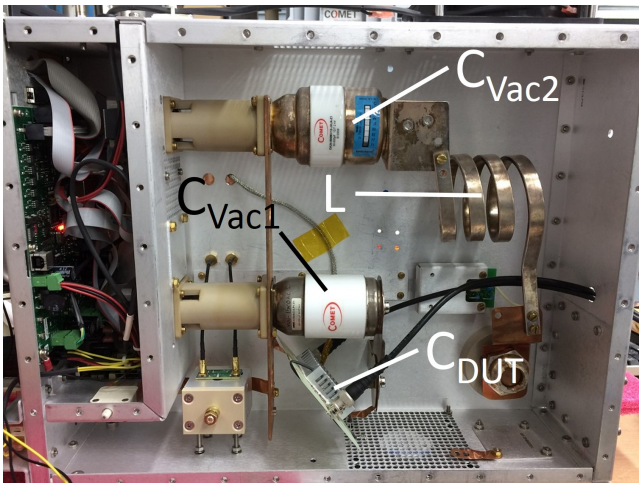

Figure 3.14: Large-signal characterization setup with a thick film varactor.

3.3 Transient Characterization

To evaluate the capacitance response time of the thick film and bulk ceramic disk varactors from unbiased to biased state, a measurement setup and circuit are developed. Commonly used techniques to characterize the transient behavior of tunable capacitive devices include standard steady-state vector network analysis (VNA) methods or non-linearity characterization, such as intercept point of 3rd order (IP3) measurements [67, 68]. For VNA based methods, the single frequency measurement time of the impedance or network analyzer is the main limitation for the resolution of the response time measurement. Modern VNA's optimized for fast data acquisition, achieve single frequency measurement times of 3.5 µs [69]. However, measurement accuracy is significantly reduced by these small acquisition times. VNA based methods are mainly applied to capacitive devices rather than material characterization, as component response times are usually significantly larger compared to intrinsic material response times. From non-linearity measurements, response times of tunable devices or materials are extracted indirectly. For these measurements, the tunable component or material is driven with a large one-tone signal capable of tuning it in the absence of a biasing voltage. The non-linear tuning of the device's capacitance by the large-signal results generates harmonics, measurable with a spectrum analyzer. By increasing the frequency of the one-tone excitation, a condition is reached, when the tuning of the capacitance is unable to follow the excitation frequency. In case of an otherwise linear measurement setup, the harmonics in the output spectrum of the measurement setup vanish. From the excitation frequency, at which the setup becomes linear, the minimum response times of the device can be extracted [68]. With this setup, respones times in the ns realm and lower can be acquired. Therefore, this setup is utilized to obtain the intrinsic response times of tunable materials, presented in [11]. In this work, the achievable extrinsic response times of high-power thick film varactors and varactor stacks with the required

circuitry for high-power operation, such as DC/RF decoupling filtering and DC bias voltage supply, are of main interest. Therefore, a simple, purely transient measurement method is developed and presented, utilizing the RF envelope voltage at a tunable resonance circuit including the DUT capacitance. The measurement is performed with an oscilloscope and the DUT capacitance is extracted from the envelope of the measured RF voltage with a simulation-based RF to capacitance transfer characteristic of the circuit. With this setup, the accurate acquisition of capacitance response times is limited by the oscilloscope bandwidth, the RF frequency, DC bias voltage supply and the DC/RF decoupling filter. The oscilloscope PicoScope 6403D has a 350 MHz bandwidth and a minimum rise time of 1 ns. With a RF frequency of 13.56 MHz, a maximum frequency according to Nyquist criterion of 6.78 MHz can be acquired, corresponding to a rise/fall time of 148 ns. The DC bias circuitry is based on a Keithley 2410 sourcemeter with a maximum output voltage of 1.1 kV. However, due to the output filtering of the source, a minimum settling time of 100 µs for a resistive load is achieved by the source. For large capacitive loads in the nF range, the minimum settling time is at least 1.2 ms. Therefore, a Behlke HTS 151-03- GSM high voltage transistor switch is used as an output stage. The switch features a push-pull stage with a breakdown voltage of 15 kV, a current carrying capacity of 30 A and a rise and fall time of 15 ns. The switch is used to discharge a 10 µF ceramic buffering capacitor to the DUT. The buffering capacitor is charged by the Keithley DC source to 1.1 kV. A waveform generator drives the switch with a 2 s cycling time and 50 % duty cycle. Concludingly, the main limitation factor of the fast transient measurement circuit are the varactor modules themselves, and in particular the RF/DC decoupling lowpass filters, optimized for response times in the 10 µs range, defined by their application in fast tunable high-power matching circuits.

Measurement Principle and Setup

The transient measurement circuit principle is based on a voltage divider between a resistor and a tunable series resonant circuit containing the DUT capacitance. The basic circuit and corresponding voltage behavior over capacitance are depicted in figure 3.15.

The LC resonant circuit is adjusted in a way that its resonance frequency is at the operational frequency of the RF source for an unbiased DUT capacitance. In the presented work, a 13.56 MHz generator is used, which is also capable of handling occurring reflections due to the detunage of the LC circuit from a matching condition. For an exemplary DUT capacitance of 2 nF, an inductance of 69 nH is required to obtain a resonance frequency of 13.56 MHz. It should be noted, that this inductance value represents a lower limit manageable in regard to the size of the inductor. Smaller unbiased capacitance values result in larger, more manageable required inductor sizes. For the transient characterization measurement, the generator voltage as well as the voltage across the LC circuit is measured. At resonance frequency, the impedance of the LC circuit is exclusively determined by the parasitic ESR of the resonant circuit, while the reactive parts of L and C in the complex impedance cancel out. Assuming resistances in the 100 mΩ range for both L and C, the

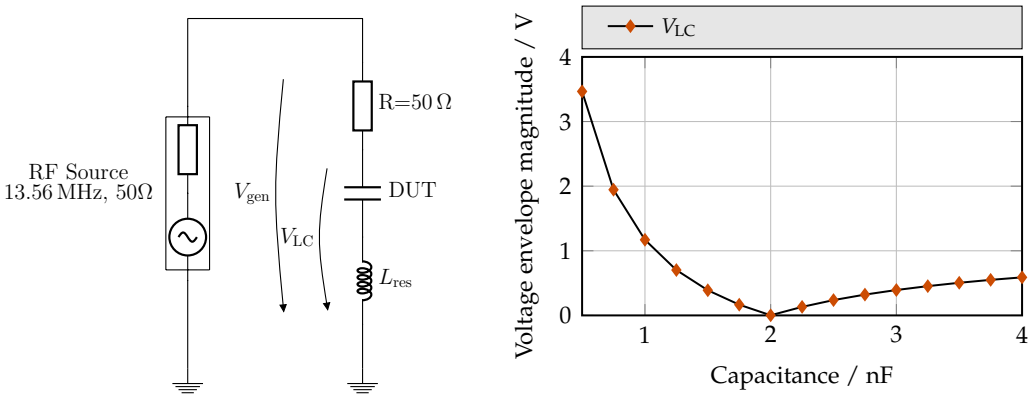

(a) RLC measurement circuit.

(b) Envelope voltage magnitude vs. capacitance in the LC circuit. The resonance frequency of the LC circuit is 13.56 MHz for $C_{DUT} = 2\,nF$.

Figure 3.15: Basic circuit for transient measurements and characteristic capacitance response.

voltage across the LC circuit at resonance is $\sim 0\,V$. For in- or decreasing capacitance values, the resonance frequency of the LC circuit is detuned, resulting in an increase of the voltage across the LC circuit. From the magnitude of the voltage envelope at the LC circuit, C can be calculated assuming knowledge of all component values and parasitics in the circuit and the input voltage from the RF generator. In figure 3.15, the voltage envelope trace shows a non-unique correspondence between voltage and capacitance. For an automated measurement evaluation, this might create issues in regard to uniqueness of capacitance extraction. Therefore, it is important for the LC measurement circuit to be well tuned to the excitation frequency of the generator. The sensitivity of the LC circuit denoted as:

$$S = \frac{dV_{LC}}{dC} \tag{3.3}$$

shows a maximum when the resonance frequency is detuned to higher frequencies. This is the case for decreasing C values compared to the C value at resonance frequency. Therefore, the selection of the resonance frequency in regard to the unbiased capacitance also denotes the operational measurement region of the circuit. In general, both regions left and right from the resonance minimum can be used for the measurement, see figure 3.15. However, the sensitivity of the circuit is significantly increased for DUT capacitances in tuned state below the resonance minimum. The integrated circuit board bulk ceramic varactors are equipped with RF/DC biasing filter solutions for a frequency range up 400 kHz, resulting in a minimum rise time of 10 µs, see section 5.2.1. However, the large ferrite filter coils with values in the µH range and high DC current capabilities introduce significant voltage overshoot when exposed to fast transient, heavy current voltage steps. To prevent these

transients from coupling into the measurement taps, an additional PI filter is implemented in the circuit. The filter consists of two 1.2 µH coils to ground and a 1.8 nF capacitance. The series capacitance of the filter introduces a DC block in case of a breakdown of one of the DUT varactors. The circuit and the voltage overshoot at measurement tap 2 for a step voltage of 1 kV and a rise time of 1 µs are depicted in figure 3.16.

To provide for a selection of measurable DUT capacitances, the implemented LC measurement circuit holds various inductance values preinstalled at different positions on the PCB. Dependent on the unbiased capacitance value, the DUT varactor module is connected to the corresponding inductance value at a certain location on the PCB to obtain a resonance frequency close to 13.56 MHz. The inductance range preinstalled on the board ranges from

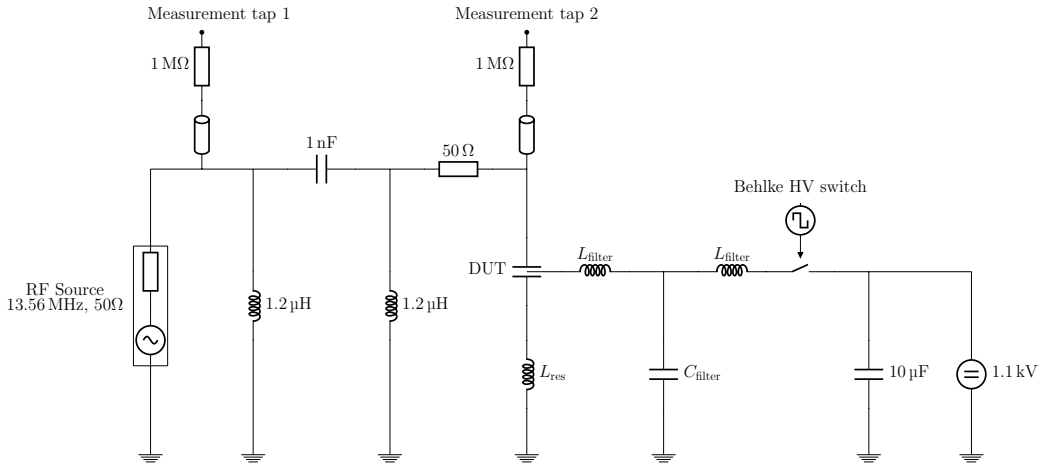

(a) RLC measurement circuit with fast transient DC suppression in the measurement path.

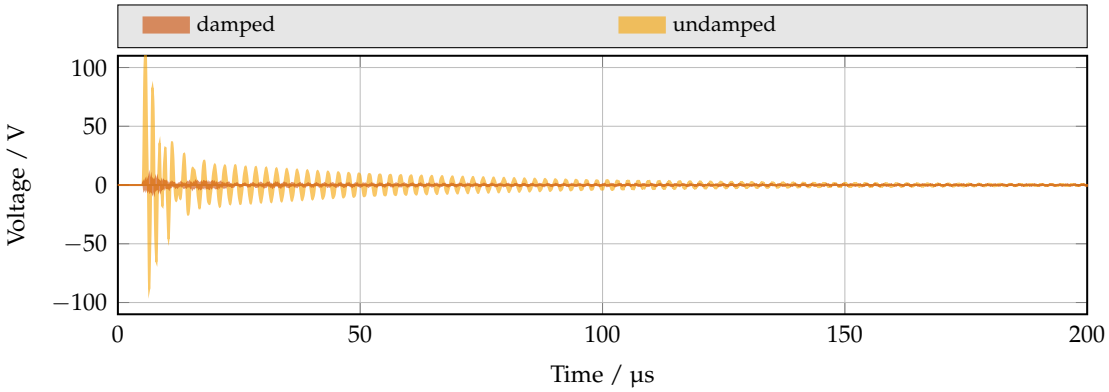

(b) ADS simulation results of the fast transient coupling into measurement tap 2 with and without filtering. A 1 kV step voltage is applied with a rise time of 1 µs.

Figure 3.16: Basic transient measurement circuit with filtering and simulation result comparison between the unsuppressed and suppressed case.

44 nH to 1820 nH, resulting in an unbiased capacitance measurement range from 3100 pF to 76 pF.

To show the robustness ot the capacitance extraction, the measurement circuit is expanded with parasitics. A $\pm$ 5 % parameter variation is applied to all relevant components in the circuit. The dominant parasitics are ohmic losses in the metalization, filter coils, the resonant circuit and a parasitic inductance of the metal strip connecting to the inductance value taps. The ohmic losses are modeled with 0.1 Ω while the parasitic inductance is included in the parameter variation of the resonance inductance. A parasitic capacitance of the PCB to ground is introduced in the model. The capacitance is modeled with a value of 2 pF from the parallel plate capacitance equation, with a gap of the board to the grounded housing of 70 mm and an electrode area of 52 mm $\times$ 300 mm. A simulation with the parameter variation is performed in Keysights ADS. The expanded transient equivalent circuit model and the results of the $\pm$ 5 % parameter variation simulation are depicted in figure 3.17.

The $\pm$ 5 % parameter variation in the circuit results in a relative error of the capacitance reading from the voltage envelope of maximum 6.6 %. By inverting the obtained curve, the RF voltage to capacitance transfer characteristic is obtained which enables an extraction of capacitance values from the RF envelope measurement. The measurement principle is performed on a thick film varactor and a circuit board integrated bulk ceramic disk varactor module in section 4.5 and section 5.2.1.

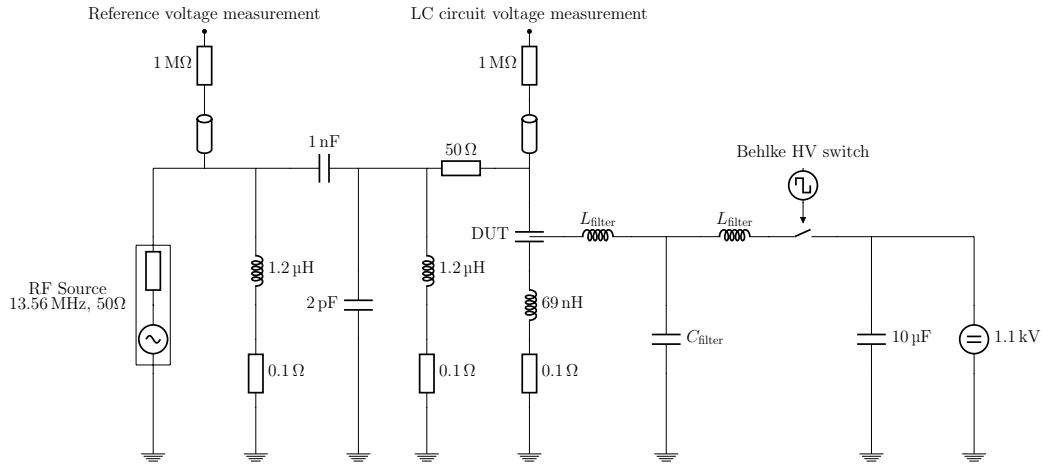

(a) Transient characterization circuit with parasitic components.

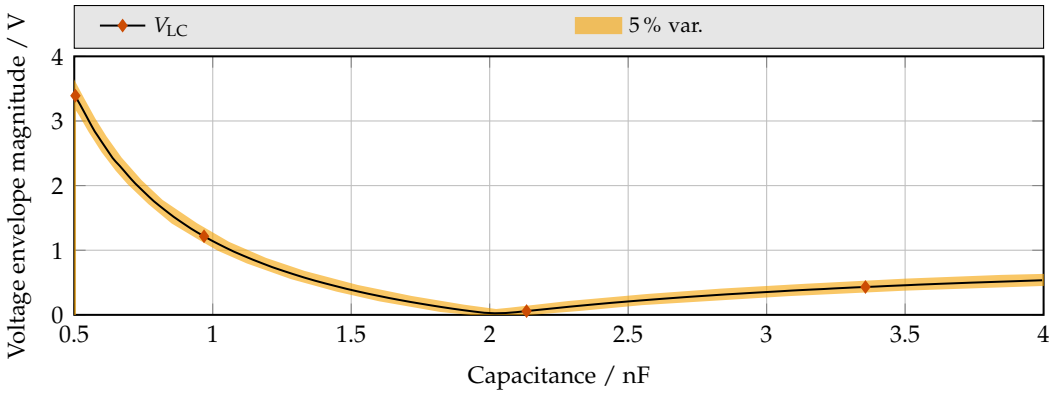

(b) Lookup curve with a ± 5 % parameter variation for robustness examination.

Figure 3.17: Transient characterization circuit with parasitic components and $V(C)$ lookup curve with ± 5 % parameter variation obtained at the LC circuit voltage measurement tap.

4 Design and Demonstration of High-Power Thick Film Varactors

The design of thick film varactors for high-power applications is driven by two sets of parameters. The first set arises from the manufacturing process and technology and defines the physical properties of the dielectric material such as density, porosity, permittivity, elasticity, etc. Most of these parameters are based on literature reference values. Possible deviations are modeled during the design process. The second set of parameters is defined by the application and its requirements on the varactor. These parameters include for example capacitance, DC biasing voltage, RF voltage amplitude, current carrying capabilities, dissipated power, etc. and are set up by the outer dimensions of the varactor and its geometry. Due to their accessibility during the design process, the second set of parameters is subject to change more frequently than the first set. Most of these parameters are correlated to each other not only in their set but also between sets. For example, an increased permittivity, due to a change in the sintering process, leads to a different unbiased capacitance value without a change in geometry of the varactor [49]. The sintering process, however, also affects the loss tangent of the material resulting in a change of required cooling surface [14]. In this work, both sets of parameters are targeted to obtain varactors suitable for application in matching circuits with power ratings up to 1 kW. The thick films are applied by screen-printing, a low cost, fast and accurate depositioning technique, see section 2.2.2. For metalization, LTCC and screen-printing compatibility is pivotal as well as solderability and electrical conductivity. These requirements limit the selection of a metalization paste to just a few Ag-based pastes. All thick film varactors presented in this work are vertically layered metal-insulator-metal (MIM) varactors. This kind of setup introduces several advantages in comparison to planar structures. The small electrode gaps and high electrode overlap regions result in high single varactor capacitance values. Additionally, the electrode setup shows a favorable field utilization in regard to the DC biasing field compared to planar structures.

4.1 High-Power Varactor Design Process and Implementation

This section presents, the design process for thick film varactors optimized for high-power operation. Compared to acoustically optimized thick film varactors, the acoustical behavior is not included in the design process but monitored and verified with accompanying

simulations. Thereby, necessary reference data is obtained to quantify the benefit-cost ratio of the more complex acoustically optimized high-power thick film varactors. In general, for the implementation of high-power thick film varactors, two design challenges occur. Due to their thin dielectric layer compared to bulk ceramic varactors, the RF voltage amplitude is in the range of the DC biasing voltage leading to self-tuning of the varactor by the RF voltage for a single MIM structure. A 1:10 ratio between RF and DC voltage is usually desired. In addition, the electrical breakdown field strength of the thick film is easily exceeded since DC and RF voltage are superimposed at the MIM structure. The second challenge is the large permittivity of the thick film resulting in small geometric dimensions for a single MIM structure to obtain the required capacitance value for the high-power application. The large cooling surface, is contradicting this design flow, but required to ensure a stable operating temperature of the varactor and avoid temperature induced self-tuning during high-power operation (see figure 2.9b). A possible solution to all of these partially contradicting design limitations is the strategy of serial stacking MIM structures to distribute RF energy among a larger area while keeping reasonably high overall capacitance values. In general, a single or uneven number of series connected MIM structure is an unfavorable setup, as the DC biasing potential requires an isolated connection point. Therefore, at least two series connected MIM structures, a MIM cell, form the basic varactor structure presented in this work. However, with increasing number of interconnected MIM cells, the complexity of the biasing circuit increases. More severe for the fast biasing scheme and motivating this work, the load capacitance increases, as the RF-wise serially stacked varactors are connected in parallel with respect to the DC source. As a compromise between complexity and power handling capabilities, a maximum serial connected stack of four MIM cells is presented in this work.

The designed varactors are monitored but not optimized in regard to their acoustic resonance locations in the impedance spectrum. An interfering resonance spike of the equivalent series resistance (ESR) of the varactor with the operational frequency of a high-power matching application causes significantly increased losses in the varactor and reduces its power handling capabilities severely, see figure 2.8. The designed varactors are developed for single frequency, high-power matching circuits utilized for plasma etching or depositioning processes. The required power ranges from a few W to 1 kW. The design flow, developed in this work for varactors capable of stably operating at these power levels, is depicted in figure 4.1.

Matching circuits, adapting the impedance of the plasma to the impedance of the RF generator, need to be capable of handling the occurring heavy currents and high voltages in the stationary case and during a change in load when the plasma is ignited or extinguished. The plasma, as a highly non-linear load, reflects harmonics of the excitation frequency back into the matching circuit superimposing with the RF voltage of the generator, resulting in additional voltage and current stresses at the components of the matching circuit [70]. Therefore, an exact model of the L-match circuit, including parasitics, is set up in Keysights ADS to estimate the expectable voltage and current stresses and the dissipated power of a thick film varactor substituting a state of the art vacuum capacitor. The utilized circuit

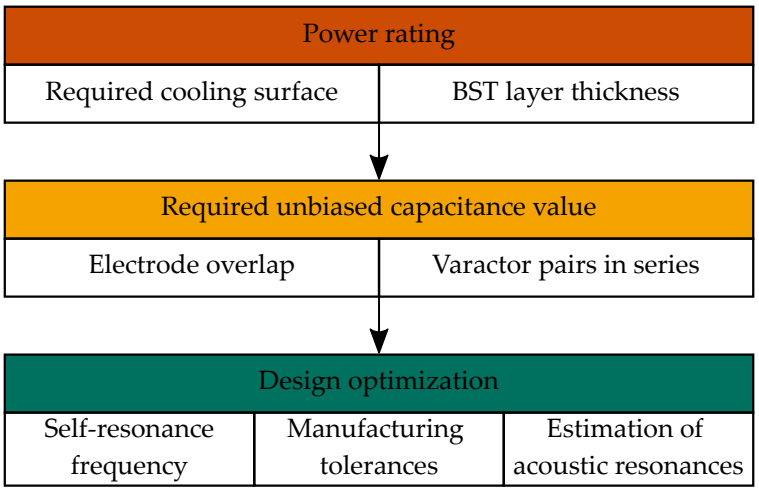

Figure 4.1: Design flow for high-power optimized thick film varactors.

is the same one used for large-signal characterization and depicted in figure 3.13. For the application of a thick film varactor, two possible positions in the L-match circuit are viable. Either C_{Vac1} or C_{Vac2} can be substituted with a thick film varactor for testing. In a final application, both varactors are supposed to be substituted. For characterization, the position of C_{Vac1} in the circuit is best suited for a substitution by a high-power thick film varactor for two reasons:

- The required capacitance value in this position is well in range of a thick film varactor without the need for serial stacks including more than three varactor cells. For three varactor cells the DC biasing network can be implemented on-substrate. For higher stack numbers this is not possible anymore, due to space limitations on the carrier substrate.
- The shunt branch supplies a direct path to DC/RF ground. As a result, the DC biasing network for the varactor can be simplified.

To design the high-power thick film varactor, the differential voltage and current through the vacuum varactor C_{Vac1} at a certain power level serves as the foundation of the design process. For this, a load is chosen according to an inductively coupled plasma with the impedance in the ignited state [70, 71]. An input impedance of $\underline{Z}_{\mathrm{M}}^{*}$ into the load of $(1.86 + 3.02\mathrm{i})\,\Omega$ and $(2.92 + 0.85\mathrm{i})\,\Omega$ is presented to the matching circuit for power levels up to 400 W, see figure 3.13. For power levels up to 1 kW a load impedance of $(3.7 + 14.9\mathrm{i})\,\Omega$ is set up. The different loading impedances are necessary, due to the temperature dependent unbiased capacitance value and the limited tuning range of thick film varactors. With an increasing power level, the temperature in each component of the circuit is increased as a consequence of the increase of dissipated power. The vacuum varactors provide for a stable base capacitance value and a tunability of up to 90 % independent of temperature. BST

based thick film varactors have a temperature dependent unbiased capacitance value and a tunability of up to 40 % at room temperature [10, 14]. Both values reduce with increasing temperature (see section 2.1.1). As a result, the load impedance has to be adapted for the changed component value of the thick film varactor.

The model depicted in figure 3.13 is set up in Keysights ADS to obtain reference data for the occurring voltage and current stresses in the circuit. First, a 1-port S-parameter simulation of the circuit is set up to adjust the matching for a certain load. To find the exact values for C_{Vac1} and C_{Vac2}, $\underline{S11}$ is evaluated. A reflection $|\underline{S11}| \leq -20\mathrm{dB}$ is assumed to be sufficient. For a given load impedance, the circuit is manually adjusted to meet the matching criteria. This is necessary, due to the large difference from the generator impedance to the load impedance, resulting in a narrow-band matching. For the application, this means that the zero-bias capacitance has to be reproducible, in regard to the varactor fabrication process. In biased state, the capacitance has to be either reproducible for each biasing voltage as well and remain static by accurately controlling the temperature or readjustable to compensate thermal detunage. With the given setup, the voltage and current stresses at C_{Vac1} are simulated for different power levels. For that, both varactors C_{Vac1} and C_{Vac2} are assumed to be of constant capacitance. During development, the parameters of C_{Vac1} are further adapted to the parameters assumed for a thick film varactor. While adapting the varactor parameters, matching has to be closely monitored as it is affected by the changes. In order to estimate the dissipated power of the thick film varactor, a quality factor of 100 is added to it, taken from [14]. The simulation results for different load impedances are shown in table 4.1. With increasing input power level and decreasing capacitance C_{Vac1}, simulating the increase in temperature of a thick film varactor, the loading of the varactor changes to less stressful states. Equilibrium operation points arise. To account for that, not only the evaluation of the input power level is taken as a benchmark value of the varactor but its exact loading condition with V_{RMS}, I_{RMS} and P_{diss}.

The voltage stresses indicate, that for power levels up to 200 W, one varactor cell is sufficient to reduce the voltage amplitude per MIM structure to 100 V. Then, with a biasing voltage of 200 V for MIM thick film varactors given in [10], a DC to RF ratio of minimum 2:1 can be achieved. Commonly, higher ratios are of course desired. However a ratio of 10:1 is hard to achieve with the given technology and for the intended application unnecessary, as prevented self-tuning of the varactors suppresses harmonics, which are introduced anyway by the highly non-linear plasma. For higher power levels, series stacks of two and three varactor cells are required to keep the same ratio. The simulated dissipated power values are used to set up a thermal simulation of the varactor to estimate the required cooling surface and therefore electrode overlap area of the varactor.

The thermal simulation is performed in COMSOL Multiphysics and combines the transfer of heat in a solid with the laminar flow of a fluid/gas for the stationary case, meaning in equilibrium state of heat inflow and outflow. It is possible to not only estimate the temperature profile in the varactor itself but also take the cooling effect of an air flow due to a fan into account. Additional cooling with a heat sink on the varactor is also considered

Table 4.1: Simulated stresses at C_{Vac1} for different load impedances and L-match input power levels.

Z_{M}^{*}	C_{Vac1}	P_{in}	V_{RMS}	I_{RMS}	P_{diss}
Ω	pF	W	V	A	W
$1.86 + j3.02$	750	99	104	6.6	6.9
		199	147	9.4	13.9
		299	180	11.5	20.8
		399	208	13.3	27.7
$2.92 + j0.85$	670	99	94	5.3	5.0
		199	132	7.6	10.0
		299	162	9.2	15.1
		399	187	10.7	20.0
$3.7 + j14.9$	600	399	187	9.6	17.9
		599	229	11.7	26.8
		799	264	13.5	35.7
		999	295	15.1	44.6

in a simulation. This approach is feasible as the varactors are placed in a fan cooled and thermally optimized case during large-signal characterization. For that, a simulation is implemented as depicted in figure 4.2. A circular substrate with a surface area of 2025 mm^2 is placed in a cubic air volume with a edge length of 120 mm. The surface area of the substrate corresponds to a 2 ″ wafer with a 81 % varactor filling of its surface. Assuming a homogeneous distribution of the dissipated power in the varactor, a maximum 45 W of heat output is applied to the surface according to the loading simulation of the varactor earlier in this chapter, see figure 4.2. The air flow temperature is set to (20 °C) and a velocity of maximum 1.4 m s^{-1} taken from [72]. The model assumes heat transfer by conduction in solids and by conduction and convection in the surrounding air. Radiation is also regarded with a homogeneous emissivity of 0.85 for the case with no heat sink applied. In the case with a heat sink, the simulation incorporating radiation becomes too computationally extensive. Advantageous in regard to the thereby introduced error is the fact, that with a heat sink the temperature in the setup should be significantly reduced and heat transfer by radiation gains impact with increasing temperature [73, 15].

Figures 4.2c to 4.2e depict the simulation results. With no heat sink applied, the temperature of the substrate rises to a maximum of 286 °C and 261 °C with an air velocity of 1 m s^{-1} and 1.4 m s^{-1} respectively. By applying a heat sink to the back of the substrate, the temperature is limited to a maximum of 135 °C. It is concluded, that with a cooling surface of 2025 mm^2, the varactor can be stably operated but a heat sink and a ventilated environment is required with increasing power levels. Even with an added heat sink, deductions have to be made to the unbiased capacitance and tunability at high-power levels and temperatures due to

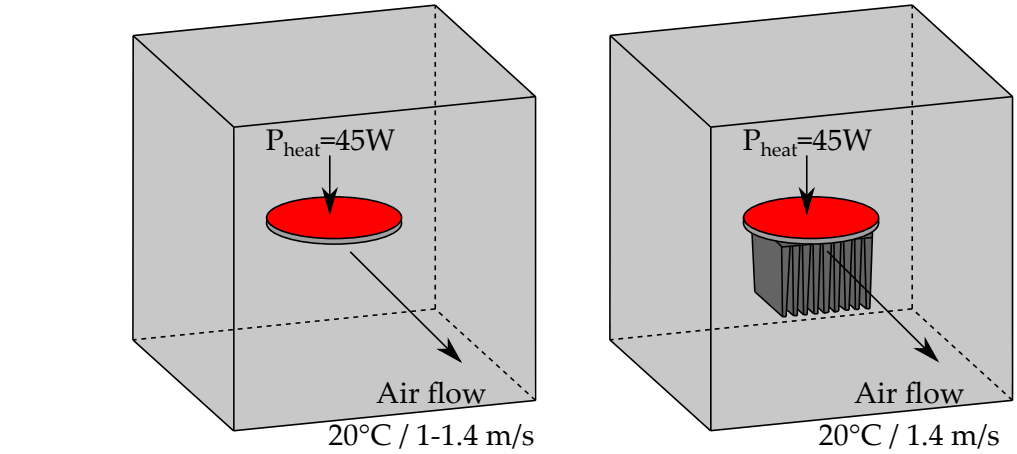

(a) Heated alumina substrate in an air flow without a heat sink.

(b) Heated alumina substrate in an air flow with applied heat sink.

(c) 1 m s^{-1} air flow velocity.

(d) 1.4 m s^{-1} air flow velocity.

(e) 1.4 m s^{-1} air flow velocity with heat sink.

Figure 4.2: Thermal simulation of the varactor in a ventilated environment for different air flow velocities with and without application of a heat sink.

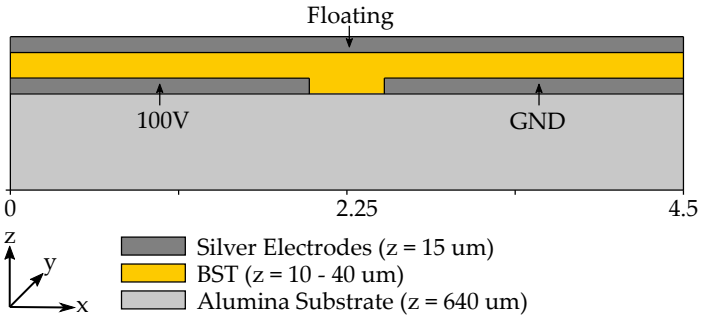

Figure 4.3: Generic piezoelectric model of a MIM cell in COMSOL.

the thermal tuning of the varactor, see section 2.1.1. Overall, the simulation indicates no thermal destruction of the varactor for 45 W dissipated power, when a heat sink is applied to the varactor and it is placed in an air flow.

The BST layer thickness of the varactor is determined from the estimated voltage stresses applied to one MIM structure and the acoustical behavior of the MIM structure. By serial stacking, the voltage stresses can be reduced further but a base value is taken from table 4.1. To estimate the acoustical behavior of the MIM structure, a piezoelectric simulation is set up in COMSOL Multiphysics.

Piezoelectric Simulation Setup

Here, the simulation setup to estimate the acoustical behavior of stacked MIM structures is summarized. For each individual thick film varactor design, the here presented approach is utilized supplemented with a customized model. The theoretical background of the simulation is presented in section 2.1.2. A basic model of a MIM cell from a COMSOL simulation in 2D view is depicted in figure 4.3.

To keep the computational effort of the simulation manageable, the size of the model is restricted to 4.5 mm $\times$ 0.71 mm $\times$ 1 mm. As described in section 2.1.2, bulk acoustic pressure modes in z direction of the structure represent the origin of acoustic resonance phenomenon in a layered structure. Surface acoustic waves are excited by the inhomogeneous height distribution of the BST layer. Therefore, it is highly important to model the layered MIM structure as precisely as possible in z direction. X direction represents the preferential propagation direction of surface acoustic waves, due to the orientation of the height irregularity of the BST layer. Therefore, a substantial length in x direction is implemented in the model. Y direction is of least interest in the simulation, therefore the expansion of the model in that direction is limited to a length, for which a homogeneous electric field distribution in the BST layer is achieved. To set up a piezoelectric simulation in COMSOL, the model is distributed in domains for which different physics environments apply. In figure 4.3, the whole model is applied to the solid mechanics physics environment of

COMSOL, as all domains contribute to the acoustic behavior of the structure with their mechanical parameters. The BST thick film is set up as a piezoelectric material. Caution is required to include the piezoelectric material in COMSOL with the properties of a thick film. Commonly, a piezoelectric simulation is performed on a homogeneous, anisotropic, piezoelectric single crystal. To accurately simulate a heterogeneous sintered ceramic, several adjustments have to be made. Firstly, grains in a sintered ceramic usually have single or polycrystalline structure [74]. By stacking enough of them, the material becomes isotropic as all spatial directions are occupied by at least one oriented single crystal. For that to be true, the grain size has to be small in comparison to the layer thickness. For printed films with thicknesses in the range of 10 µm to 40 µm and grain sizes from 0.5 µm to 1 µm this requirement is barely fulfilled. To account for that in the simulation, the elasticity and piezolectric coupling matrix is altered. In regard to elastic compliance, a single coefficient is assumed for transversal and shear stresses. In regard to coupling, COMSOL provides for a general anisotropic matrix, which is valid if the material is deployed in single crystal form, see equation (4.1). To reduce computing time and suppress spurious modes generated from inhomogeneities in the model, the coupling matrix is reduced to a single coupling coefficient d_{33} (see equation (4.1)).

$$d = \begin{bmatrix} d_{xxx} & d_{xyy} & d_{xzz} & d_{xyz} & d_{xxz} & d_{xxy} \\ d_{yxx} & d_{yyy} & d_{yzz} & d_{yyz} & d_{yxz} & d_{yxy} \\ d_{zxx} & d_{zyy} & d_{zzz} & d_{zyz} & d_{zxz} & d_{zxy} \end{bmatrix} = d_{33} = \begin{bmatrix} 0 & 0 & 0 & 0 & 0 & 0 \\ 0 & 0 & 0 & 0 & 0 & 0 \\ 0 & 0 & d_{zzz} & 0 & 0 & 0 \end{bmatrix} \tag{4.1}$$

The notation reads as the coupling coefficient d_{xyz} for the strain component ε^m_{yz} caused by the electric field component E_x. With this notation, coupling factors d_{*xx}, d_{*yy}, d_{*zz} cause transversal stress while all others cause shear stress. The coupling matrix is oriented in z direction meaning, that only E-field components in z direction cause transversal stress. E-field components in all other directions only cause shear stresses. Therefore, the MIM structure is aligned with the normal vector of the electrode surface pointing in z direction, which is also parallel to the dominant electric field vector in such an electrode configuration. Secondly, the porosity of a sintered film needs to be low enough for gas inclusions to be not influential. Again, as sintered films are not compressed prior to sintering, high porosities have to be expected. To account for that, the density of the material is severely decreased [75, 76, 77, 78]. In regard to the electrodes, the properties of elemental silver provide for a good comparability to a silver thick film conductor paste [79]. The electrodes as well as the alumina substrate contribute as linear elastic materials, described by Young's modulus and Poisson's ratio. A second physics environment is added to the simulation, including only the BST layer of the structure. Only for this domain, the electrical field quantities are required and therefore calculated. An isotropic permittivity is assumed. The adjacent silver electrodes, as well as the substrate, are excluded from the simulation as the field distribution within them is irrelevant for the simulation outcome. However, the interfaces of the electrodes and the BST layer are assigned with electrical potentials, completely determining the relevant region for the electric field solver. One of the bottom electrode

Table 4.2: Material parameters for piezoelectric/acoustic simulation in COMSOL for thick film based varactors. ρ: Density, $E^{(m)}$: Young's modulus [78], ν: Poisson ratio, s_{33}: Elastic compliance ($1/E^{(m)}$), d_{33}: Piezoelectric coupling factor, ε_r: Permittivity

	General	**Mechanical**				**Electrical**
Material	ρ $\mathrm{kg\,m^{-3}}$	$E^{(m)}$ GPa	ν	s_{33} $\mathrm{TPa^{-1}}$	d_{33} $\mathrm{pC\,Pa^{-1}}$	ε_r
Alumina	3900	300	0.222	-	-	-
Silver	10500	83	0.37	-	-	-
BST	3500	117	-	8.57	85.6	230

interfaces is assigned as a 50 Ω terminal with an AC potential of 100 V. The other bottom electrode interface is set to 0 V, while the top electrode interface is assigned a floating potential. The coupling between the electrical and mechanical physics environment is implemented by the inverse piezoelectric effect, utilizing the piezoelectric coupling matrix. The exact material values assigned to each domains are summarized in table 4.2.

The simulation is performed for a frequency range between 10 MHz to 25 MHz. Main limitation of the simulation, is the lack of information acquired about the magnitude of losses caused by acoustic resonances. As described in section 2.1.2, BST in paraelectric phase is not piezoelectric. Piezoelectricity of BST in the paraelectric phase is a result of the applied DC biasing voltage with superimposed RF voltage caused by the quadratic dependency of the electrostrictive term in the constitutive piezoelectric equation. Under the aforementioned conditions, the electrostrictive coefficient a is amplified by a term $2\hat{E}_{DC}$, resulting in the apparent piezoelectric coupling factor $e = 2a\hat{E}_{DC}$. As a result, in paraelectric phase, the coupling and therefore the magnitude of losses caused by acoustic resonances are dependent on the DC biasing field strength. This link is not included in the simulation, as COMSOL uses a constant piezoelectric coupling factor. The simulation results are evaluated in regard to input impedance of the piezoelectric structure. Quality factor and ESR are extracted as main assessment parameters for the acoustical behavior of the structure. However, a variety of electrical and mechanical quantities, such as electric displacement and field distribution, mechanical displacement, stresses and strains are generated by the simulation. An exemplary mechanical displacement field analysis of the structure from figure 4.3 at 13.56 MHz with a BST layer thickness of 40 µm is depicted in figure 4.4. The simulation results quantify the relevance of bulk acoustic pressure waves to surface acoustic waves in stacked piezoelectric structures, which are presented in more detail in appendix C.2.

The simulation in x direction depicted in figure 4.4a shows a surface wave characteristic particle displacement in the BST layer. The wave originates from the irregularity introduced by the gap between to bottom electrodes, resulting in an increased BST layer thickness in the gap. Displacement amplitudes up to 25 nm are simulated, however, due to the lack of information about the exact coupling factor, these values have to be considered

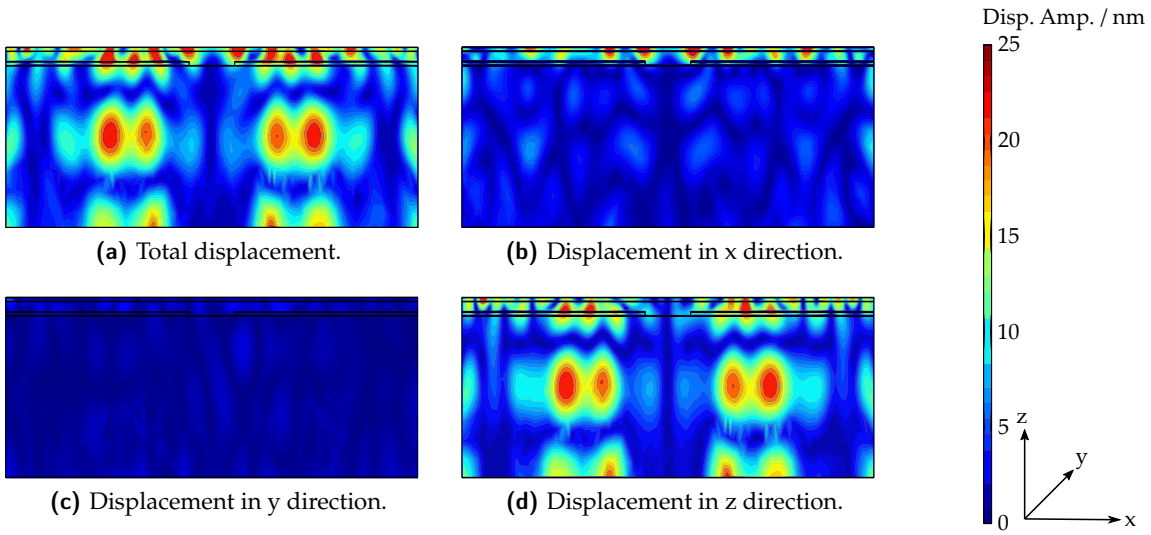

(a) Total displacement.

(b) Displacement in x direction.

(c) Displacement in y direction.

(d) Displacement in z direction.

Figure 4.4: Acoustic simulation result for the generic model depicted in figure 4.3 in regard to mechanical displacement for a piezoelectric film with a thickness of 40 µm and an excitation amplitude of 100 V at 13.56 MHz.

carefully. The wave intensity decays with increasing distance to the gap. In y direction, barely any displacement is visible on the same scale, consistent with the theory presented in section 2.1.3. In z direction, a major mechanical displacement field is visible, coupling into the alumina substrate. For this vertical pressure wave, the substrate serves as a resonant cavity and therefore contributes to the acoustical behavior of the structure. The simulation results in regard to ESR and therefore the evaluation of the acoustic behavior of this particular structure are depicted in figure 4.5.

The simulation results shows distinctive resonances as spikes in the ESR spectrum. A strong BST layer dependency is obtained in regard to the location in the frequency spectrum. A validation of this dependency and conformity of the simulation results to measurement data is given in appendix C.2.

High-Power Varactor Implementation

The presented varactor in this section evolves from of the development on acoustically unoptimized thick film varactors and is based on the single MIM cell design presented in appendix C.1. To increase power and voltage handling capabilities of the varactor, the serial stacking approach is applied. In total, three MIM cells are connected in series and the corresponding biasing network is implemented on substrate. The varactor design is depicted in section 4.1.

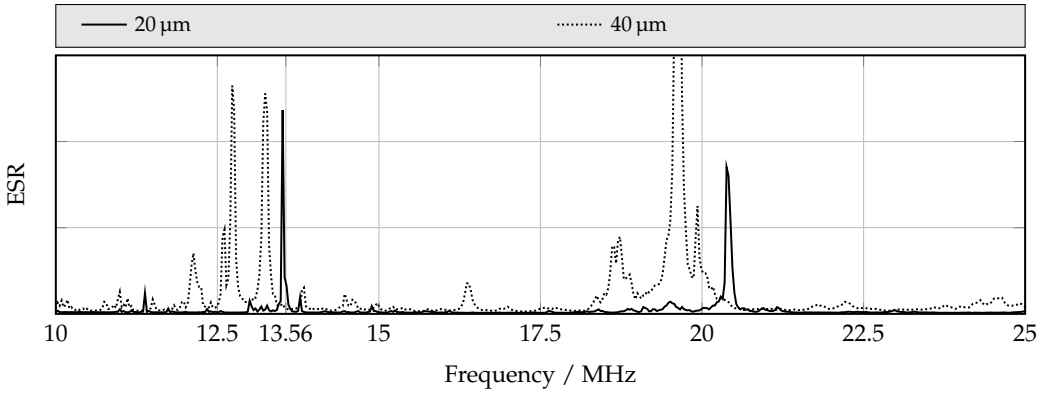

Figure 4.5: Simulated impedance spectrum of a 20 µm and 40 µm thick film.

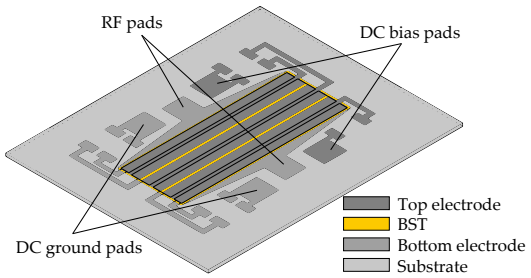

(a) 3D view of the high-power varactor design.

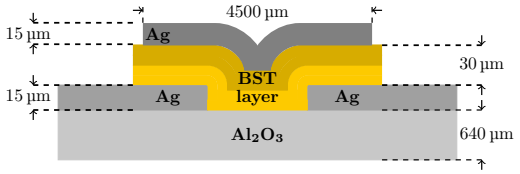

(b) Cut through one of three varactor cells with main dimensions.

Figure 4.6: 3D view and cut plane view of the varactor design. The BST layer in different colors indicates varying mechanical properties, due to an inhomogeneous sintering program.

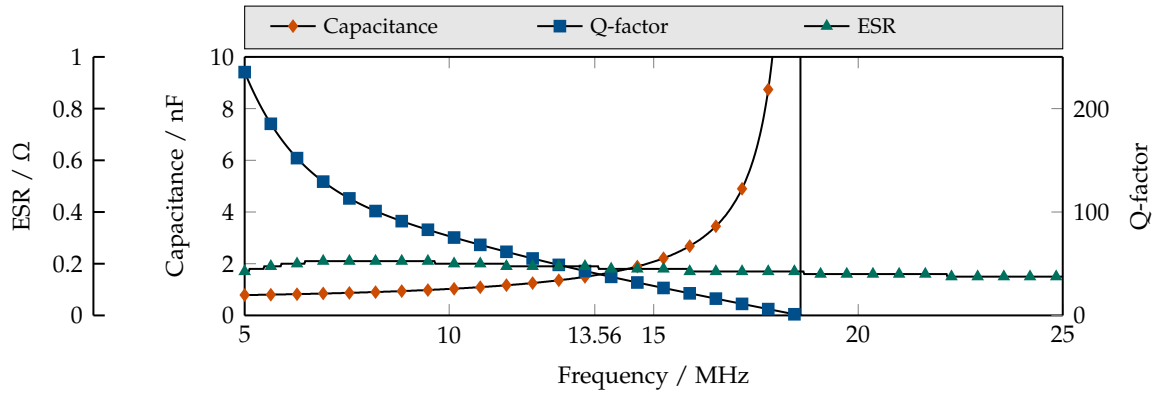

Figure 4.7: Simulated capacitance, quality factor and ESR of the high-power varactor structure.

The varactor is set up for power levels up to 1 kW with a load impedance of $(3.7 + 14.9\mathrm{i})\,\Omega$ resulting in a maximum expected RF voltage of 295 V, see table 4.1. A serial stacking of 6 MIM structures or 3 MIM cells is chosen to maintain a relatively simple biasing concept which fits on-substrate. With a superimposed DC biasing voltage of 200 V, a total voltage of 249 V is expected per MIM structure. In the design given in appendix C.1, a BST layer thickness of 10 µm, which marks the lowest possible thickness, is set up. However, the BST layer proved to be less electrically solid than expected. Therefore, a BST layer thickness of 30 µm is targeted in this design. A 20 µm thick film is not taken into consideration, as its lower acoustic resonance might interference with the operational frequency of 13.56 MHz, see figure C.3, and is therefore discarded as a possible option. To obtain the required BST layer thickness, a total of four layers are printed on top of each other. For this, a sintering step is added with 850 °C for 10 min after printing two BST layers to prevent the BST layer from spreading due to the increased thickness. As a result, most likely inhomogeneous mechanical properties occur in the BST layers, as two of the four BST layers are sintered for a longer time. A changed acoustical behavior can be expected compared to a single homogeneously sintered BST layer. To account for that, two different acoustical simulations are set up later for this structure. The electrode overlap area is set to 480 mm^2, while the whole 2 ” substrate is used as cooling surface (2581 mm^2). The electrical behavior of the design is depicted in figure 4.7 in regard to capacitance, quality factor and ESR. The results are obtained from a full wave simulation in CST Microwave Studio. A capacitance of 1.55 nF is obtained with a self-resonance frequency at 18 MHz. A Q-factor of 41 is calculated as a result of the metalization and dielectric losses of the varactor.

In regard to acoustical behavior, for the first case, a simulation with a single coherent BST layer is performed with an elastic compliance of 8.57 TPa^{-1}, taken from table 4.2. In the second case, the BST layer is divided into two layers with different material properties. For the top layer, which is exposed to the sintering process half of the time, an elastic compliance of 9.57 TPa^{-1} is assumed, which means the material is more elastic, fitting

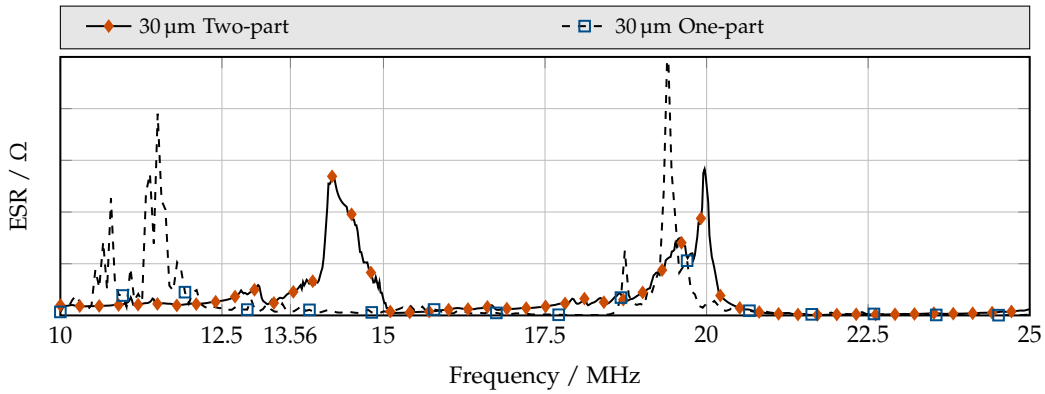

Figure 4.8: Acoustically simulated impedance spectrum of the high-power varactor structure. Due to the two-part sintering process, required as a result of the large BST layer thickness, a mechanically heterogeneous BST layer is obtained. The simulation shows the deviating acoustic resonance locations of a one-part sintering process compared to a two-part sintering process.

the measured result. However, the influence of sintering time on the elastic behavior is non-linear, therefore also a reduced elasticity is possible [80]. The simulation results are depicted in figure 4.8.

For the single-layer simulation the resonances are conform with the simulation for the 10 µm and 20 µm films, meaning the resonance locations are shifted towards lower frequencies with increasing BST layer thickness, see figure C.3. For the two-layered simulation the lower resonance is shifted up to 14 MHz, counteracting the aforementioned trend. As a result, interference with the operational frequency is to be expected. The varactor is processed by the Institute for Applied Materials of Karlsruhe Institute of Technology (KIT).

Varactor Processing

Cu-F codoped $Ba_{0.6}Sr_{0.4}TiO_3$ is prepared in a modified sol-gel process [49, 81]. The MIM varactor is processed in three steps. In a first step, the bottom RF electrodes are screen-printed on an alumina substrate. For the electrodes the conductor paste C 1076 SD (LPA 609-022) from Heraeus is chosen. It is a solderable Ag/Pt conductor paste suitable for temperatures up to 850 °C. In a second step, two layers of BST thick film are screen-printed on the bottom electrode and dried at 80 °C. Subsequently, two more layers of BST are printed on top. Prior investigations have shown that a minimum of four BST layers is needed to obtain a sufficient electrical strength of the ferroelectric layer in regard to the biasing voltage. A total BST layer thickness of 20 µm is obtained. In a final step, the top electrodes are screen-printed on top of the BST layers. The varactor is co-sintered at 850 °C for 10 min. The implemented varactor design with the on-substrate biasing network, consisting of 100 kΩ

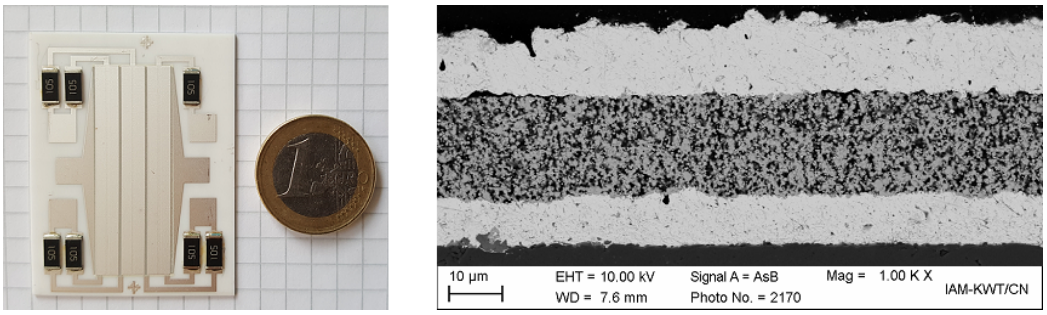

Figure 4.9: Manufactured high-power varactor with on-substrate DC biasing circuit consisting of 100 kΩ resistors on the left. The SEM cross-sectional image of the MIM structure is depicted on the right. ©2017 IEEE.

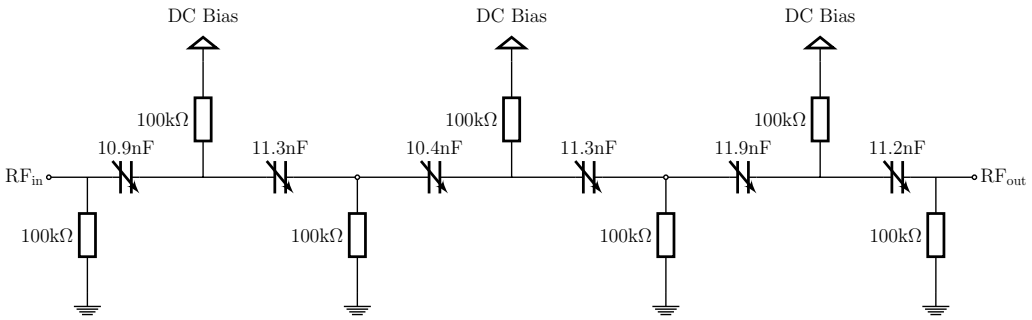

Figure 4.10: Manufactured varactor with the equivalent circuit model and SEM cross-sectional image of the MIM thick film structure. ©2017 IEEE.

resistors is depicted in figure 4.9. A SEM cross-sectional image shows the texture of the 20 µm BST layer and silver electrodes.

Prior to small-signal characterization, the partial capacitance values of each MIM structure are included from a LCR meter measurement at 1 MHz. This is necessary, as a large variety in capacitance values across the 6 MIM structures lead to inhomogeneous load distribution during large-signal characterization. A 12 % difference between the smallest and largest capacitance value is obtained. As a result, an inhomogeneous load distribution between the MIM cells in the varactor is expected during high-power operation. To further analyze the behavior of the varactor, a circuit based simulation is implemented for a serial and parallel stacked case, as both introduce RF power distribution and are equally applicable. The equivalent circuit model with the partial capacitance values is depicted in section 4.1.

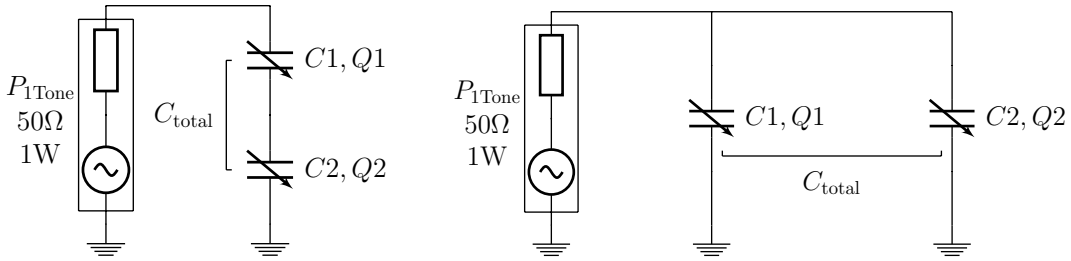

(a) Serial stack model used to estimate overall Q-factor based on partial C and Q values.

(b) Parallel stack model used to estimate overall Q-factor based on partial C and Q values.

Figure 4.11: Serial and parallel stack model implemented in ADS to analyze the load and dissipated power distribution in varactor stacks with inhomogeneous C and Q values.

Analysis of Inhomogeneous Load Distribution in Serially/Parallely Connected Varactors

The problem of inhomogeneous load distribution in serial/parallel stacked varactors due to different capacitance values is closely connected to the problem of inhomogeneous power dissipation of serial stacked varactors due to different Q-factors. Both problems are analyzed with a circuit based simulation in Keysights ADS. For both setups, a one tone power source at 13.56 MHz with a constant output power of 1 W is used. Two scenarios are evaluated. In the first one, a large degradation of varactor performance is assumed, i.e. as a result of damage during long-term operation. In the second one, small deviations in capacitance and Q-factor are focused on, as they occur from processing tolerances.

For the serial stack, the simulation consists of two Q-factor based capacitors in series connection. For the first case, the Q-factors of the capacitors are set up inhomogeneously to $Q_1 = 100$ and $Q_2 = 50$. The capacitance of C_1 is varied between 1 nF and 4 nF with C_2 compensating for the variation, such that the overall capacitance of the setup is fixed at 1 nF. The results of the analysis are depicted in figure 4.12a. With increasing capacitance C_1, the dissipated power distribution is shifted from C_1 to C_2. Due to the reduced quality factor of C_2, the overall losses increase and quality factor decreases. The overall Q-factor is dominated by the quality factor of the smallest capacitance. For the second case, to evaluate the impact of an inhomogeneous Q-factor on an otherwise homogeneous stack, the setup parameters are altered. Q_2 is set to 100 with Q_1 being variable. C_1 is equal to C_2 with 2 nF, resulting in an overall capacitance of C_{total}= 1 nF. The results of the analysis are depicted in figure 4.12b. The losses in C_1 increase with decreasing Q-factor Q_1 consistent with the overall Q-factor of the stack. The equilibrium point of the setup is at $Q_1 = 100$.

For the parallel setup and both described cases, the results of the analysis are depicted in figure 4.13. The completely inhomogeneous case with $Q_1 \neq Q_2$ and C_1 variable is depicted in figure 4.13a. The dissipated power is shifted from C_2 to C_1 with increasing C_1. The overall losses decrease, as C_1 has the larger Q-factor. The overall Q-factor is dominated

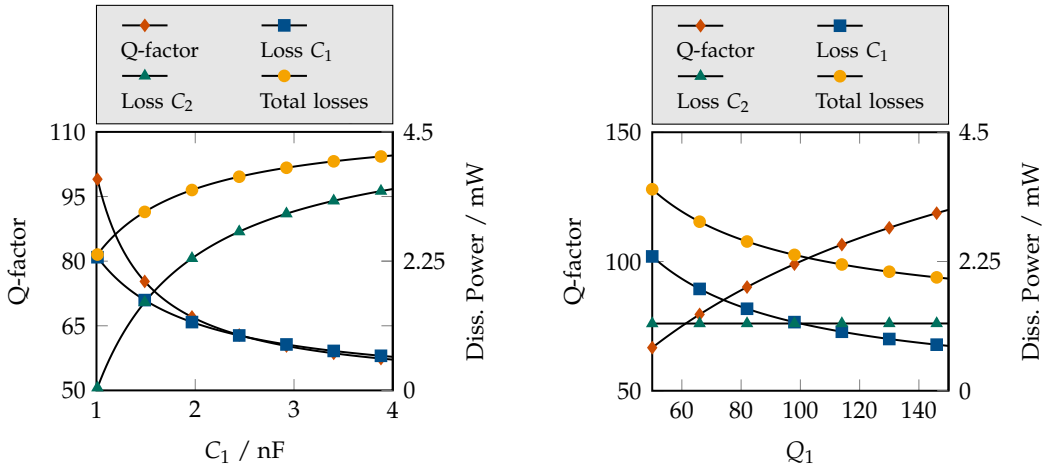

(a) $Q_1 = 100$, $Q_2 = 50$, P_{in} =1 W, C_{total} =1 nF. **(b)** $Q_2 = 100$, P_{in} =1 W, $C_1 = C_2$= 2 nF, C_{total} =1 nF.

Figure 4.12: Serial stack simulation results for largely inhomogeneous partial C and Q values in the stack and their impact on the overall Q-factor and dissipated power.

by the largest capacitor in the stack. Compared to the serial stack a completely linear behavior of the stack is observed. For the second case, which evaluates the distribution of dissipated power in relation to inhomogeneous partial Q-factors but homogeneous capacitances, the results are depicted in figure 4.13b. With decreasing Q-factor Q_1, the losses of the stack increase as the overall Q-factor decreases. Compared to the serial stack a more linear behavior is observed.

To account for a more realistic inhomogeneous scenario where C and Q values deviate just slightly, a deviation of $\pm 5\,\%$ is assumed for C and Q values of both stacks. The previously measured 12 % are included in the prior presented, large deviation case. Evaluated is the overall Q-factor of the stack in regard to percentage of deviation. The results of the analysis for a serial and parallel stack are depicted in figure 4.14a and figure 4.14b, respectively.

For the serial and parallel stack, a similar result is obtained. The main impact factor on the overall Q-factor is the deviation in partial Q-factor, directly mapping to the overall Q-factor. For 5 % reduced C values, an additional 5 % deviation in partial Q is amplified to 5.1 % in overall Q for both stack types. For constant partial Q values, the deviation of C results in a maximum change in overall Q of 1.3 ‰. In conclusion, for mainly homogeneous stacks, which are expectable by the manufacturing process, in serial as well as parallel configuration, the partial Q factor is identified as the most critical parameter, as it directly maps to the overall Q factor of the stack.

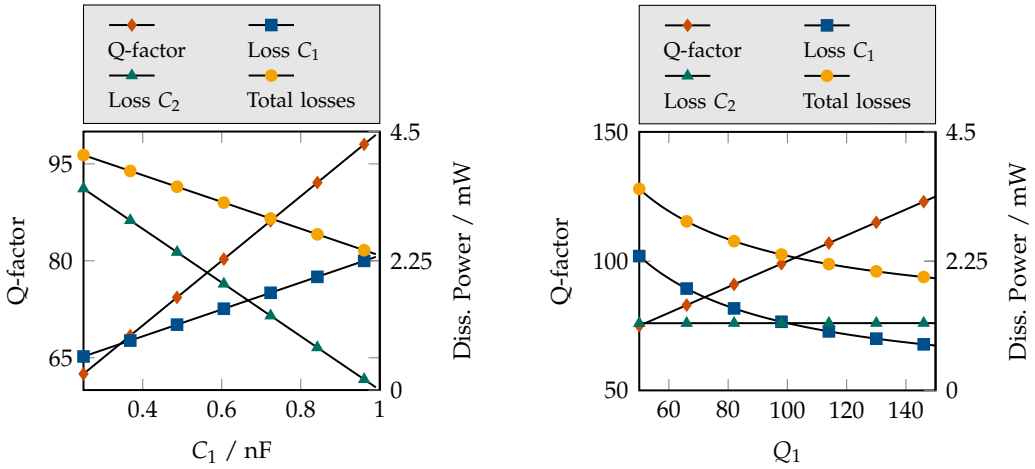

(a) $Q_1 = 100$, $Q_2 = 50$, P_{in} =1 W, C_{total} =1 nF. **(b)** $Q_2 = 100$, P_{in} =1 W, $C_1 = C_2$= 0.5 nF, C_{total} =1 nF.

Figure 4.13: Parallel stack simulation results for largely inhomogeneous partial C and Q values in the stack and their impact on the overall Q-factor and dissipated power.

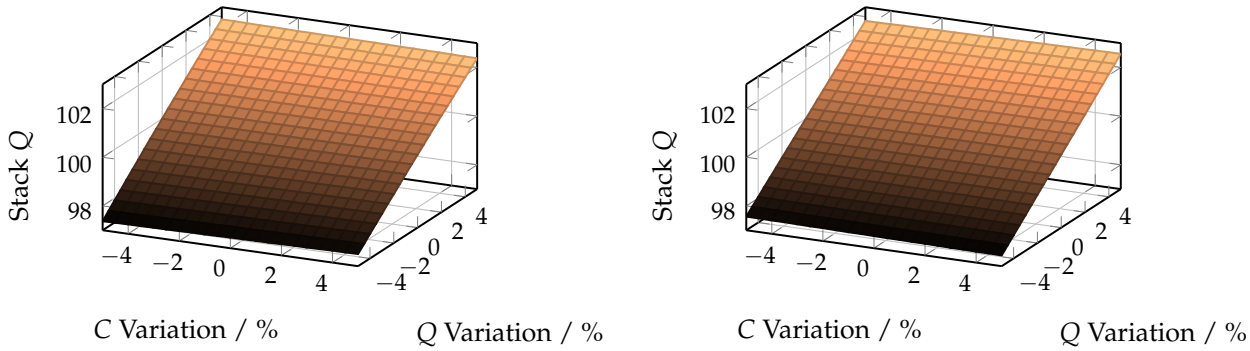

(a) Serial stack. **(b)** Parallel stack.

Figure 4.14: C and Q value variation of 5 % and its impact on the overall Q-factor of a serial/parallel stack.

Small-Signal Characterization Results

The varactor is characterized from 5 MHz to 25 MHz over a temperature range of 20 °C to 70 °C. In order to characterize the varactor, it is placed in a measurement fixture that connects to the RF pads, as well as its RF decoupled DC biasing pads, as depicted in section 3.1. A fixture compensation is performed prior to the measurements, utilizing open/short structures of the designed varactor to account for the parasitic impedance of the fixture. For the temperature characterization, two subminiature heating elements with a combined heating power of 18 W are applied to the back of the alumina substrate of the varactor while it is mounted into the measurement fixture. A homogeneous substrate temperature of maximum 75 °C is achieved with this setup. The fixture itself is connected to the impedance analyzer. The biasing voltage is adjusted in a range of 0 V to 200 V. The results of the characterization are shown in figure 4.15.

At 13.56 MHz, the varactor shows a voltage dependent tunability of 37 % at room temperature and 22 % at 70 °C. The temperature dependent change in capacitance is 31 % in the unbiased state and 14 % in the biased state from 20 °C to 70 °C, respectively. The quality factor of the varactor at room temperature in the unbiased state is 58 and increases to 93 at 70 °C. However, in the biased state, the quality factor decreases at room temperature as well as at 70 °C to 41 and 67, respectively. The measurement results of the quality factor suggest acoustic resonances of the structure at 14.2 MHz and 19.6 MHz, see section 2.1.3 [82].

Large-Signal Characterization Results

The large-signal characterization measurements are carried out in a setup as described in section 3.2. The results presented in this work apply for a load state of $\underline{Z}_{\mathrm{M}}^{*} = (3.05 + 10.07\mathrm{i})\,\Omega$ at power levels up to 400 W and a matching $|\underline{S}_{11}| \leq -20\,\mathrm{dB}$ to the 50 Ω source. A load of $\underline{Z}_{\mathrm{M}}^{*} = (3.7 + 14.9\mathrm{i})\,\Omega$ is set up for power levels between 400 W to 1000 W to maintain a matchable state. For input power levels from 700 W to 1000 W, a passive heat sink is applied to the back of the varactor substrate.

For input power levels below 400 W, the varactor shows reduced tunability. At 400 W input power, a conditioning effect is observed, increasing the varactor performance drastically. The tunability increases from 6.3 % to 33 % with a biasing voltage of 250 V. The conditioning effect is observed in all large-signal characterized thick film varactors. Bulk ceramic based varactors do not show the effect. A detailed explanation of the effect is given later in this section. Compared to the small-signal characterization, at 400 W of input power, the varactor shows a reduced electrical tunability of 33 % with 250 V biasing voltage. The reason for this is the increased temperature of the varactor resulting in a lower permittivity and therefore lower tunability. While operating, the unbiased varactor capacitance shifts due to the increasing temperature from 1.9 nF to 1.6 nF. At this power level, the RMS voltage at the varactor is 77 V and the RMS current through the varactor is 11 A. The varactor dissipates 16.3 W. At 800 W input power, the electrical tunability of the varactor is 27 %, but with a

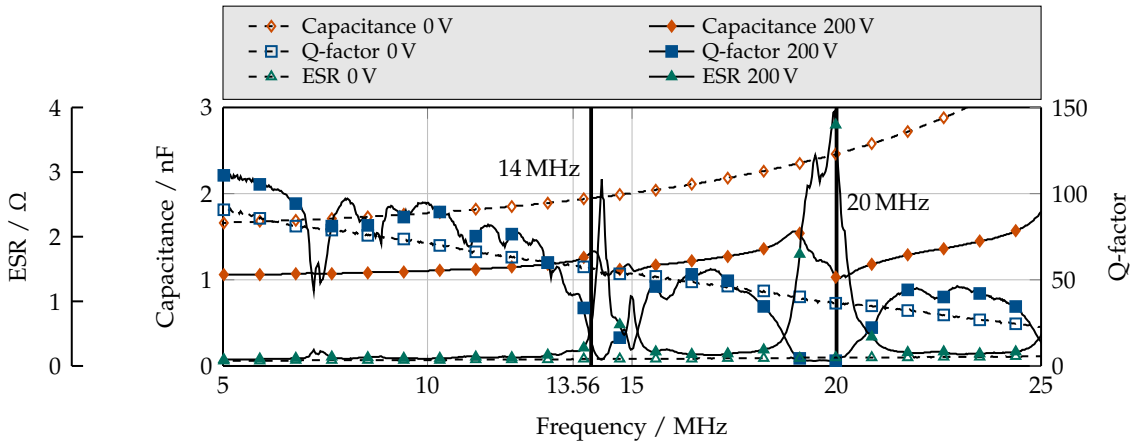

(a) Characterization results at 20 °C.

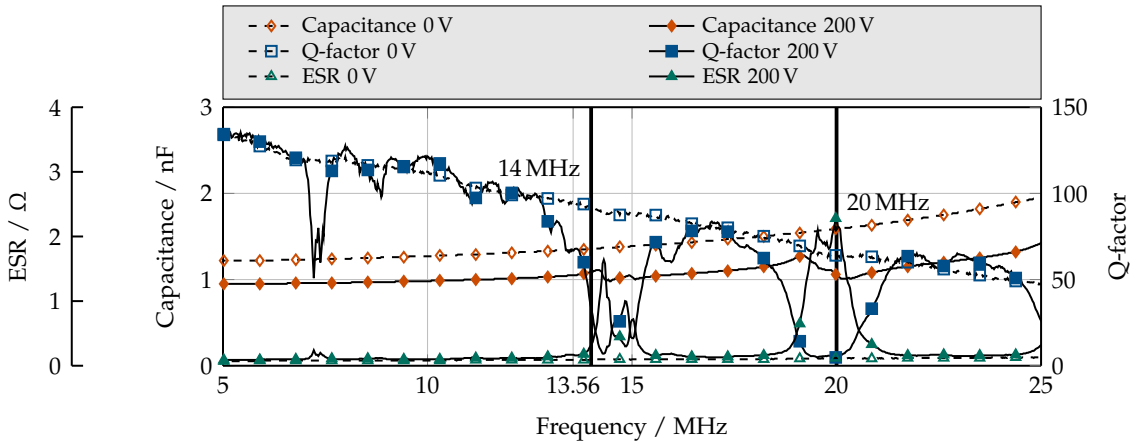

(b) Characterization results at 70 °C.

Figure 4.15: Measured capacitance, Q-factor and ESR of the high-power varactor over frequency in biased and unbiased state at 20 °C and 70 °C. The simulated acoustic resonance locations are marked in both graphs.

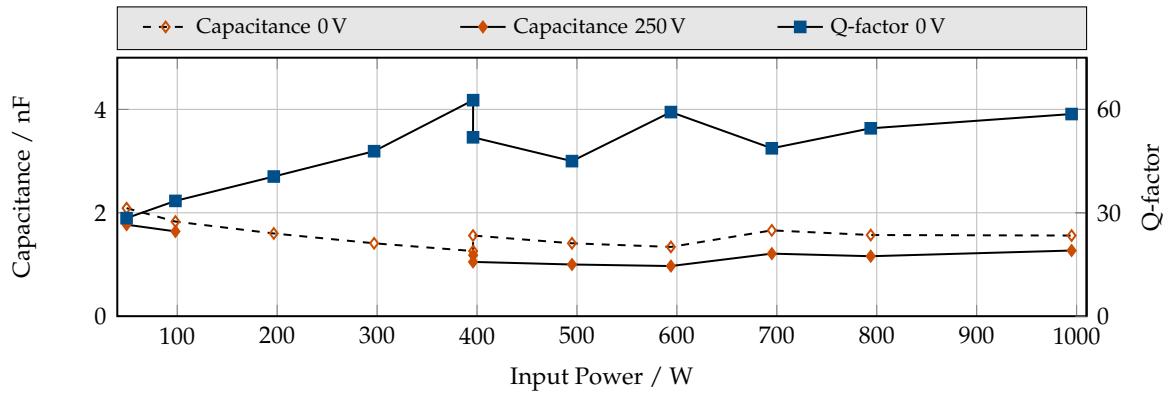

(a) Capacitance and Q-factor for various input power levels.

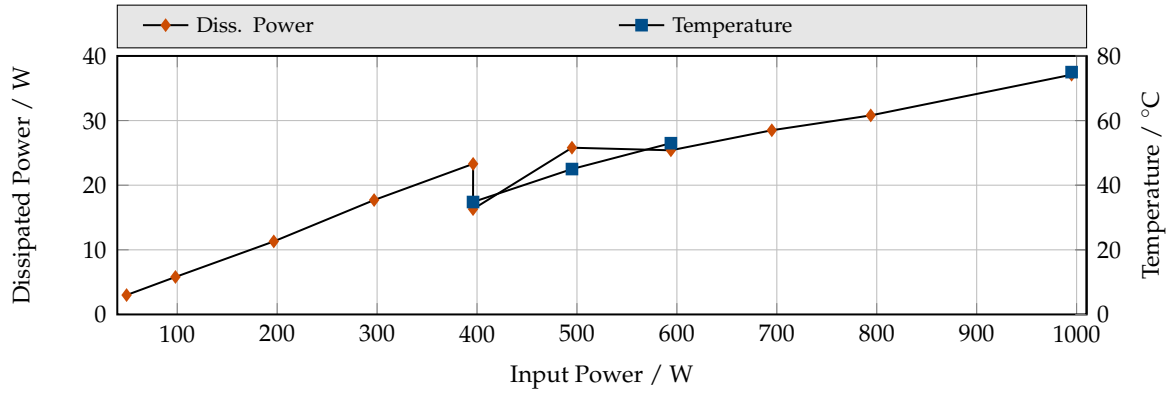

(b) Dissipated power and temperature measurements over input power.

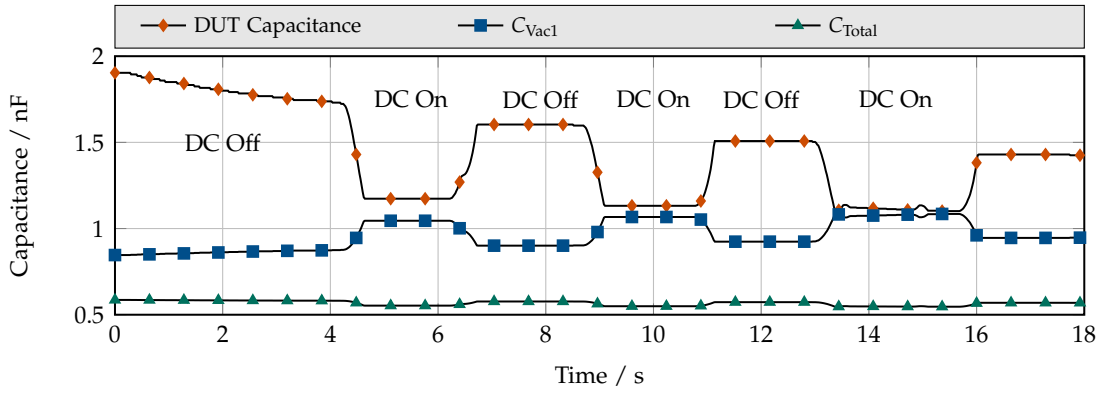

(c) Varactor heating up process during startup of the system at an input power level of 1 kW.

Figure 4.16: Large-signal characterization measurements of the high-power varactor in regard to capacitance, Q-factor, dissipated power and temperature. The varactor startup process is depicted with an input power level of 1 kW over time, during which a DC biasing voltage of 250 V is applied periodically.

Table 4.3: Summary of large-signal characterization data obtained for the high-power varactor at different RF input power levels in unbiased state.

Load and power level			DUT measurements						
$\lvert Z_M^* \rvert$	P_{in}	P_{out}	V_{rms}	I_{rms}	$C(0\,V)$	$Q(0\,V)$	τ	P_{diss}	T
Ω	W	W	V	A	nF		%	W	°C
10.5	49.3	43.6	25.2	3.9	2.0	28.5	15.6	3	-
	98.2	86.8	35.6	5.5	1.8	33.5	10.5	5.8	-
	197	174	46.4	7.9	1.6	40.5	-	11.3	-
	297	262	59.9	10	1.4	48	-	17.7	-
	396	350	73.4	12.5	1.2	63	6.3	23.3	-
15.3	396	350	76.7	10.6	1.6	51.9	33	16.3	35
	495	447	85.3	11.8	1.4	45	29.3	25.8	45
	594	540	95	13.1	1.3	59.2	27.5	25.4	53
	695	631	103	14	1.7	48.7	26.9	28.5	57
	794	722	111	15	1.6	54.5	26.5	30.8	61
	995	902	121	17	1.6	58.6	18.8	37.1	75

reduced biasing voltage of 150 V. The biasing voltage is reduced in order to avoid damage to the varactor. Again, the varactor capacitance in unbiased state is reduced by 16 % from 1.9 nF to 1.6 nF due to heating. The varactor dissipates 31 W of power with 111 V and 15 A RMS voltage and current, respectively.

At 1 kW of input power the varactor shows an electrical tunability of 19 % with 150 V of biasing voltage. The thermal capacitance reduction is again 16 % during startup. Afterwards, stable operation is possible, however, biasing the varactor leads to a changed loading condition of the varactor itself, resulting in changing capacitance values due to temperature variation. The dissipated power in unbiased state of the varactor is 37 W. The RMS voltage and current at the varactor are 121 V and 17 A. A detailed loading condition of the L-match in regard to load impedance and input power level as well as the voltage and current stresses and the dissipated power in the DUT are shown in table 4.3.

RF/DC Conditioning of the Varactors

A major issue identified within the scope of this work is the vaporization of organic solvents in the printed BST layer during the sintering process. As a result, holes and craters arise on the BST surface. After printing the top electrode on the dielectric layer, channels between the electrodes arise, which significantly reduce the electrical breakdown field strength of the layer and in some cases reach as far as to the bottom electrode. In that case, an immediate short circuit is introduced. Figure 4.17 shows interferometer based height profiles of the

varactor design presented in appendix C.1. In figure 4.17a a major crater is visible on the right side of the varactor. Figure 4.17b shows significantly smaller, needle-like holes which still reach down to the bottom electrode, introducing a short circuit. A varactor consists at least of two MIM structures connected in series. As a result, only when both MIM structures are short-circuited, the varactor appears to be defect during characterization judging from C and Q values. Therefore, biasing current and layer resistance of each MIM structure are evaluated prior to characterization.

During large-signal characterization (see especially section 4.3) with high RF power levels, a conditioning effect is observed. During RF operation of a partially short-circuited varactor, a recovery of the damaged cell occurs. The varactor is fully functional afterwards. Conditioning with high DC currents shows a different effect. Continuous discharges are observed, increasing in size until a short circuited condition is reached. In general, high voltage conditioning is a well known technique to ensure proper discharge free high voltage vacuum devices [83, 84]. Known techniques include DC, AC and high frequency based conditioning [83, 85, 86]. A key aspect during the conditioning process is the power brought into the discharge and how long it is applied [85]. High-power levels vaporize the metal irregularities more violent and tend to produce new ones [85]. Short high-power bursts melt the sharpest parts of an irregularity, creating a more homogeneous surface [44, 85]. A fundamental introduction of the conditioning process, covering this particular aspect, is given in section 2.3. It is assumed, that DC based conditioning of the varactors causes explosions of the metal channels between the electrodes, damaging the dielectric channel walls and increasing the hole. The arc is extinguished when the current limiter of the DC source responds. Then, condensation of the vaporized metal on the dielectric walls leaves an electrically weakened channel, which reignites when the electric fields rise again. RF conditioning at 13.56 MHz introduce high-power durations in the ns region. Partial discharges take place in the same time domain, meaning no continuous arc is created [87, 88]. Therefore, it is assumed, that a more gentle conditioning occurs, resulting in a gradual regression of the metal channel until an isolating state is reached.

4.2 Acoustic Suppression Methods for Thick Film Varactors

The suppression techniques presented in this section are dedicated to acoustical optimization methods in the design process of high-power thick film varactors. The presented methods are more complex than simple design optimizations and therefore evaluated in regard to their cost benefit ratio, by comparing the results of suppressed varactors with unsuppressed ones. From the gained insight into the mechanisms of suppressing acoustic resonances in thick film varactors, a final design is derived, including all effective design optimizations and suppression methods investigated in the scope of this work, see section 4.3. The first presented suppression technique is based on the mechanical loading of the varactor cells. The suppression technique is applicable even on already implemented varactors by adding weight to the top electrode. The mechanical Q-factor of the acoustic resonator is reduced,

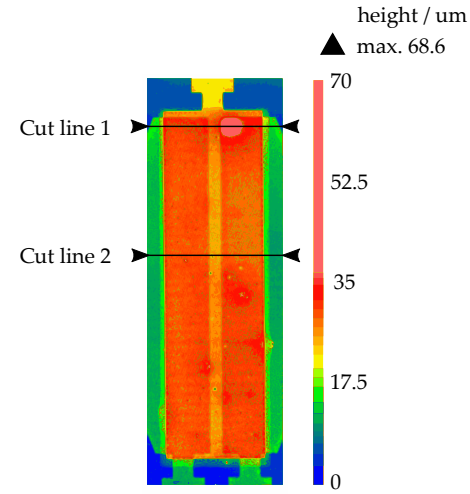

(a) Height profile of the varactor from an interferometer measurement.

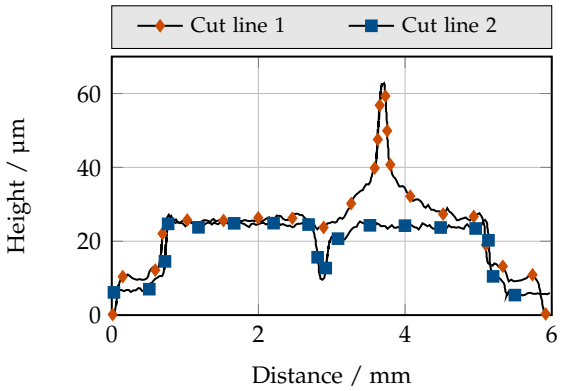

(b) Height profile along cut line 1 and 2.

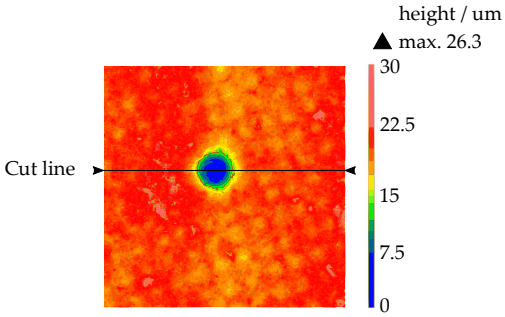

(c) Magnified region around a hole in the surface of the top electrode reaching through the BST layer.

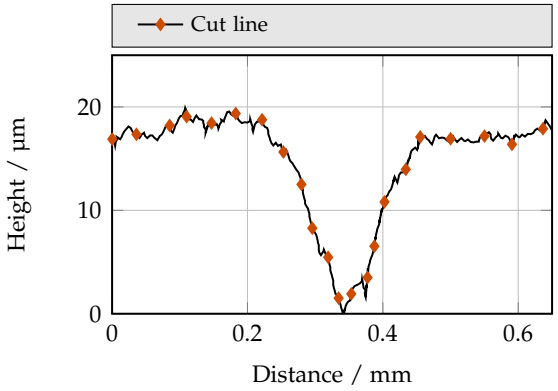

(d) Height profile along the cut line through the hole.

Figure 4.17: Interferometer-based height profile of a thick film varactor. The evaluation shows localized peaks and holes, generated by vaporized solvents in the printed BST layer. In particular, holes in the BST layer are critical, as they significantly lower the electrical breakdown field strength or even short-circuit the varactor.

resulting in a broader but lower peak in the impedance spectrum of the varactor. For narrow-band and single frequency applications like plasma etching or depositioning, an interfering acoustic resonance with the operational frequency can be significantly reduced. For broad-band application, however, this suppression technique is less useful, as the resonance peak is reduced but a significantly larger frequency spectrum is affected by the resonance. The second acoustic suppression technique is based on destructive acoustic interference by introducing an anti-polar apparent piezoelectric coupling factor e_{33}. This technique has to be considered during the design of the varactor and is not applicable later on.

4.2.1 Mechanical Loading

The MIM varactor structure with the piezoelectric layer in between two silver electrodes is modeled as a damped spring mass system with forced harmonic excitation. The bottom electrode is assumed to be fixed while the top electrode acts as the mass on top of the spring which is the piezoelectric BST layer. Such a system can be described with the motion equation [15]:

$$m \cdot \frac{d^2x}{dt^2} + b \cdot \frac{dx}{dt} + B \cdot x = F_1 \cdot \sin(\omega_1 t) \tag{4.2}$$

with the displacement x, time t, friction constant b, mass m, spring constant B and excitation force F_1. The solution to equation (4.2) is a harmonic vibration with the amplitude term [15]:

$$x_0 = \frac{\frac{F_1}{m}}{\sqrt{(\omega_0^2 - \omega_1^2)^2 + (\frac{\omega_1 \cdot b}{m})^2}} \tag{4.3}$$

with the self-resonance $\omega_0 = \sqrt{\frac{D}{m}}$ of the spring mass system and the shifted resonance frequency ω_1 originating from the forced harmonic excitation [15]:

$$\omega_1 = \sqrt{\frac{D}{m} - \frac{b^2}{4m^2}} \tag{4.4}$$

From equation (4.3), one can deduce, that by changing the mass on the spring mass system the amplitude of the resonance is reduced while the resonance peak is widened. As a result, a larger frequency range is affected by the decrease in quality factor caused by the acoustic resonance, but the local drop in quality factor is significantly reduced. For narrow-band and single frequency applications such as RF heating, etching or welding, a reduced but widened resonance peak is less problematic than a sharp acoustic resonance interfering

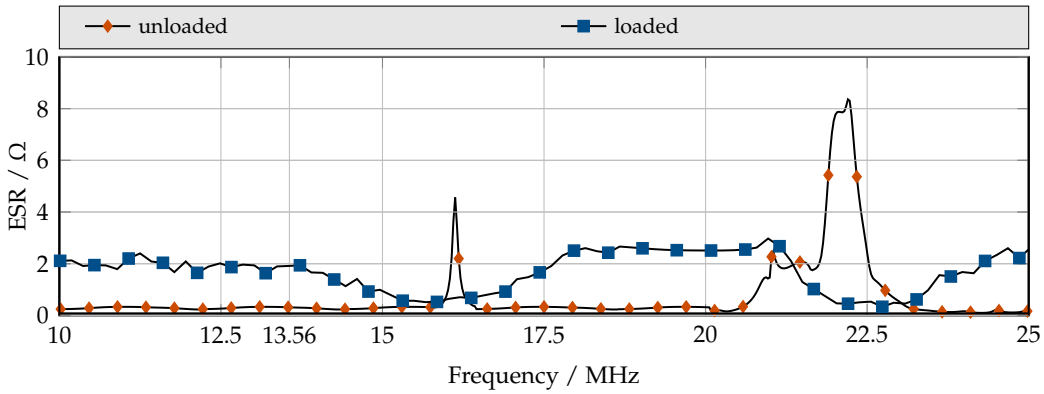

Figure 4.18: Simulated impedance spectrum of mechanically loaded and unloaded MIM cell.

with the operational frequency. Regarding broad-band application, a widened resonance peak will affect a larger frequency range, however, a smooth output power level can be achieved. In addition, equation (4.4) indicates that the position of the resonance is shifted towards lower frequencies with increasing mass, enabling the option to design the acoustical behavior of a component. The comparison of the simulation results of a loaded cell with an unloaded cell is depicted in figure 4.18. For the loaded varactor, a boundary mass of $m = 17$ mg is applied to the top electrode.

The results indicate a locally optimized behavior of the suppressed varactor in regard to ESR. In general, however, an overall increased ESR is obtained, illustrating the narrow-band application of the technique.

4.2.2 Destructive Interference

The presented acoustic suppression technique is based on the work of [32, 89], where it was verified for thin-film varactors. The fundamental structure is shown in figure 4.19. A double MIM structured varactor at the acoustic resonance frequency is assumed with an infinitesimal thin electrode in between the two ferroelectric layers and infinitely thick top and bottom electrodes. The mechanic strain $\varepsilon^{(m)}$ can be written as [27]:

$$\varepsilon^{(m)} = \underbrace{a(\hat{E}_{\mathrm{DC}}^2 + \frac{1}{2}\hat{E}_{\mathrm{RF}}^2)}_{\text{static}} + \underbrace{2a\hat{E}_{\mathrm{DC}}\hat{E}_{\mathrm{RF}}\sin(\omega_{\mathrm{RF}}t)}_{\text{piezoelectric}} - \underbrace{\frac{1}{2}a\hat{E}_{\mathrm{RF}}^2\sin(2\omega_{\mathrm{RF}}t + \frac{\pi}{2})}_{\text{electrostrictive}},$$

see section 2.1.2. The suppression technique utilizes the tunable apparent piezoelectric coupling factor $e = 2a\hat{E}_{\mathrm{DC}}$ by applying an anti-polar electric DC field in the two BST layers. As a result, two antipolar apparent piezoelectric coupling factors $e_1 = 2a\hat{E}_{\mathrm{DC}}$ and

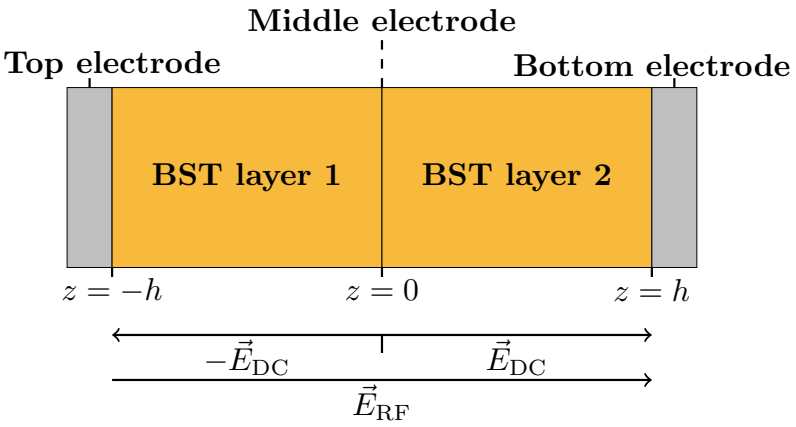

Figure 4.19: Double MIM fundamental model. ©2018 IEEE.

$e_2 = -2a\hat{E}_{\mathrm{DC}}$ in the BST layers are introduced. The mechanic strain in the layers is coupled with a 180° phase shift. Thereby, an excited acoustic wave is unable to couple to adjacent layers, resulting in significantly reduced losses. However, the technique is only applicable when both BST layers behave exactly the same properties. Otherwise, an excited acoustic wave is not confined within the dielectric but couples to adjacent layers. To further evaluate the suppression approach, an acoustic simulation of the structures is set up. The reference single MIM varactor is identical with the varactor cell presented in appendix C.3 apart from a variation in BST layer thickness to 20 µm. The electrode overlap area is 0.75 mm × 1 mm, resulting in a capacitance of 76 pF estimated with the parallel plate capacitance equation and a permittivity of the printed BST thick film layer of $\varepsilon_{\mathrm{r}} = 230$ [42]. Consequently, the double MIM varactor consists of two 20 µm thick BST layers and a middle electrode with a thickness of 15 µm. The electrode overlap area is the same as for the single MIM varactor, resulting in an estimated capacitance of 38 pF. The varactor designs and the DC/RF decoupling networks are shown in figure 4.20 for both, the single and double MIM varactor.

The results of the piezoelectric simulation for the double MIM structure are depicted in figure 4.21. The results of two different simulations are shown. In the homogeneous case, the material properties of both BST layers are identical. In the heterogeneous case, the elastic compliance of one BST layer is set to 6 TPa^{-1} from 8.57 TPa^{-1} to simulate non-ideal resonance cancellation. However, the change of other material parameters, such as piezoelectric coupling or density, lead to similar results.

Based on the presented theory, no or highly suppressed acoustic resonances should be visible in the ESR spectrum of the homogeneous case compared to the heterogeneous case and to a single MIM cell. As expected, the simulated ESR trace for the homogeneous case shows no acoustic resonance at 15 MHz in contrast to the heterogeneous case, see figure 4.21. At 21 MHz, a highly damped spike is visible indicating a non-perfect cancellation of strain waves in the structure, caused by parasitically excited surface acoustic waves due to the

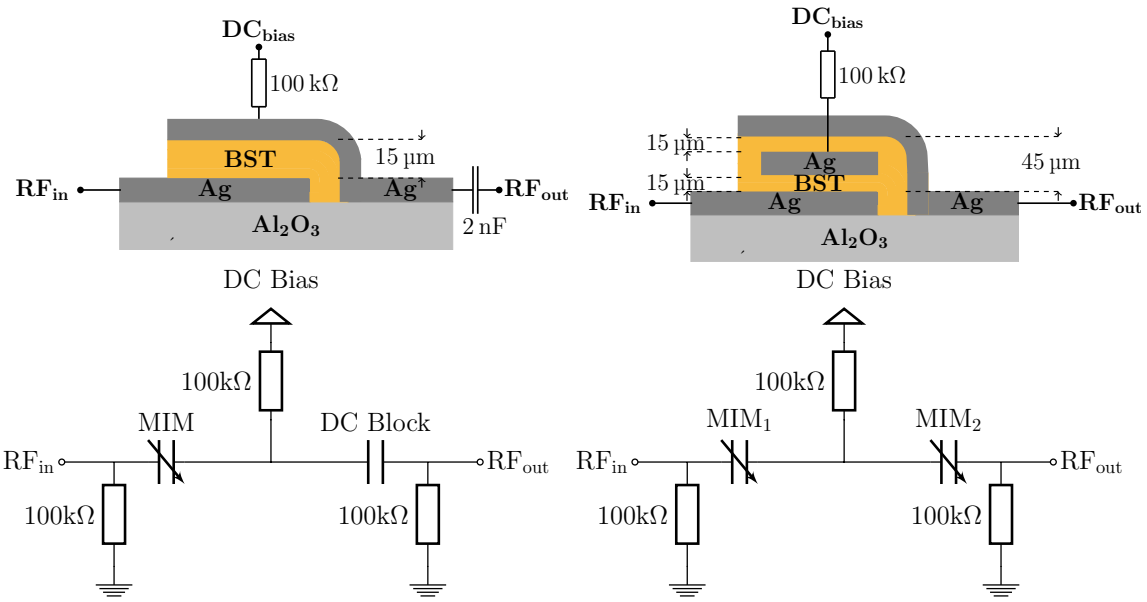

Figure 4.20: Cut through the single and double MIM structure with equivalent circuit model and its connection to the structures. ©2018 IEEE.

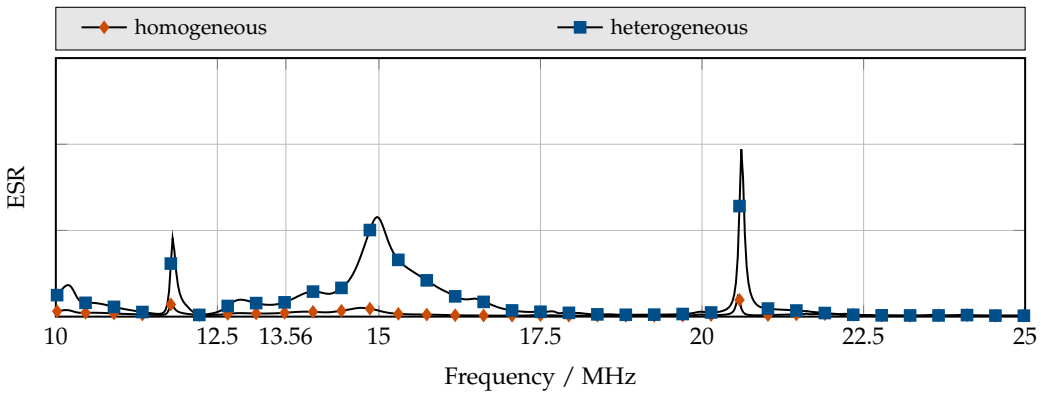

Figure 4.21: Simulated impedance spectrum of a heterogeneously and homogeneously sintered double MIM varactor cell.

inhomogeneous model. An additional highly damped resonance at 12 MHz is visible, caused by the same reason. The trace for the heterogeneous case shows a significant acoustic resonance at 15 MHz and 21 MHz, indicating the validity of the suppression approach. A third resonance is found at 12 MHz, which occurs in the homogeneous simulation as well. Compared to the simulation results of the single MIM cell, see figure 4.18, the homogeneous double MIM cell shows significantly reduced acoustic activity, indicating the effectiveness of the presented suppression method. To validate the approach, the matrix varactor design presented in appendix C.3 is altered by adding a middle electrode to the MIM structure creating a double MIM structure. The matrix varactor design excels for the validation of the interference based suppression approach due to its isolated miniature cell structure. Small-signal characterization can be performed on the small varactor cells, without the parasitics introduced by the large varactor structures of the previous designs. For this, a screen is designed which enables the possibility to include an additional middle electrode layer between the two intended layers of BST. The obtained samples are characterized under small-signal conditions and the suppression approach is evaluated in regard to its effectiveness for homogeneous and heterogeneous material parameters in the BST layers.

Double MIM Structure Processing

In a first step, the bottom RF electrode is screen printed on an alumina substrate. For the electrodes the conductor paste C 1076 SD (LPA 609-022) from Heraeus is chosen. It is a solderable Ag/Pt conductor paste suitable for temperatures up to 850 °C. In a second step, two layers of BST thick film are screen printed on the bottom electrode and dried at 80 °C. For the heterogeneous case, the structure is now sintered at 850 °C for 10 min. Subsequently, the middle electrode and two more BST layers are printed and dried at 80 °C. Eventually, the top electrode is printed and the whole structure is sintered at 850 °C for 10 min. In conclusion, for the heterogeneously processed varactors, the bottom BST layers are sintered two times and the top BST layers are sintered once. As a result, varied material properties in the top and bottom BST layers can be assumed. For the homogeneously processed case, all four BST layers are sintered at once, resulting in equal material properties in the top and bottom BST layers. A SEM cross-sectional image of the homogeneously co-sintered double MIM structure is depicted in figure 4.22.

Small-Signal Characterization

The varactors are characterized with a 1-port measurement from 5 MHz to 25 MHz with the impedance analyzer connected to a wafer prober with a 1250 µm ground-signal (GS) probe. A biasing voltage range from 0 V to 120 V is used for characterizing the varactors and a 100 kΩ resistive needle is included into the measurement setup, connecting to the middle electrode of each varactor structure. The equivalent circuit diagram of the biasing

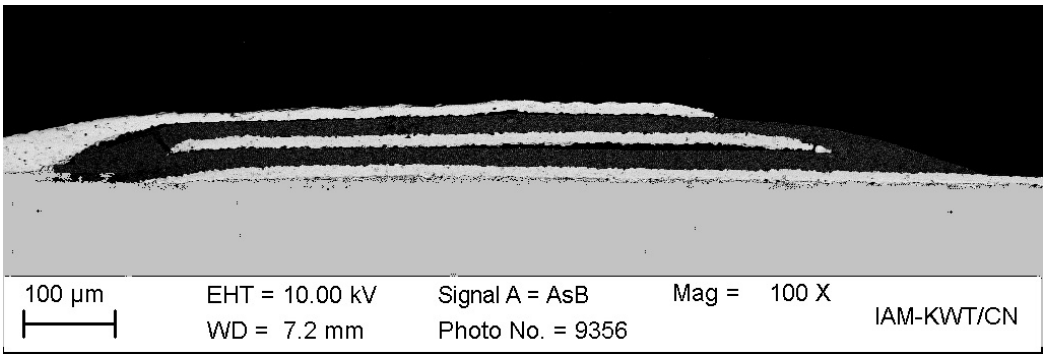

Figure 4.22: SEM cross-sectional image of the double MIM structure. ©2018 IEEE.

concept is depicted in figure 4.20. The varactors are characterized in regard to capacitance and Q-factor.

The measurement results comparing C and Q-factor for the homogeneously and heterogeneously sintered varactors are depicted in figure 4.23. The heterogeneously sintered varactors show an increased unbiased capacitance of 122 pF attributed to the increased sintering duration. A tunability of 37 % is measured with 120 V biasing voltage. The Q-factor graph shows acoustic resonances in the heterogeneously sintered double MIM structures at 14 MHz and 18.7 MHz in biased state. The re-occurring acoustic resonance peaks in the Q-factor spectrum of the heterogeneously sintered varactor cells indicate a working acoustic suppression principle. Compared to the piezoelectric simulation in Figure 4.21 the resonances are shifted by 1 MHz from 15 MHz to 14 MHz and by 2.3 MHz from 21 MHz to 18.7 MHz. A reduction in resonance frequency can be attributed to an increased weight on the resonating structure, which reduces the amplitude peak of the resonance as well. A thickness measurement indicated an increased top and bottom electrode thickness of 3 µm and 2 µm respectively, compared to the homogeneously sintered single MIM varactors. The change of the piezoelectric coupling factor of the top BST layer in the simulation for the heterogeneously sintered varactors has no effect on the position of the resonances in the spectrum. The amplitude of the resonances is affected by the coupling factor exclusively.

4.3 Acoustically Optimized and Vertically Stacked High-Power Varactors

In this section, the design of an acoustically optimized varactor is discussed. The design marks the end of the acoustically optimized varactor development process and includes all techniques, identified within the scope of this work, effective on the improvement of the acoustical behavior. Preliminary designs are presented in appendix C.2 and appendix C.3. It has to be noted, that the application of the presented varactor in this section is also in the

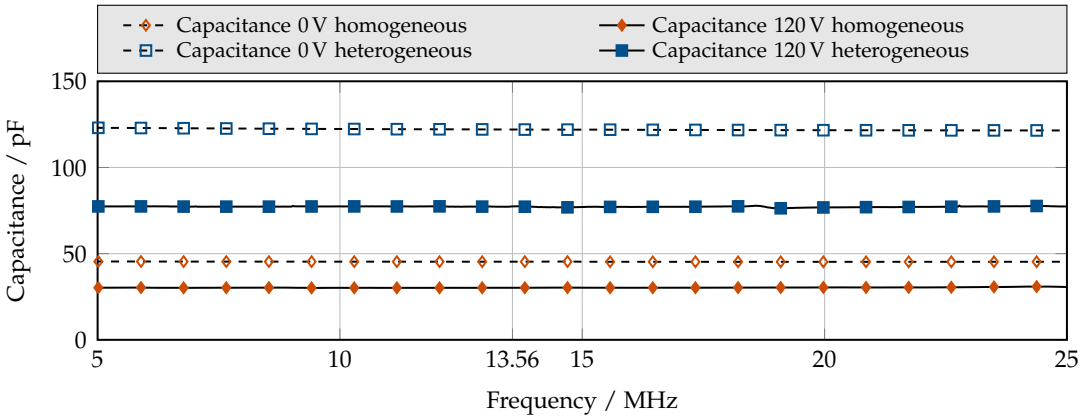

(a) Capacitance vs. frequency in unbiased and biased state.

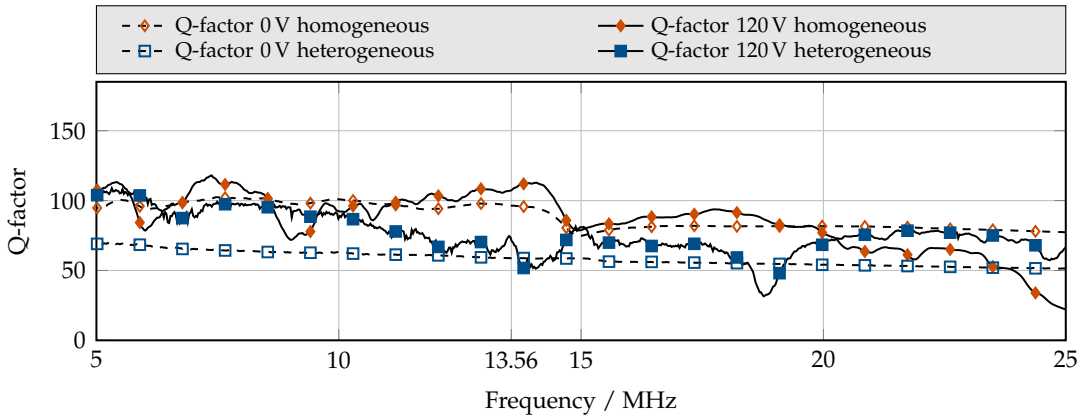

(b) Q-factor vs. frequency in unbiased and biased state.

Figure 4.23: Verification of the interference based acoustic suppression approach presented in section 4.2.2. The homogeneously and heterogeneously processed double MIM cells behave differently. Due to varying mechanical properties, the heterogeneously sintered cells show incomplete acoustic suppression with resonances at 14 MHz and 18.5 MHz in the Q-factor spectrum. The homogeneously sintered cells show no resonances.

high-power domain. Therefore, basic design rules presented in section 4.1 apply for this section as well. However, main focus of the presented varactor is the optimization in regard to its acoustical behavior and thereby improving also its power handling capabilities. This includes surface acoustic waves as well as longitudinal acoustic pressure waves between the electrodes. Surface acoustic waves are prevented by dividing the large BST layer into smaller areas. It is known that in structures with large lateral dimensions in combination with an inhomogeneous height distribution of the ferroelectric layer and for the adjacent layers, shear waves travelling along the surface of the structure are generated [90]. It is possible to suppress these waves by interrupting the dielectric layer and implement the varactor not in a continuous structure but in an interrupted parallel connection of varactor cells. In such a structure, mainly acoustic resonances based on vertical pressure waves are excited, which are dependent on the vertical dimensions and parameters of adjacent material layers, see section 2.1.3. However, longitudinal pressure waves represent the dominant type of acoustic wave in a layered structure. Therefore, the main focus is laid upon the dampening, suppression and relocation of the longitudinal pressure mode in the frequency spectrum. For this, the presented acoustic suppression techniques from section 4.2.2 and section 4.2.1 are utilized and implemented in the design. An interconnectable matrix of spatially separated MIM cells is set up with vertical electrode bars in between, establishing parallel and serial connection of several cells to a macroscopic varactor. First, each cell is disconnected from the rest of the matrix for characterization purposes. After small-signal characterization, the cells are connected to the vertical electrode bars with a conductive silver coating. Several rows of parallel connected cells can be connected in series connection, forming the macroscopic varactor. Beside the acoustical optimization, the advantages of this design is the enlargement of cooling surface per cell, the possibility to characterize each varactor cell individually and avoid parasitics introduced by interconnecting metalization or measurement fixtures. Additionally, damaged varactor cells can be excluded from the macroscopic varactor, resulting in a higher yield of working manufactured varactors. The main disadvantage are the increased metalization losses and inductive parasitics from the interconnecting electrode bars. A reduction of the self-resonance-frequency (SRF) of a matrix varactor is expected compared to a concentrated design. The varactor design process is now explained in detail.

Vertically Stacked High-Power Varactor

The macroscopic varactor consists of $16 \cdot 4 = 64$ cells with a cell size of 5.5 x 1.1 mm, resulting in a total electrode overlap area of $387\,\mathrm{mm}^2$. To chose a BST layer thickness, insights gained from the previous design are applied. In particular, the BST thickness to resonance frequency location evaluation performed in appendix C.2 provides for a good foundation of the thickness selection process. The results, depicted in figure C.11, indicate that a BST layer thickness smaller than 25 µm shows favorable positions of its acoustic resonances, the capability of handling biasing voltages up to 250 V as well as the absence of thermal runaway due to heat accumulation in the BST layer. Therefore, a BST layer

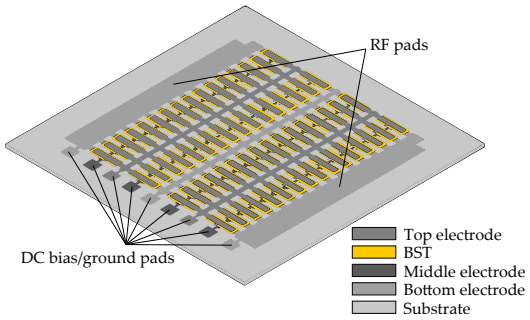

(a) 3D view of the double MIM varactor design.

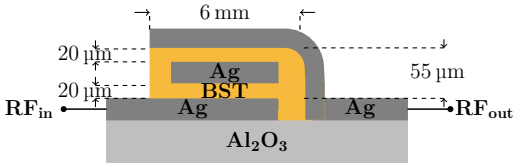

(b) Cut through a double MIM varactor cell with dimensions.

Figure 4.24: 3D and cut plane view of the acoustically optimized varactor design. ©2019 IEEE.

thickness of 20 µm is aimed at in the design process for both BST layers of the double MIM cell. The matrix design is chosen to suppress acoustical shear waves, as described in section 4.3. Theoretically, a capacitance of 620 pF per MIM structure and therefore 310 pF per cell is obtained, as two serially connected MIM structures are integrated into one cell. Then, with this setup a reasonable overall zero-bias capacitance of 1.24 nF can be achieved by interconnecting all cells, see figure 4.25. Similar to section 4.1, the complete back of the 2 ″ substrate serves as cooling surface (2581 mm^2).

The structure is evaluated in regard to capacitance, Q-factor and ESR with a full wave simulation in CST Microwave Studio. The results are depicted in figure 4.25 and verify the theoretically obtained base values of the varactor.

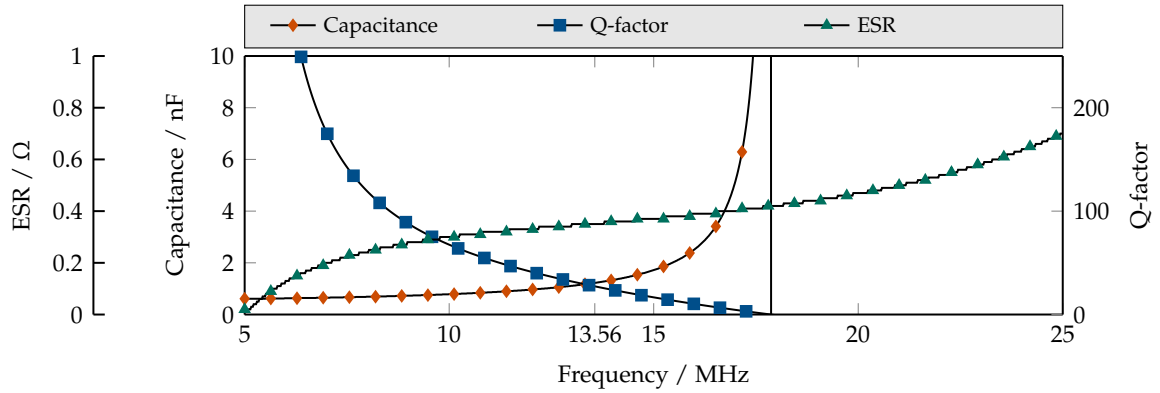

Figure 4.25: Simulated capacitance, quality factor and ESR of the structure.

To suppress bulk acoustic pressure waves, the two introduced acoustic suppression techniques, see section 4.2.1 and section 4.2.2, are applied in this design. Therefore, the MIM structures are designed differently compared to section 4.1, as they suppress longitudi-

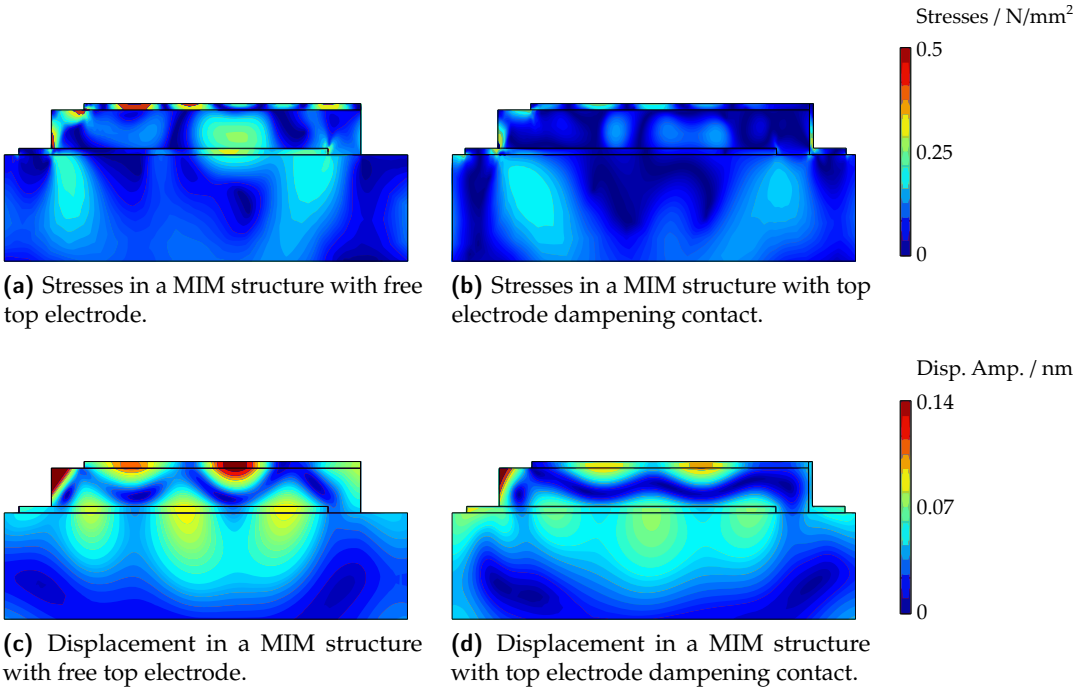

(a) Stresses in a MIM structure with free top electrode.

(b) Stresses in a MIM structure with top electrode dampening contact.

(c) Displacement in a MIM structure with free top electrode.

(d) Displacement in a MIM structure with top electrode dampening contact.

Figure 4.26: Comparison of two different MIM structure designs with a mechanically free top electrode (left) and a top electrode dampening contact (right). A BST thickness of 20 µm and an excitation amplitude of 100 V at 13.56 MHz are applied to the structure in both cases.

nal pressure waves in the BST layer by artificially increasing the weight on the structure, see section 4.2.1. In section 4.1, the top electrode can oscillate freely, as it does not share a connection to the substrate. In the new design, the top electrode acts as a dampening system of the vibrating BST thick film, utilizing the adhesion of the silver paste to the substrate surface and the cohesion of the hardened silver paste. The effectiveness of the set up is evaluated in a piezoelectric simulation. The results of the simulation in regard to total stresses in the structure and resulting displacement are depicted in figure 4.26.

The results indicate significantly reduced stresses and displacement in the structure with the locked top electrode. In this structure, the main stresses occur in the dampening contact and the top electrode. In particular the BST layer and the bottom electrode are shielded from stresses compared to the free top electrode case. The characteristic displacement pattern in the structure with the free electrode remains in the structure with the locked electrode, however, a significant reduction in regard to displacement amplitude is observed. In regard to electrical Q factor, an increase of 24 % is achieved in the structure with the electrode dampening contact at 13.56 MHz. Further expected advantages of the presented design include:

- Reduction of irregularities, conducting channels, holes in the BST layer caused by

vaporization of liquid solvents in the BST, see section 4.1.

- Individual on-wafer characterization of each cell with ground-signal (GS) 1250 µm probes is possible due to the reduced MIM structure size. As a result, a more accurate measurement of the varactor is possible, by excluding otherwise required external measurement fixtures.
- Additional acoustic suppression techniques, discussed in section 4.2, are applicable to single MIM structures, increasing the comparability with unsuppressed cells on the same substrate.
- All other advantages for matrix varactors, such as enlargement of cooling surface and exclusion of damage cells from the capacitive matrix.

The main attribute of the varactor, is the applied acoustic interference method presented in section 4.2.2. To verify the approach on the newly designed structure, it is setup for a piezoelectric simulation in COMSOL. The suppression approach itself is based on equation (2.15). The simulation is setup with an RF voltage of 100 V on the middle electrode and a grounded top and bottom electrode. This setup does not agree with the later intended voltage application where the RF voltage is applied between top and bottom electrode and the DC voltage is applied to the middle electrode with DC ground on top and bottom electrode. However, the described setup is necessary to simulate the interference effect for which an in phase electric field is required in both BST layers. The DC induced opposite sign for the apparent piezoelectric coupling factors is simulated by opposing the sign manually in the material options of the piezoelectric material. The simulation results with and without opposing apparent piezoelectric coupling factors are depicted in figure 4.27.

The piezoelectric simulation results in regard to displacement in the structure indicate a significantly reduced activity in the suppressed case by a factor of 5. The displacement pattern in the unsuppressed case shows maxima at the top and bottom electrodes, describing the coupling of the acoustic wave to the adjacent material. In the suppressed case, the displacement pattern changes. Its maximum is located on the middle electrode of the double MIM structure with significantly reduced displacement activity on the bottom and top electrode. The result indicates a properly working suppression in the newly designed structure. Processing of the varactor is identical to the process described for the homogeneous case in section 4.2.2. For the fabrication, a high viscosity paste is first used to prevent vaporization of organic solvents during sintering and spreading of the BST layer. A SEM cross-sectional image of the obtained double MIM structure is given in figure 4.28. A BST layer thickness of 30 µm is obtained, larger than assumed in the design process, due to a higher viscosity of the paste. However, small-signal characterization shows a cell capacitance close to the designed one, indicating a higher permittivity of the paste as a result of a higher density.

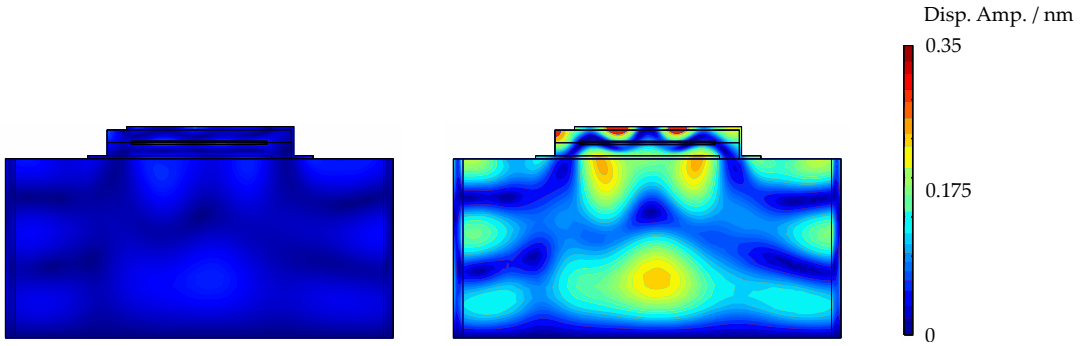

(a) Double MIM cell with acoustic intereference suppression.

(b) Double MIM cell without acoustic intereference suppression.

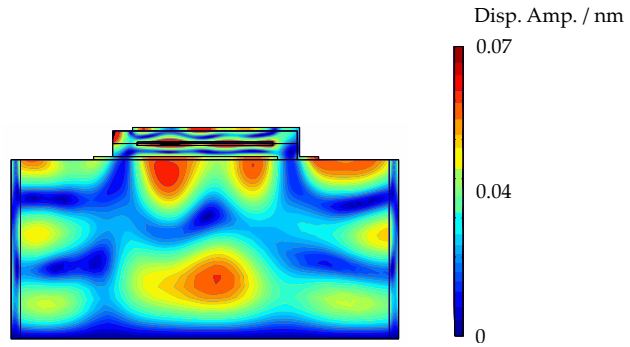

(c) Displacement in the suppressed cell with different scaling. Displacement of the middle electrode validates the proposed theory.

Figure 4.27: Comparison between a double MIM varactor cell with and without correctly applied DC biasing potential at the middle electrode to provide for acoustic interference suppression, see section 4.2.2. The bottom result of the suppressed cell with different scaling shows a displacement mainly of the middle electrode, validating the underlying theory.

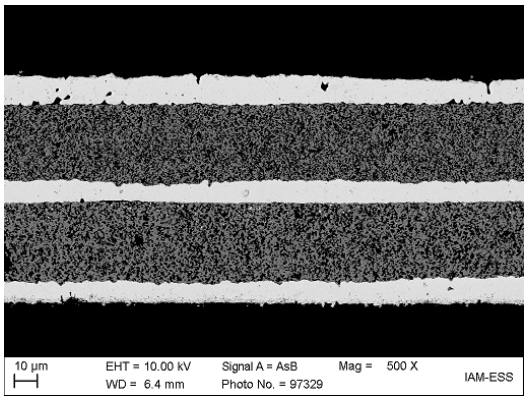

Figure 4.28: SEM cross-sectional image of the double MIM cell. ©2019 IEEE.

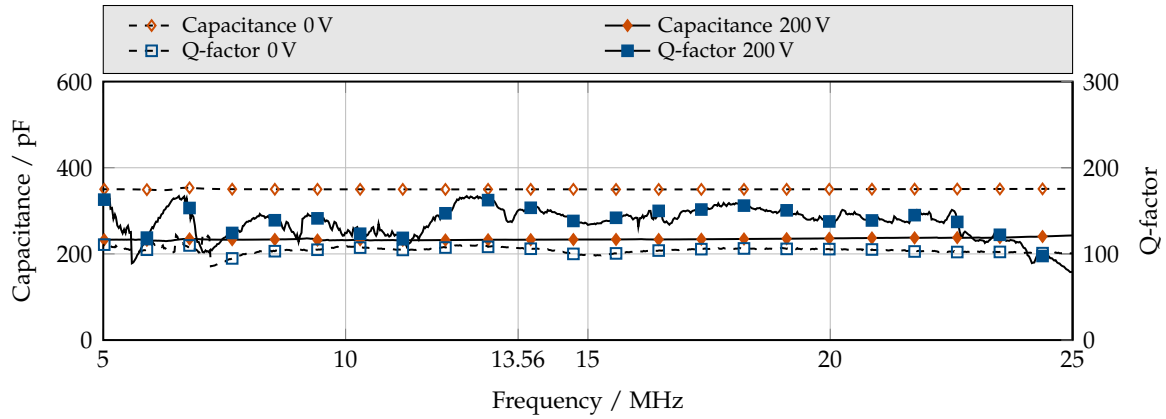

Figure 4.29: Capacitance and Q-factor of a double MIM varactor cell in unbiased and biased state. The measured Q-factor trace shows no indication of acoustic resonances.

Small-Signal Characterization

Each varactor cell is characterized with the wafer prober set up described in appendix C.3. The DC biasing voltage is increased to 200 V, as the BST layer thickness for the new design is significantly increased from 20 µm to 40 µm. The varactor cell small-signal characterization results in regard to capacitance, Q-factor and tunability are depicted in figure 4.29. The varactor cells show a tunability of 34 % reducing the capacitance from 350 pF in unbiased state to 232 pF in biased state at 13.56 MHz. A resonance free Q-factor spectrum is measured with an increased Q-factor of 151 in biased state from 107.

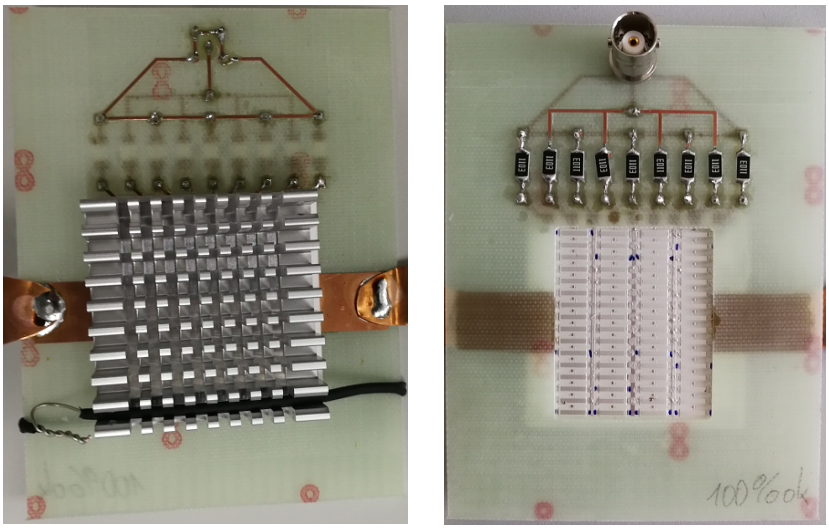

Figure 4.30: Varactor module consisting of the varactor substrate soldered to a PCB holding the resistive RF/DC decoupling network. (Left) Module with a passive heat sink mounted on the backside of the varactor substrate. (Right) Front of the module with the BNC DC connector and biasing resistors. ©2019 IEEE.

Large-Signal Characterization

The high-power measurements are carried out in a 50 Ω setup with two L-match circuits in back to back configuration and a 50 Ω high-power load. The exact measurement setup can be found in section 3.2. The implemented varactor module consisting of the matrix varactor substrate mounted to the RF/DC decoupling network holding FR4 board is depicted in figure 4.30. To achieve the highest possible power handling capability, all functional cells are connected to a macroscopic varactor.

For large-signal characterization, two different load conditions are taken, as each load condition only provides for a limited measurement range of DUT capacitance. The first load condition of $\underline{Z}_{\mathrm{M}}^{*} = (2.68 + 1.26\mathrm{i})\ \Omega$ is taken for power levels from 300 W up to 500 W. It creates a stressful loading state of the DUT varactor visible in the dissipated power trace of figure 4.31.

At 500 W of input power, the dissipated power of the varactor as well as the temperature increases from 13.5 W and 35 °C to 19.5 W and 42 °C respectively. The tunability of the varactor decreases from 34.4 % to 19.3 % as the Q-factor increases from 34.8 to 55.8 at 300 W of input power. The varactor capacitance is thermally reduced by 28 % from 2.5 nF to 1.8 nF. At this power level, an RMS voltage and current of 85 V and 13 A are applied to the DUT varactor. A conditioning effect is observed as the biasing voltage of 200 V is applied to the varactor. The effect is explained in more detail in section 4.1. During conditioning, the tunability of the varactor erratically increases to 30 %, as the isolation of the BST layer

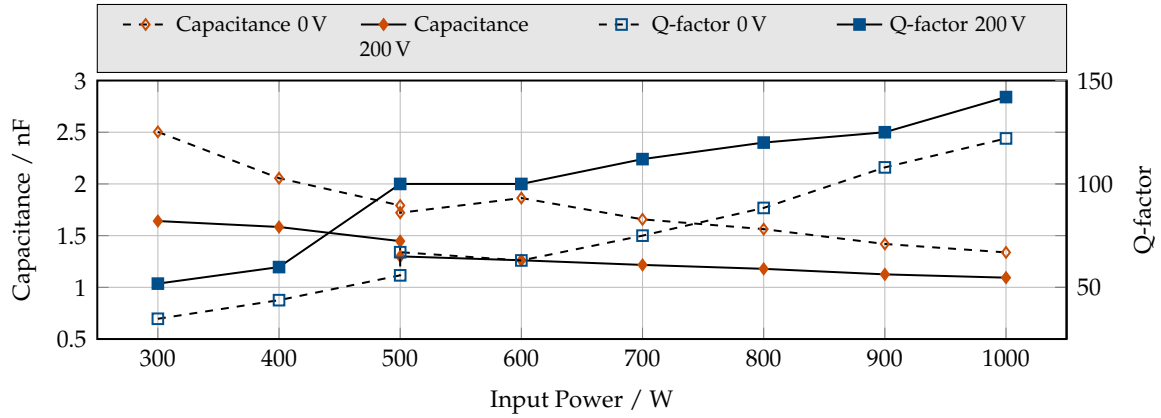

(a) Capacitance and Q-factor for various input power levels.

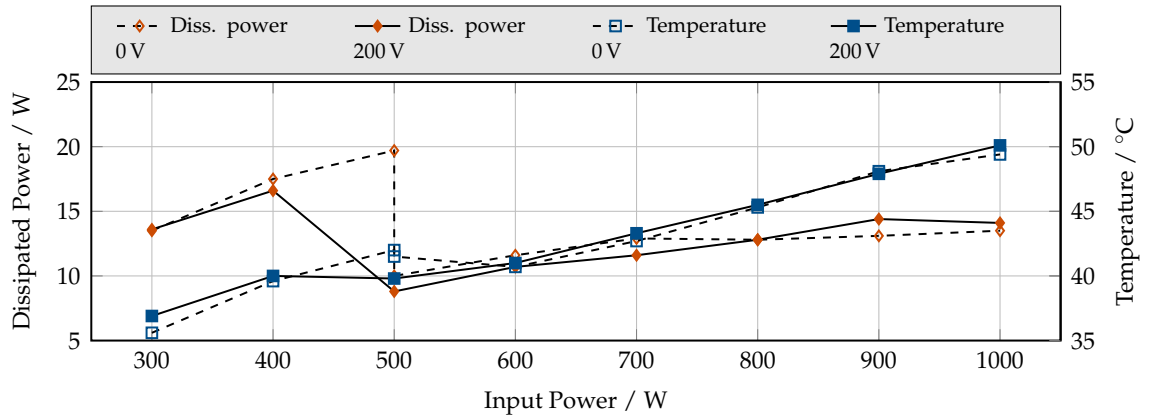

(b) Dissipated power and temperature measurements over input power.

Figure 4.31: Large-signal characterization of a varactor module with all cells interconnected varactor cells in regard to capacitance, Q-factor, dissipated power and temperature.

Table 4.4: Summary of large-signal characterization data obtained for the double MIM matrix varactor at different RF input power levels in unbiased state. * marked values are obtained during RF/DC conditioning process, see section 4.1.

Power level		DUT measurements						
P_{in} W	P_{out} W	V_{rms} V	I_{rms} A	$C(0\,V)$ nF	$Q(0\,V)$	τ %	P_{diss} W	T °C
291	258	47	10	2.5	35	34	13.5	36
386	344	66	11.5	2	44	23	17.5	40
480*	429*	85*	13*	1.8*	56*	19*	19.7*	42*
482	441	67	10	1.7	67	25	10	40
577	528	78	11	1.8	63	32	12	41
674	618	93	12	1.7	75	27	12.9	43
765	704	108	12	1.6	88	25	12.8	45
861	792	123	13	1.4	108	21	13.1	48
955	880	140	14	1.3	122	18	13.5	50

increases, resulting in a DUT capacitance value outside of the measurement range of the circuit and an increase in Q-factor from 55.8 to 67. To readjust the measurement range, a load impedance of $\underline{Z}_M^* = (3.35 + 13.55i)\,\Omega$ is set, creating a less stressful loading of the varactor. At 500 W of input power and the new loading state, an RMS voltage and current of 67 V and 10 A are applied to the DUT varactor, resulting in significantly reduced dissipated power and temperature, see figure 4.31. At 1 kW input power in unbiased state, the varactor shows a Q-factor of 122 increasing by 16 % to 142 in biased state. The varactor disspates 13.5 W and 14.1 W, respectively, due to the deviating power distribution between C_{Vac1} and the varactor when biased. Its capacitance is thermally decreased by 47 % from 2.5 nF to 1.3 nF. During high-power operation, the varactor withstands an RMS voltage and current of 140 V and 13.7 A with a maximum temperature of 50.2 °C. Compared to the varactor presented in section 4.1, the results show a decrease in losses of 63 % and a decrease in temperature of 33 %. In conclusion, the results show the potential of acoustically optimizing a thick film varactor design to increase its high-power capabilities at the cost of complexity. All detailed results of the large-signal characterization in unbiased state are given in table 4.4.

4.4 Power Handling Comparison of Thick Film Varactors

To compare the presented varactor designs in regard to their high-power capabilities, the different load impedances, applied during large-signal characterization for each design, have to be considered. Additionally, the impact of the acoustic optimization on the varactor losses is an important aspect. To summarize both, the apparent power at the varactor is

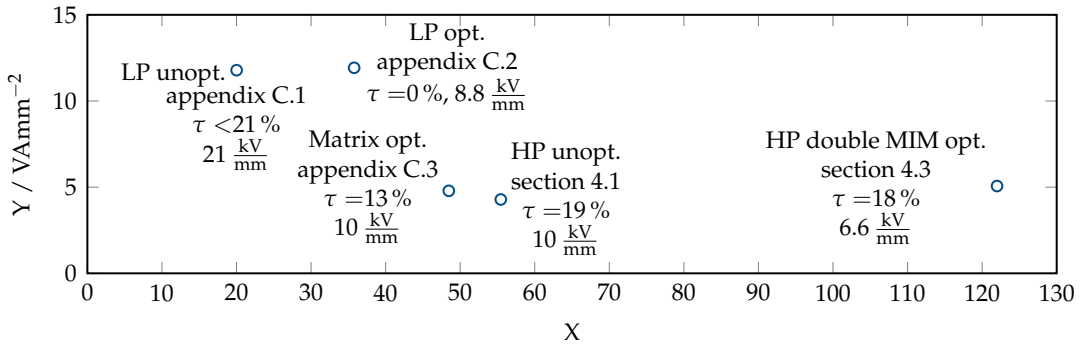

Figure 4.32: Comparison of the developed designs in regard to power handling capability. For optimal power handling, a design is situated in the top right region of the graph. Acoustically optimized designs are termed with „opt. “, while unoptimized designs are termed with „unopt. “. The capacitance tunability with the corresponding applied DC biasing field strength is given for each varactor.

divided by its dissipated power. The power-per-loss-factor is obtained:

$$X = \frac{V_{\text{rms}} \cdot I_{\text{rms}}}{P_{\text{diss}}} = \sqrt{\frac{1 + \tan^2\delta}{\tan^2\delta}} \tag{4.5}$$

with voltage and current RMS values V_{rms} and I_{rms} at the varactor. The loss tangent $\tan\delta$ is taken from the unbiased measurement. To account for the power dissipation capabilities of the design, mainly determined by the size of the varactor, the electrode overlap region is correlated to the apparent power of the varactor to again account for the different loading states. The power-per-area-factor is given by:

$$Y = \frac{V_{\text{rms}} \cdot I_{\text{rms}}}{A_{\text{electrode}}} \tag{4.6}$$

with the electrode overlap area $A_{\text{electrode}}$. The resulting graph is depicted in figure 4.32.

On the abscissa, the graph shows the performance of the design in regard to losses per power that is applied to it. For optimal performance, a design is situated on the far right of the graph. On the ordinate, the surface utilization of the design is visible. Here, for a maximum utilization of the substrate surface and therefore cooling capability of the varactor, an optimal design is situated in the upper area of the graph. However, as the varactor will be increasingly thermally tuned by increasing its power per area factor and therefore lose its electrical tunability, a compromise between power handling and tunability has to be found. The two half substrate medium power varactor designs given in appendix C.1 and appendix C.2 show the highest power per area ratio, while having the worst power per

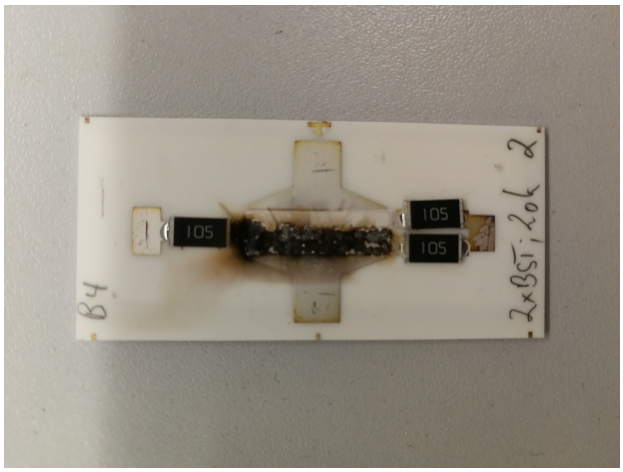

Figure 4.33: A varactor, broken down electrically during large-signal characterization.

loss ratio. Both varactor designs are operated close to the breakdown limit, as redundant samples broke down during large-signal characterization and applied biasing voltage, see figure 4.33.

However, the acoustically optimized varactor design shows a significant increase in power per loss factor, indicating the improvement due to the performed acoustical optimization. This is a surprising result, as the optimized design is not measured in a fixture but soldered to an FR4 PCB, holding the DC/RF decoupling network. Additional losses due to the soldered contacts, FR4 material and additional circuitry occur less impacting than the dielectric losses of the thick film varactor. For the matrix varactor design, given in appendix C.3, a further increase in power per loss factor is obtained, while the power per area factor is almost halved due to the full substrate design. However, the losses affected by the increase in metalization, caused by the matrix design implementation, is clearly visible as it performs worse compared to the unoptimized high-power design presented in section 4.1. The HP design, as the second full substrate varactor, shows a better performance in regard to power per loss compared to even some of the acoustically optimized designs. The reason is the overall higher Q-factor of the varactor compared to the worse performing designs, even though it suffers from acoustical resonances in the biased state. The higher Q-factor of the unoptimized high-power design is attributable to a different BST paste batch. In regard to the surface utilization, the design is far from its possible maximum. This results in a high tunability of 19 %, as the thermal tuning of the varactor does not exceed its overall tunability. The acoustically optimized double MIM approach shows a significant increase of the power per loss factor, mainly attributed to the decreased losses of the design, especially in the biased case. The low power per area factor indicates that the varactor is operated at a safe distance from its breakdown limit, which is supported by the high tunability of 18 % with less electrical field strength compared to the unoptimized high-power design. In conclusion, as varactors with high power per area factor show reduced tunability or are

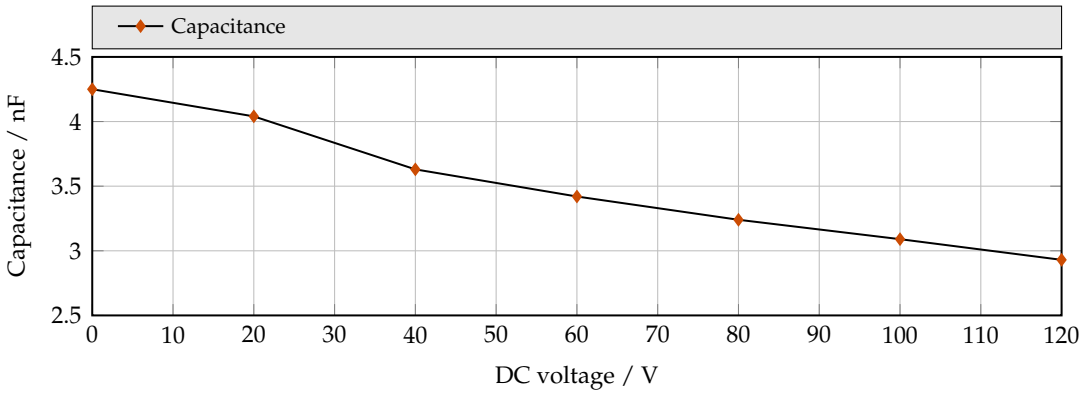

Figure 4.34: Capacitance over voltage of the thick film varactor, which is to be transiently characterized.

electrically destroyed, a value of $5\,\mathrm{V\,A\,mm^{-2}}$ is found to be a decent compromise between power handling and tunability for a varactor. In regard to power per loss factor, a maximum of $122\,\mathrm{V\,A\,W^{-1}}$ is achieved, proofing the effectiveness of acoustically optimized designs.

4.5 Transient Characterization

To obtain the switch characteristic of thick film varactors, a transient characterization is performed. A detailed description of the theory behind the presented characterization is given in section 3.3. Prior to transient characterization, the varactor is measured in regard to its small-signal characteristics to obtain its unbiased and biased capacitance values. The transient characterization circuit is designed to hold the varactor substrates without them mounted to any additional fixture or PCB. This is only possible with the designs presented in appendix C.1 and section 4.1, which are mounted in a measurement fixture for small-signal characterization. The acoustically optimized varactors are designed to be soldered onto FR4 modules holding the resistive DC biasing circuitry. The design presented in appendix C.1 shows a significantly more simple DC biasing circuitry compared to the design in section 4.1. Hence, it is chosen for transient characterization representative for all other presented thick film designs. The small-signal characterization is performed according to section 3.1. The results in regard to capacitance over biasing voltage at 13.56 MHz are depicted in figure 4.34. The varactor features a reduced tunability of 31 % compared to the identical varactor presented in appendix C.1. The unbiased capacitance, however, is comparable to the presented varactor design. Compared to the simulated circuit with a DUT capacitance of 2 nF (see section 3.3), a changed RF voltage to capacitance transfer characteristic is expectable with a reduced sensitivity of the circuit.

To apply the DC biasing voltage to the DUT varactor in the time frame of 1 µs, the varactors

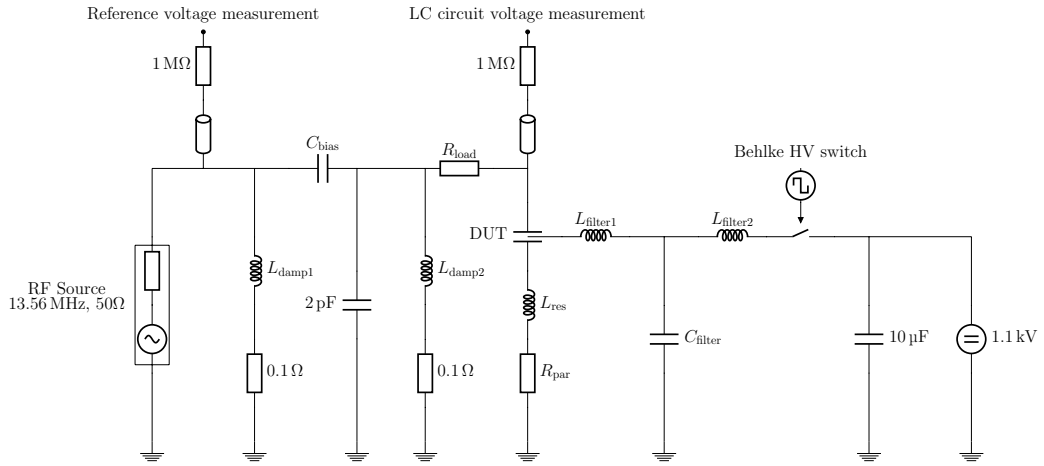

Figure 4.35: Implemented and characterized transient measurement circuit. The circuit deviates from the simulated circuit in section 3.3 in some component values and parasitics. A detailed summary of measured component values is given in table 4.5.

Table 4.5: Component and parasitic values of the transient characterization circuit.

L_{damp1} µH	L_{damp2} µH	C_{bias} nF	L_{res} nH	R_{load} Ω	$R_{res.,par.}$ Ω
1.1	1.1	1.68	173	50.6	2.4

resistive on-substrate biasing network is removed. With its 100 kΩ and 16 nF combined capacitance, a time constant of $\tau_t = RC = 1.6$ ms is too high for the intended characterization. Therefore, the RF/DC biasing filter presented in section 5.2.1 is connected to the DUT varactor. The filter is designed for response times of down to 10 µs, therefore the intended response time of 1 µs will result in a significant voltage overshoot. To counteract the voltage spike, which also couples to the measurement taps, two damping coils are installed in the transient measurement circuit, see figure 3.16 and figure 4.35.

The circuit's components are characterized with an LCR meter at 1 MHz and the input impedance of the circuit is measured with a copper strap installed at the position of the DUT varactor at 13.56 MHz. The circuit is then modeled and simulated in ADS at 13.56 MHz and the simulation and measurement result are compared. It is assumed, that all lumped component values are measured correctly. This is valid, considering the insensitivity of the RF voltage envelope to capacitance transfer characteristic towards variation of the lumped component values, see figure 3.17. However, the line impedance on the measurement board and the connection resistance of the DUT measurement fixture are adjusted to match simulation and measurement result. The obtained values of the transient measurement circuit are given in table 4.5.

Compared to the assumed component values in the simulation of the circuit, see section 3.3, large deviation is obtained for L_{res} with 173 nH to expected 69 nH and $R_{\text{res.,par.}}$ with 2.4 Ω compared to expected 0.1 Ω. The large inductance is indispensable and attributed to the length of the connection to the DUT varactor. The large resistance is generated by the suboptimal connections of the DUT varactor substituted with a copper strap. However, the bad connections will remain in the circuit with the DUT varactor installed, as the copper strap then establishes connection between the DUT varactor and the transient measurement circuit board. Therefore, the simulation presented in section 3.3 is set up with the obtained component values and DUT varactor installed and the RF voltage envelope to capacitance transfer characteristic is created for a DUT capacitance and tunability according to figure 4.34. The characteristic curve is depicted in figure 4.36b. For transient characterization, a 13.56 MHz RF generator with an output power of 5 W is connected to the circuit. The RF input voltage is measured with a DC voltage independent amplitude of 48 V. Figure 4.36a depicts the DC-dependent LC circuit RF voltage and applied DC voltage at the DUT varactor. A DC voltage rise time of 1.5 µs is achieved with the setup. A significant envelope constriction from 3.28 V to 2.80 V is visible, caused by the change of DUT capacitance with voltage. A harmless voltage spike created by the filter coils remains in the LC circuit RF envelope at 1.4 µs. The voltage constriction follows the DC voltage rise time with good agreement.

From the LC circuit RF envelope voltage, the corresponding capacitance is extracted with the RF to capacitance transfer characteristic. The measured voltage values are good agreement with the simulated voltages expected at the DUT varactor. Furthermore, the measured LC circuit RF envelope voltage is strictly monotonously falling, therefore a unique extraction from the in general ambiguous RF to capacitance transfer characteristic is very well possible. The DUT capacitance over time is depicted in figure 4.36c and in good agreement with the expected capacitance over voltage values from the small-signal characterization depicted in figure 4.34. The result indicates an instantaneous capacitance change with DC biasing voltage, and therefore, thick film response times smaller than 1.5 µs.

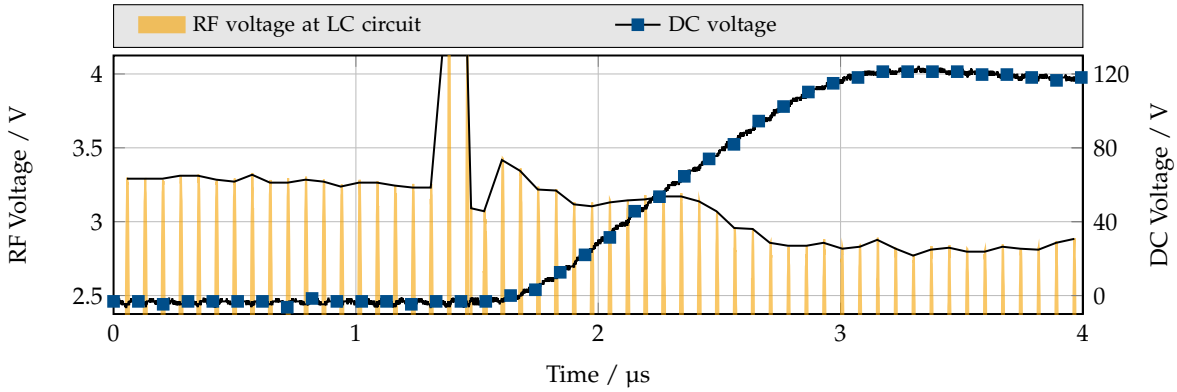

(a) Measured RF envelope voltage at the LC circuit and DC voltage at the DUT varactor over time.

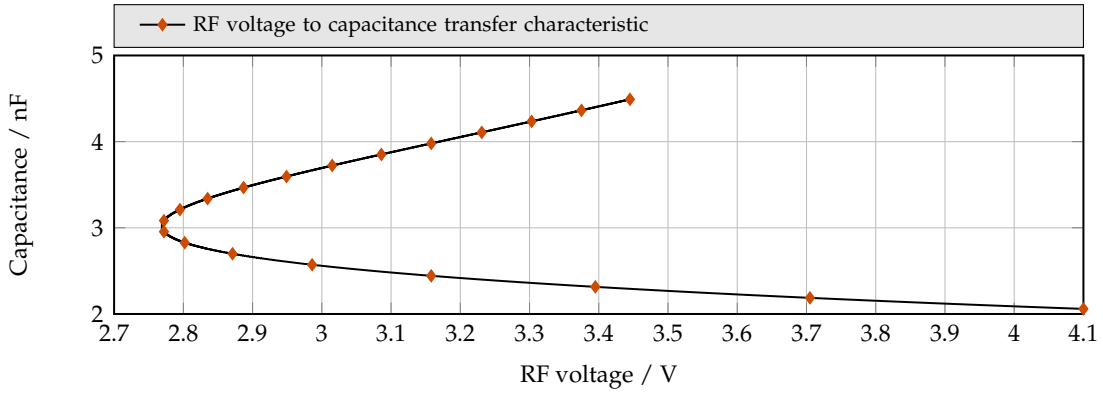

(b) RF voltage to capacitance transfer characteristic for the transient measurement circuit.

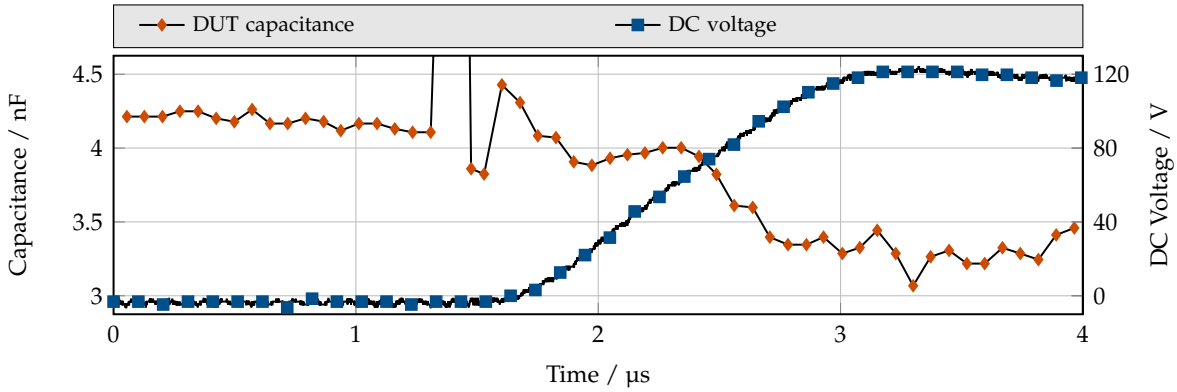

(c) Extracted capacitance from RF voltage envelope over time with corresponding DC biasing voltage at the DUT varactor.

Figure 4.36: Transient characterization measurement result of the thick film varactor, the required voltage to capacitance transfer characteristic and the obtained capacitance over time trace.

5 Design, Processing and Demonstration of High-Power Bulk Ceramic Varactors

An alternative to the presented thick film based varactors are bulk ceramic disk varactors. These cylindrical pellets are employed on a printed circuit board to form a circuit board integrated bulk ceramic disk varactor module (CBIVM). The CBIVM holds the DC biasing network and provides for the RF connectors to the matching circuit. In this work, a CBIVM consists of four serial connected bulk ceramic disk varactors. Theoretically, more disk varactors can be integrated in such a module and their stacking scheme can be altered arbitrarily, however, due to size limitations of the PCB larger or in parallel connected stacks are waived. The main focus is put on the evaluation of suitable bulk ceramic material for the varactor pellets in regard to Q-factor, tunability and acoustical behavior. For this, different base material compositions, additives, dopants, metalizations and processing routines are considered. All material compositions have their Curie temperature at to room temperature (20 °C), see section 2.1.1. The operational temperature of the pellets is 50 °C, therefore they are characterized in a heated fixture, see section 3.1.3. The behavior of the pellets is evaluated in a frequency range of 5 MHz to 25 MHz with biasing voltages up to 1.1 kV. The same parameters apply for the characterization of CBIVMs. The acoustical behavior of the pellets is further evaluated to identify influencing geometrical or processing parameters such as sintering temperature and duration. The evaluation is simulation-based and verified with measurements on individually processed bulk ceramic disk varactor samples. Varactor pellets themselves, are not characterized in regard to their large-signal behavior. For this, a CBIVM is utilized and characterized in the same way as the thick film varactors were characterized in chapter 4. Large-signal characterization is performed with biasing voltages up to 1.1 kV even though voltages up to 6 kV are intended for later application. Technical restrictions of the measurement circuit and safety are the reason for this limitation. For bulk ceramic varactors, the selection of a metalization is bound to RoHS compatibility, adhesion to the BST surface and compatibility to subsequent PCB integration processes. Among those, materials with high conductivity are preferred naturally. In this work, silver and copper based metalization is evaluated.

5.1 Bulk Ceramic Disk Varactors

For the design and application of bulk ceramic varactors the challenges are of a different nature compared to thick film varactors. The cylindrical bulk ceramic disk varactor lacks a

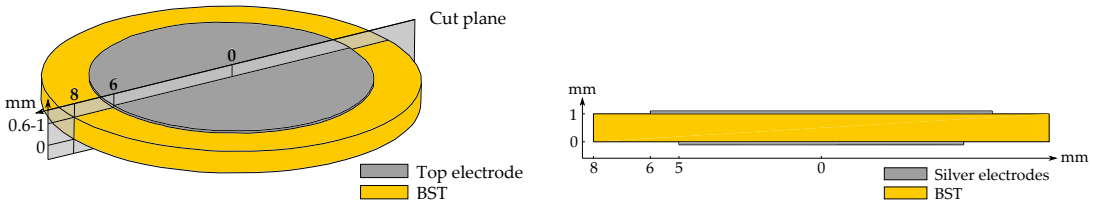

(a) 3D view of a bulk ceramic disk varactor.

(b) 2D cut plane view of the pellet.

Figure 5.1: Bulk ceramic disk varactor geometry.

mechanically stabilizing substrate, therefore the pellet itself requires mechanical stability. As as result, for a given diameter, a minimum thickness is predefined, providing for the required mechanical stability of the pellet. Counteracting, a minimized DC biasing voltage is desired, requiring pellet thicknesses as low as possible. A minimum thickness of 0.6 mm is found to be manageable in regard to handling and manufacturing. A cylindrical geometry offers several advantages compared to other shapes. In regard to manufacturing, the compression of a round body provides for a homogeneous pressure distribution in the material as opposed to an angular geometry. From an electrical point of view, stray fields are distributed homogeneously around the disk, providing for a homogeneous field loading of adjacent materials. The geometry of the bulk ceramic disk varactors with metalization are depicted in figure 5.1.

In regard to electrical behavior, the increased thickness of bulk ceramic pellets compared to thick films introduces new challenges. The DC biasing voltages for bulk ceramics are orders of magnitude larger for equal electrical field strength in the dielectric, due to increased thickness. Furthermore and opposite to the mere characterization scenario, fast biasing plays a larger role in this chapter, as the presented varactor modules are intended for the actual application in high-power matching circuits. Bulk ceramics feature significantly larger permittivities compared to thick films, see figure 2.10, which result not only in higher tunabilities but also in larger electric field displacement and therefore higher stresses for adjacent materials. Therefore, the partial discharge effect and overall the isolation scheme is playing a larger role compared to thick-film-based varactors. A closer look is now taken on the field displacement problematic in both the pure DC and the transient case. The field distribution in a cross-layered medium with two different permittivities and conductivities is dominated by the conductivities in the purely DC case [91]. For a parallel plate capacitor surrounded by air and a low electrical conductivity in the dielectric, the electric field distribution is mainly confined within the dielectric. Stray field components in the adjacent medium occur but are significantly lower than in the dielectric. For the transient case, however, the field distribution is no longer defined by the conductivities of the materials in the field region but by their permittivities [91]. As a result, for the parallel plate capacitor containing a dielectric with a high permittivity, the electric field is significantly displaced into the surrounding air with the low permittivity. This correlation can be derived from Ampère's circuital law and harmonic excitation [15]:

$$\begin{aligned} \mathrm{rot}\vec{H} &= \vec{J}_{\mathrm{cond}} + \frac{\partial \vec{D}}{\partial t} \\ \vec{J} &= \sigma\vec{E} + j\omega\varepsilon\vec{E} \\ I &= \iint_A (\sigma\vec{E} + j\omega\varepsilon\vec{E})\mathrm{d}\vec{A} \end{aligned} \tag{5.1}$$

The boundary condition, defining the responsible material property for the current density and therefore electric field distribution, can be deduced from equation (5.1). For $\sigma \gg \omega\varepsilon$, the stationary DC current dominates the electric field distribution, which is valid for good electrical conductors. In isolators, for which $\sigma \ll \omega\varepsilon$, the displacement current dominates the field distribution. In figure 5.2 an exemplary simulation is set up. A circular BST pellet with a diameter of 16 mm, a thickness of 1 mm, a top and bottom electrode with a diameter of 10 mm and 12 mm and a thickness of 100 µm is set up. The surface of the BST pellet is loaded with a surface resistance. The BST and surrounding air have a permittivity of 3000 and 1, respectively. For the DC case a steady potential of 6 kV is applied, while for the transient case a harmonic excitation with 250 kHz is used, mimicking a 1 µs transient rise and fall time of a charging/discharging process.

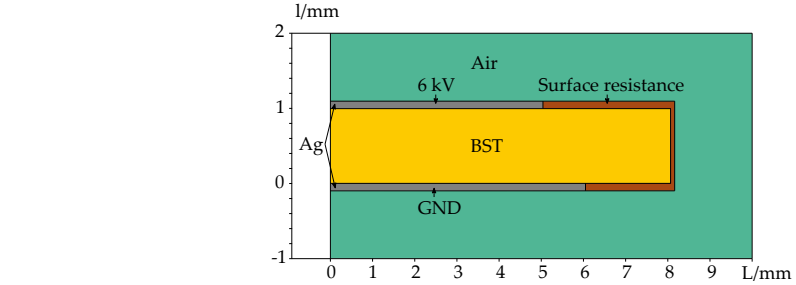

(a) Simulation Modell

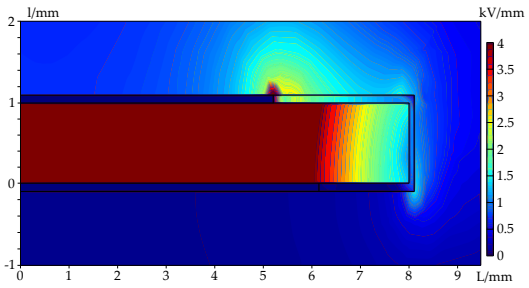

(b) Purely DC excitation.

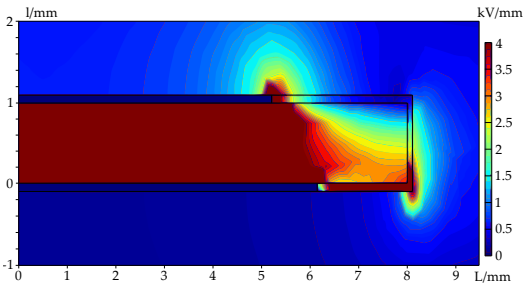

(c) Harmonic AC excitation with 250 kHz.

Figure 5.2: Simulation of a parallel plate capacitor filled with dielectric material and a low conductive surface layer surrounded by air for b) purely DC excitation and c) harmonic AC excitation with 250 kHz.

Due to the path length difference through the dielectric and over the surface, the electric field is still largely confined in the dielectric in the DC case, see figure 5.2b. For the transient case, however, due to the significantly larger permittivity of bulk ceramics compared to the surrounding material including the conductive surface layer, the electric field during application or removal of the DC biasing voltage is displaced in the surrounding medium, see figure 5.2c [91]. As a result, the electrical field load of the surrounding air is largely increased compared to the DC case and the electrical breakdown field strength of the air ($3\,\mathrm{kV\,mm^{-1}}$, [44]) locally exceeded. For the application, the requirement for an envelope of the pellet arises, capable of resisting the electric field load in DC and transient cases. The envelope needs to be free of gas inclusions and ideally provides for a surface coating with a lower conductivity compared to the BST bulk material. For thick film varactors, this problem is of minor importance due to two reasons. First, the bottom electrode of thick film varactors is usually covered by dielectric. Therefore, creepage between the electrodes is interrupted by a completely isolating solid. Secondly, larger creepage distance to dielectric thickness ratios of up to 20 to 1 can be implemented. For bulk ceramic pellets, a thickness to creepage ratio of 8.5 to 1 represents the maximum. A similar problem is introduced due to the porosity of the bulk ceramic pellets. Within the dielectric, the electric field is displaced into the gas volume of the pores, when stressed with a biasing voltage. The gas filled pores act as weak spots, due to the reduced electrical breakdown field strength of gas compared to solids. To estimate the field strength within the pores at 6 kV biasing voltage, which is desired for the intended application, and the electrical breakdown field strength of the trapped gas dependent on the pressure and gap size, an electric field simulation is set up and Paschen's Law is applied, see section 2.3. Measurements have shown, that bulk ceramic pellets include a porosity of 5 % with pore diameters in the 5 µm to 20 µm range. Due to the high temperatures during manufacturing, the subsequent cooling process and the impermeability of the solid, a reduced gas pressure of 500 mbar in the pores is assumed. The gap width is taken from the pore diameter. As a result, a gas pressure gap width product of 2.5 mbar mm to 10 mbar mm is obtained, resulting in breakdown voltages from 460 V to 310 V [62]. A normalization of these values to the gap width gives breakdown field strengths of $92\,\mathrm{kV\,mm^{-1}}$ to $15.5\,\mathrm{kV\,mm^{-1}}$.

A simulation is set up to estimate the electrical field strength in the pores with applied biasing voltage. The simulation model is a confined in a 1.5 x 1 x 0.2 mm volume with spherical inclusions, see figure 5.3a. A 6 kV biasing voltage is applied to the model. A relative permittivity of 3000 and 1 are assumed for the BST and air inclusions, respectively. The simulation results in regard to the cutting plane depicted in figure 5.3a are presented in figure 5.3.

The simulation indicates a significant field displacement perpendicular to the E-field vector around the spherical inclusions. However, the electrical breakdown field strength of $32\,\mathrm{kV\,mm^{-1}}$ of BST [92] is not exceeded. For the inclusions a largely homogeneous E-field is obtained with a maximum 8 % increase to $6.5\,\mathrm{kV\,mm^{-1}}$. Taking into account the estimated electrical breakdown field strength of the inclusions of minimum $15.5\,\mathrm{kV\,mm^{-1}}$, the biasing voltage is considered unproblematic.

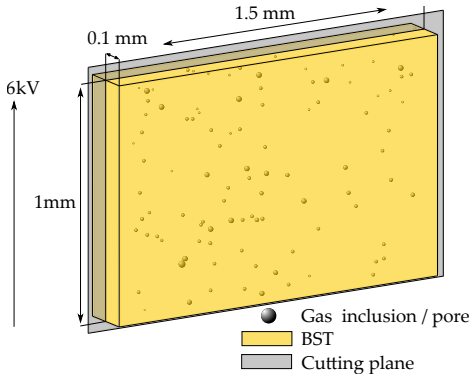

(a) Porous bulk ceramic BST model.

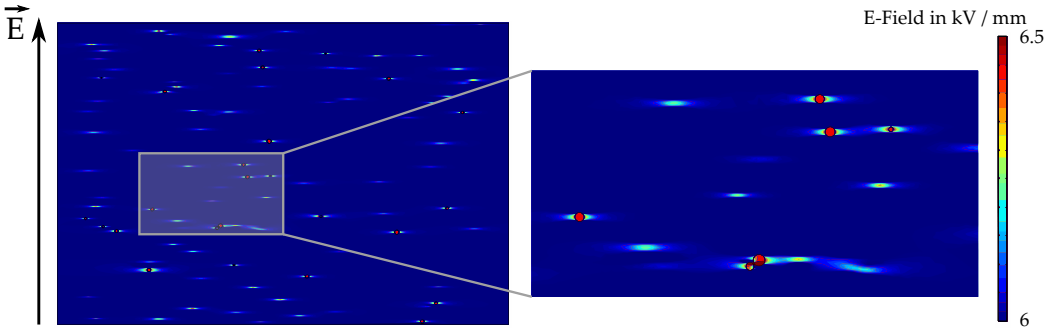

(b) Simulation results.

Figure 5.3: DC simulation of the field distribution in a bulk ceramic pellet with a porosity of 5 % and d_{50} radius of 10 µm. 6 kV are applied over a distance of 1 mm.

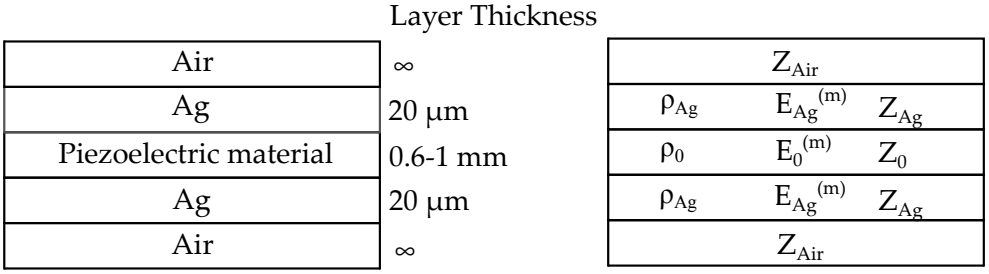

Figure 5.4

5.1.1 Acoustic Modeling

As described before, the geometry of the disk varactors plays an important role in the design process. In particular the pellets thickness, is identified as a highly important design parameter, as it influences both the mechanical as well as the electrical behavior of the pellet significantly. Additionally, in a vertically layered structure, the thickness also affects the acoustical behavior of the structure predominantly. Therefore, a possibility to estimate the acoustical behavior of the pellet for a given thickness is important. Bulk ceramic pellets offer a favorable geometry for an analytical modeling approach as longitudinal acoustic waves are dominant. Compared to a piezoelectric simulation in COMSOL or the implementation of bulk ceramic samples to obtain their acoustical behavior, an analytical approach requires much less time and computational effort. Its accuracy is evaluated by comparing the analytically obtained resonance spectrum for a pellet thickness range of 0.6 mm to 1 mm with a piezoelectric simulation and verifying it with small-signal measurements on fabricated samples. For these, a class 1 base material is used, specifically a $BaTiO_3$, $CaTiO_3$ composite material with a mixed phase of both, as it creates a clutter-free ESR spectrum with narrow and distinguishable resonances. The model presented in [93] is set up and its results are compared to a piezoelectric simulation in COMSOL and validated with the fabrication of corresponding bulk ceramic samples. To estimate the acoustical behavior of stacked piezoelectric structures, such as parallel plate capacitors, the modeling scheme uses a transmission line approach. The piezoelectric excitation layer, creating the acoustic wave, is termed with index 0. The input impedance into this layer is consecutively calculated, from the outer to the inner layers. The characteristic acoustic impedance of air (sandwiching layers) is then transformed across the adjacent silver electrode layers to the excitation layer. Each layer has a characteristic density ρ and elasticity $E^{(m)}$ resulting in an acoustic impedance Z and wave propagation velocity $c^{(a)}$, see figure 5.4.

The acoustic impedance based on the mechanical properties of the material is given by [16, 89]:

$$Z_{\text{mat}} = c^{(a)}\rho = \sqrt{E^{(m)}\rho} \tag{5.2}$$

Table 5.1: Material properties used for the analytical modeling approach.

Material	Z $\mathrm{kg\,m^{-2}\,s^{-1}}$	ρ $\mathrm{kg\,m^{-3}}$	$E^{(\mathrm{m})}$ GPa	$c^{(a)}$ $\mathrm{m\,s^{-1}}$	l mm	d $\mathrm{C\,m^{-2}}$	ε_r
Air	400	-	-	360	∞	-	-
Ag	3.78e7	10500	83	2811	0.02	-	-
Class 1 dielectric	3.11e7	5000	200	6230	1	3.66	1180

The transformed acoustic impedance Z_{Trans} over a material layer with the characteristic impedance Z_{layer} is given by [93]:

$$\underline{Z}_{\mathrm{Trans}} = \frac{Z_{\mathrm{mat}} + jZ_{\mathrm{layer}}\tan(\omega l_{\mathrm{layer}}/2c^{(a)}_{\mathrm{layer}})}{Z_{\mathrm{layer}} + jZ_{\mathrm{mat}}\tan(\omega l_{\mathrm{layer}}/2c^{(a)}_{\mathrm{layer}})} \tag{5.3}$$

Then, the acoustic impedance of the structure can be calculated according to [93]:

$$\underline{Z}_{\mathrm{in}} = \frac{1}{j\omega C_0}\left[1 - K^2\frac{\tan\beta}{\beta}\cdot\frac{(\underline{z}_{\mathrm{ac2}} + \underline{z}_{\mathrm{ac3}})\cos^2\beta + j\sin 2\beta}{(\underline{z}_{\mathrm{ac2}} + \underline{z}_{\mathrm{ac3}})\cos 2\beta + j(\underline{z}_{\mathrm{ac2}}\underline{z}_{\mathrm{ac3}} + 1)\sin 2\beta}\right] \tag{5.4}$$

with the iteratively transferred acoustic impedances $\underline{Z}_{\mathrm{ac2}}$ and $\underline{Z}_{\mathrm{ac3}}$ at the boundaries of the piezoelectric layer, the characteristic acoustic impedance of the piezoelectric layer Z_0 and the coupling factor K [93]:

$$\underline{z}_{\mathrm{ac2}} = \frac{\underline{Z}_{\mathrm{ac2}}}{Z_0}, \quad \underline{z}_{\mathrm{ac3}} = \frac{\underline{Z}_{\mathrm{ac3}}}{Z_0}, \quad \beta = \frac{\omega l_0}{2c_0^{(a)}}, \quad K = \frac{d_{33}}{E^{(\mathrm{m})}\varepsilon_0\varepsilon_r(E) + d_{33}^2} \tag{5.5}$$

The input parameters are the layer impedances Z, densities ρ, mechanical elasticities $E^{(\mathrm{m})}$, sound velocities $c^{(a)}$ and thicknesses l. The excitation layer is considered additionally with piezoelectric coupling factor d and permittivity ε_r. A detailed summary of the utilized values is given in table 5.1. The elasticity of 200 GPa for the class 1 dielectric is extracted from the measured first acoustic resonance. The class 1 dielectric is a $BaTiO_3$, $CaTiO_3$ composite material with a mixed phase of both. From the mixed crystal system BST, it is known, that with increasing percentage of strontium the elasticity increases [80]. However, the extracted value of 200 GPa for the class 1 dielectric appears to be quite high, considering the values for $BaTiO_3$ and $CaTiO_3$ of 117 GPa and 161 GPa, respectively [78, 94]. The analytically obtained resonance locations are given in table 5.2.

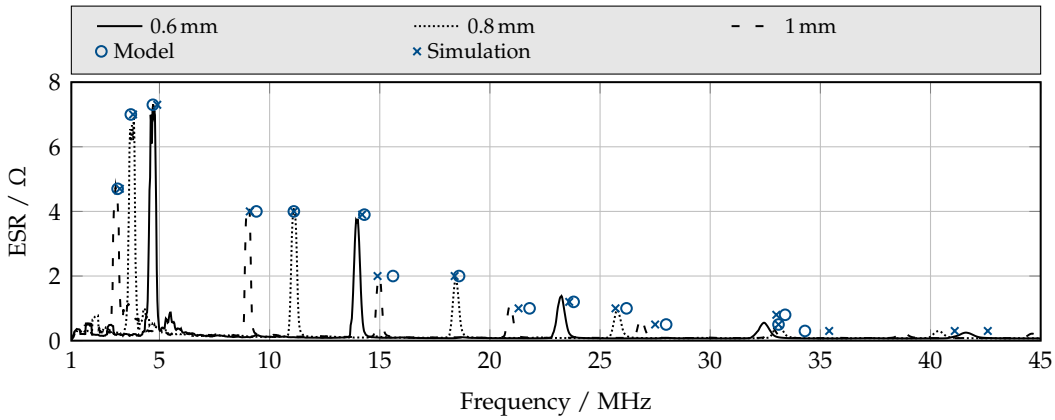

Figure 5.5: Measured impedance spectrum for several pellet thicknesses with marked resonances from the presented model and acoustic simulation.

Table 5.2: Resonance location in MHz obtained with the analytical model, the piezoelectric simulation and the measurement for pellet thickness of 1; 0.8; 0.6 mm.

Resonances	Model	Simulation	Measurement
f_{res1}	3.1; 3.7; 4.7	3.2; 3.8; 4.9	3.1; 3.8; 4.7
f_{res2}	9.4; 11.1; 14.3	9.1; 11.1; 14.2	8.9; 11.2; 13.9
f_{res3}	15.6; 18.6; 23.8	14.9; 18.4; 23.6	15.0; 18.5; 23.3
f_{res4}	21.8; 26.2; 33.4	21.3; 25.7; 33	21.0; 25.8; 32.2
f_{res5}	28.0; 33.1; –	27.5; 33.1; 42.6	27.0; 33.1; 41.6
f_{res6}	34.3; –; –	35.4; 41.1; –	33.0; –; –

The piezoelectric simulation is set up with the pellet model identical to figure 5.1 in the frequency range from 1 MHz to 45 MHz. The simulation is set up in the strain charged form with the same material properties used for the analytical model, seein table 5.1. The results are given in table 5.2 together with the results of the analytical approach and the measured data. To verify the analytical approach and the piezoelectric simulation, bulk ceramic disk varactor samples are fabricated with thicknesses from 0.6 mm to 1 mm. The samples are characterized from 1 MHz to 45 MHz and biasing voltages up to 1.1 kV. The characterization results are depicted in figure 5.5 with marked resonance locations from the model and piezoelectric simulation.

Both, the analytical model approach as well as the simulation generate resonances close to the frequency locations of the measurement. Not all measured resonances are obtained from the analytical model, which is a result of perfect destructive interference. In the measurement, these resonances occur with a significantly reduced amplitude, indicating an imperfect cancellation. The piezoelectric simulated resonance locations deviate on average from the measured ones by 1.7 %. For the analytical model, the resonances deviate from the

measured ones on average by 2.5 % over the whole frequency range. Taking into account the significantly reduced computation time of the analytical approach, it offers a good performance/cost ratio for resonance estimation.

5.1.2 Varactor Characterization

The implementation of bulk ceramic varactors includes several different processing steps compared to thick film varactor fabrication. Both varactor types share the powder preparation and calcination step prior to the manufacturing process of the varactors themselves. For bulk ceramic varactors, a shaping process, including the implementation of a compressed green body prior to sintering is performed, which is excluded for thick film varactors. The compression of the powder into the shape of a cylindrical pellet enables an increased sintering activity, resulting in a more dense ceramic later on with reduced porosity compared to uncompressed thick films [95, 96]. In contrast to the screen-printed thick film varactors, the electrode metalization can be applied to the pellet after the sintering process, enabling the exposure of the pellet to temperatures above 850 °C. Within the scope of this work, a variety of different base materials, additives, dopants, metalizations and processing routines are evaluated. For the intended application, the two main criteria of a good bulk ceramic pellet is the tunability and the Q-factor in both the biased and unbiased state. As the Q-factor decreases with bias, commonly attributed to an unfavorable position of acoustic resonances, these two quality parameters also cover the acoustical behavior of the pellet. All characterized disk varactors share a diameter of 16 mm and a thickness of 1 mm with electrode diameter of 10 mm on one side and 12 mm on the other side to account for misalignment. The bulk ceramic varactor pellets are characterized in regard to their small-signal behavior according to section 3.1.3 with a biasing voltage of 1.1 kV. A biasing field strength of 1.1 kV mm^{-1} is obtained. The results of the characterization in regard to tunability and Q-factor in zero-bias and biased state at 13.56 MHz are depicted in figure 5.6.

Applicable materials for the intended application in high-power impedance matching circuits, require a high tunability and a high Q-factor in both zero-bias and biased state. In the graph, this criteria is met in the upper right corner. For some of the materials, the tunability is extrapolated to 6 kV biasing voltage using the Weil model [10].

Two commercially available base materials are evaluated, indicated as Class1 and Class2 in figure 5.6, where the class 1 dielectric is better suited for high voltage AC and DC application. A tunability of 2.5 % is obtained with a corresponding Q-factor of 75 in unbiased state increasing to 79 in biased state. The second one is a class 2 Y5U specified, commercially available dielectric [21]. Therefore, a larger electrical and thermal tunability compared to the class 1 dielectric comprised of $BaTiO_3$ and $CaTiO_3$ is expected, as well as increased dielectric losses. A tunability of 40 % is obtained and an unbiased Q-factor of 44. In biased state, the Q-factor increases by 71 % to 75.

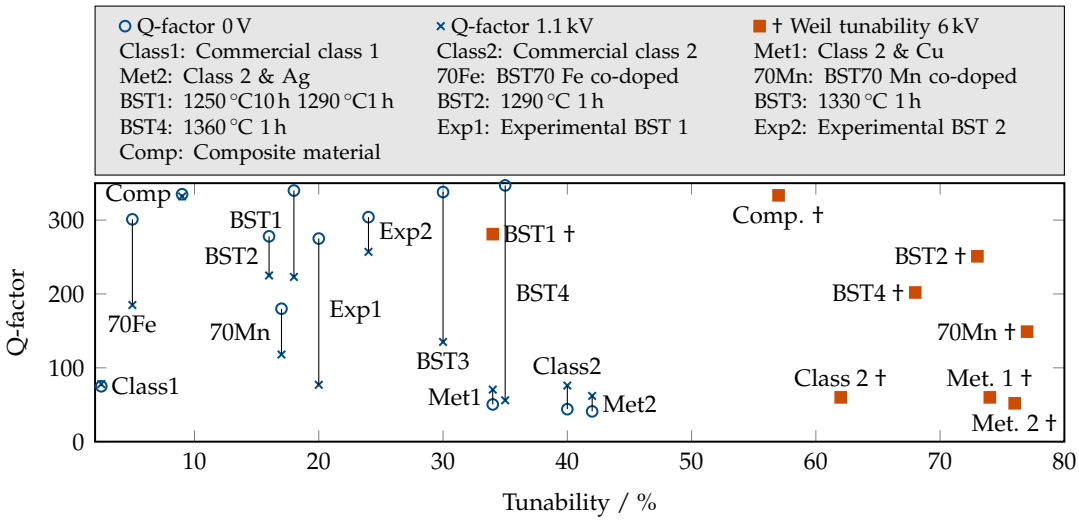

Figure 5.6: Comparison of different bulk varactor base materials, dopants, additives, metalizations and processing routines in regard to capacitance tunability and corresponding Q-factor for unbiased and 1.1 kV biased state at 13.56 MHz. A negative Q-factor gradient indicates high acoustical activity of the material composition at 13.56 MHz. A positive or zero gradient indicates the absence of acoustical resonances at 13.56 MHz. For some base materials, the tunability is extrapolated to 6 kV according to the Weil model [10].

The two dopants, iron and manganese are compared (70Fe and 70Mn). Iron as a loss but also tunability reducing dopant is problematic in industrialized processes as it is ferromagnetic. The contamination of other processes could lead to a significantly changed high frequency behavior of the produced devices. It is compared to the more common paramagnetic dopant manganese, which is applied similarly. The results, however, indicate a completely different behavior of the two materials. As iron-doped BST shows a significantly increased Q-factor but also increased acoustical activity, the tunability on the other hand is heavily reduced. Overall, the manganese-co-doped BST appears to be a more promising candidate for the intended application.

Experimental material 1 (Exp1) is a manganese co-doped $Ba_{0,7}Sr_{0,3}TiO_3$ ceramic, milled in water. Water as a milling lubricant washes barium from the ceramic powder, resulting in a barium depletion. Isopropanol is an alternative to water as a milling lubricant, preventing the barium washout. However, due to its flammability it is less common in industrialized processes. Here, experimental material 2 (Exp2) represents the same material composition as experimental material 1 but it is milled in isopropanol. The results indicate a significantly increased acoustical activity in the water-milled ceramic as the Q-factor deviates strongly with bias. A slightly reduced tunability of 20 % compared to 24 % is obtained for experimental material 1 and an overall reduced Q-factor. Overall, experimental material 2 represents a suitable candidate for the intended application, due to its high tunability and low acoustical

activity.

In regard to processing routine, a set of measurements is performed on manganese-co-doped $Ba_{0,7}Sr_{0,3}TiO_3$ sintered at temperatures from 1250 °C to 1360 °C (BST1 to BST4). With increasing sintering temperature and time, the tunability of the material increases and also its acoustical activity. The reason for this is the changing texture of the ceramic. In general, the texture of a sintered ceramic consists of grains connected by sintering necks. The grains themselves contain a single crystal or polycrystalline lattice which is broken up into an amorphous structure in the sintering necks. Single crystals and polycrystals introduce lower dielectric losses due to a reduced number of defects. The sintering necks with their amorphous structure and introduction of impurities, in case of incomplete formation due to insufficient sintering temperature and duration, are prone for higher, defect-based dielectric losses [40]. In general, higher sintering temperatures and longer sintering durations result in an increased shrinkage of the green body, promoting the creation of complete sintering necks between grains and therefore in higher densities of the pellet. However, with increasing sintering temperature and time, the probability for the occurence of melting phases and giant grains in the bulk ceramic compound increases. Giant grains and melting phases represent grain conglomerates, which completely lost their single crystal or polycrystalline lattice structure and became amorphous. Macroscopically, the permittivity of the material drastically increases and the zero-bias, defect based losses drastically decrease [39, 97, 98]. In tuned state, however, the material is more prone to acoustical activity due to its homogeneity. Therefore, in regard to the acoustical behavior, smaller grains are assumed favorable. Acoustic waves are scattered at material boundaries and propagate in homogeneous material. Therefore, large grains or melting phases promote the propagation of acoustic waves, while small grains reduce their intensity [99]. As a result, the best candidate of the set is the pellet sintered at 1290 °C, as it shows decent tunability with the smallest acoustical activity.

Two experimental metalization pastes are compared, which are suitable for the integration process of the disk varactors on a circuit board integrated varactor module (CBIVM). The pastes (Met1 and Met2) are silver and copper based, respectively. Both are applied to a class 2 specified Y5U ceramic. The choice fell on this particular base material due to its well-established industrial manufacturing process, resulting in a high reproducibility of the electrical, mechanical and thermal quantities of the pellets. As a result, a separation of the influence of the metalization on the electrical properties is very well guaranteed, providing comparability. The results indicate no impact on the acoustical activity as well as on the losses. A slight increase in tunability for the silver based paste is observed, attributed to a slight deviation in pellet thickness.

The composite material (Comp) represents a novel approach for the suppression of acoustic resonances and secondarily increasing the materials Q-factor by introducing an additional low loss magnesium based metal oxide dielectric in the BST matrix. A detailed analysis of the composite is given in section 5.1.3. The composite material shows the most promising properties as a bulk dielectric for tunable varactors, as its Q factor is almost static for

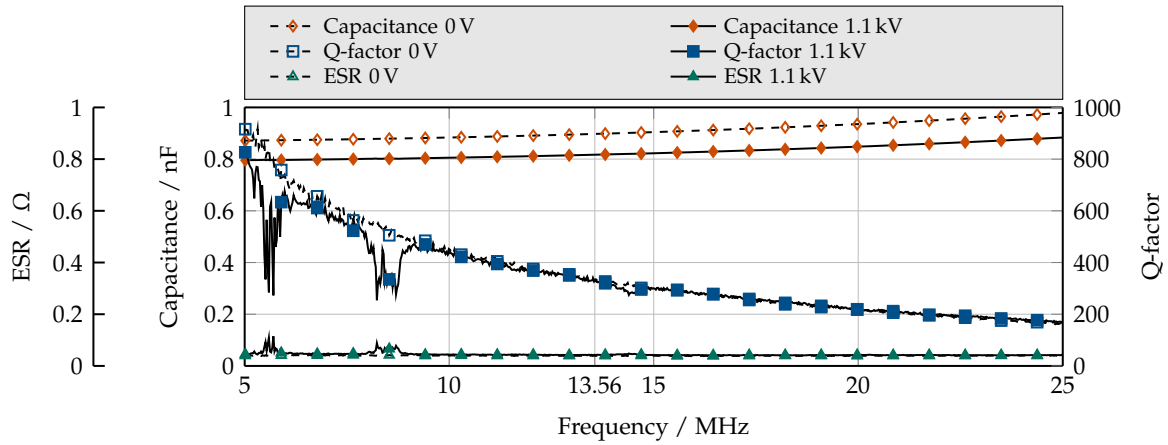

Figure 5.7: C, Q and ESR of a BST composite and silver metalization at 50 °C.

unbiased and biased case. With 1.1 kV, the material shows a tunability of 10 %, less than most other evaluated materials. However, as the biasing curve is non-linear and in particular for low electrical biasing fields runs flat, an acceptable tunability of 57 % is obtained from Weil model for 6 kV of biasing voltage [10].

5.1.3 Acoustically Optimized Composite Bulk Ceramic Disk Varactors

In this section, a novel approach to suppress acoustic resonances in bulk ceramic disk varactors is presented. As shown in section 5.1.2, tunable bulk ceramics based on ferroelectrics severely suffer from acoustical resonances in the ESR spectrum. Within the scope of this work, several different mechanical properties have been identified, impacting the location and intensity of the acoustical resonances. They enable the possibility of modeling the material in a way, that the acoustic resonances interfere less with the operational frequency, see appendix D.2.1 and appendix D.2.2. However, a satisfactory result is not achieved as either, the overall Q-factor is too low for the intended application (see figure D.1) or still significantly reduced in biased state, even though acoustic resonances do not interfere with the operational frequency directly but reducing the overall Q-factor spectrum, see figure D.5. In [14], a $Ba_{0,7}Sr_{0,3}TiO_3$ composite material is presented, lowering the dielectric losses of $Ba_{0,7}Sr_{0,3}TiO_3$ by adding a non-tunable, non-piezoelectric but loss reduced magnesium based metal oxide dielectric. The resulting composite material shows sufficiently high tunability for low volume percentages of the dielectric with significantly reduced losses compared to pure $Ba_{0,7}Sr_{0,3}TiO_3$ based bulk ceramic. Due to the non-piezoelectric nature of the dielectric an additional suppressing effect is expectable for the composite material. The small signal characterization results are depicted in figure 5.7.

An unbiased capacitance of 0.9 nF is measured at 13.56 MHz, decreasing by 9 % to 0.817 nF

in biased state. A corresponding Q-factor of 336 is measured in unbiased state, decreasing by 1.2 % to 332 in biased state. The material shows significantly reduced acoustic activity with resonances at 2.9 MHz, 5.7 MHz and 8.7 MHz with a characteristic gap of 2.9 MHz between resonances. It should be noted, that no further acoustic resonances above 8.7 MHz are observable, representing a unique feature of the material. It has yet to be evaluated how the dielectric acts as an acoustic resonance suppressing agent. The reduced tunability is the main drawback of the base material. However, with a tuning voltage of 6 kV a tunability of 57 % is extrapolated with Weil model [10]. In addition, by reducing the dielectrics percentage, the tunability of the material may be further increased while keeping the acoustic resonance suppressing effect. Overall, such a material represents in most aspects an ideal candidate as a dielectric in high-power bulk ceramic varactors.

5.2 Circuit Board Integrated Varactor Modules

Single varactor pellets, as presented in section 5.1.2, are unsuitable for direct implementation in a high-power matching circuit. To include the varactors, external connectors and circuitry are required, which can not be mounted on the pellets themselves. In addition, for DC biasing purposes, two-folded varactor stacks consisting of serially connected varactors are required to obtain a simple DC biasing circuit network, see section 4.1. As a result, the varactor pellets are integrated on a printed circuit board, which holds the RF/DC decoupling filters and provides for external connectors to the matching circuit and the DC biasing source. Conductor tracks on the PCB establish the connection between four serially connected pellets, the RF connectors, the DC/RF decoupling network and DC connectors. The biasing concept for the CBIVMs, in contrast to thick film varactors, is optimized for fast response times. Therefore, a network including lowpass filters is developed, which is complemented with resistors due to the significantly increased complexity of such an approach. The implemented network is capable of charging or discharging a maximum load capacitance of 8 nF, consisting of maximum four varactors in a minimum time of 200 µs. The fast response times of the implemented filters themselves and a detailed explanation of their design is given in section 5.2.1. The boards are designed for DC biasing voltages up to 6 kV. However, due to safety reasons, characterization is performed only up to 1.1 kV. The equivalent circuit model of the circuit board integrated varactor module (CBIVM) and the implemented version are depicted in figure 5.8.

5.2.1 DC Biasing Filter Concept for Fast Response Times

In general, the here presented filter design is applicable to thick film varactors as well. The charging and discharging time of a capacitive load depends on the time constant, comprised of the size of the capacitive load and the resistance of the biasing circuitry according to $\tau = R \cdot C$ [15]. For a 99 % charging level of the capacitance, a time $t = 5 \cdot \tau$ is

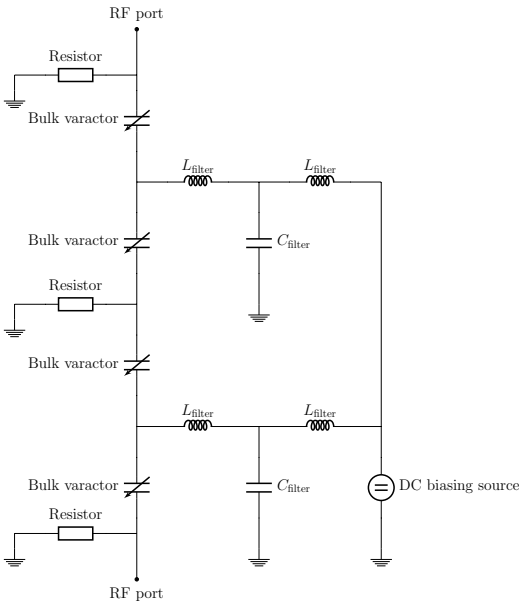

(a) Equivalent circuit model of the CBIVM.

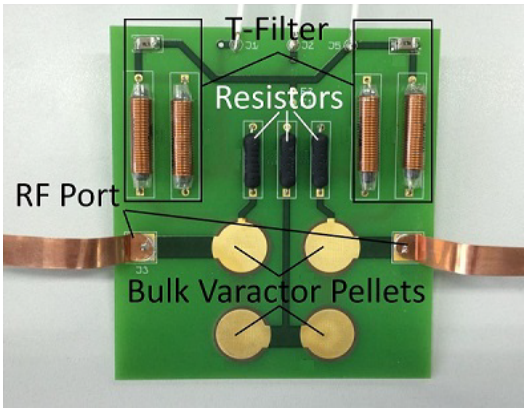

(b) Manufactured CBIVM with RF/DC decoupling filters and external copper connection straps.

Figure 5.8: CBIVM equivalent circuit model (left) and the implemented version of the CBIVM (right).

required, which determines the minimum response time for the intended application. As a result of the capacitive stacking strategy to distribute RF energy among several varactors, see section 5.2, capacitance values of up to 40 nF are expectable for the biasing network, as serially connected varactors for the RF path appear in parallel connection for the DC path. Minimum response times of 10 µs are intended for the final application, resulting in a required R value of 50 Ω. For RF power levels in the kW range and the resulting RF voltage amplitudes of several hundred volt applied to the DC decoupling circuitry, 50 Ω resistance is far too less to provide for a decent RF/DC isolation. Therefore, a lowpass filter concept is developed to provide for low transient impedance and a high impedance at the operational RF frequency for the necessary isolation. A lowpass filter based on the T-design to connect the varactor with a series connected element is chosen, opposed to the also possible π-design. To achieve the minimum possible charging/discharging time, a full filter based DC/RF decoupling network has to be implemented with even the DC ground decoupling components being filters, opposed to the CBIVM design presented in section 5.2. In regard to frequency behavior, the filter requires a passband frequency of 400 kHz with $|\underline{S}_{21}| < 3\text{dB}$ and an isolation at 13.56 MHz of $|\underline{S}_{21}| > 30\text{dB}$, to be suitable for high-power operation with input power levels up to 1 kW. Concerning its transient behavior, the passing biasing signal should be distorted as little as possible, especially the voltage overshoot needs to be limited. The coils have to handle currents of up to several Ampere without the core material being saturated. Ferrite based coils are chosen with a

Table 5.3: Biasing filter design specification.

Layout	f_{pass}	f_{stop}	Rise time	Isolation	Max. V_{ripple}	Max. Current
	kHz	MHz	µs	dB	%	A
T-filter	400	5	10	30	2	4

current rating of 4 A. Key design data going into the design process of the filter is presented in table 5.3.

The T-filter design consists of two coils in series connection with a shunt capacitance connected to ground in between the coils. Roughly, the filter behavior in regard to its component values can be described as follows:

- With increasing inductance of the coils the filter becomes more narrow-banded and the high frequency isolation increases. In regard to transient behavior, the voltage overshoot of the filter increases. A compromise between isolation and transient voltage overshoot has to be found.
- With increasing filter capacitance, the passing frequency is decreased. As a result, the filter becomes more narrow-banded. Voltage overshoot is reduced with increasing capacitance. On the downside, the filter capacitance adds to the overall capacitance, that has to be charged or discharged by the DC biasing source. As a result, the tuning time is increased.
- The connected load capacitance of the varactors acts similar as the shunt capacitance of the filter. In other words, the filter characteristic is dependent on the varactors capacitance and therefore its biasing state.

The simulated and measured frequency characteristic of the filter is depicted in figure 5.9.

Simulation and measurement data of the filter are in good agreement. The filter features a 5 MHz bandwidth with and an isolation better than 30 dB at 13.56 MHz. A matching better 10 dB below 400 kHz is achieved with an insertion loss better than 1 dB. With this data, the filter suffices the specification given in table 5.3 in regard to frequency behavior.

For the DC path, the bulk varactors are connected in series to the filter. As a result, a significant impact on the transient behavior of the circuit is expected, depending on the bias state of the load varactors. To account for that, the transient behavior of the filter is evaluated in zero-bias and fully biased state. For the zero-biased state with large capacitive loading, the intended minimum rise time has to be achieved and voltage overshoot has to be within its intended limits, while for the biased state only the voltage overshoot is critical. Two load cases are simulated with variable C_2 as the capacitance of the load varactors

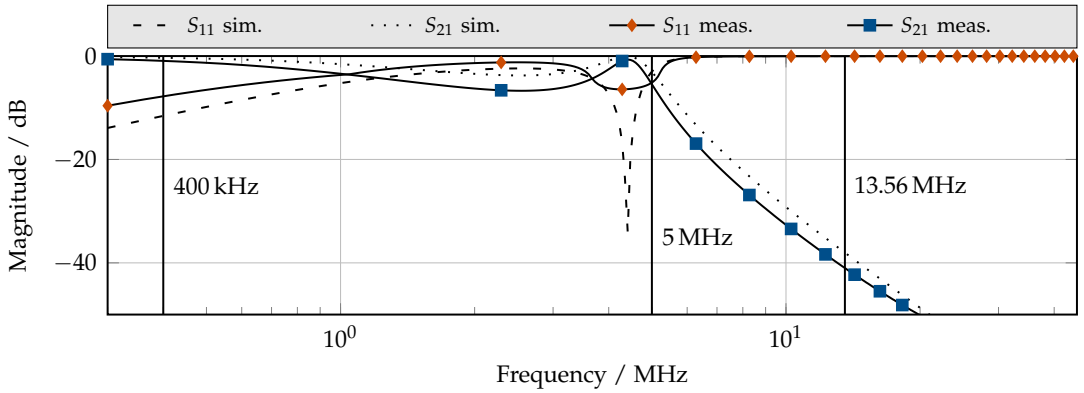

Figure 5.9: Measured RF/DC decoupling filter characteristic.

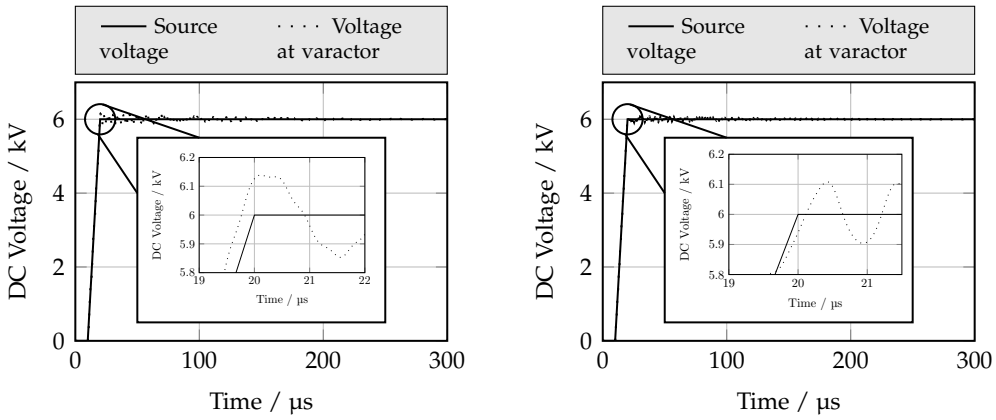

(a) Transient characteristic of the filter with heavy capacitive load (10 nF total).

(b) Transient characteristic of the filter with small capacitive load (1.72 nF total).

Figure 5.10: Transient characteristic of the filter for a large and a small capacitive loading, simulating unbiased and biased state of the bulk ceramic varactors.

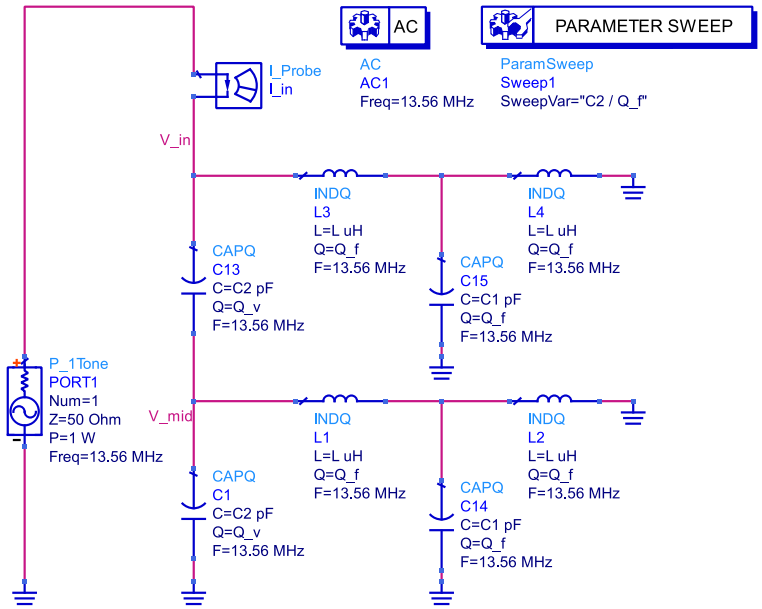

Figure 5.11: ADS model to evaluate the impact of the filter on the overall Q-factor of a CBIVM.

equal to 5 nF and 800 pF, representing a heavy load zero-bias and low load biased case. The simulation results are depicted in figure 5.10.

For the biased case in figure 5.10 (right), a voltage overshoot of 105 V is obtained with a settling time of 300 µs fulfilling the specification of a maximum 2 % (120 V for 6 kV biasing voltage) voltage ripple. For the unbiased heavy load case, a voltage overshoot of 136 V is obtained with an equal settling time of 300 µs. In regard to the 6 kV biasing voltage, the specified 2 % overshoot is not met with the filter. The main reason is the inductance value of the coils in combination with the large $\mathrm{d}I/\mathrm{d}t$ during the charging/discharging process. To account for this issue, the coils have to be replaced with less inductive ones.

In a final step, the impact of the filter on a varactor stack is evaluated, subsidiary for a CBIVM. The implemented model is depicted in figure 5.11. A serial stack of two varactors with a variable capacitance between 0.8 nF to 5 nF but static Q-factor of 100, independent from their capacitance, is set up and connected to a one tone source at 13.56 MHz. Two decoupling T-filters are connected to the circuit, one at the input to simulate DC ground decoupling and one between the varactors to simulate the DC bias decoupling. The DC source is shorted. The RF/DC decoupling filters are set up with a variable Q-factor between 1 and 100. The Q-factor of the varactor stack including the filters is calculated from its input voltage and current. As not only the filter losses affect the losses of the stack but also the varactors capacitance distribution, the simulation is separated into these two parameters. The varactor capacitance is swept for two different filter Q-factors and vice versa to identify the more significant parameter on the stack Q-factor. The simulation results are depicted

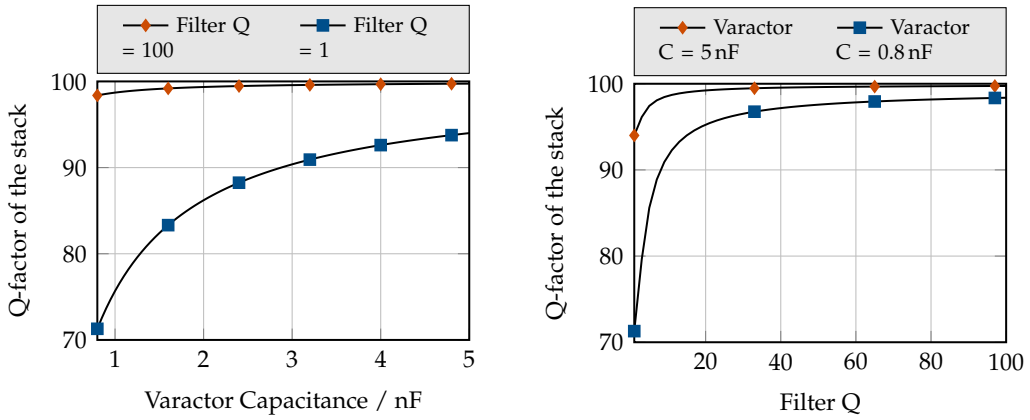

(a) CBIVM Q-factor dependent on the tuning state of the varactors for high and low filter Q.

(b) CBIVM Q-factor dependent on the filter Q-factor for zero-bias and biased state of the varactors.

Figure 5.12: Impact of the filter Q on the varactor stack Q-factor of a CBIVM for various bias states.

in figure 5.12.

For varied varactor capacitances, a decrease in stack Q-factor with capacitance is visible. This is caused by the changing impedance ratio between the capacitance and filter path, in favor of the filter path. As a result, the increased absolute losses of the filter path gain impact. Overall, this is a surprising result, as both the filter and varactor Q-factor are equal to 100 for the whole sweep. Unsurprising is the significant decrease in stack Q-factor for the same sweep with a filter Q of 1. However in this case, the impedance ratio between filter and capacitance path has a positive impact as even with a 99 % reduction in filter Q, a significantly less reduction in stack Q-factor of 28 % is obtained. A similar result is achieved for the other evaluated case. Both biasing states result in a significant drop in stack Q, only for filter Qs below 20. For filter Qs larger than 20, the stack Q drop can be limited to less than 5 %. Overall, the simulation indicates a significantly larger impact of the filter losses on the stack losses compared to the varactor biasing state. As a result, with a filter Q above 20, the reduction in stack Q can be limited to 5 % for both biasing states.

5.2.2 Small-Signal, Large-Signal and Transient Characterization

The implemented CBIVM is characterized in regard to small and large-signal as well as transient behavior. For small-signal characterization, the measurement fixture presented in section 3.1.4 is utilized. The CBIVM is heated to a temperature of 50 °C to guarantee a measurement in the paraelectric phase of $Ba_{0,7}Sr_{0,3}TiO_3$. The biasing voltage is adjusted in a range of 0 kV to 1.1 kV with a stepping of 100 V. Large-signal characterization is carried

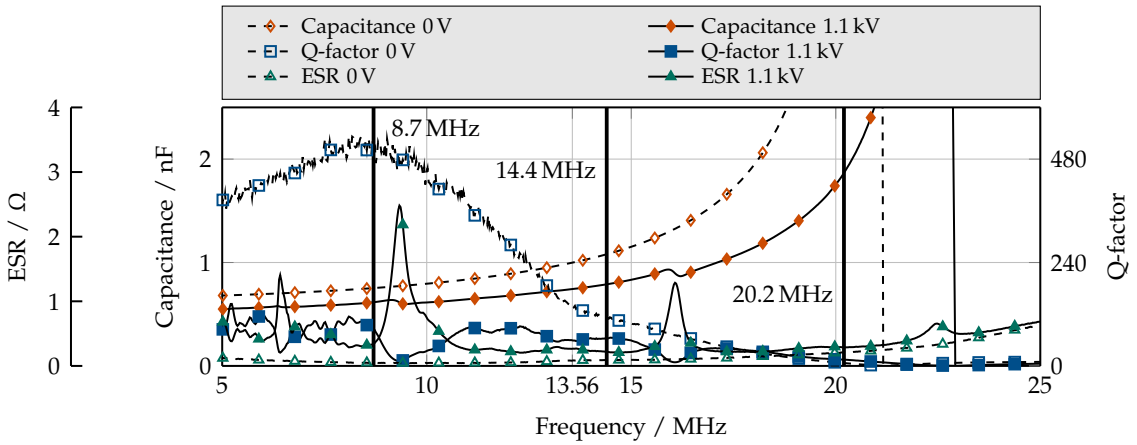

Figure 5.13: C, Q and ESR of a $Ba_{0,7}Sr_{0,3}TiO_3$ + 0.5 % manganese based CBIVM characterized at a temperature of 50 °C. The acoustic resonance positions of the corresponding pellets are marked.

out in accordance to section 3.2, ensuring comparability to the large-signal measurement results of the presented thick film varactors. The biasing voltage during large-signal characterization is limited to 3 kV, for safety reasons. A class 1 based CBIVM is characterized, as its tunability does not exceed the measurement range of the characterization circuit. The transient characterization setup is described in section 3.3.

Small-Signal Characterization

The characterized CBIVMs use pellets based on the materials $Ba_{0,7}Sr_{0,3}TiO_3$ co-doped with manganese and the commercially available Y5U specified class 2 dielectric as well as a class 1 dielectric. The class 1 based CBIVM is used for large-signal characterization. Compared to the first mentioned base materials, the class 1 dielectric has a significantly lower tunability and acoustical activity, see figure D.1. These properties are favorable for large-signal characterization, as the given setup is limited in handling large capacitance tuning ranges. In addition, a heavily varying power dissipation in zero-bias and biased state is diminished. All pellet types are metalized with silver. The small-signal characterization results of these pellet types are depicted in figure D.2 and figure D.9. The small-signal characterization results of the CBIVM, separated by the base material, are presented in figure 5.13 and figure 5.14.

For the 0.5 % co-doped $Ba_{0,7}Sr_{0,3}TiO_3$ based CBIVM an unbiased capacitance of 1 nF at 13.56 MHz is obtained, decreasing by maximum 26 % in biased state to 743 pF. This data indicates a two times larger capacitance of the CBIVM compared to the expectable value from the characterization of a single pellet. To account for that deviation, the impact of the parasitic board inductance is evaluated, as it adds to the measured capacitance below the self-resonance frequency (SRF). The SRF of the CBIVM is measured at 22.6 MHz while the

pellets SRF is far above 25 MHz, indicating a significant parasitic inductance introduced by the PCB conductor tracks of the board. The parasitic inductance of the board is estimated from the self-resonance frequency by:

$$f_{\text{res}} = \frac{1}{2\pi\sqrt{LC}}$$
$$L = \frac{1}{4\pi^2 f_{\text{res}}^2 C} \tag{5.6}$$

with the $C = C_{\text{pellet}}/4$ and $f_{\text{res}} = 22.6$ MHz. An inductance of 91 nH is obtained, which is in decent agreement with the estimation of 83 nH based on the theoretical conductor track formula [100] for the given conductor geometry. In addition, varying partial capacitances of the pellets included in the CBIVM may account for the remaining difference. Therefore, the parasitic inductance of the board is identified as a possible parameter responsible for the capacitance deviation of board and pellet. The tunability of the module is in good agreement with the pellet characterization, indicating the absence of delamination or electrical breakdown of a pellet. For the module, a Q-factor of 140 is obtained in unbiased state, which decreases by 58 % to 60 in biased state. Compared to the Q-factor of a de-embedded pellet of 180 in unbiased and 118 in biased state, a good comparability is achieved taking into account the additional losses introduced by the PCB. Acoustic resonances are obtained at 9.3 MHz and 16.1 MHz with a characteristic gap of 6.8 MHz. Intermediate resonances, which are visible in the ESR spectrum of the pellet, are not observed. Compared to the pellet, a relative shift of 0.6 MHz of the first resonance and 1.7 MHz of the second resonance is observed towards higher frequencies, which can be attributed to the mechanical loading of the pellets as a result of their encapsulation.

The Y5U class 2 dielectric based CBIVM shows a zero-bias capacitance of 1.2 nF with a tunability of 45 % at 13.56 MHz, see figure 5.14. Taking into account the pellets capacitance, see figure D.2, of 3.3 nF at 13.56 MHz, a stack capacitance of 825 pF is expected, a reduction of the measured capacitance of 31 %. To account for that deviation, a parasitic board inductance of 77 nH is required, calculated with equation (5.6), a self-resonance frequency of 20 MHz and a capacitance $C = C_{\text{pellet}}/4 = 825$ pF. Compared to the previously presented co-doped $Ba_{0,7}Sr_{0,3}TiO_3$ based CBIVM, the parasitic inductance should be similar. However, a deviation of 15 % is calculated. Again, a possible reason are varying partial capacitances of the pellets included into the CBIVM. A zero-bias Q-factor of 32, decreasing to 27 in biased state by 14 % at 13.56 MHz is measured. The main reason for the Q-factor degradation is an acoustical resonance in the vicinity of the operational frequency of 13.56 MHz. Compared to the Q-factor of a single pellet, a reduction of $\sim$50 % is observed for the CBIVM, see figure D.2. Compared to the $Ba_{0,7}Sr_{0,3}TiO_3$ based module, a less significant impact of the integration process on the acoustical behavior is observed for the class 2 dielectric based one. The acoustical resonances of the CBIVM are obtained at 8.4 MHz and 14.5 MHz, in good agreement with the resonance positions of the pellet.

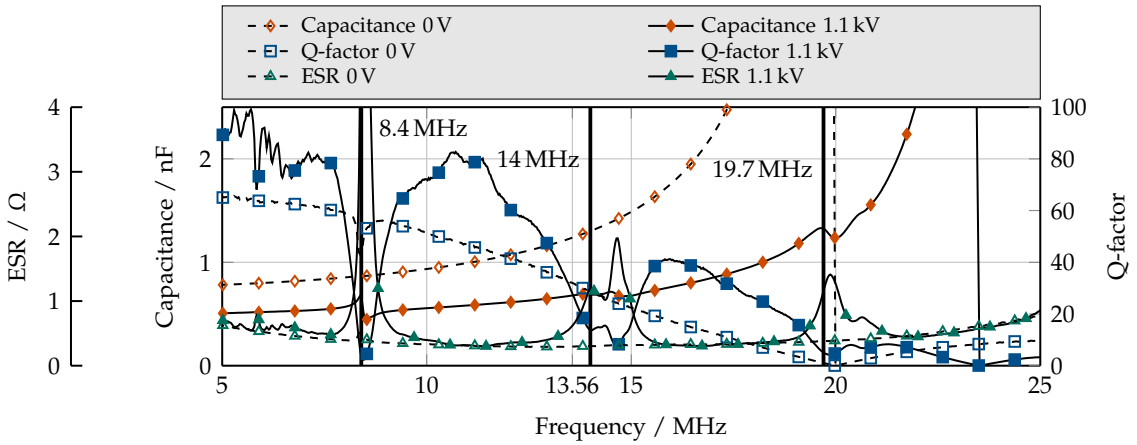

Figure 5.14: C, Q and ESR of a class 2 ceramic based CBIVM characterized at a temperature of 50 °C. The acoustic resonance positions of the corresponding pellets are marked.

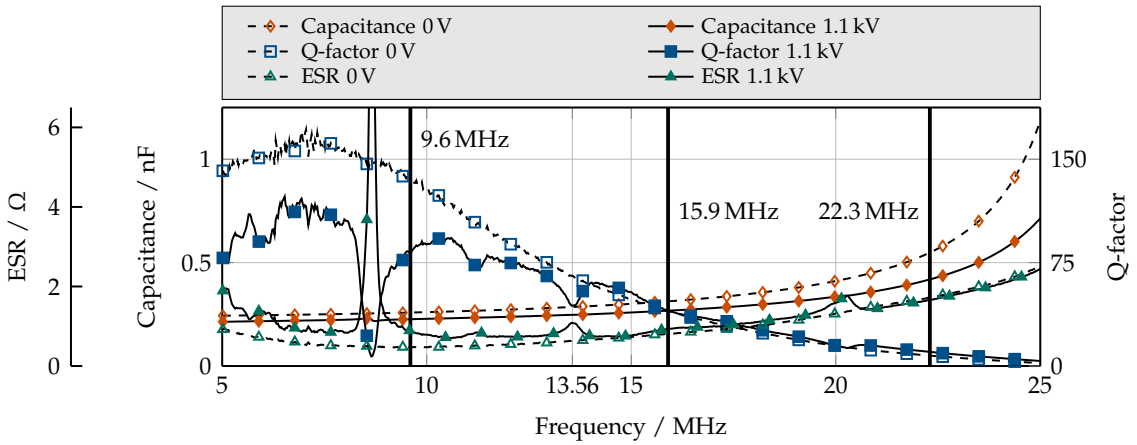

Figure 5.15: C, Q and ESR of a class 1 dielectric CBIVM characterized at a temperature of 50 °C. The acoustic resonance positions of the corresponding pellets are marked.

The small-signal characterization results of the class 1 dielectric based CBIVM are given in figure 5.15. At zero bias and 13.56 MHz, a capacitance of 286 pF is measured, decreasing by 5 % to 271 pF in biased state. Compared to the pellet characterization, the CBIVM measurement result is in good agreement as the capacitance of the pellet in unbiased state of 805 pF is nearly quartered for the CBIVM, as expected. A Q-factor of maximum 65 is obtained at 13.56 MHz, reducing to 44 in biased state due to an interfering acoustic resonance. In contrast to the other CBIVMs, the class 1 dielectric based one shows an unfavorable acoustic resonance shift towards lower frequencies compared to the single pellet measurement. The reason might be the mechanical loading of the pellets, due to the integration with the circuit board. The acoustic resonances of the class 1 dielectric based pellet appear more narrow-banded compared to the other base materials, suggesting a higher mechanical Q-factor [15]. As a result, the mechanical loading due to the PCB integration process is relatively more impacting than for CBIVMs employing pellets with a worse mechanical Q-factor.

Large-Signal Characterization

CBIVM large-signal characterization in the given circuit is much more complicated compared to characterizing thick film varactors. BST bulk ceramic as well as $BaTiO_3$ based CBIVM have a significantly larger electrical and thermal tunability, exceeding the measurement range of the characterization circuit. To establish a stable measurement without the necessity of changing the load impedance during characterization, the class 1 dielectric based CBIVM is used, which showed the lowest tunability during small-signal characterization. To establish a reasonable RF to DC voltage ratio, a DC biasing voltage of 3 kV is applied. To minimize the thermal capacitance drift during characterization, the CBIVM is temperature stabilized. The CBIVM is connected in series to C_{Vac1}, see section 3.2. A biasing voltage of up to 3 kV is applied during characterization. Due to the small capacitance of the CBIVM a relatively large load impedance of $\underline{Z}^*_M = (24 + 2.7\mathrm{i})\ \Omega$ is set up, creating a less stressful loading state compared to some of the low impedances presented to thick film varactors. The characterization results are depicted in figure 5.16.

A largely power independent electrical tunability in the range of 12 % to 13 % is obtained, attributed to the temperature stabilization. Thermally, a change in capacitance of up to 3 % is measured. In biased state, the Q-factor of the CBIVM increases between 13 % to 20 % from minimum 50 to maximum 67. In contrast to the small-signal characterization result, an increase in Q-factor with biasing voltage is obtained. Over input power, a nearly linear increase of dissipated power in the CBIVM is obtained, indicating a power independent relative loss of 1.8 %. Overall, the results show the immense potential of the CBIVM approach. Especially, considering the CBIVM using disk varactors with the lowest electrical tunability and a Q-factor of maximum 67, far below the highest one measured with over 300 for the $Ba_{0,7}Sr_{0,3}TiO_3$ composite material, see section 5.1.3. A complete summary of the data measured during large-signal characterization is given in table 5.4.

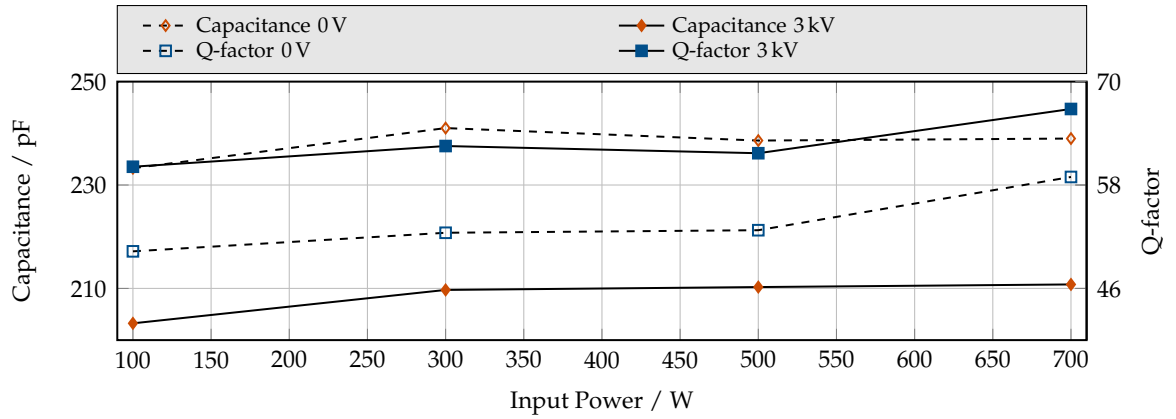

(a) Capacitance and Q-factor for various input power levels.

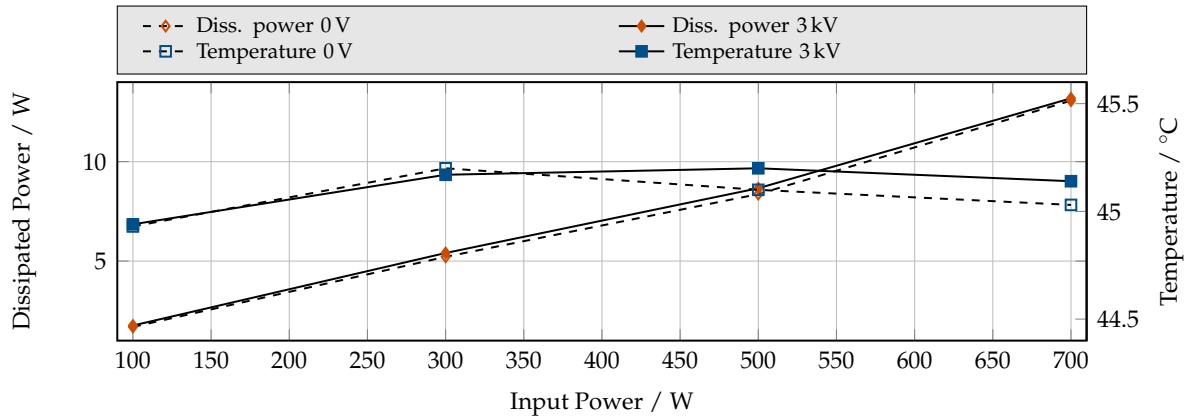

(b) Dissipated power and temperature measurements over input power.

Figure 5.16: Large-signal characterization of a CBIVM with bulk ceramic pellets based on a class 1 dielectric in regard to capacitance, Q-factor, dissipated power and temperature in unbiased and biased state.

Table 5.4: Summary of large-signal characterization data obtained for the CBIVM at different RF input power levels in unbiased state.

Power level		DUT measurements						
P_{in} W	P_{out} W	V_{rms} V	I_{rms} A	$C(0\,V)$ pF	$Q(0\,V)$	τ %	P_{diss} W	T °C
97	92	98	1.3	233	50	13	1.8	45
293	277	144	2.2	241	53	13	5.2	45
485	461	186	2.8	239	53	12	8.0	45
681	644	219	3.3	239	59	12	13.1	45

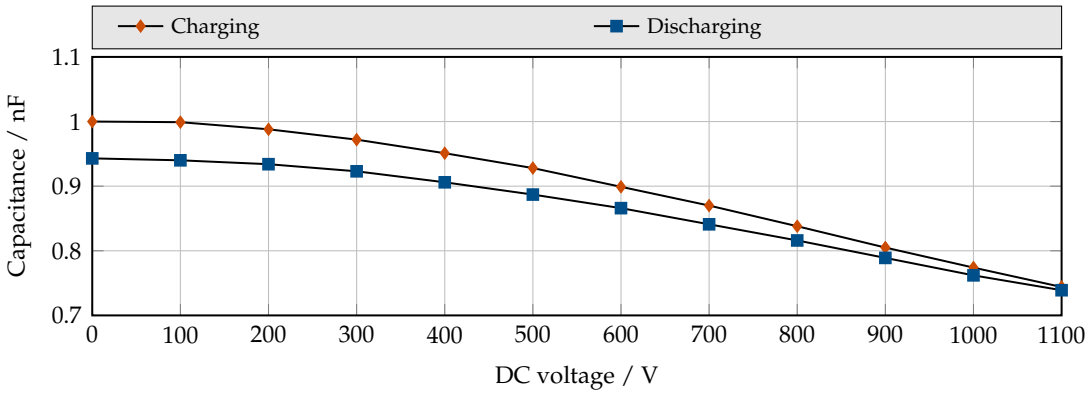

Figure 5.17: Capacitance over voltage at 13.56 MHz of the $Ba_{0,7}Sr_{0,3}TiO_3$ based CBIVM.

Transient Characterization

The assembled CBIVM is characterized in regard to transient behavior. The measurement is performed with the circuit described in section 3.3. Prior to transient characterization, the CBIVM capacitance over voltage trace at 13.56 MHz needs to be known, to adjust the circuit for maximum sensitivity. The trace is extracted from small-signal characterization data and depicted in figure 5.17. The CBIVM shows an unbiased capacitance of 1 nF at 13.56 MHz, decreasing by 26 % in biased state to 743 pF. The trace indicates a hysteresis effect. This is connected to a reduced but remaining hysteresis in the varactor, due to isolated ferroelectric domains in the otherwise paraelectric ceramic and polarizable grain boundary defects.

To extract the capacitance over time trace from the RF over time measurement, the RF voltage to capacitance transfer characteristic of the circuit needs to be known. It depends on the impedance of the DUT, as well as of the component values of the circuit and its parasitics. Since the same circuit is utilized for the CBIVM transient characterization as for thick film transient characterization, the same component values and most of the parasitics apply, see table 4.5. A prominent deviating parasitic is the contact resistance of the CBIVM to the circuit. The exact measurement setup of the transient circuit with the DUT included and its corresponding RF/DC decoupling network is depicted in figure 5.18. A detailed view of the DUT is given in figure 5.8. Note, that the DC ground decoupling resistors mounted on the CBIVM are partially bypassed by the transient measurement circuit. For the transient characterization measurement itself, no negative influence is expected from this fact.

Compared to thick film transient characterization, the stricter requirements on the measurement circuit as a result of the increased biasing voltage turned out to be problematic. A buffering capacitor with the required capacitance of 10 µF and voltage rating of >1.1 kV is not available. Therefore, a 100 nF capacitor is installed instead. However, due to the significantly increased DUT capacitance of 16 nF, the required ratio between buffering and charged capacitor of 10:1 could not be achieved. As a result, the DC bias charging trace

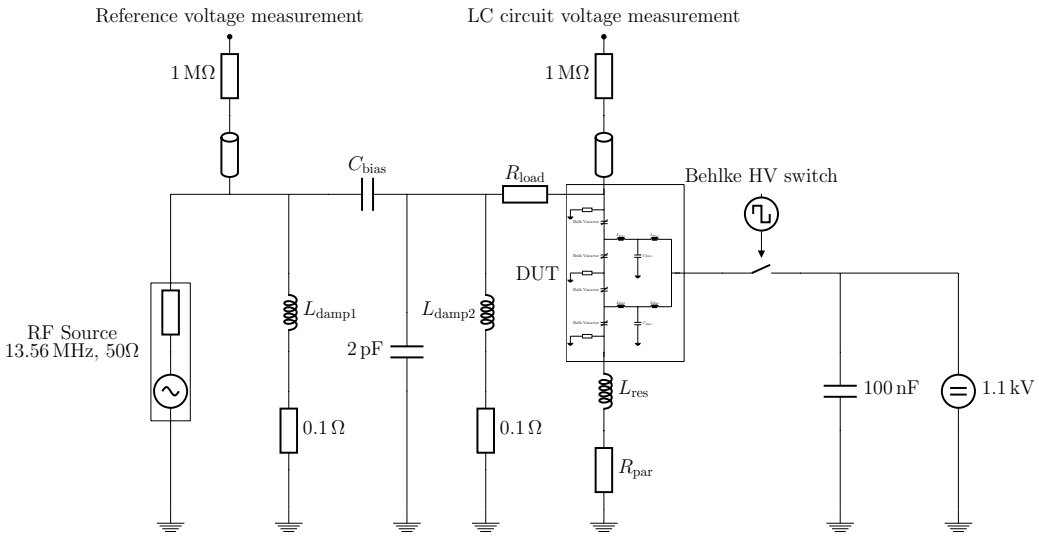

Figure 5.18: Implemented transient measurement circuit with the CBIVM included. Most component values are similar to the circuit used for transient characterization of thick film varactors.

is heavily distorted. The discharging trace, however, shows no sign of distortion, due to the lower output impedance of the Keithley biasing source for voltages below 20 V. However, caution is required due to the aforementioned hysteresis, resulting in a non-identical charging and discharging characteristic, see figure 5.17.

The transient characterization results are presented in figure 5.19. Figure 5.19a depicts the RF trace at the LC circuit voltage measurement port with the corresponding DC biasing trace applied to the varactors. Similar to section 4.5, the fast transient DC voltage couples into the measurement tap and distorts the results in the vicinity of the response time. The falling time of the DC bias from 1.1 kV to 0 V is measured with 2.2 µs. As the varactors are discharged, the capacitance is increased with decreasing biasing voltage, resulting in a constriction of the RF amplitude from 5 V to 3.1 V in 1.2 µs. At this point in time, the DC biasing voltage is reduced to 194 V. No further constriction or change in RF voltage amplitude is observed with decreasing bias voltage. From the small-signal characterization depicted in figure 5.17, a non-linear decreasing tunability with decreasing biasing voltage is observed. This effect is even larger for the discharging trace of the capacitance resulting in tunability smaller than 1 % for 200 V of biasing voltage, exceeding the sensitivity of the measurement circuit.

The obtained RF voltage to capacitance transfer characteristic of the circuit, indicates a resonance frequency of the circuit above 13.56 MHz, see figure 5.19b. Therefore, with increasing capacitance the RF envelope amplitude decreases, see figure 3.15. The tuning range of the varactor is not sufficiently large to reduce the resonance frequency of the circuit below 13.56 MHz, resulting in an unique correlation between RF envelope amplitude and

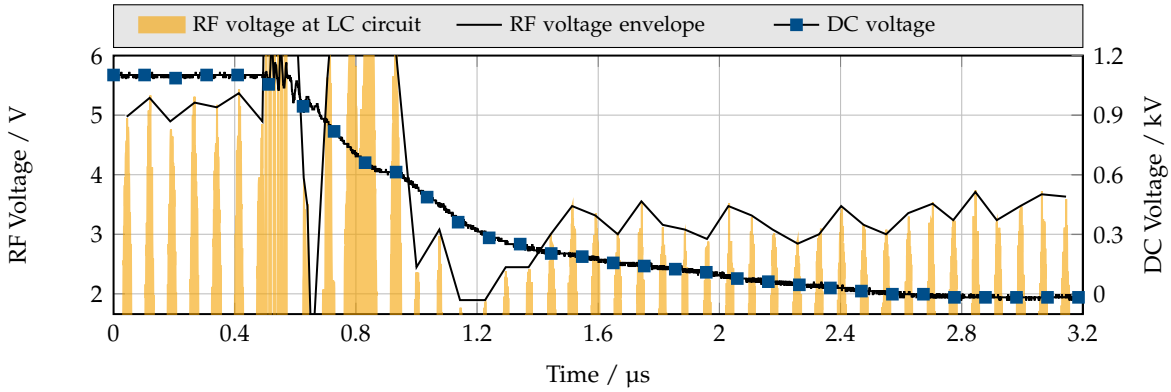

(a) Measured RF envelope voltage at the LC circuit and DC voltage at the DUT varactor over time.

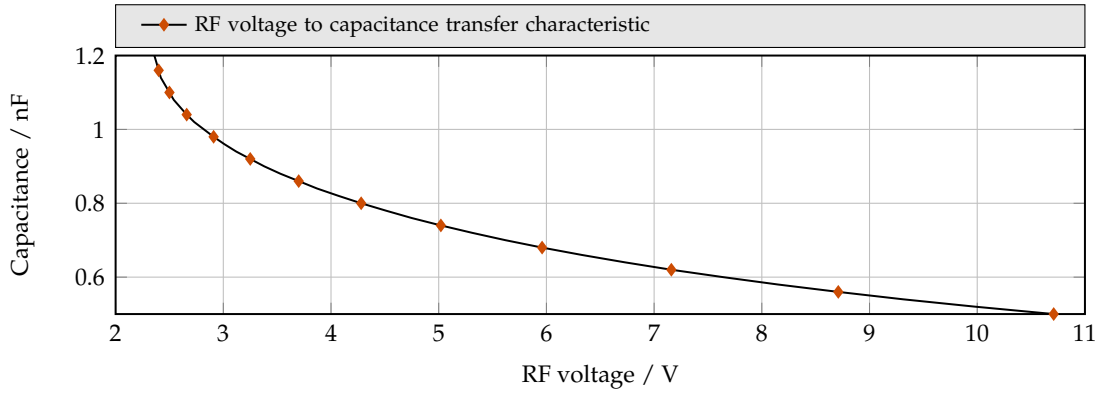

(b) RF voltage to capacitance transfer characteristic for the transient measurement circuit.

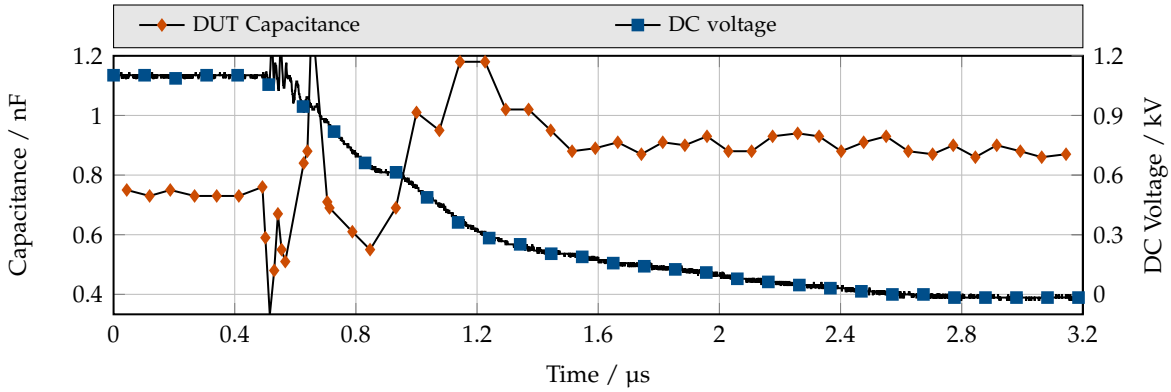

(c) Extracted capacitance from RF voltage envelope over time with corresponding DC biasing voltage at the DUT varactor.

Figure 5.19: Transient characterization measurement result, utilized RF envelope to capacitance transfer characteristic of the circuit and obtained capacitance over time result.

capacitance. Applying the transfer characteristic to the RF envelope measurement, the capacitance over time trace depicted in figure 5.19c is obtained. Compared with the small-signal characterization data, the capacitance over time trace is in good agreement taking into account the corresponding tuning. In biased state, the varactors show a capacitance of 760 pF, increasing by 25 % in unbiased state to 950 pF. The measurement results indicate an instantaneous tuning of the varactors with applied biasing voltage and possible tuning times smaller than 1.2 µs.

6 Conclusion and Outlook

Tunable components in RF matching networks have been used for several decades now. In mobile communication applications, not only the continuously changing environment is reflected in a constantly varying antenna impedance, requiring real time matching but also multiple used frequency bands make need of compact tunable matching solutions. For this application, high linearity over a wide frequency and power level range, high tunability and low losses are key parameters to their suitability in mass production. In this field of function, RF micromechanical-electrical systems (MEMS), semiconductors, liquid crystal and ferroelectrics are in competition as they all introduce unique advantages towards each other. Ferroelectrics are known for their high-power handling capabilities but reduced applicable frequency range less than 10 GHz. Commonly, they are implemented as planar thin and thick film based varactor components on a substrate rather than bulk ceramics, due to manageability and the high permittivity of bulk ceramics, introducing unsuitable capacitance values for the intended frequency region of 0.5 GHz to 3 GHz. Recently, due to the reduction of the sintering temperature of thick films down to about 850 °C, the possibility arose to implement vertically stacked metal-insulator-metal (MIM) structures. Main advantages are the significantly improved field distribution compared to planar structures and the increased electrical breakdown field strength due to the reduction of stray field components in the adjacent air. Large-signal characterization of these new structures indicated their suitability, typically in high-power applications, even though dielectric losses were increased compared to thick films sintered at higher temperatures above 1150 °C. Bulk ceramics are most commonly used as large MIM buffer capacitors in low frequency applications. In most cases, their tunability is considered a parasitic property.

A significantly smaller market for tunable matching networks is the application in RF based high-power plasma processes for the unidirectional depositioning or etching of fine structures in the micro- and nanoelectrical domain. These most commonly single frequency processes in the lower ISM frequency bands, such as 13.56 MHz, 27.12 MHz and 40.68 MHz introduce high power levels up to 10 kW. In recent times, the increasing integration level of modern electronics created the need for decreasingly short processing times during manufacturing. Atomic layer etching (ALE) and atomic layer depositioning (ALD) introduce the requirement of processing durations in the second range. A plasma process can be subdivided into plasma ignition, a working cycle and the plasma extinction. During plasma ignition and extinction, the plasma impedance is continuously changing. Plasma ignition is the most critical part, as stable power transfer from the generator to

the plasma is required to complete the ignition process. Currently, mechanically tunable vaccum capacitors connected to stepper motors are utilized as tunable components in these matching circuits. However, due to the limited rotation speed of the stepper motors, the tuning time from C_{min} to C_{max} or vice versa is more than 1 ms. As the working cycle time of the plasma decreases with process time, the impact of the ignition and extinction phase increases. Therefore, faster matching components are required for these upcoming challenges.

This work focuses on the development and evaluation of tunable components for fast matching applications based on the material barium strontium titanate (BST). BST as a tunable dielectric in varactors has been under investigation for several years now and shows promising results regarding Q-factor, tunability and power handling capabilities. The tunability of BST originates from the displacement of titan ions in the lattice resulting in presumably high tuning speed in the µs range. The dielectric losses, however, are significantly larger compared to vacuum varactors. A thermally dependent permittivity is introduced with BST and its piezoelectric nature induces acoustical resonances, which, in regard to frequency behavior, locally increase losses even more. Taking into account the intended power levels of the application, the dielectric losses and as a result the thermal power dissipation are the most crucial parameters to evaluate BST based components in regard to their applicability in matching circuits.

Beside this main task, holders and PCBs are developed, providing for convenient, low parasitic connection possibilities of the developed varactors to the existing measurement equipment. The main focus is laid upon the accurate de-embedding of the characterized varactors from the utilized external characterization fixtures. For that, custom made SOL calibration standards are developed and evaluated. For transient response time characterization, a novel measurement method is developed and implemented utilizing an LC circuit. Commonly, to obtain a capacitance value with an LC circuit, its resonance frequency is evaluated. For this, a frequency sweep is necessary, rendering it unsuitable for fast transient characterization. In the developed method, the change in magnitude of a static RF voltage is evaluated, which is directly connected to the capacitance value in the LC circuit. Thereby, transient response times down to the µs domain can be acquired. The circuit is set up and characterized in regard to component values and parasitics, necessary to extract the tunability of capacitance from the change in RF envelope magnitude. For a fast response time optimized thick film varactor, a minimum response time of smaller than 1.5 µs with 120 V DC biasing voltage is obtained. With a similar circuit, a minimum response time of smaller than 1.2 µs and 1.1 kV for a bulk ceramic based CBIVM is obtained.

Two different approaches are chosen to implement BST based high-power varactors. The first one is based on screen-printed thick films. Main advantage of the approach is the integrability of a serially interconnected varactor with biasing network on a single side of a carrier substrate. Serial interconnection of varactor cells acts as the fundamental strategy in this work to distribute the dielectric losses among a larger cooling surface. The backside of the substrate is available for applying a heat sink. The printed BST layer features thicknesses

below 50 µm, facilitating the application of biasing voltages of up to several hundred V. Various designs are implemented with different goals. A high-power optimized varactor marks the beginning of the design process, focusing on the maximization of cooling surface by a serial connection of six MIM structures. For convenience, a resistive biasing network is implemented on-substrate. Even though the varactor suffers from acoustic resonances near the operational frequency of 13.56 MHz, with a maximum input power of 1 kW to the matching circuit, a remaining tunability of 19 % is achieved. The varactor dissipates 37 W of power with an apparent power of 2057 VA applied. Based on this approach, main focus is laid upon the improvement of the varactors acoustical behavior. A simulation based approach is implemented in COMSOL Multiphysics, resulting in the possibility to exactly model the acoustical behavior of the MIM structures. Furthermore, acoustic suppression methods are developed and prior to implementation, simulated to estimate their effectiveness. As a result, a radically changed matrix varactor concept is developed, consisting of serial and parallel interconnectable capacitive cells, which successfully prevent surface acoustic resonances. To improve the acoustical behavior in regard to the more severe bulk acoustic waves, besides some minor improvements of the MIM structure geometry, an interference based suppression technique is applied to the cells, successfully freeing the Q-factor spectrum from acoustic resonances. With that varactor design, at an input power level of 1 kW, a tunability of 18 % is achieved. The apparent power applied to varactor is 1960 VA, 5 % less compared to the high-power optimized varactor. However, the varactor dissipates 13.5 W at 1 kW of input power, 64 % less energy compared to the previous design. With a Q-factor of 122, a maximum temperature of 50 °C is measured at the varactor during high-power operation.

The second approach is based on metalized BST bulk material. Cylindrical pellets are processed with a thickness of 1 mm and a diameter of 16 mm. BST bulk material offers several advantages compared to BST thick films. Due to the compression of the green body and the increased sintering temperature, bulk ceramic compounds offer significantly higher densities. The utilized powder usually contains larger grains compared to printed thick films. Both properties increase the permittivity and their tunability and decrease their dielectric losses. Disadvantage of bulk ceramics is the thickness of the pellet, required for sufficient manageability, resulting in significantly increased biasing voltages compared to thick film varactors. In this work, biasing voltages of 1.1 kV are applied, the design, however, is made for biasing voltages up to 6 kV. Within the scope of this work, several different commercial and custom made bulk ceramic compounds beside BST are evaluated in regard to their suitability as high-power varactors. With the piezoelectric simulation approach in COMSOL not only internal parameters, such as density and elastic compliance are identified as highly important to the acoustical behavior of the pellets but also geometrical properties are pinpointed. The simulation results are verified with a series of measurements. In particular, the impact of the pellet geometry, co-doping, processing and metalization on its dielectric and acoustical behavior is investigated. Eventually, the complete acoustical suppression of resonances above 11 MHz is achieved with a composite material comprised of BST and a non-tunable, low loss magnesium based metal oxide dielectric. Bulk ceramic

BST pellets alone, however, are not suitable for application in high-power matching circuits, as a DC biasing network and connection to the matching circuit can not be applied to a single pellet. Therefore, circuit board integrated bulk ceramic varactor modules (CBIVM) are developed, which consist of four series connected bulk ceramic pellets and providing for the biasing network and RF connectors. For the CBIVM the necessary fast response time RF/DC decoupling filter is developed providing for response times of minimum 10 µs. With a CBIVM using class 1 dielectric based disk varactors, large-signal characterization is performed up to 700 W of input power. During characterization, the CBIVM temperature is stabilized. With that setup, an electrical tunability of maximum 13 % and 3 kV of biasing voltage is achieved. A nearly input power and biasing voltage independent loss of 1.8 % is measured, showing the immense potential of the CBIVM based approach in combination with a temperature control system.

The thick film varactor approach showed promising results in regard to power handling capability and tunability even though it suffered from the mediocre RF to DC bias voltage ratio and missing cooling solution. Taking into account the suboptimal operation temperature of the varactors during large-signal characterization of around 50 °C compared to their optimal thermal operation point of 25 °C, determined by the stoichiometric barium to strontium ratio, a significant increase in tunability can be expected with proper cooling or stoichiometric adjustment. During small-signal characterization, thick film varactors showed a maximum tunability of 40 %. Taking into account the cheap manufacturing process of these varactors in combination with the substantially reduced biasing voltages, the thick film approach should not be underestimated. With a corresponding fast response time RF/DC bias decoupling network, substituting the resistive one presented in this work, the full potential of a printed thick film based solution can be evaluated. A major drawback of thick film varactors is the reduced tunability compared to bulk ceramic disk varactors and mechanically tunable vacuum varactors. This context becomes more clear when the matchable load impedances of an L-match circuit and the corresponding varactor tunability are superimposed in a smith chart, see figure 6.1.

The simulation shows the shrinking load impedance range, matchable with the L-match circuit, with decreasing tunability. Bulk ceramic disk varactors with up to 80 % tunability and 6 kV of biasing voltage cover most of the matchable load impedance range of the state of the art vacuum varactors and their 90 % tunability. For thick film varactors, however, with an estimated maximum tunability of 35 % during high-power operation, the matchable impedance range is too low to operate a plasma in the ignition and extinguishing phase. A solution might be a hybrid system with vacuum varactors and thick film varactors. In general, during plasma ignition, the vacuum varactors are tuned to a set point, from which a fastest descent algorithm finds the optimal matching adjustment. The most time critical part is finding the optimal tune point, due to the mechanical adjustment of the varactors. In a hybrid system, vacuum varactors can tune to set points from which thick film varactors adjust to the optimal matching condition fast. In addition, power transfer fluctuations around the optimal tune point can be accounted for and compensated by the fast tunable thick film varactors. In conclusion, the presented acoustically optimized high-power thick

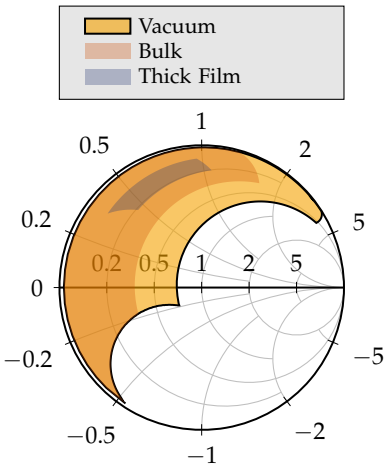

Figure 6.1: Simulated load impedance region of an L-match circuit for various varactor tunabilities. Vacuum and bulk ceramic varactors are simulated with a tunability of 90 % and 80 %, respectively. A zero-bias capacitance of 1.5 nF for C_1 and 0.5 nF for C_2 is assumed. Thick film varactors are simulated with a tunability of 35 % and a zero-bias capacitance of 0.6 nF for C_1 and 0.2 nF for C_2.

film varactor approach appears most promising. In particular, the double MIM based acoustic interference approach proves to be highly effective and should be applied in all future designs. Acoustic resonances are widely suppressed and a good Q-factor is obtained, resulting in acceptable losses during high-power operation. To further increase the varactors performance, the operational temperature needs to be adjusted to 50 °C by stoichiometric adjustment or a proper cooling solution. More serially connected MIM structures are an additional option to increase the varactors high-power capabilities and also its tunability by creating a more advantageous DC to RF voltage ratio at each MIM structure. Larger carrier substrates are required for that. The application of thick film varactors alone in a matching circuit is not feasible, due to their insufficient tunability. For a hybrid system, however, their application is feasible as they combine low-cost production with low biasing voltages, reducing the expenditure for a fast DC bias source and circuitry. The presented on-substrate biasing has not proven effective. The required carrier substrate space is too large and the second approach with the varactor soldered to an FR4 PCB, holding the DC biasing network, did not show worse results in regard to Q-factor.

Bulk ceramic disk varactors with their significantly larger tunability and higher Q-factor represent a good candidate to completely substitute state of the art vacuum varactors. A hybrid system approach appears less feasible due to the complex and expensive disk varactor integration process, cooling solution and DC biasing source and circuitry for the up to 6 kV of biasing voltage. Bulk ceramic disk varactors, as well as thick film varactors, suffer from acoustic resonances. However, the interference based suppression approach, implemented in thick film varactors, is not applicable, as no continuous acoustic connection

can be established with bulk ceramic pellets. In this work, an intrinsic acoustic suppression method is presented and demonstrated, introducing a non-piezoelectric material in a piezoelectric $Ba_{0,7}Sr_{0,3}TiO_3$ ceramic. The obtained composite base material shows a slightly reduced tunability but an unbiased Q-factor of over 300 with an acoustic resonance free Q-factor spectrum above 11 MHz. With Weil model extrapolation, a tunability of 57 % is expected with a biasing voltage of 6 kV. Due to time constraints, the large-signal characterization result of a CBIVM, employing these novel disk varactors, is pending. However, the large-signal characterization result of a CBIVM, based on a significantly worse class 1 dielectric, already shows the large potential of the approach. Even with a relatively low CBIVM Q-factor of maximum 67, an input power and biasing voltage independent power dissipation of 1.8 % is achieved. Considering these results, the substitution of state of the art vacuum varactors in fast matching circuits with CBIVMs, employing the aforementioned low loss, acoustically optimized disk varactors, appears highly feasible.

A Appendix: Fundamentals

A.1 Ferroelectric to Paraelectric Phase Transition derived from Helmholtz Free Energy

A homogeneous lattice volume is assumed with N cells of tetragonal form, as depicted in figure 2.4. The thermodynamic system is evaluated at constant temperature ($\Delta T = 0 \rightarrow \Delta Q = 0$, with Q being the heat) and constant volume ($\Delta V = 0$). The cells have a positive or negative dipole orientation s_i and dipole moment p_0. Then the overall polarization of the volume is [101]:

$$P = \frac{p_0}{V} \sum_{i=1}^{N} s_i \tag{A.1}$$

Equation (A.1) can be rewritten assuming $P_s = N p_0 / V$ to be the saturation polarization and N_+ and N_- to be the number of cells having positive and negative polarization direction [101]:

$$P = \frac{P_s}{N}(N_+ - N_-) \tag{A.2}$$

With equation (A.2) and $N = N_+ + N_-$ the number of cells with positive and negative polarization can be writting as [101]:

$$N_\pm = \frac{N}{2}\left(1 \pm \frac{P}{P_s}\right) \tag{A.3}$$

Now, assuming the energy required to reorient a single dipole to be Φ_0, the energy required to reorient all positive to negative dipoles or vice versa can be expressed as [101]:

$$\Phi_{+-} = \frac{N_+}{N}\Phi_0 \quad , \quad \Phi_{-+} = \frac{N_-}{N}\Phi_0 \tag{A.4}$$

Now, assuming constant temperature and volume ($\Delta Q = 0$, $\Delta V = 0$) the change in internal energy is only affected by mechanical work or entropy. From a macroscopic point of view,

the change in internal energy in the volume due to the reorientation of dipoles is given by the first law of thermodynamics:

$$\begin{aligned} \Delta U &= \Delta Q + \Delta W = T\Delta S - p\Delta V \\ \Delta U &= \Delta W = T\Delta S \\ \Delta U &= (\Phi_{+-}\Delta N_- + \Phi_{-+}\Delta N_+)\frac{1}{V} \end{aligned} \tag{A.5}$$

Integrating equation (A.5) and setting the reference energy of the completely ordered state $U_0 = 0$, the internal energy can be expressed by [101]:

$$U = \frac{\Phi_0 N}{2V}\left(1 - \frac{P^2}{P_s^2}\right) \tag{A.6}$$

In equation (A.5) the inner energy U has the independent variable entropy S. In order to decouple the energy state of the system from the entropy, the Legendre transform can be utilized. As a result the Helmholtz free energy equation is obtained. It represents a thermodynamic state or potential and as a result of the Legendre transform, the independent variable of the Helmholtz free energy $\Psi = U - ST$ changed to temperature T. The constant entropy for the given system, normalized to the volume, can be calculated from statistical mechanics using Boltzmann's equation [102]:

$$\begin{aligned} S &= \frac{k_B}{V}\ln\left(\frac{N!}{\prod_{i=1}^{I} N_i!}\right) \\ S &= \frac{k_B}{V}\ln\left(\frac{N!}{N_-!N_+!}\right) \\ S &= \frac{-k_B N}{2VP_s}\left[P\ln\left(\frac{P+P_s}{P_s-P}\right) + P_s\ln\left(1-\left(\frac{P}{P_s}\right)^2\right)\right] \end{aligned} \tag{A.7}$$

resulting in the Helmholtz free energy equation for the described thermodynamic system [101]:

$$\Psi(P,T) = \frac{\Phi_0 N}{2V}\left[1-\left(\frac{P}{P_s}\right)^2\right] + \frac{Tk_B N}{2VP_s}\left[P\ln(\frac{P+P_s}{P_s-P}) + P_s\ln\left(1-\left(\frac{P}{P_s}\right)^2\right)\right] \tag{A.8}$$

$$\Psi(P,T) = \frac{EP_s}{2}\left[1-\left(\frac{P}{P_s}\right)^2\right] + \frac{ET}{2T_c}\left[P\ln(\frac{P+P_s}{P_s-P}) + P_s\ln\left(1-\left(\frac{P}{P_s}\right)^2\right)\right] \tag{A.9}$$

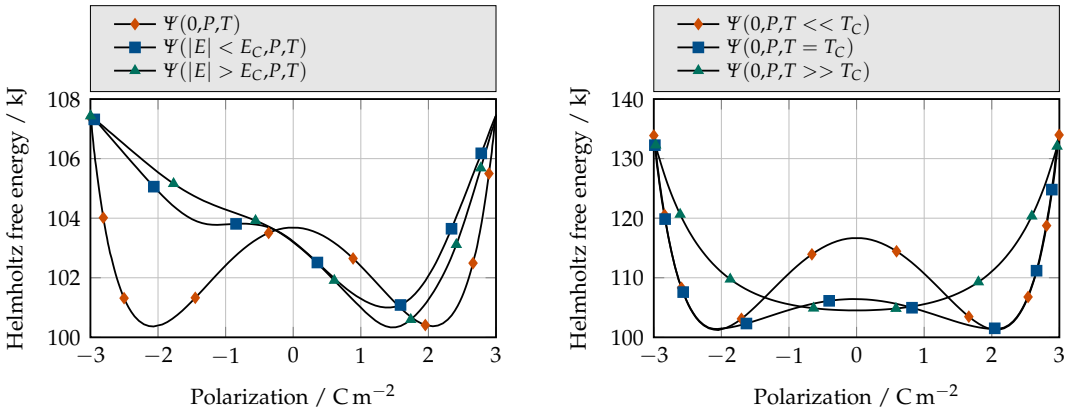

(a) Helmholtz energy over polarization for different electric DC biasing fields.

(b) Helmholtz free energy distribution over polarization below and above the Curie temperature of the material.

Figure A.1: Helmholtz free energy distribution in a non-centrosymmetric tetragonal cell for different electric DC biasing fields (left) and below and above the characteristic Curie temperature of the material.

Especially equation (A.9) is of significant interest. By substituting Φ_0/k_B in equation (A.8) with the Curie temperature T_C, Ψ assumes shape of a double well function for $T < T_C$ and a single well function for $T > T_C$. Moreover, by substituting $N\Phi_0/(VP_s)$ in equation (A.8) with an electrical field E, the distortion of the double and single well function can be modelled. The resulting curves of Helmholtz free energy are depicted in figure A.1 for a distortion of the double well function due to an electrical biasing field E (left) and for increasing temperature T (right) in range from $T < \mathrm{T_C}$ to $T > \mathrm{T_C}$.

A.2 Piezoelectric Constitutive Equations derived from Gibbs Free Energy

The Gibbs free energy is defined at constant temperature and pressure, while Helmholtz free energy is defined for constant temperature and volume. With mechanical stress $\sigma^{(m)}$, mechanical strain $\varepsilon^{(m)}$, electric field E, electrical displacement D, entropy S, internal energy U and absolute temperature T the Gibbs free energy G is given by [103, 16]:

$$G = U - \sigma^{(m)}\varepsilon^{(m)} - ED - TS \tag{A.10}$$

with the indices $i,j,k \in [1,2,3]$ according to the crystallographic axis. In a thermally insulated system, the change in internal energy can be written as:

$$\mathrm{d}U = \sigma^{(m)}\mathrm{d}\varepsilon^{(m)} + E\mathrm{d}D + T\mathrm{d}S \tag{A.11}$$

resulting in the change of Gibbs free energy [103]:

$$\begin{aligned}\mathrm{d}G &= \sigma^{(m)}\mathrm{d}\varepsilon^{(m)} + E\mathrm{d}D + T\mathrm{d}S + \mathrm{d}(-\varepsilon^{(m)}\sigma^{(m)} - ED - ST)\\ \mathrm{d}G &= -\varepsilon^{(m)}\mathrm{d}\sigma^{(m)} - \mathrm{d}ED - S\mathrm{d}T\end{aligned} \tag{A.12}$$

Due to the initial condition $T = const$, term $-S\mathrm{d}T = 0$ is omitted in the following. By expanding equation (A.12) in a Taylor series and neglecting higher order terms the mechanical stress and electric displacement can be written as:

$$\varepsilon^{(m)} = -\left(\frac{\partial G}{\partial \sigma^{(m)}}\right)_{\mathrm{E,T}} \tag{A.13}$$

$$D = -\left(\frac{\partial G}{\partial E}\right)_{\sigma^{(m)},\mathrm{T}} \tag{A.14}$$

with E, T held constant for equation (A.13) and $\sigma^{(m)}, T$ for equation (A.14). The mechanical stress in a piezoelectric material at constant temperature can be attributed to the mechanical displacement and the electric field exclusively [16]. Consistently, the electric displacements dependency can be found in the mechanical stress and the electric field. As a result, the total differentials given as functions of independent variables are:

$$\mathrm{d}\varepsilon^{(m)} = \left(\frac{\partial \varepsilon^{(m)}}{\partial \sigma^{(m)}}\right)_{E,T} \mathrm{d}\sigma^{(m)} + \left(\frac{\partial \varepsilon^{(m)}}{\partial E}\right)_{\sigma^{(m)},T} \mathrm{d}E \tag{A.15}$$

$$\mathrm{d}D = \left(\frac{\partial D}{\partial \sigma^{(m)}}\right)_{E,T} \mathrm{d}\sigma^{(m)} + \left(\frac{\partial D}{\partial E}\right)_{\sigma^{(m)},T} \mathrm{d}E_n \tag{A.16}$$

In equation (A.15) and equation (A.16) the differential terms can be substituted with the corresponding material coefficients for the elastic compliance s, piezoelectric coupling d and electric permittivity ε_r [16]:

$$s^{E,T} = -\left(\frac{\partial^2 G}{\partial \sigma^{(m)2}}\right)_{E,T} = \left(\frac{\partial \varepsilon^{(m)}}{\partial \sigma^{(m)}}\right)_{E,T} \tag{A.17}$$

$$d^T = -\left(\frac{\partial^2 G}{\partial \sigma^{(m)} \partial E}\right)_T = \left(\frac{\partial \varepsilon^{(m)}}{\partial E}\right)_{\sigma^{(m)},T} = \left(\frac{\partial D}{\partial \sigma^{(m)}}\right)_{E,T} \tag{A.18}$$

$$\varepsilon_r^{\sigma^{(m)},T} = -\left(\frac{\partial^2 G}{\partial E^2}\right)_{\sigma^{(m)},T} = \left(\frac{\partial D}{\partial E}\right)_{\sigma^{(m)},T} \tag{A.19}$$

Eventually, the constitutive equations for the piezoelectric effect can be written as [11]:

$$\varepsilon^{(m)} = s^{E,T}\sigma^{(m)} + d^T E \tag{A.20}$$

$$D = d^T \sigma^{(m)} + \varepsilon_r^{\sigma,T} E \tag{A.21}$$

A.3 Vector and Tensor Notation

To describe the directions for electrical and mechanical quantities in a given coordinate system, the following relations are used.

For mechanical stress there is:

$$\sigma^m = \begin{bmatrix} \sigma_{xx} \\ \sigma_{yy} \\ \sigma_{zz} \\ \sigma_{yz} \\ \sigma_{xz} \\ \sigma_{xy} \end{bmatrix} \tag{A.22}$$

in which σ_{xx} etc. are defined normal (normal stresses) and σ_{xy} etc. tangential (shear stresses) to the cubic surfaces. For mechanical strain there is:

$$\varepsilon^m = \begin{bmatrix} \varepsilon_{xx} \\ \varepsilon_{yy} \\ \varepsilon_{zz} \\ 2\varepsilon_{yz} \\ 2\varepsilon_{xz} \\ 2\varepsilon_{xy} \end{bmatrix} \tag{A.23}$$

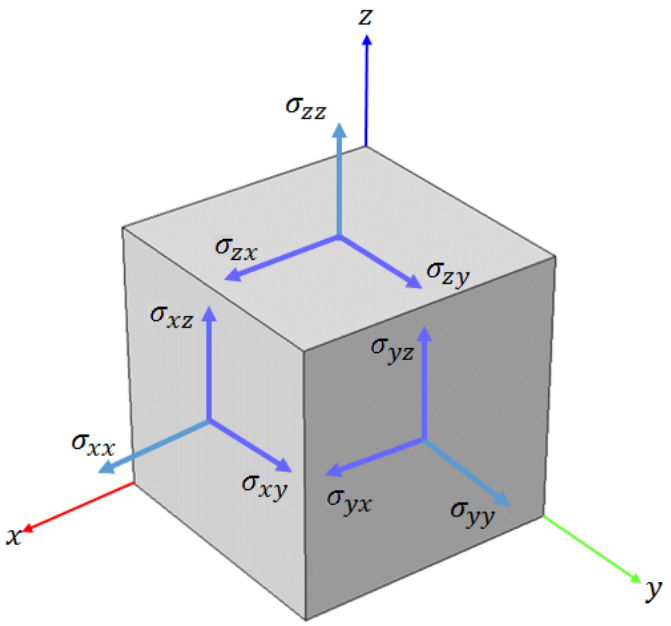

Figure A.2: The stress components in a cubic volume.

with the coupling via elasticity tensor c:

$$\begin{bmatrix} \sigma_{xx} \\ \sigma_{yy} \\ \sigma_{zz} \\ \sigma_{yz} \\ \sigma_{xz} \\ \sigma_{xy} \end{bmatrix} \begin{bmatrix} c_{xxxx} & c_{xxyy} & c_{xxzz} & c_{xxyz} & c_{xxxz} & c_{xxxy} \\ c_{yyxx} & c_{yyyy} & c_{yyzz} & c_{yyyz} & c_{yyxz} & c_{yyxy} \\ c_{zzxx} & c_{zzyy} & c_{zzzz} & c_{zzyz} & c_{zzxz} & c_{zzxy} \\ c_{yzxx} & c_{yzyy} & c_{yzzz} & c_{yzyz} & c_{yzxz} & c_{yzxy} \\ c_{xzxx} & c_{xzyy} & c_{xzzz} & c_{xzyz} & c_{xzxz} & c_{xzxy} \\ c_{xyxx} & c_{xyyy} & c_{xyzz} & c_{xyyz} & c_{xyxz} & c_{xyxy} \end{bmatrix} \cdot \begin{bmatrix} \varepsilon_{xx} \\ \varepsilon_{yy} \\ \varepsilon_{zz} \\ 2\varepsilon_{yz} \\ 2\varepsilon_{xz} \\ 2\varepsilon_{xy} \end{bmatrix} \tag{A.24}$$

The given relationship can be inversed by using elastic compliance tensor s. For linear elastic materials, symmetry can be applied to the given relationship. For the piezoelectric coupling there is coupling matrix d:

$$d = \begin{bmatrix} d_{xxx} & d_{xyy} & d_{xzz} & d_{xyz} & d_{xxz} & d_{xxy} \\ d_{yxx} & d_{yyy} & d_{yzz} & d_{yyz} & d_{yxz} & d_{yxy} \\ d_{zxx} & d_{zyy} & d_{zzz} & d_{zyz} & d_{zxz} & d_{zxy} \end{bmatrix} = \begin{bmatrix} d_{11} & d_{12} & d_{13} & d_{14} & d_{15} & d_{16} \\ d_{21} & d_{22} & d_{23} & d_{24} & d_{25} & d_{26} \\ d_{31} & d_{32} & d_{33} & d_{34} & d_{35} & d_{36} \end{bmatrix} \tag{A.25}$$

which relates electric field to mechanic strain via:

$$\begin{bmatrix} \varepsilon_{xx} \\ \varepsilon_{yy} \\ \varepsilon_{zz} \\ \varepsilon_{yz} \\ \varepsilon_{xz} \\ \varepsilon_{xy} \end{bmatrix} = \begin{bmatrix} d_{xxx} & d_{yxx} & d_{zxx} \\ d_{xyy} & d_{yyy} & d_{zyy} \\ d_{xzz} & d_{yzz} & d_{zzz} \\ d_{xyz} & d_{yyz} & d_{zyz} \\ d_{xxz} & d_{yxz} & d_{zxz} \\ d_{xxy} & d_{yxy} & d_{zxy} \end{bmatrix} \cdot \begin{bmatrix} E_x \\ E_y \\ E_z \end{bmatrix} \tag{A.26}$$

Similar relations are given for the electrostrictive coupling coefficients. Correlation between x, y, z to crystallographic axis 1, 2, 3 is given by Voigt notation:

$$x \rightarrow 1 \tag{A.27}$$
$$y \rightarrow 2 \tag{A.28}$$
$$z \rightarrow 3 \tag{A.29}$$
$$xx \rightarrow 1 \tag{A.30}$$
$$yy \rightarrow 2 \tag{A.31}$$
$$zz \rightarrow 3 \tag{A.32}$$
$$yz \rightarrow 4 \tag{A.33}$$
$$xz \rightarrow 5 \tag{A.34}$$
$$xy \rightarrow 6 \tag{A.35}$$
$$\tag{A.36}$$

B Appendix: Characterization

B.1 SOL Error Term Calculation

The error term calculation is performed according to [104]:

$$
\begin{aligned}
\underline{e}_0 &= \underline{S}_{11,\text{short,true}}\underline{S}_{11,\text{load,true}}(\underline{S}_{11,\text{short,meas}} - \underline{S}_{11,\text{load,meas}}) \\
&\quad + \underline{S}_{11,\text{open,true}}\underline{S}_{11,\text{short,true}}(\underline{S}_{11,\text{open,meas}} - \underline{S}_{11,\text{short,meas}}) \\
&\quad + \underline{S}_{11,\text{open,true}}\underline{S}_{11,\text{load,true}}(\underline{S}_{11,\text{open,meas}} - \underline{S}_{11,\text{load,meas}}) \\
\underline{e}_{11} &= (\underline{S}_{11,\text{short,true}}\underline{S}_{11,\text{load,true}}\underline{S}_{11,\text{open,meas}} \cdot (\underline{S}_{11,\text{short,meas}} - \underline{S}_{11,\text{load,meas}}) \\
&\quad + \underline{S}_{11,\text{open,true}}\underline{S}_{11,\text{short,true}}\underline{S}_{11,\text{load,meas}} \cdot (\underline{S}_{11,\text{open,meas}} - \underline{S}_{11,\text{short,meas}}) \\
&\quad + \underline{S}_{11,\text{open,true}}\underline{S}_{11,\text{load,true}}\underline{S}_{11,\text{short,meas}} \cdot (\underline{S}_{11,\text{load,meas}} - \underline{S}_{11,\text{open,meas}})) \\
&\quad / \underline{e}_0 \qquad \text{(B.1)} \\
\underline{e}_{12} &= (\underline{S}_{11,\text{open,true}} - \underline{S}_{11,\text{short,true}})(\underline{S}_{11,\text{open,true}} - \underline{S}_{11,\text{load,true}}) \\
&\quad \cdot (\underline{S}_{11,\text{short,true}} - \underline{S}_{11,\text{load,true}})(\underline{S}_{11,\text{open,meas}} - \underline{S}_{11,\text{short,meas}}) \\
&\quad \cdot (\underline{S}_{11,\text{open,meas}} - \underline{S}_{11,\text{load,meas}})(\underline{S}_{11,\text{short,meas}} - \underline{S}_{11,\text{load,meas}}) \\
&\quad / \underline{e}_0^2 \qquad \text{(B.2)} \\
\underline{e}_{21} &= 1 \qquad \text{(B.3)} \\
\underline{e}_{22} &= \underline{S}_{11,\text{load,true}}(\underline{S}_{11,\text{short,meas}} - \underline{S}_{11,\text{open,meas}}) \\
&\quad + \underline{S}_{11,\text{short,true}}(\underline{S}_{11,\text{open,meas}} - \underline{S}_{11,\text{load,meas}}) \\
&\quad + \underline{S}_{11,\text{open,true}}(\underline{S}_{11,\text{load,meas}} - \underline{S}_{11,\text{short,meas}}) \\
&\quad / \underline{e}_0 \qquad \text{(B.4)}
\end{aligned}
$$

with the predetermined calibration values $\underline{S}_{11,\text{xxx,true}}$ and the calibration measurements $\underline{S}_{11,\text{xxx,meas}}$. The real DUT measurement results can be extracted from the measurement data and error terms with:

$$
\underline{S}_{11,\text{DUT,true}} = \frac{\underline{e}_{21}^{-1} + \underline{e}_{22}^{-1}\underline{S}_{11,\text{DUT,meas}}}{\underline{e}_{11}^{-1} + \underline{e}_{12}^{-1}\underline{S}_{11,\text{DUT,meas}}} \qquad \text{(B.5)}
$$

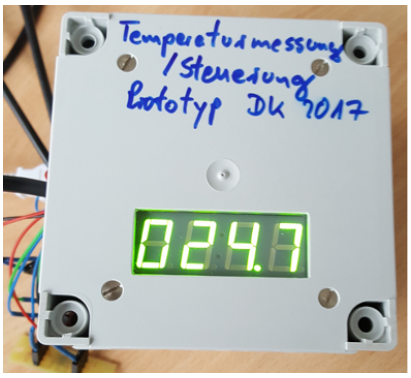

(a) Temperature control unit front.

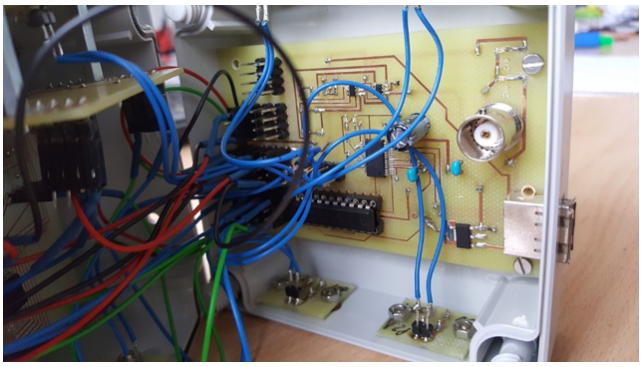

(b) Mainboard holding the TI MSP430 microcontroller and FTDI FT232R UART communication converter.

Figure B.1: Temperature control unit for circuit board integrated bulk ceramic disk varactor characterization.

B.2 Temperature Control Unit

To characterize circuit board integrated bulk ceramic varactors in the presented fixture over temperature, a temperature measurement and control unit is developed. As described in section 3.1.3, the bulk ceramic disk varactors are setup for an operational temperature of 50 °C with the barium to strontrium mixing ratio and a Curie temperature of 25 °C. Therefore, small characterization has to be performed at the design temperature 50 °C. The unit consists of a Texas Instruments MSP430g2553 microcontroller with a clock speed of 16 MHz, a FTDI FT232R USB to RS232 converter for UART communication with the measurement PC, a Melexis MLX90614 contactless infrared thermometer, an Analog Devices AD5282 digital potentiometer, a four digit 7-segment temperature display driven by a Maxim MAX6955 and two DAWN DN505 9 W heating elements, applied to a 2 ″ alumina substrate. The developed heating unit is depicted in figure figure B.1.

The unit can be remote controlled with a PC or stand alone by setting up a temperature with two buttons. In-system programming (ISP) of the microcontroller with a new software is possible. IR sensor, potentiometer and 7-segment display are controlled via digital I2C by the microcontroller. The IR sensor is applied to a rigid cable and can be installed anywhere in the measurement setup. The temperature is read from the IR sensor every 0.5 s and directly displayed on the 7-segment display. The temperature reading from the sensor can also be acquired from the PC utilizing the USB to RS232 converter. In the other direction, the PC can set up a certain temperature that the circuit should regulate to. The temperature is controlled by the microcontroller with the digital potentiometer. The heating elements are self regulating on a temperature, that can be set up with a resistance, see section 3.1.3. The digital potentiometer provides that resistance and thereby regulates the temperature. The two heating elements are glued to the back of an alumina substrate, providing for a good

thermal conductivity and electrical isolation, when applied to DC bias voltage carrying wires. Again, a rigid cable is used to connect to the heating elements on the substrate, rendering it suitable for application anywhere in the measurement circuit. A temperature accuracy of 0.5 °C is possible with this setup. However, a second, optional, control loop is implemented in the microcontroller, dependent on the temperature reading at a certain point in the set up from the IR sensor. Thereby, a certain temperature at an arbitrary point in the measurement construction can be achieved. The only limitation of the setup is the heating power of 18 W from the two heating elements.

C Appendix: Thick Film Varactors

C.1 Medium-Power Varactor Design

The first design is set up to handle dissipated power up to 25 W with an estimated Q-factor of 100. A cooling surface of 630 mm^2 is estimated to handle the maximum dissipated power. With an electrical breakdown field strength of 32 $kV\,mm^{-1}$ for bulk material [92], a theoretical maximum voltage amplitude of 320 V is applicable to a 10 µm BST MIM structure. Due to the reduced density and increased porosity of printed BST thick film compared to bulk ceramic material, however, the electrical breakdown field strength for thick film can be assumed to be reduced [14, 105]. For a load of $(1.86 + 3.02\mathrm{i})\,\Omega$ and an input power level of 100 W a maximum RF voltage level of 103 V is expected in the position of C_{Vac1} in the L-match circuit, see figure 3.13, with a required match capacitance of $C_{\mathrm{Vac1}} = 750\,\mathrm{pF}$, see table 4.1. Including the DC biasing voltage of 200 V, the total voltage stresses are estimated to be 300 V. With a reduced DC biasing voltage of 100 V, the varactor is capable of handling up to 400 W of input power, resulting in 208 V of RF voltage stresses, without exceeding its electrical breakdown field strength. However, for 400 W of input power, a dissipated power of 27 W is calculated, exceeding its power dissipating capabilities of 25 W. To obtain the required BST layer thickness and therefore electrical breakdown field strength of the varactor, a minimum of two BST layers have to be printed on top of each other, see section 2.2.2 [49]. An unbiased capacitance value for the varactor cell of 3 nF is chosen, resulting in a MIM structure capacitance of 6 nF. There are two reasons for the discrepancy of the required and chosen unbiased capacitance value:

- Table 4.1 gives the required capacitance value for the matched case at the position of C_{Vac1}. During large-signal characterization, however, the position of C_{Vac1} is occupied by a mechanically tunable vacuum varactor sampling the capacitance value of the thick film varactor, connected to it in series, see section 3.2. The overall capacitance of the series connection meets the matching requirement in this branch of the circuit. Due to the fact, that in a series connection of capacitors, the smallest one dominates the overall capacitance value, it is necessary for the tunable vacuum varactor to be smaller and therefore dominant compared to the thick film varactor.
- For large capacitance values in position of C_{Vac1} there are more realistic load conditions, even though they are less stressful for the varactor in that position. Therefore, it can be accounted for a scenario in which the thick film varactor reacts more fragile to the applied stresses.

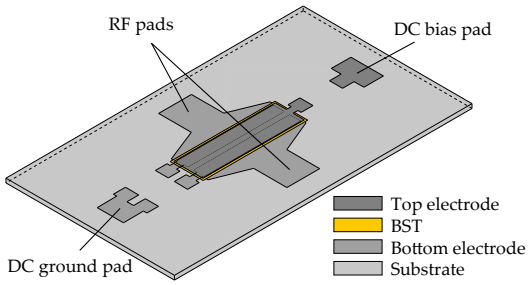

(a) 3D view of the low power varactor design.

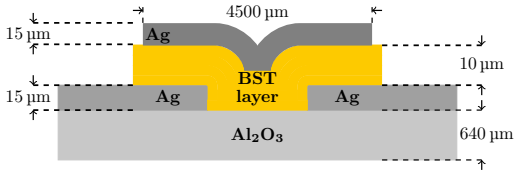

(b) Cut through the layered varactor structure with main dimensions.

Figure C.1: 3D view and cut plane view of the varactor design.

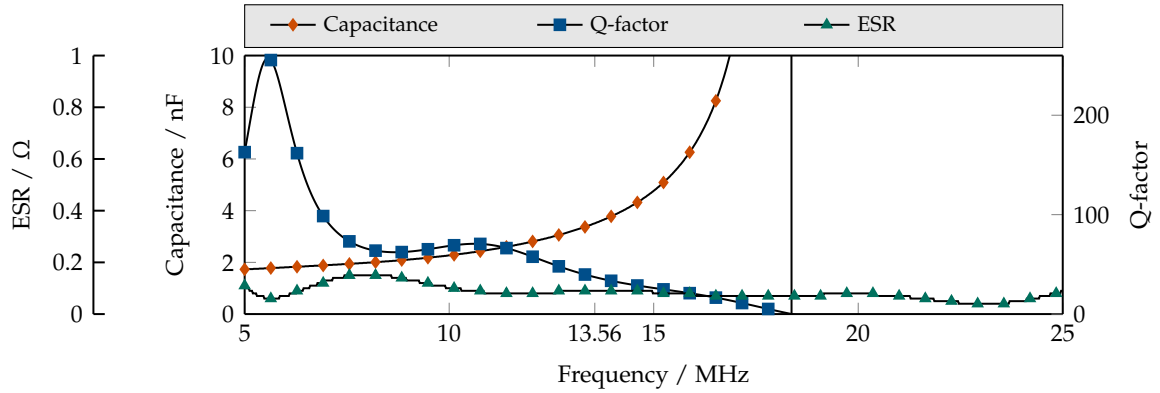

Figure C.2: Simulated capacitance, quality factor and ESR of the structure.

With a relative permittivity of 230 [42], an electrode overlap area of 30 mm^2 is required, calculated with the parallel plate capacitance formula [18, 15]. To account for fringing field components on the varactor edges and manufacturing tolerances especially in the BST layer thickness, a MIM structure overlap area of 2.1 mm $\times$ 15 mm is chosen resulting in a theoretical varactor cell capacitance of 3.2 nF. The varactor design is depicted in figure C.1 together with a cut plane view through the structure. A full wave simulation of the structure is performed in CST Microwave Studio to validate the analytical approach. The results of the simulation in regard to capacitance, Q-factor and ESR are depicted in figure C.2.

The varactor design shows the analytically calculated capacitance value. With a loss factor of 0.01 at 13.56 MHz of the BST, resulting in a theoretical maximum Q-factor of 100, the overall Q-factor of the varactor is significantly decreased to 37.2 by the limited metalization conductivity of $6.3 \cdot 10^7\,\mathrm{S\,m^{-1}}$ of silver. The simulation also includes substrate losses. A port correction is implemented with an inductance of 27 nH calculated from a groundless strip conductor formula [100]:

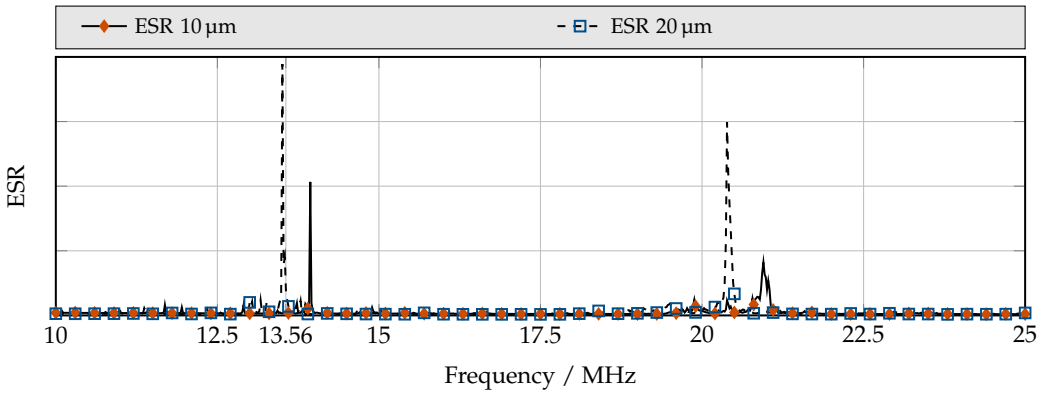

Figure C.3: Simulated impedance spectrum of a 10 µm and 20 µm piezoelectric thick film between two silver electrodes.

$$L = \frac{\mu_0 l}{2\pi}\left[\ln\left(\frac{2l}{w}\right) + 0.5\right] \tag{C.1}$$

with a length of the strip line of $l = 35.65$ mm, a width of the conductor of $w = 2.6$ mm and the magnetic constant $\mu_0 = 1.257\,\mathrm{nH\,mm^{-1}}$ accounting for the unconventionally large port in the simulation. The self-resonance frequency of the design, which is introduced by the parasitic inductance of the metal electrodes and connection pads, is located at 18.4 MHz and unproblematic, due to the single frequency application. For broad-band applications, the operational frequency is recommended to be one decade below the SRF for stable component values in the whole used frequency band. The acoustical behavior of the varactor is estimated with a piezoelectric simulation in COMSOL Multiphysics. The simulation is set up in the strain-charged form of inverse piezoelectric effect, calculating the resulting stress and displacement of the material from the induced strain, coupled by the electrical excitation. The theoretical background is given in section 2.1.2 and the exact setup of piezoelectric simulations in COMSOL is given in section 4.1. As a model, the layered structure depicted in figure C.1 is implemented in COMSOL with a depth of 1 mm to reduce simulation time. This is valid, since all vertical dimensions are still much smaller compared to all lateral dimensions of the geometry. Basic mechanical properties of the materials are taken from the material library of COMSOL. The BST thick film and silver electrodes are substituted with $BaTiO_3$ and elemental silver, respectively. The simulation results for a 10 µm and 20 µm film are depicted in figure C.3.

Two main resonances occur in the impedance spectrum depicted in figure C.3 at 14 MHz and 22 MHz for the 10 µm film, as well as 13.56 MHz and 21 MHz for the 20 µm film. They are accompanied by spurios modes at lower frequencies. These modes are excited by the stepped structure of the bottom electrodes and should be damped in the manufactured varactor due to the less erratic form of the electrodes. The simulation indicates interference

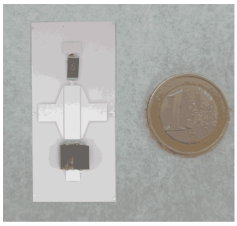

(a) Screen-printed varactor with on-substrate biasing network.

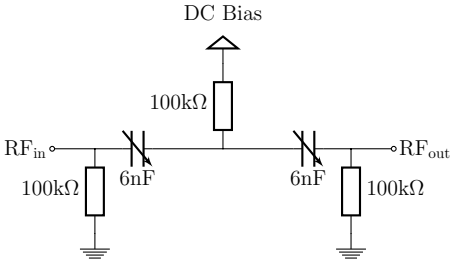

(b) Equivalent circuit model of the varactor with biasing network.

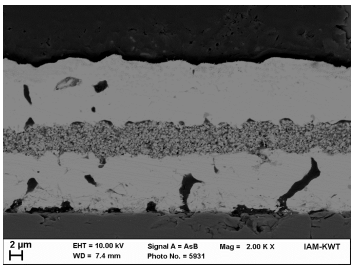

(c) Scanning electrode microscope (SEM) cross-sectional image of the MIM structure.

Figure C.4: Manufactured varactor with the equivalent circuit model and SEM cross-sectional image of the MIM thick film structure. ©2016 IEEE.

of the resonances with the operational frequency at 13.56 MHz for the 20 µm film. Therefore, for fabrication, the 10 µm film thickness appears feasible.

BST preparation and varactor processing

Cu-F codoped $Ba_{0.6}Sr_{0.4}TiO_3$ is prepared in a modified sol-gel process [81]. The calcination of the spray-dried metal-organic precursor was done at 900 °C for 1 h. A fine grained powder is obtained, that is supplemented with 5 vol.% ZnO and H_3BO_3, which is necessary for the powder to be suitable for low temperature sintering [48]. To obtain a suitable screen printing paste the powder mixture is dispersed in the organic solvent terpineol with binder (ethylcellulose) and dispersant. The MIM varactor is processed in three steps. In a first step the bottom RF electrodes are screen printed on an alumina substrate. For the electrode material the conductor paste C 1076 SD (LPA 609-022) from Heraeus is chosen. It is a solderable Ag/Pt conductor paste suitable for temperatures up to 850 °C. The paste is dried at 150 °C for 20 min and sintered at 850 °C for 10 min. In a second step three layers of BST thick film are screen printed on the bottom electrode, dried at 80 °C and sintered in purified air at 850 °C for 1 h. In a final step the top electrodes are screen printed on top of the BST layers and dried at 150 °C for 20 min. The varactor is then sintered at 850 °C for 10 min. Two varactors are obtained from one 2 ″ wafer by milling the substrate to a size of 23 mm × 50 mm after the manufacturing process. One varactor substrate exceeds the required cooling surface, calculated in this chapter, by 520 mm^2. The varactor substrate is assembled with three 100 kΩ resistors to ensure RF/DC decoupling. The mounted design is depicted in figure C.4 together with the equivalent circuit model of the varactor and a cross-sectional scanning electron microscope (SEM) image of the MIM structure.

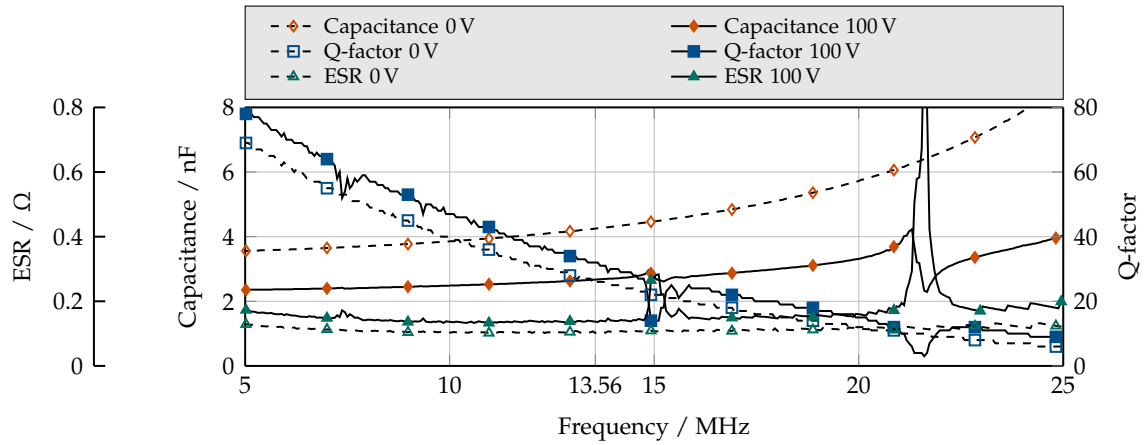

Figure C.5: Measured capacitance, Q-factor and ESR of the medium power varactor over frequency in biased and unbiased state.

Small-Signal Characterization Results

The varactor is characterized with the setup described in 3.1.2 and depicted in 3.5 in a frequency range of 5 MHz to 25 MHz. The measurement results are depicted in figure C.5.

At 13.56 MHz the capacitance is tuned from 4.25 nF down to 2.67 nF, resulting in a tunability of 37.2 % with a maximum biasing voltage of 100 V. The quality factor is increased from a value of 26 at 0 V to a maximum 32 at 100 V. At 15 MHz the trace of the quality factor shows a localized minimum of 14 with a biasing voltage of 100 V, indicating an acoustic resonance at this frequency. A second acoustic resonance is observed at 21 MHz resulting in a localized minimum in quality factor of 3. The self-resonant frequency (SRF) of the varactor in unbiased state is at 33.6 MHz and shifts to 38.9 MHz with 100 V of biasing voltage. Compared to the electric simulation results, depicted in figure C.2, C and Q value at 13.56 MHz are in good agreement. However, the frequency behavior of both values does not match the measured ones. The Q-factor trace for low frequencies is dominated by a local minimum of the ESR, resulting in a value above 200. The capacitance trace of the simulation indicates the self-resonance frequency at 18.4 MHz, a relative deviation of 45 % to the measurement. The reason for this, is presumably the incorrect port correction performed on the simulation results. A much larger port inductance than assumed solves the problem, however, the cause for large port inductance is not yet resolved.

Large-Signal Characterization Results

The large-signal setup is explained in detail in section 3.2. For large-signal characterization, the varactor is placed in characterization fixture, similar to the small-signal characterization fixture presented in section 3.1.2 and depicted in figure 3.5. A biasing voltage of up to

128 V is applied to the varactor during characterization. The results of the large-signal measurements in regard to tunability are shown in Fig. C.6. Figure C.6a presents the capacitive behavior of the varactor at different power levels in regard to tunability up to an RF input power level of 300 W and a load impedance of $(1.86 + 3.02\mathrm{i})\ \Omega$. At an input power level of 100 W the varactor exceeds a maximum tunability of 47 %. A minimum tunability is measured at an input power level of 300 W and 13.2 %. The measurement results in regard to tunability up to an input RF power level of 400 W are shown in Fig. C.6b. It should be noted that for measurements above 300 W the load condition of the circuit is changed. With the changed load condition the varactor shows at an input power level of 300 W and 128 V of biasing voltage a tunability of 30.7 %. With an input power level of 400 W the tunability is reduced to 21.3 % for the same biasing voltage. This effect can be reduced to the increase in temperature with increasing dissipated power in the varactor. BST thick films are known to have a non-linear thermal dependent permittivity which decreases with increasing temperature. As a result the tunability of the varactor decreases with increasing temperature as well [11].

A detailed loading condition of the L-match in regard to load impedance and input power level as well as the voltage and current stresses and the dissipated power in the DUT are shown in table C.1. For input levels higher than 300 W the limitation of the tuning range of C_{Vac1} prohibits to meet the required matching condition of $\underline{Z}_{\mathrm{M}}^{*}$. Therefore, the impedance at $\underline{Z}_{\mathrm{M}}^{*}$ is set to $(2.92 + 0.85\mathrm{i})\ \Omega$ in order to reduce the required capacitance value of C_{Vac1} for a sufficient matching condition. However as a result, the voltage and current at the DUT are reduced in comparison to the load condition for lower input power levels which explains the increased tunability at 300 W with the changed load impedance. At 500 W of input power, the varactor operates stably in unbiased state. In biased state, the varactor electrically breaks down, see figure C.7. The whole electrode and BST structure is destroyed by the burning arc fed from the RF power. However, a thermally induced breakdown is not observed.

Overall, the varactor performance is ambiguous. The varactor is designed with an expected Q-factor of 100, which is significantly reduced in the implemented design to maximum 48. Therefore, the varactor performs worse than expected. However, for the reduced Q-factor the varactor performs better than expected. Its power dissipating capabilities of up to 37.1 W, exceed the expected value of 25 W. No thermal runaway is observed and the tunability of the varactor remains on an acceptable value of 21 %. By serial stacking MIM cells, the partial voltage stresses on a single MIM structure can be significantly reduced, rendering the presented design successful.

C.2 Acoustically Optimized Medium-Power Varactor Design

The first acoustically optimized varactor structure presented in this work is based on the approach to suppress acoustical shear waves in the dielectric layer in order to study the

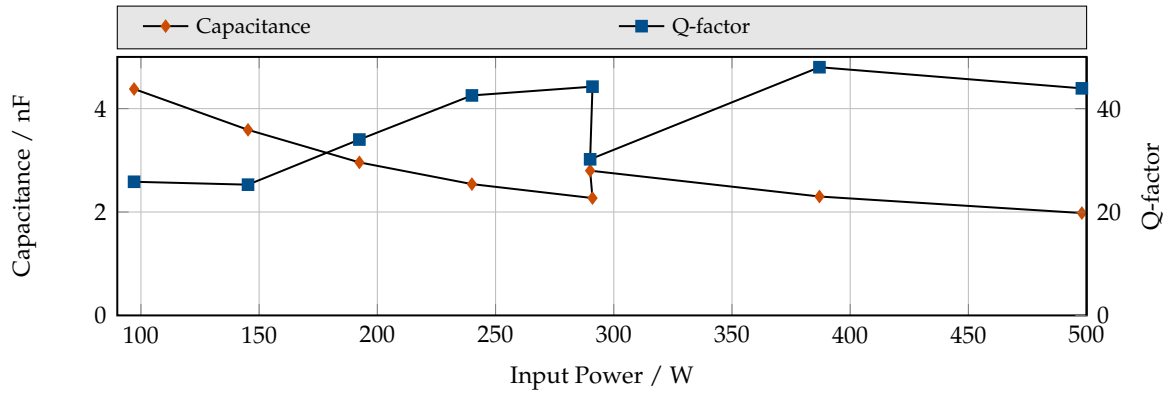

(a) Capacitance and Q-factor for various input power levels. A change in loading is performed at 300 W of input power.

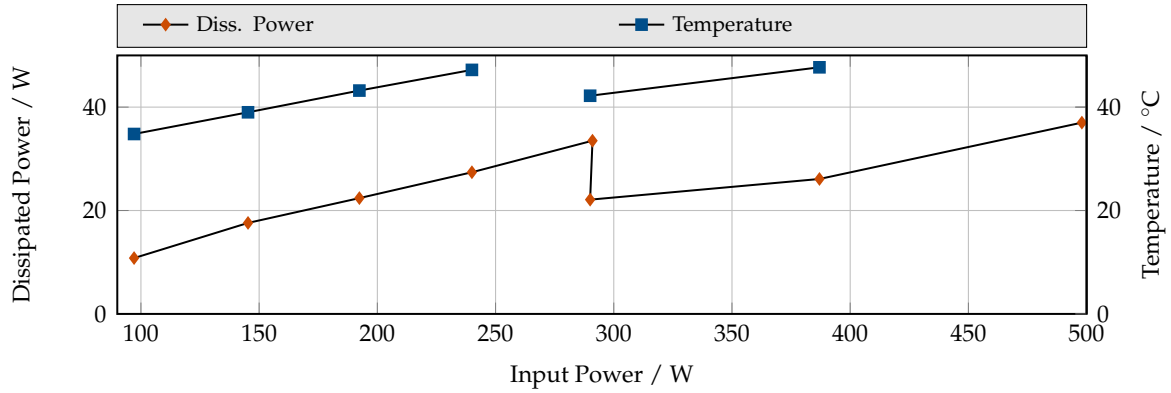

(b) Dissipated power and temperature measurements over input power.

Figure C.6: Large-signal characterization measurements of the medium power varactor in regard to capacitance, Q-factor, dissipated power and temperature.

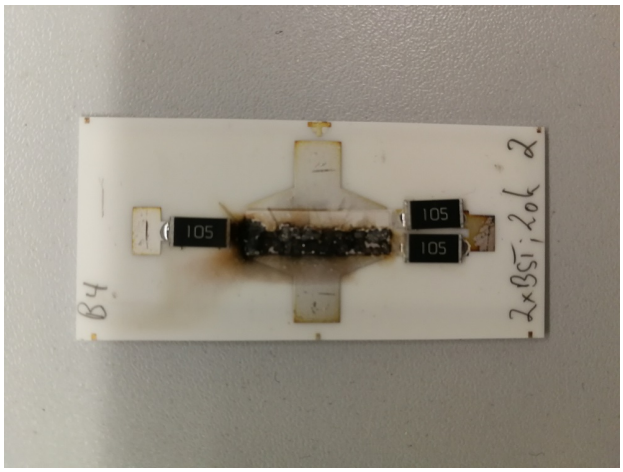

Figure C.7: Varactor electrically broken down during large-signal characterization.

Table C.1: Summary of large-signal characterization data obtained for the medium-power varactor at different RF input power levels in unbiased state.

Load and power level			DUT measurements						
$\lvert Z_M^* \rvert$	P_{in}	P_{out}	V_{rms}	I_{rms}	$C(0\,V)$	$Q(0\,V)$	τ	P_{diss}	T
Ω	W	W	V	A	nF		%	W	°C
	97.1	83.5	17	6.4	4.4	25.9	47	10.8	34.8
	145.3	123.7	27.2	7.8	3.6	25.3	37	17.6	39
3.55	192.4	166.2	37.4	9.0	3.0	34.0	28	22.4	43.2
	240.1	208.4	49.0	10.1	2.5	42.5	22	27.4	47.2
	291	249	60.8	11.0	2.3	44.3	-	33.5	-
	290	262.6	38.8	8.6	2.8	30.2	31	22.1	42.2
3.04	387.1	353.8	52.7	9.9	2.3	48	21	26.1	47.7
	498	451.6	66.3	11.2	-	-	-	37.1	-

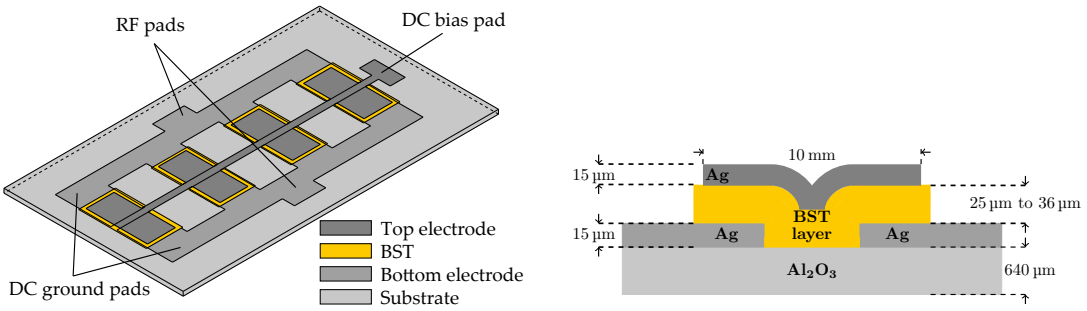

(a) 3D view of the acoustically optimized, medium power varactor design.

(b) Cut through one of the four varactor cells with main dimensions.

Figure C.8: 3D view and cut plane view of the varactor design.

impact of vertical pressure waves on the varactor performance exclusively. It is known that in structures with large lateral dimensions in combination with an inhomogeneous height distribution of the ferroelectric layer and for the adjacent layers, shear waves travelling along the surface of the structure are generated [90]. It is possible to suppress these waves by interrupting the dielectric layer and implement the varactor not in a continuous structure but in an interrupted parallel connection of varactor cells. In such a structure, mainly acoustic resonances based on vertical pressure waves are excited, which are dependent on the vertical dimensions and parameters of adjacent material layers. In this first attempt, the varactor is divided into four, initially unconnected varactor cells consisting of two MIM structures in series connection, see figure C.8.

The varactor cells themselves are only interconnectable in parallel. The resulting varactor is electrically similar to the design presented in appendix C.1. The top electrode on the BST layer is interconnected between all cells and extends to the surface of the substrate in between cells. Thereby, the DC biasing voltage is applied to all top electrodes of the structure. The varactor design is implemented with three different thicknesses of the BST layer to evaluate the acoustical behavior of these structures and their power handling capabilities during large-signal characterization. With increasing BST layer thickness the fabricated thick film varactors are termed C_1 to C_3. The varactor is set up for dissipated power levels up to 40 W. However, the cooling surface of 630 mm^2 is taken from the varactor design in appendix C.1, which proofed to be more than sufficient for dissipated power levels of up to 37 W. The electrode overlap area is set to 162 mm^2 and increased compared to the prior design for 25 W of dissipated power. Main reason for this is to ensure capacitance values above 1.5 nF even for large BST thicknesses to stay within the limited measurement range of the large-signal characterization circuit. Theoretical capacitance values for the design are calculated from 1.5 nF to 6 nF for thicknesses between 10 µm to 40 µm. An on-substrate DC/RF decoupling network is intentionally waived, due to the limited space on the substrate. Instead, an FR4 PCB with the RF/DC decoupling network is designed to which the varactor is soldered. Again, 100 kΩ resistors are chosen for the resistive biasing network. The resulting ESB is identical to the one presented in figure C.4. The varactor

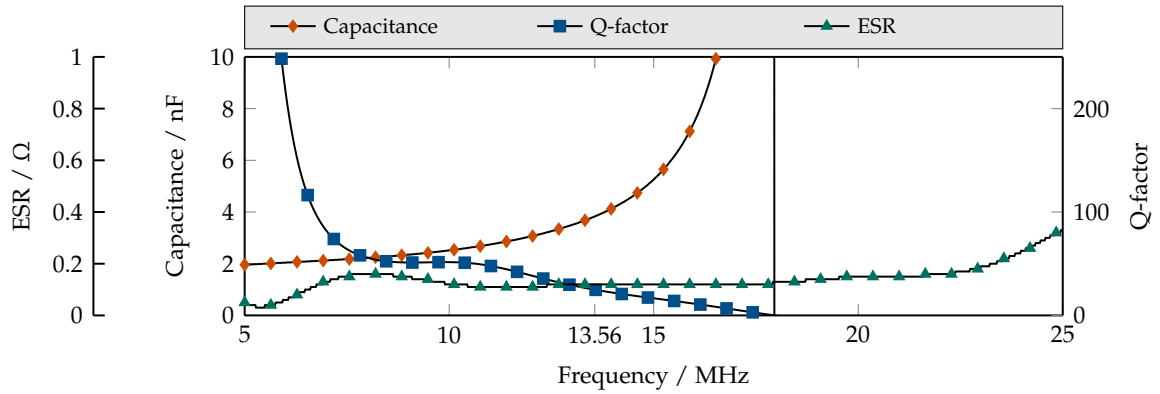

Figure C.9: Simulated capacitance, quality factor and ESR of the structure.

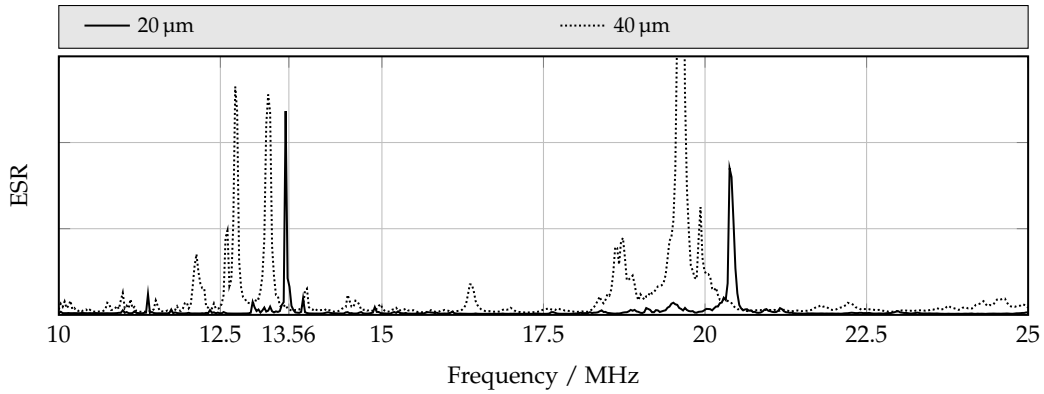

Figure C.10: Simulated impedance spectrum of a 20 µm and 30 µm thick film.

setup with a cut through the layered structure and the simulation results in regard to C, Q-factor and ESR are depicted in figure C.9.

The acoustical behavior of the structures is estimated with an acoustical simulation for BST layer thicknesses between 20 µm to 40 µm of a single varactor cell. The results of the simulation are depicted in figure C.10.

The simulation results for the 20 µm BST layer are in good agreement with the simulation results for the unoptimized 25 W design from appendix C.1. In both simulations surface acoustic waves are not considered, therefore the simulation results are supposed to be similar. However it is important to note, that no change in the simulation results is visible, even though the design was radically altered. Therefore it can be assumed, that the obtained results for different BST layer thicknesses can be applied independently from the exact geometry, as long as the longitudinal pressure mode is dominant in the structure. For the 40 µm BST film thickness, a shift of the resonances from 13.56 MHz and 20.5 MHz to 13 MHz and 19 MHz is visible. As a conclusion, the simulation results indicate that the BST

layer thickness is an appropriate tool to adjust the acoustical behavior of the capacitive MIM structures to the intended operation frequency.

Varactor Processing

Cu-F codoped $Ba_{0.6}Sr_{0.4}TiO_3$ is prepared in a modified sol-gel process [49, 81]. The MIM varactor structures are processed in three steps. In a first step, the bottom RF electrodes are screen printed on an alumina substrate. For the electrodes, the conductor paste C 1076 SD (LPA 609-022) from Heraeus is chosen. It is a solderable Ag/Pt conductor paste suitable for temperatures up to 850 °C. In a second step, the BST thick film layer is printed. Dependent on the desired height, two and four layers of BST are printed on top of each other, resulting in a height of 25 µm to 30 µm for the two printed layers and 32 µm to 36 µm for the four printed layers. The structure is dried at 80 °C. In a final step, the top electrodes are screen printed on top of the BST layers. The varactors are co-sintered at 850 °C for 10 min.

Small-Signal Characterization Results

After processing, the varactors are soldered to an FR4 PCB which holds the resistive RF/DC decoupling network and provides a biasing connector. The varactor modules are characterized from 5 MHz to 25 MHz with the impedance analyzer. To characterize the varactor modules, they are placed in a characterization fixture which is calibrated using a standard SOL calibration, see section 3.1. The DC biasing voltage is adjusted in a range of 0 V to 220 V. The characterization results over frequency are shown in figure C.11a and figure C.11b.

The unbiased capacitance of the varactors at 13.56 MHz ranges from 1.8 nF to 3.2 nF. The varactors show decreasing tunability with increasing BST layer thickness from 28 % to 17 % with a thickness from 25 µm to 36 µm. The main reason is the unadjusted DC biasing voltage, while the thickness of the BST layer is different for each sample. However, following the tunability approximation of BST with electrical field strength by Weil et. al., the drop in tunability is in good agreement with the drop of electrical field strength in the material [106]. A maximum unbiased quality factor of 61 is measured for the sample with a BST thickness of 36 µm. The samples with a BST layer thickness of 32 µm and 36 µm show an increasing quality factor with DC biasing voltage from 37 to 43 and 61 to 67, see figure C.11c. The sample with a BST layer thickness of 25 µm shows a contradictive behavior. The quality factor decreases with DC biasing voltage from 43 to 39. As depicted in figure C.11a and figure C.11b and with good agreement to the piezoelectric/acoustic simulation in figure C.10, the first acoustic resonance of the varactor with a BST layer thickness of 25 µm is interfering with the operational frequency at 13.56 MHz. As a result the resonance is decreasing the quality factor with increasing DC biasing voltage. For the samples with 32 µm and 36 µm, the first acoustic resonance is shifted towards lower frequencies and as a result the quality factor shows its known behavior from BST by increasing with DC biasing voltage [107].

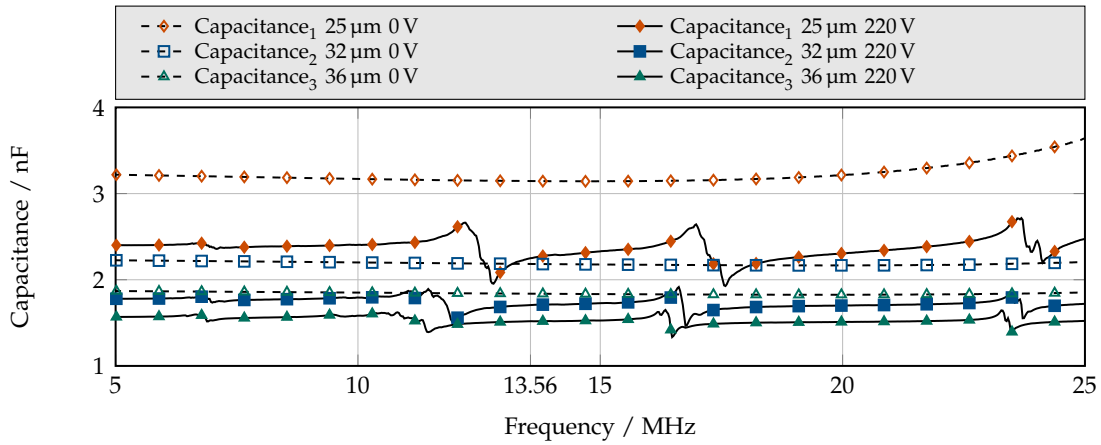

(a) Capacitance vs. frequency in unbiased and biased state.

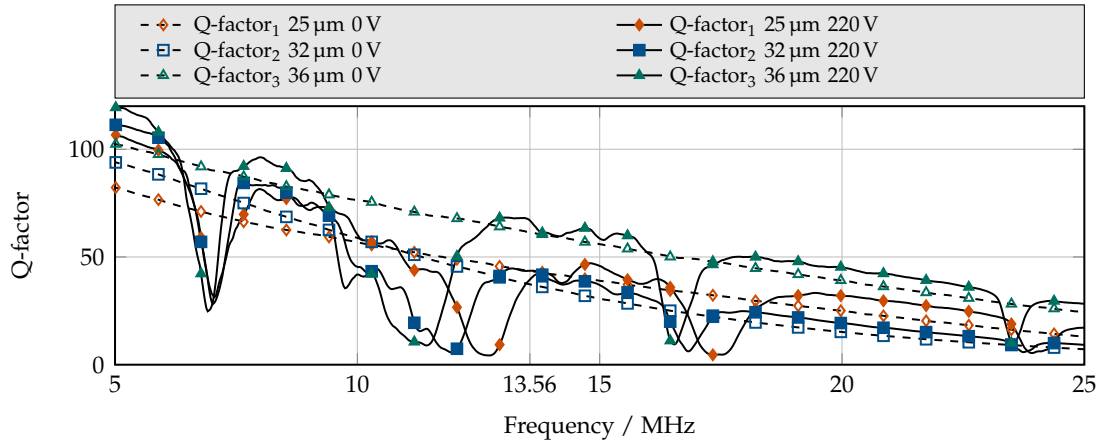

(b) Q-factor vs. frequency in unbiased and biased state.

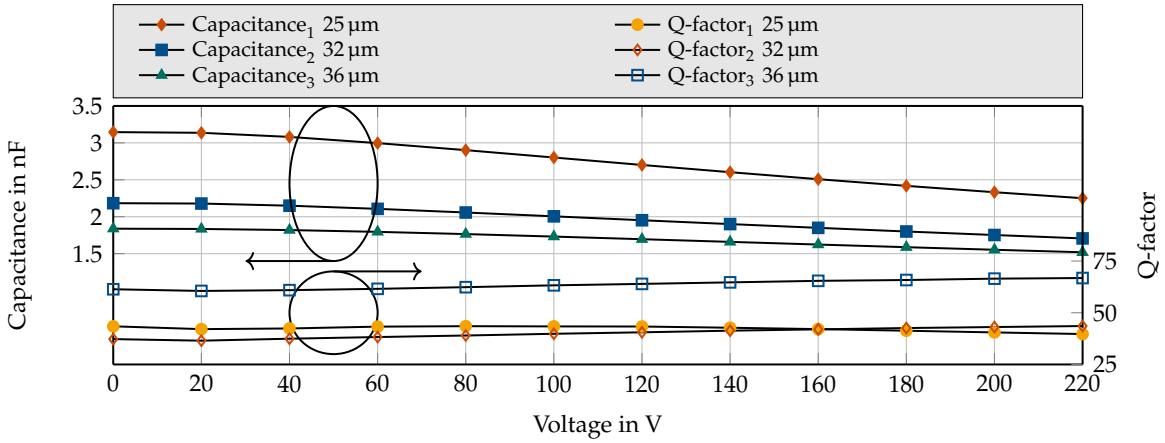

(c) Capacitance and Q-factor for various biasing voltages at 13.56 MHz.

Figure C.11: Small-signal characterization results of the acoustically optimized medium power varactor for different BST film thicknesses.

Table C.2: Summary of large-signal characterization data obtained for the acoustically optimized, medium-power varactor at different RF input power levels in unbiased state.

Load and power level			DUT measurements						
Var.	P_{in} W	P_{out} W	V_{rms} V	I_{rms} A	$C(0\,V)$ nF	$Q(0\,V)$	τ %	P_{diss} W	T °C
C_1	97.6	87.7	16.7	4.8	3.2	10.2	28	8.3	31.5
C_2	97.7	87.4	32.4	5	1.8	20	14	8.3	37.5
C_3	97.5	86.7	37	5	1.8	16.3	16	9.9	33.4
C_1	293.5	264.6	45.3	9	2.3	17.2	19.6	24	49
C_2	293.6	263.4	81	9.2	1.3	27.3	2.5	28	64.7
C_3	292.7	261.5	91	8.6	1.1	27.2	3	29	59.2
C_1	680	613	106	13.2	1.5	23.1	7	59	65
C_2	535	480	135	11.7	1.1	27.6	6	53	87.7
C_3	534	478	168	11.5	0.8	36	0	54	89

Large-Signal Characterization Results

The large-signal measurement is performed at 13.56 MHz with a biasing voltage of 200 V. A detailed description of the large-signal characterization setup is given in section 3.2. During characterization, no cooling is applied to the varactors. To achieve good comparability, the load impedance $\underline{Z}_M^*$ is set to $(2.68 + 1.25\mathrm{i})\,\Omega$ in accordance to appendix C.1. The results of the measurements are depicted in table C.2.

The varactors show a decreasing capacitance value as well as decreasing tunability with increasing input power level. The decreasing capacitance value can be attributed to the increasing temperature of the varactors. The decreasing tunability is caused by the temperature increase of the varactors as well as a decreasing DC biasing voltage to RF voltage amplitude ratio. Varactor C_1 with a BST layer thickness of 25 µm and an unbiased quality factor of 43 shows the lowest dissipated power at equal input power levels, inconsistent with the characterization measurement. The reason for this is the large capacitance of the varactor compared to the other two samples, which generates a less stressful loading state of the varactor C_1, indicated by the lower dissipated power and RMS voltage values. Adjusting the capacitance of C_1, while leaving the quality factor unchanged leads to consistent data with the characterization measurement. In biased state the dissipated power of C_1 increases significantly, a result of the decreasing quality factor with DC biasing factor due to the interfering acoustical resonance at 13.56 MHz. Consisting with the characterization measurements, the varactors with a BST layer thickness of 32 µm and 36 µm show a different behavior, with a less significant or no increase in dissipated power with biasing voltage.

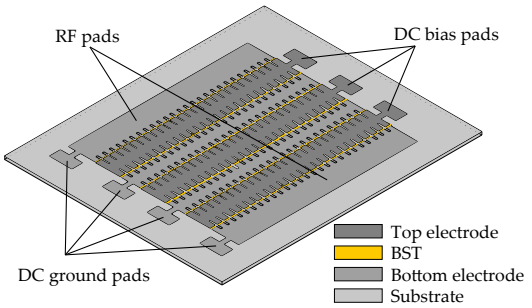

(a) 3D view of the high-power matrix varactor design.

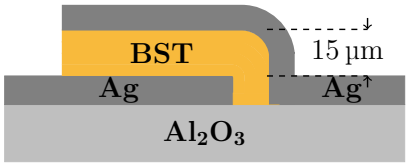

(b) Cut through one MIM structure with main dimensions.

Figure C.12: 3D view and cut plane view of the varactor design.

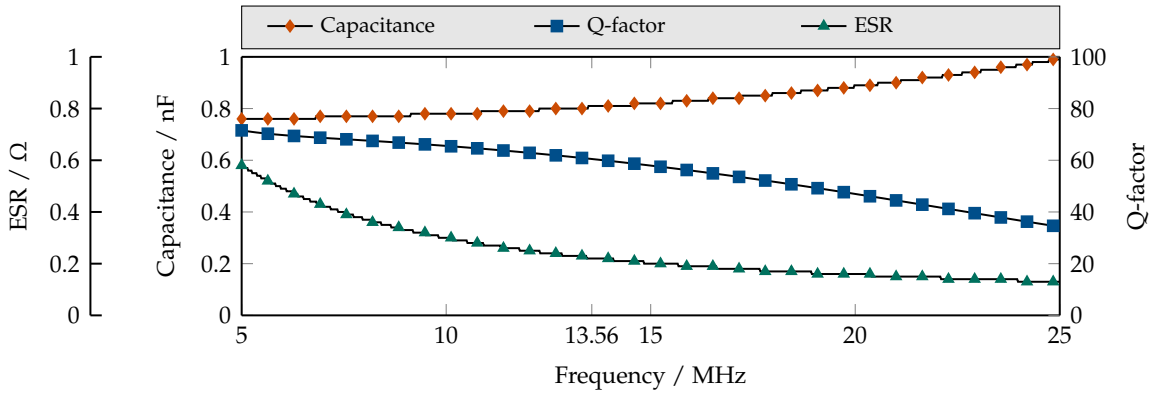

Figure C.13: Simulated capacitance, quality factor and ESR of the structure.

C.3 Acoustically Optimized Matrix Varactor Design

For the acoustically optimized high-power design the approach from the acoustically optimized low power varactors is taken and implemented in a more radical way, see figure C.12.

The macroscopic varactor consists of $27 \cdot 6 = 162$ cells, resulting in a total electrode overlap area of 121.5 mm^2, with a single cell capacitance of 161 pF. Theoretically, by interconnecting all cells, an overall capacitance of 729 pF is achieved. Similar to section 4.1, the complete back of the 2 ″ substrate serves as cooling surface (2581 mm^2). The varactor design, with a cut through a single MIM structure and the electric simulation in regard to C, Q and ESR are depicted in figure C.13.

The acoustical behavior of a single MIM structure with the dampening electrode connector is depicted in figure C.14.

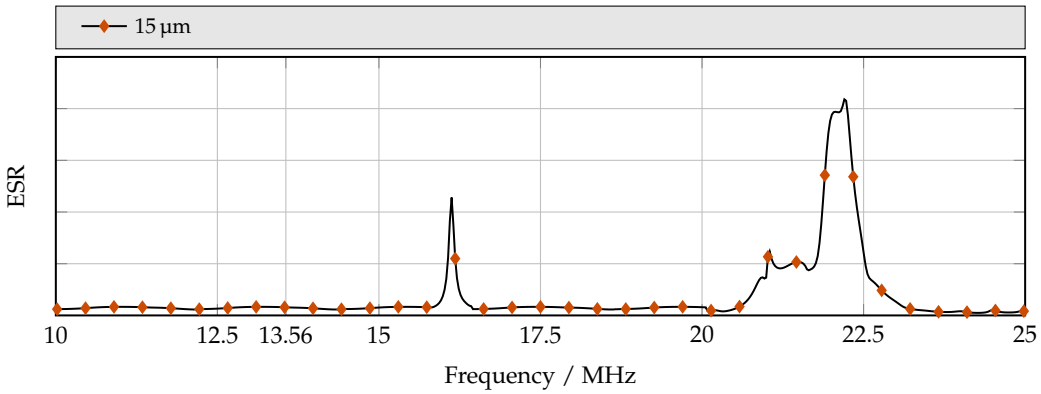

Figure C.14: Simulated impedance spectrum of a single MIM structure with a dampening electrode contact 15 µm thick film.

The smaller cells with the dampening electrode contact show acoustic resonances at 15.9 MHz and 22 MHz. An interference with the operational frequency is not expected with the design.

Varactor Processing

Cu-F codoped $Ba_{0.6}Sr_{0.4}TiO_3$ is prepared in a modified sol-gel process [49, 81]. The MIM varactor structures are processed in three steps. In a first step, the bottom RF electrodes are screen printed on an alumina substrate. For the electrodes, the conductor paste C 1076 SD (LPA 609-022) from Heraeus is chosen. It is a solderable Ag/Pt conductor paste suitable for temperatures up to 850 °C. In a second step, two layers of BST thick film are screen printed on the bottom electrode and dried at 80 °C. A total BST layer thickness of 15 µm is obtained. In a final step, the top electrodes are screen printed on top of the BST layers. The varactors are co-sintered at 850 °C for 10 min. The processed varactor and the varactor module are depicted in figure C.15

Small-Signal Characterization

Two separate measurements are performed. First, each MIM structure is characterized on a wafer prober with 1250 µm ground-signal (GS) probes. Subsequently, 6 MIM structures per column and row are loaded with 17 mg of tin weight and remeasured to evaluate the mechanical loading suppression technique presented in section 4.2.1. 6 MIM structures result in 3 MIM cells consisting of 2 MIM structures each, which represent a favorable configuration for the DC biasing circuitry, see appendix C.1. The second characterization measurement is performed on a 6 by 6 MIM structure interconnected macroscopic varactor. The MIM structures are interconnected using a silver filled polymer. Subsequently, the

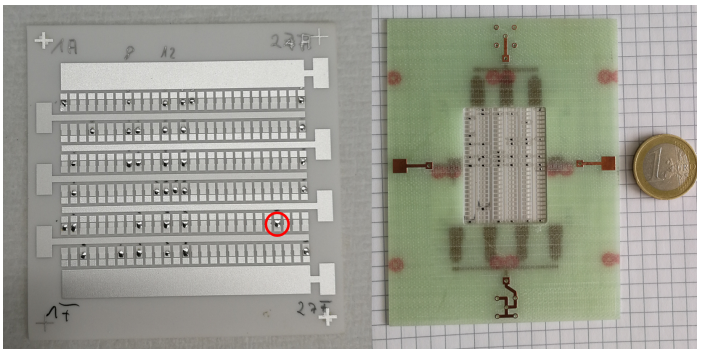

Figure C.15: The screen printed acoustically optimized varactor design with tin weights on some of the cells (left, cell marked) and the varactor design soldered to the FR4 RF/DC decoupling network (right). ©2017 IEEE.

structure is soldered to an FR4 PCB, which holds the resistive RF/DC decoupling network and placed in a measurement fixture, see section 3.1.

As described earlier, the on wafer small-signal characterization is performed on mechanically loaded and therefore suppressed MIM structures and unloaded MIM structures. A detailed description of the implemented acoustic suppression technique by mechanically loading the cells is given in section 4.2.1. Characterization is performed over a biasing voltage range from 0 V to 120 V. The results are shown in figure C.16. The unloaded MIM structures show a maximum tunability of 31 % reducing the cell capacitance from 161 pF to 114 pF. In biased state, the quality factor is increased by 31 % from 57 to 74. The unloaded cells show acoustic resonances at 15 MHz and 22 MHz. For the loaded MIM structures an identical capacitance and quality factor is measured in unbiased state while the biased capacitance is further reduced to 104 pF increasing the tunability to 35 %. In comparison to the unloaded cells, the quality factor is tuned by 30 % in the opposite direction and reduced to 43 in biased state. At the first acoustic resonance frequency of the unloaded cells, however, a significantly increased quality factor of the loaded cells is measured with 58 in comparison to 28. A maximum increase of 620 % in quality factor at the second acoustic resonance frequency is measured increasing the quality factor locally from 5 to 36.

The results for the interconnected varactor matrix consisting of acoustically suppressed and unsuppressed MIM structures is shown in figure C.17. The acoustically unsuppressed matrix shows a tunability of 41 % with a biasing voltage of 0 V to 200 V at 13.56 MHz reducing the capacitance from 104 pF to 61 pF. The quality factor in unbiased state is 60 and reduced to 57 in biased state at 13.56 MHz. In comparison to the high-power varactor design the quality factor in biased state at 13.56 MHz is significantly increased from 41 to 57 as a result of the shifted acoustic resonance at 14 MHz. For the acoustically suppressed varactor matrix the unbiased capacitance is 161 pF and shows a tunability of 47 % reducing the capacitance to 79 pF at 13.56 MHz. The quality factor is reduced by 50 % from 72 to 36. At 15 MHz the acoustically suppressed varactor matrix shows a quality factor of 55 compared to 22 of the

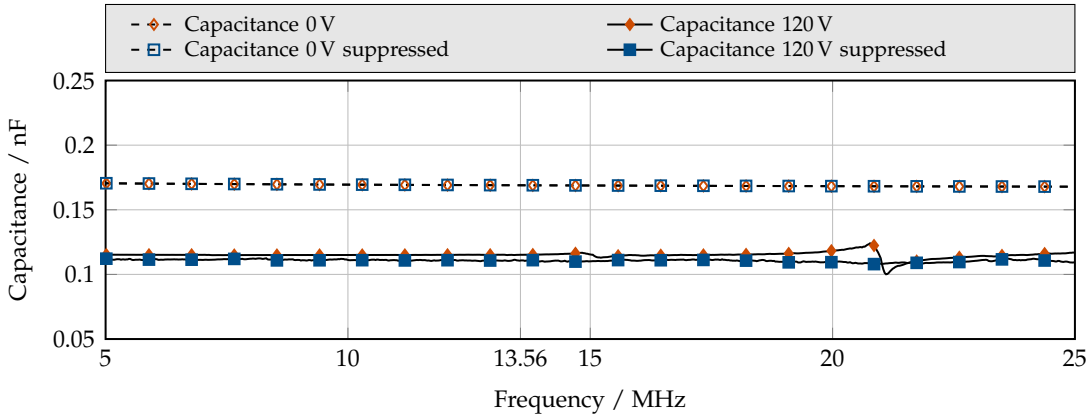

(a) Capacitance vs. frequency of the mechanically unloaded and loaded MIM structures.

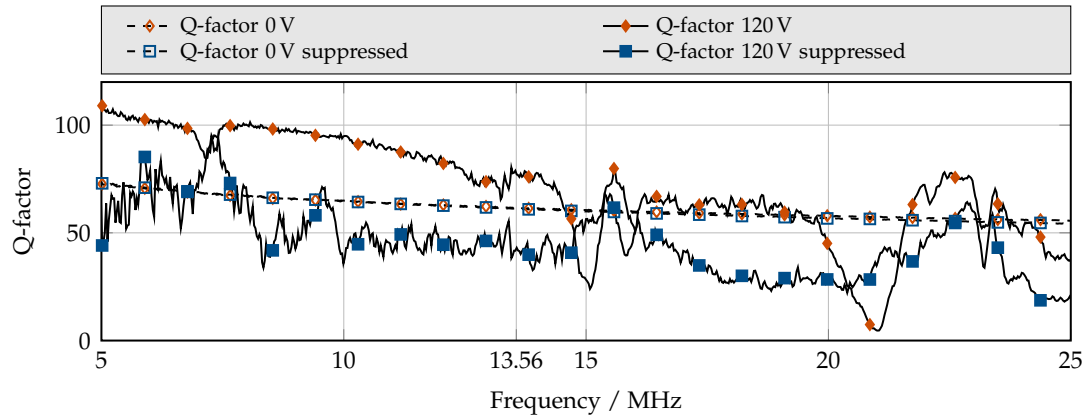

(b) Q-factor vs. frequency of the mechanically unloaded and loaded MIM structures.

Figure C.16: Small-signal characterization results of the mechanically unloaded and loaded MIM structures in regard to capacitance and Q-factor.

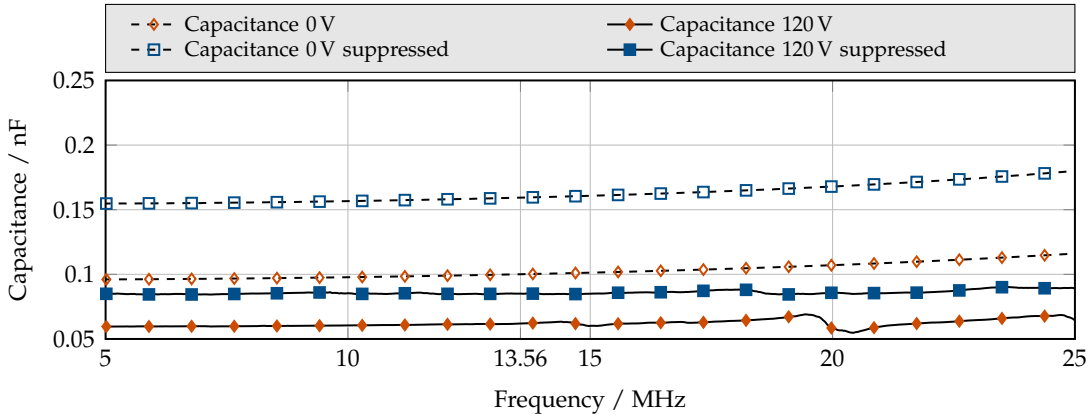

(a) Capacitance vs. frequency of an 6x6 matrix of mechanically unloaded and loaded MIM structures.

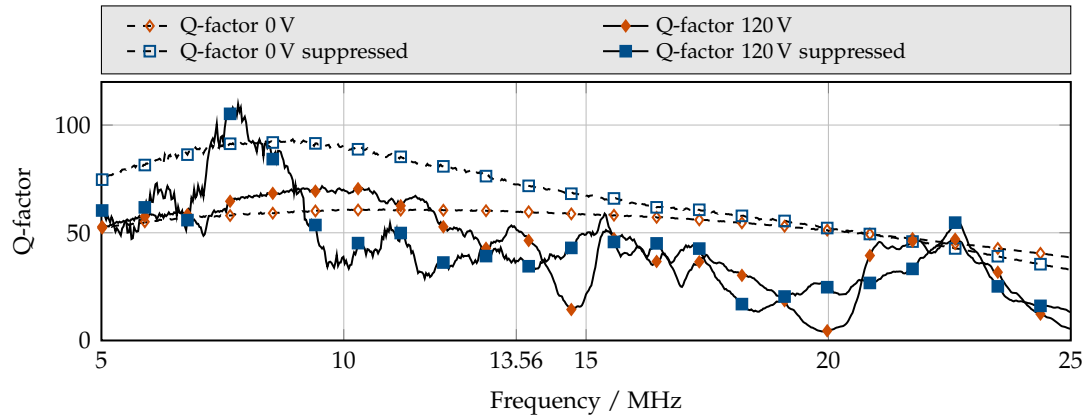

(b) Q-factor vs. frequency of an 6x6 matrix of mechanically unloaded and loaded MIM structures.

Figure C.17: Small-signal characterization results of a macroscopic varactor consisting of a 6x6 matrix of unloaded and loaded interconnected MIM structures and the RF/DC bias circuit holding FR4 PCB, to which the varactor is soldered.

unsuppressed design resulting in a significant increase of 145 %. At the second acoustic resonance frequency, the increase in quality factor of the acoustically suppressed design is 400 % from 4.8 to 24.

Large-Signal Characterization

A varactor module with 6x6 interconnected, unloaded MIM structures is characterized under high-power conditions. During characterization, no cooling is applied to the varactor. Due to the small capacitance of $\sim 160\,\mathrm{pF}$ of the varactor module, the large characterization circuit described in section 3.2 is altered. Only then, reasonable plasmalike load impedances can be matched to $50\,\Omega$ by the circuit, providing for realistic operation conditions of the DUT varactor. The series connection of C_{Vac1} and the DUT varactor is changed to a parallel connection. Then, an overall capacitance in the range of 550 pF to 650 pF in the shunt branch is achievable, similar to all other large-signal characterization setups. As a result, the varactor loading is voltage dominated with less current stresses in contrast to the setup of all other large-signal characterized varactors, which are current dominated. For the varactor itself, this is a favorable condition, due to the excessive serial stacking of 3 varactor cells between which the RF voltage is divided. A load impedance of $(2.68 + 1.25\mathrm{i})\,\Omega$ is set up for the measurement. The characterization results are depicted in figure C.18.

With increasing input power and temperature, the unbiased varactor capacitance decreases by 24 %. The biased capacitance slightly decreases by 4 %. A maximum tunability of 37 % is measured with a biasing voltage of 150 V at an input power level of 100 W, which is in good agreement with the small-signal characterization measurement indicating a maximum tunability of 47 % at room temperature. At 1 kW of input power, the varactor heats up to 38 °C independent from tuning state. The maximum dissipated power in the varactor at this power level is 12 W, resulting in a tunability of 13 %. The detailed DUT measurements during large-signal characterization for each input power level are summarized in table C.3.

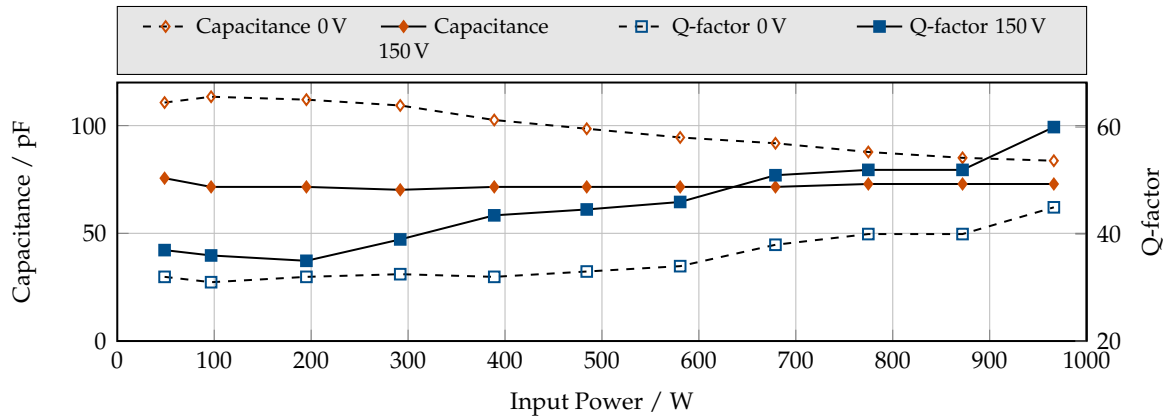

(a) Capacitance and Q-factor for various input power levels.

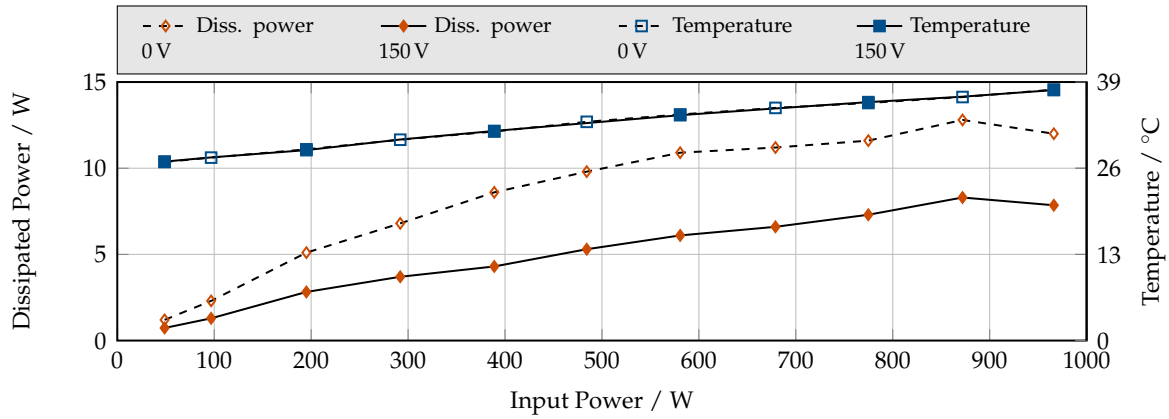

(b) Dissipated power and temperature measurements over input power.

Figure C.18: Large-signal characterization of a varactor module with 6x6 interconnected MIM structures in regard to capacitance, Q-factor, dissipated power and temperature.

Table C.3: Summary of large-signal characterization data obtained for a 6x6 MIM structure array at different RF input power levels in unbiased state.

Power level		DUT measurements						
P_{in} W	P_{out} W	V_{rms} V	I_{rms} A	$C(0\,V)$ pF	$Q(0\,V)$	τ %	P_{diss} W	T °C
48.8	44.6	65	0.4	110	32	32	1.2	27
96.7	87.4	87	0.8	113	31	37	2.3	28
195	176	125	1.2	112	32	36	5.1	29
292	264	153	1.4	109	33	36	6.8	30
389	353	177	1.6	103	32	30	8.6	32
484	440	196	1.7	99	33	27	9.8	33
581	528	215	1.8	95	34	24	10.9	34
679	619	234	1.9	92	38	22	11.2	35
775	708	249	1.9	88	40	17	11.7	36
872	797	265	2	85	40	14	12.8	37
966	885	277	2.1	84	45	13	12	38

D Appendix: Bulk Ceramic Varactors

D.1 Influence of Base Material, Dopants, Processing and Metalization on Electrical Properties

D.1.1 Base Material Evaluation

A commercially available low loss class 1 dielectric designed for high voltage AC and DC applications is evaluated [21, 22]. As a result, low electrical and thermal tunability can be expected. A loss/Q-factor of $\leq 0.002/\geq 500$ at 1 kHz is specified, confirming the classification as a class 1 dielectric. RF characterization data is not available from the manufacturer. The varactors are obtained in the described cylinderical shape without further information on the manufacturing process. Energy dispersive X-ray spectroscopy (EDX) shows a $BaTiO_3$, $CaTiO_3$ composite material with an additional mixed phase of both. Main reason for this is the adjustment of the Curie temperature. Temperature measurements indicate the Curie temperature of the material at $\sim 25\,°C$. The texture of the material is depicted in figure D.3. The varactor pellets are metalized with a not further specified silver paste in the aforementioned dimensions. Characterization is performed at 50 °C with

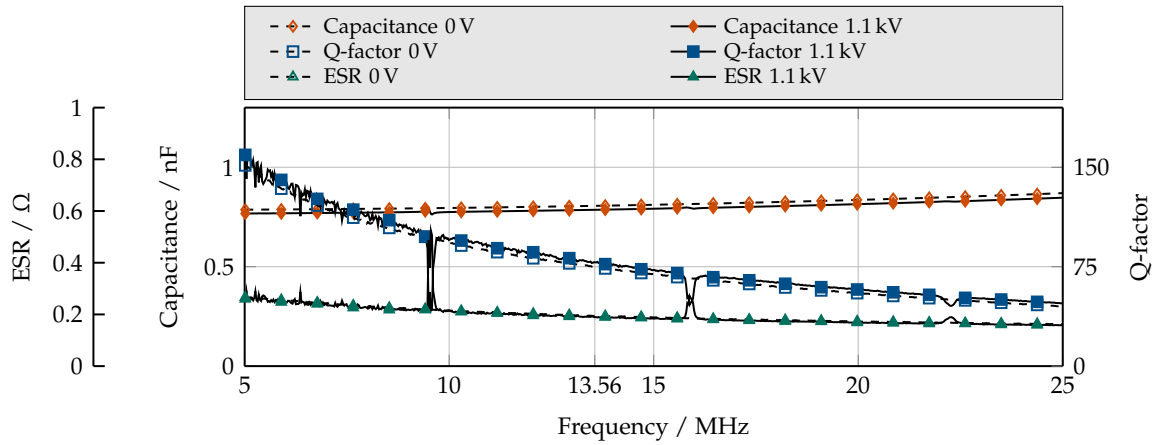

Figure D.1: C, Q and ESR of a class 1 dielectric based bulk ceramic disk varactors with silver metalization at 50 °C.

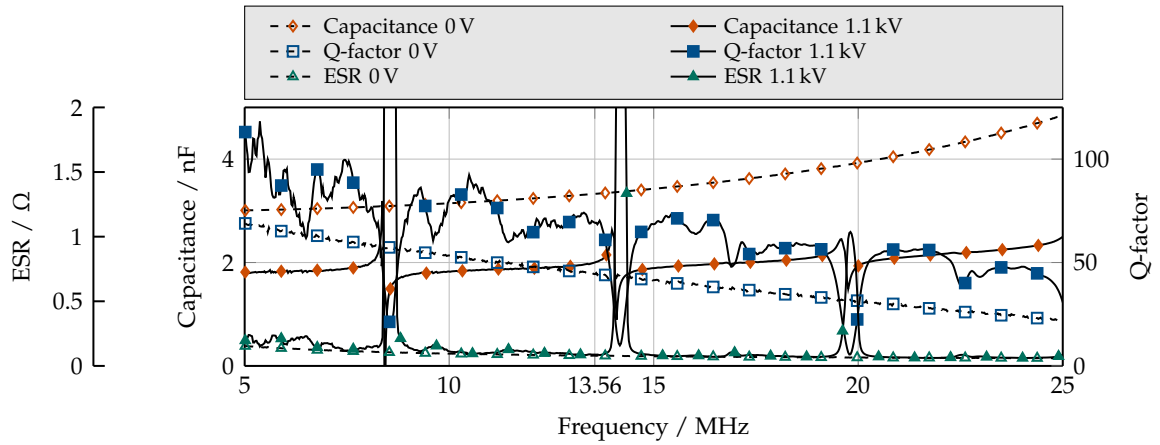

Figure D.2: C, Q and ESR of class 2 Y5U specified dielectric based bulk ceramic disk varactors with silver metalization at 50 °C.

biasing voltages up to 1.1 kV. The characterization results are depicted in figure D.1. An unbiased capacitance of 0.805 nF is measured at 13.56 MHz, decreasing by 2.5 % to 0.786 nF in biased state. A corresponding Q-factor of 75 is measured in unbiased state, increasing to 79 in biased state. The material shows acoustic activity with resonances at 9.6 MHz, 16 MHz and 22.3 MHz with a characteristic gap of 6.3 MHz between resonances.

A commercially available class 2 dielectric of specification Y5U is evaluated, see figure 2.3. Therefore, a larger electrical and thermal tunability compared to the class 1 dielectric is expected, as well as increased dielectric losses. The bulk ceramic pellets are obtained in the aforementioned dimensions and with a not further specified silver metalization. EDX data indicates single phase $BaTiO_3$ as the base material. The Curie temperature of $BaTiO_3$ is 120 °C [108]. Therefore, the characerization data of the material is obtained in the ferroelectric phase at 50 °C. As a result, the material exhibits increased hysteris losses due to spontaneous polarization, see section 2.1.1. The application of the material in an RF environment is therefore not reasonable. However, due to the established industrial manufacturing process, RF characterization on the material is performed anyway. The texture of the material is depicted in figure D.3.

The small-signal characterization results of the class 2 dielectric based disk varactors are depicted in figure D.2. At 13.56 MHz, the varactors show a significantly larger unbiased capacitance of 3.3 nF compared to class 1 dielectric, decreasing by 40 % in biased state to 2 nF. A reduced corresponding Q-factor of 44 is obtained in unbiased state, which increases by 71 % to 75 in biased state. The acoustical activity is significantly increased compared to class 1 dielectric, even impacting the capacitance trace of the measurement. Resonances are obtained at 8.4 MHz, 14 MHz and 19.7 MHz with a characteristic gap of 5.6 MHz. Additional, less intensive intermediate resonances are measured at 16.8 MHz and

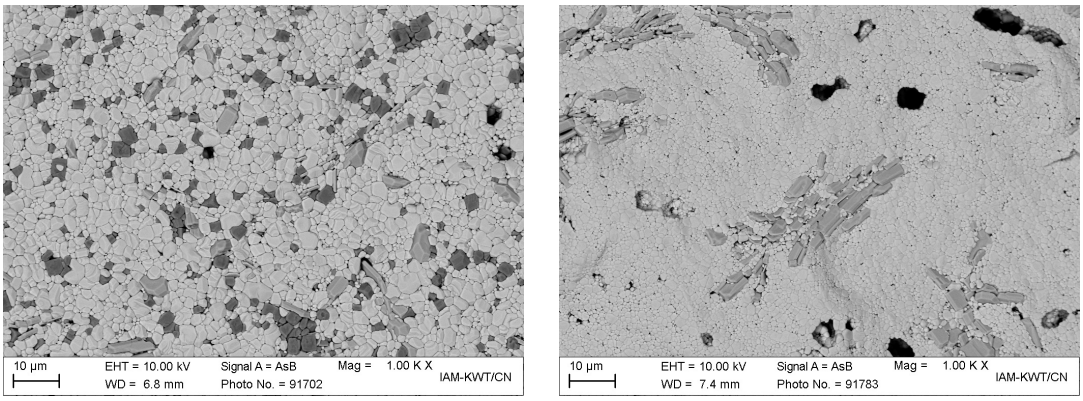

Figure D.3: SEM cross-sectional image of the texture of the class 1 dielectric (left) and the class 2 dielectric (right). Both are commercially available and manufactured in an industrial process.

22.4 MHz. Intermediate resonances are not observed in the frequency behavior of pellets based on the class 1 dielectric. Overall, the measurement results confirm the classification of both dielectric materials made by the manufacturer. However, for the application as a dielectric in a tunable high-power varactor, the class 1 dielectric lacks the required tunability (2.5 % to 40 %) and in return does not provide for significantly decreased losses compared to the class 2 dielectric (in unbiased state 41 % reduced losses, in biased state 5 % reduced losses). In general, the Q-factor of both materials is too low in regard to the expected Q-factor of bulk ceramic material taken from literature [11].

D.1.2 Influence of the Processing Routine on Electrical Properties

In regard to custom made bulk ceramics, the impact of the manufacturing process on the electrical properties of the obtained pellets is evaluated. From a large variety of manufacturing parameters of the ceramic powder as well as of the varactor pellets, the sintering temperature and duration is evaluated more closely. The reason for this is the grain size effect [97], which is known to have significant influence on the electrical behavior of a technical ceramic. Especially, the effect of giant grain growth and the creation of liquid phases in the ceramic is a source for large amorphous crystal domains, which significantly increase the permittivity, tunability but also dielectric losses of the ceramic. The suitability of this effect for the manufacturing of highly tunable bulk ceramic varactors is investigated. As a base material, custom made $Ba_{0,7}Sr_{0,3}TiO_3$ co-doped with 0.5 % manganese is set up. For sintering, three one-step and one two-step profile are applied. The exact profiles are 1250 °C for 10 h plus 1290 °C for 1 h, 1290 °C for 1 h, 1330 °C for 1 h and 1360 °C for 1 h. The ceramic texture of the obtained ceramic sintered at at 1290 °C for 1 h and at 1330 °C for 1 h are depicted in figure D.4.

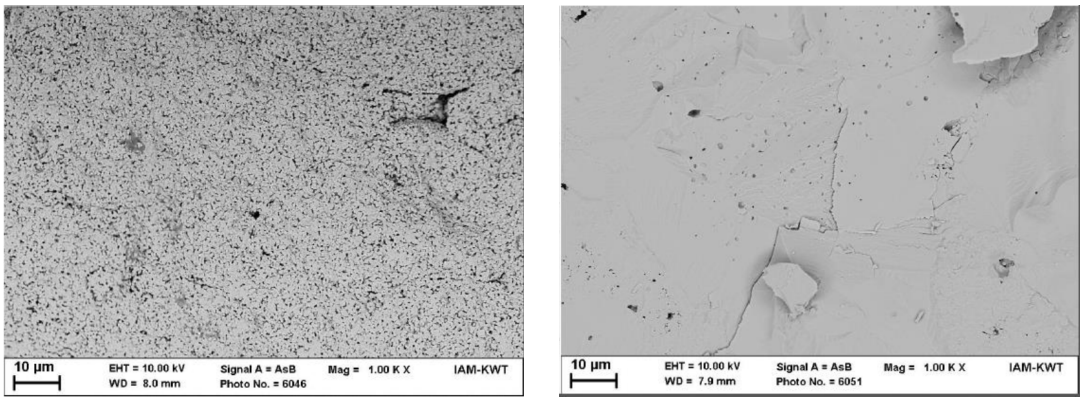

Figure D.4: SEM cross-sectional image of $Ba_{0,7}Sr_{0,3}TiO_3$ co-doped with 0.5 % manganese sintered 1290 °C for 1 h (left) and sintered at 1330 °C for 1 h (right). The images show the loss of grain texture in the pellet sintered at a higher temperature (right). Giant grain growth and liquid phases are the consequence.

A significant loss of grain texture and the introduction of giant grains and liquid phases are the consequence of the increased sintering temperature of 1330 °C. A silver metalization is applied to all pellets in a screen-printing process and the pellets are characterized at 50 °C with biasing voltages up to 1.1 kV. In figure D.5 the characterization results of the $Ba_{0,7}Sr_{0,3}TiO_3$ sintered at 1250 °C are depicted. At 13.56 MHz, the varactor shows a capacitive tunability of maximum 17.2 %, reducing the capacitance from 1.7 nF to 1.4 nF. The quality factor of 340 in unbiased state decreases by 35 % to 222 in biased state. The acoustic resonances of the pellet are measured at 7.5 MHz, 12.5 MHz and 17.3 MHz with periodic repetition in biased state, resulting in a static spacing of $\sim$ 5 MHz. Intermediate resonances occur at 9.8 MHz, 14.8 MHz and 19.7 MHz with a static periodic spacing of 5 MHz.

For the pellet sintered at 1290 °C for 1 h an unbiased capacitance of 1.5 nF and a tunability of maximum 15.8 %, reducing the capacitance to 1.3 nF in biased state at 13.56 MHz. A corresponding Q-factor of 278 is obtained in unbiased state, decreasing to 225 in biased state by 19 %. Compared to the varactor sintered at 1250 °C, these values are consistent. In regard to acoustics, characterization data shows a significantly changed behavior. Acoustic activity of the pellet is measured at 7 MHz, 12 MHz and 16.8 MHz in biased state, resulting in a static periodical spacing of $\sim$ 5 MHz. The resonances are much broader compared to the pellet sintered at a lower temperature and intermediate resonances have completely vanished. A detailed evaluation of this effect is presented in section 5.1.1.

At sintering temperatures above 1330 °C, giant grain growth and liquid phased are introduced in the ceramic texture. As a result, the electrical behavior of the pellet drastically changes. At 13.56 MHz, an increased capacitance of 5.3 nF is measured, decreasing by 31 % to 3.6 nF in biased state. An unbiased quality factor of 540 is obtained. Compared to the

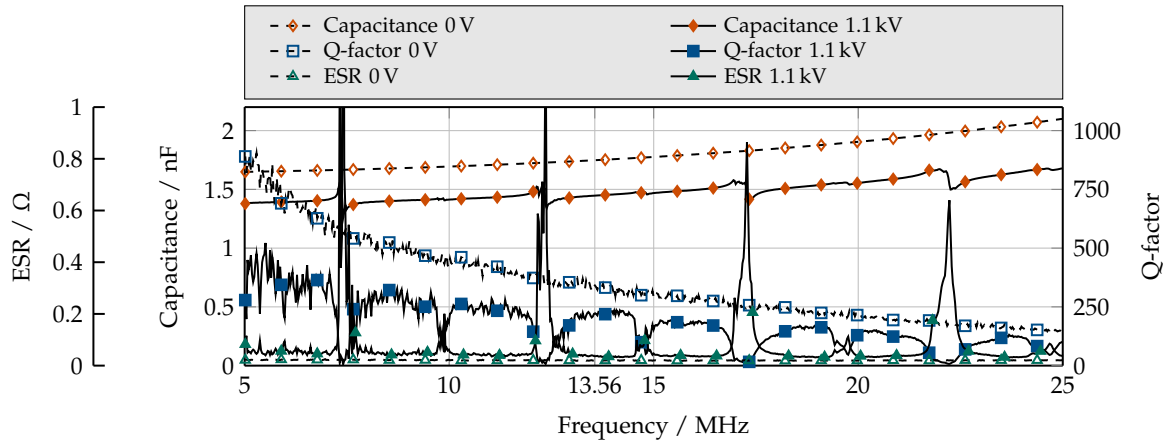

Figure D.5: C, Q and ESR of a BST based bulk ceramic disk varactor sintered at 1250 °C for 10 h. Measurement temperature 50 °C.

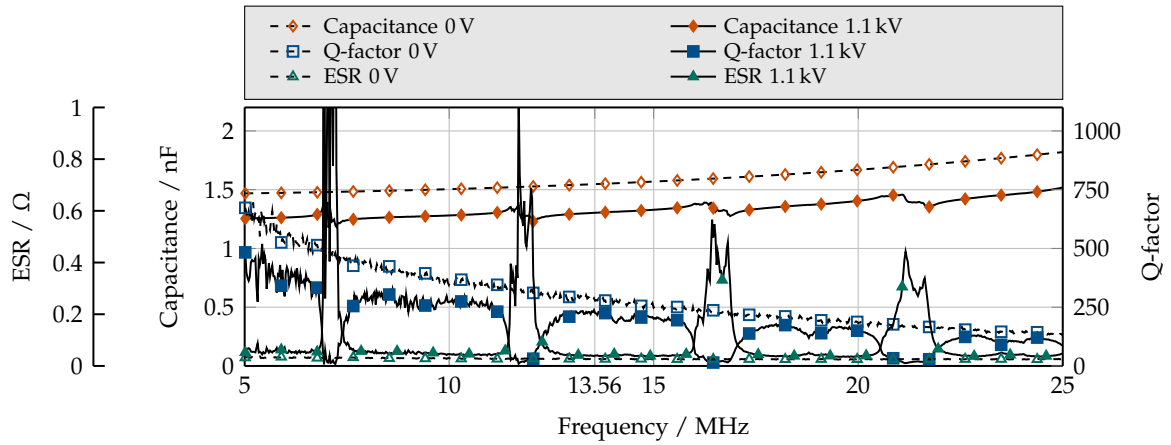

Figure D.6: C, Q and ESR of a BST based bulk ceramic disk varactor sintered at 1290 °C for 1 h. Measurement temperature 50 °C.

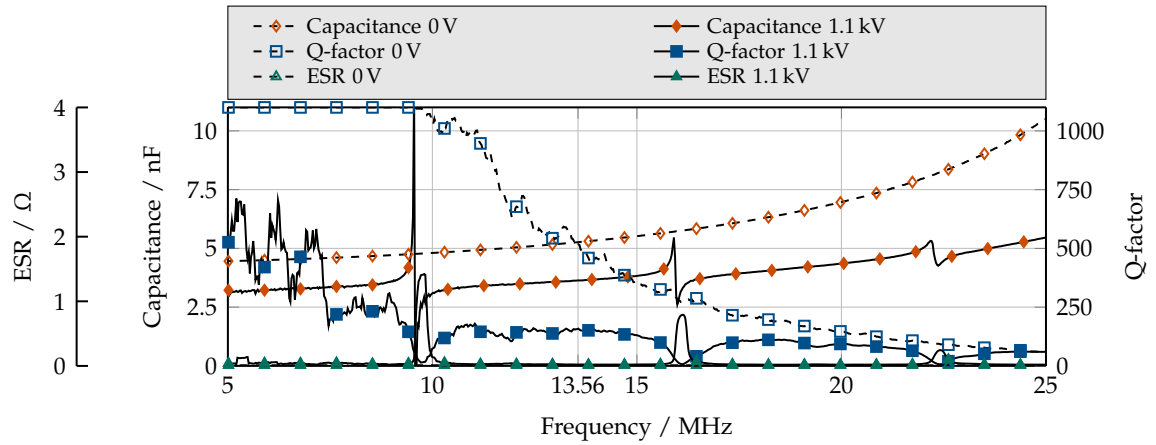

Figure D.7: C, Q and ESR of a BST based bulk ceramic disk varactor sintered at 1330 °C for 1 h. Measurement temperature 50 °C.

same base material sintered at 1290 °C, this means a decrease in ESR of 86 % from 0.028 Ω to 0.004 Ω. However in biased state, a significant decrease in Q-factor by 75 % to 134 is obtained, compared to 225 for the pellet sintered at 1290 °C. The acoustic resonances of the pellet are measured at 9.4 MHz, 16 MHz and 22.4 MHz, resulting in a static spacing of ∼ 7.4 MHz. Intermediate resonances are not measured.

For a sintering temperature of 1360 °C, the ceramic texture is indistinguishable from the one at 1330 °C. Consistently, the electrical behavior is well comparable to the one of pellet sintered at 1330 °C. The varactor introduces an unbiased capacitance of 5.6 nF and a tunability of maximum 37 %, reducing the capacitance to 3.6 nF in biased state at 13.56 MHz. A corresponding Q-factor of 660 is obtained in unbiased state, significantly decreasing to 56 in biased state by 91 %. Acoustic activity of the pellet is measured at 9.4 MHz, 15.8 MHz and 21.9 MHz in biased state, resulting in a static periodical spacing of ∼ 5.4 MHz.

Overall, a significant impact of sintering time on the electrical behavior is observed. For the intended application in combination with the presented manganese co-doped base material $Ba_{0,7}Sr_{0,3}TiO_3$, a sintering time of 1290 °C for 1 h appears to be advantageous compared to the others. The pellets introduce an acceptable high Q-factor in unbiased state with only a slight decrease in biased state. The acoustical behavior of the pellet is significantly improved compared to pellets sintered at 1250 °C. For pellets sintered at temperatures >1330 °C, giant grain growth and liquid phases in the ceramic texture are observed, as proclaimed. The intended significant increase in permittivity and tunability as well as reduced dielectric zero-bias losses are also obtained with this set up. In unbiased state, the pellets show Q-factors larger than any other material evaluated within the scope of this work. In biased state, however, the structure is prone to acoustic resonance excitation, as the scattering boundaries between grains are removed by giant grains and liquid phases. As a result,

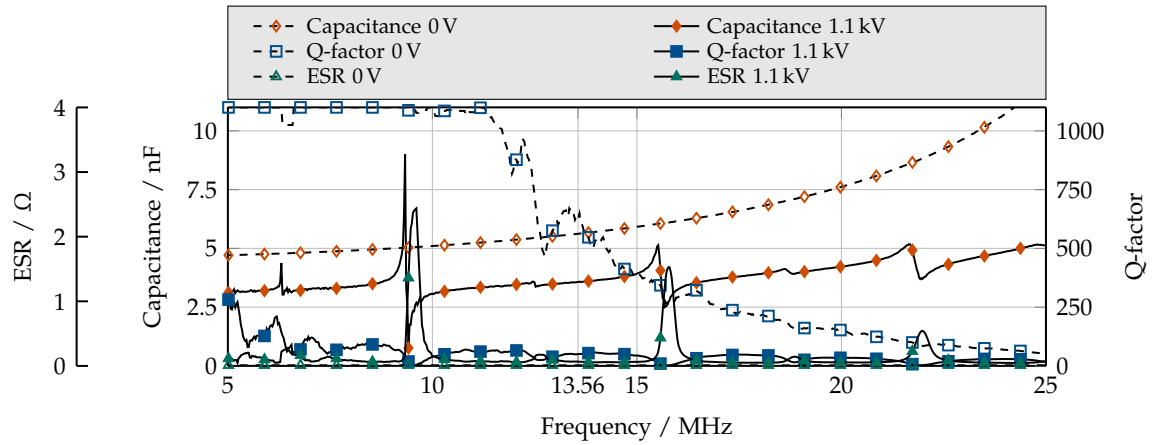

Figure D.8: C, Q and ESR of a BST based bulk ceramic disk varactor sintered at 1360 °C for 1 h. Measurement temperature 50 °C.

the Q-factor significantly deteriorates in biased state, rendering them unsuitable for the intended application.

In figure D.9, the characterization results of a custom made $Ba_{0,7}Sr_{0,3}TiO_3$ based ceramic are presented. The ceramic is 0.5 % manganese co-doped and sintered at 1315 °C for 1 h. A relative density of 92.6 % is obtained with a d_{50} diameter of 2 µm. The ceramic texture contains isolated giant grains, indicating a too high sintering temperature. The pellets are metalized by hand with a stencil. A commercially available silver paste is utilized. The texture of the material is depicted in figure D.10.

At 13.56 MHz, the varactors show an unbiased capacitance of 2.3 nF, decreasing by maximum 17 % in biased state to 1.9 nF. A corresponding Q-factor of 237 is obtained in unbiased state, which decreases by 16 % to 198 in biased state. The acoustical activity impacts the capacitance trace of the measurement. Resonances are obtained at 9.7 MHz, 16.1 MHz and 22.5 MHz with a characteristic gap of 6.4 MHz. Intermediate resonances are not observed.

D.1.3 Influence of Dopants on Electrical Properties

Dopants play an important role in the processing of technical bulk ceramics. Small amounts of up to 1 % not only significantly alter the processing parameters, such as required sintering time and temperature, but also influence the electrical parameters of the ceramic. Dopants, known to have impact on the electrical parameters, are among others copper, iron, nickel, magnesium and flour [14, 109, 110, 111, 112, 113]. Electrical parameter alteration includes the reduction of dielectric losses, reduced thermal dependency of the permittivity, increased electrical tunability and reduced electrical conductivity. In this work, doping is performed

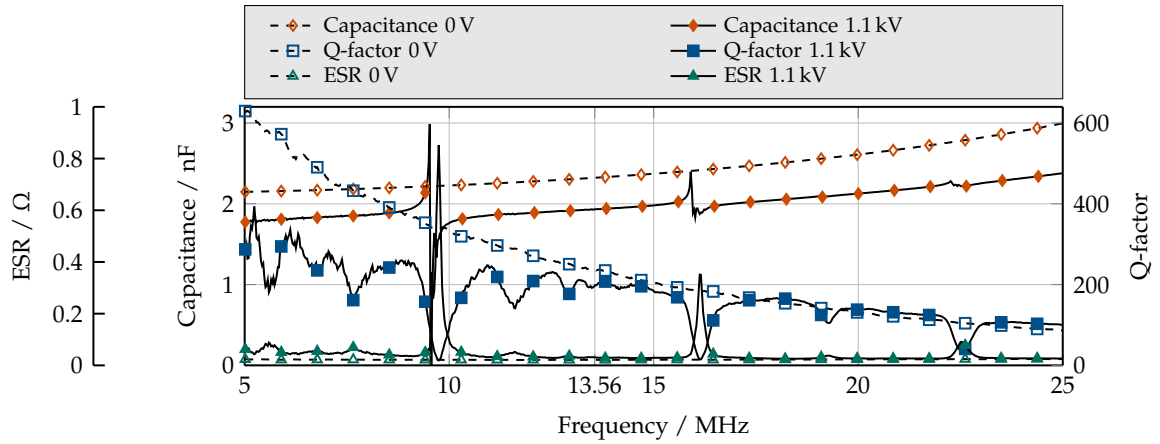

Figure D.9: C, Q and ESR of $Ba_{0,7}Sr_{0,3}TiO_3$ based bulk ceramic disk varactors with silver metalization at 50 °C.

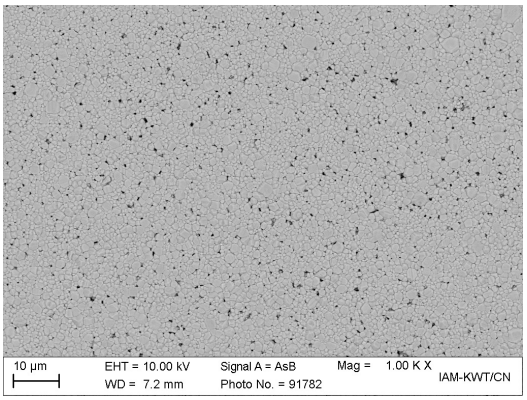

Figure D.10: SEM cross-sectional image of the texture of $Ba_{0,7}Sr_{0,3}TiO_3$. The ceramic is processed in a laboratory environment.

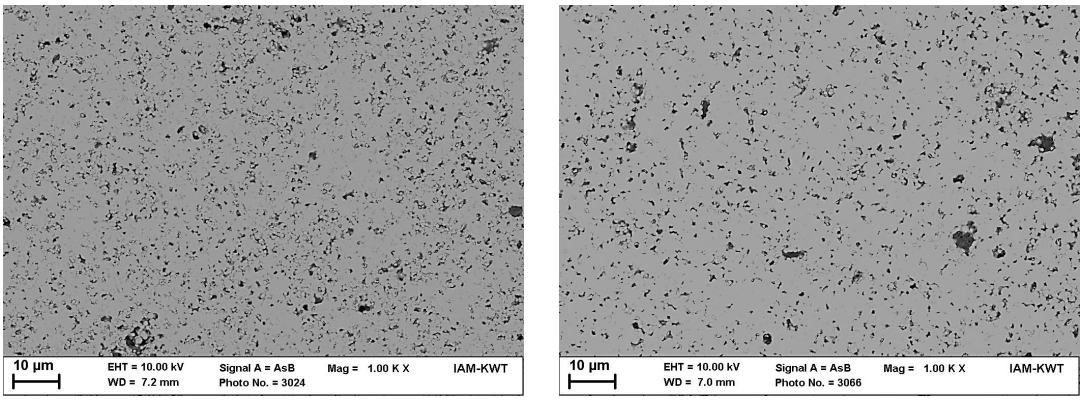

Figure D.11: SEM cross-sectional image of the texture of a 1 % Iron co-doped (left) and 0.5 % manganese co-doped (right) BST bulk ceramic.

to reduce the dielectric losses of the ceramic during RF operation. Iron and flour are known to have that influence on the ceramic and are therefore used in the scope of this work. A significant drawback of iron is its ferromagnetic nature. In combination with the intended RF application, the contamination of bulk ceramic pellets with elemental iron is of concern, as it will result in significantly increased dielectric losses. In a laboratory environment with small numbers of produced pellets, the risk of contamination is acceptable. For an industrialized process, however, an alternative for iron is required. Therefore, manganese as a dopant is evaluated and compared to iron in regard to the resulting electrical differences of the obtained bulk ceramic pellets. Manganese is a paramagnetic metal with similar properties compared to iron [114]. Both base materials are $Ba_{0,7}Sr_{0,3}TiO_3$ based with a silver metalization and sintered at 1250 °C for 1 h. The obtained ceramic compound is depicted in figure D.11.

Both ceramic textures look similar in regard to porosity, density and inclusion of larger pores. The grain sizes are slightly increased for the manganese doped ceramic with a d_{50} diameter of 1.2 µm compared to 1 µm for the iron doped ceramic.

The varactor pellets are characterized, utilizing the presented fixture in section 3.1.3. A temperature of 50 °C is setup for the pellet and characterization is performed from 5 MHz to 25 MHz with a biasing voltage of 1.1 kV. For the iron doped ceramic, the characterization results are depicted in figure D.12. At 13.56 MHz, the varactor shows a capacitive tunability of maximum 6.2 %, reducing the capacitance from 1.3 nF to 1.2 nF. The quality factor of 300 in unbiased state drops by 49.2 % to 152 in biased state. The acoustic resonances of the pellet are measured at 8 MHz, 13.1 MHz and 18.3 MHz in biased state, resulting in a static spacing of $\sim$ 5.1 MHz. For the iron doped pellet, no intermediate resonances are observable. For the manganese doped ceramic, the characterization results are depicted in figure D.13. At 13.56 MHz, the varactor shows an increased capacitive tunability of maximum 21.4 %, reducing the capacitance from 2.2 nF to 1.8 nF. The reduced quality factor of 180 in unbiased state drops by 34.6 % to 118 in biased state. The acoustic resonances

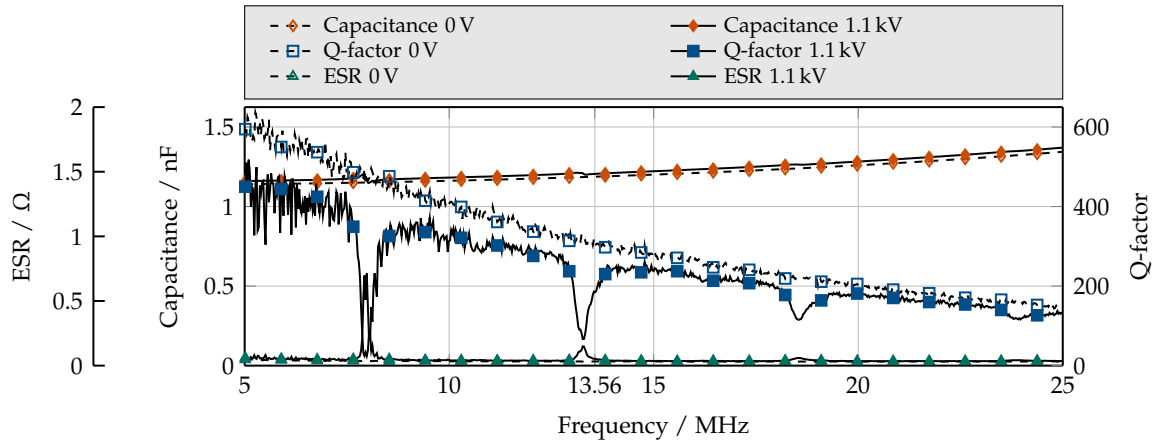

Figure D.12: C, Q and ESR of a BST based bulk ceramic disk varactor with 1 % iron dopant and silver metalization at 50 °C.

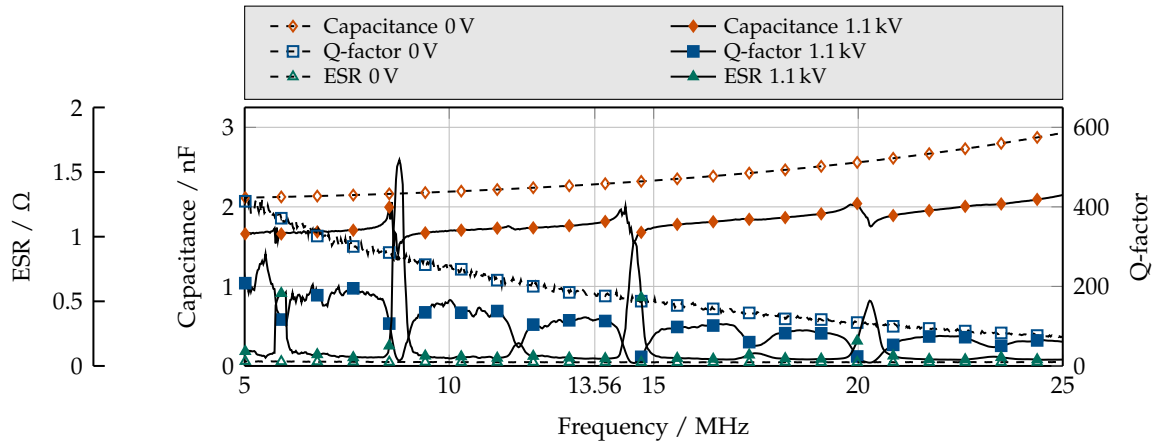

Figure D.13: C, Q and ESR of a BST based bulk ceramic disk varactor with 0.5 % manganese dopant and silver metalization at 50 °C.

of the pellet are measured at 8.7 MHz 14.4 MHz and 20.2 MHz in biased state, resulting in a static spacing of $\sim$ 5.8 MHz. Intermediate, less intensive resonances are measured at 11.5 MHz, 17.4 MHz and 23.2 MHz, resulting a static spacing of 5.9 MHz. Compared to the iron doped pellet, the main acoustic resonances appear to be more intense for the manganese doped one. An increase in ESR larger than 4 Ω is measured compared to less than 1 Ω for the iron doped varactor. The acoustically unaffected capacitance spectrum of the iron doped varactor has completely disappeared for the manganese doped pellet. From an electrical point of view, the manganese doping results in completely different properties of the varactor. An increased tunability is obtained, comparable to the effect of copper doping. Especially, the desired reduced dielectric losses are not obtained with the doping and additionally, the acoustically behavior of the pellet is significantly deteriorated.

D.1.4 Influence of the Metalization on Electrical Properties

Bulk ceramic disk varactors are integrated on a printed circuit board, holding the DC biasing circuitry and providing for RF and DC connectors. For that, two different metalizations are evaluated. Copper as a metalization paste is less common than silver pastes, due to its incompatibility to most semiconductor processes [115]. In last couple of years, however, progress has been made to overcome this incompatibility and bring forth low cost copper based pastes. In the scope of this work, the electrical properties of a commercially available Y5U specified class 2 dielectric material are measured, metalized with a silver and copper paste. The choice fell on this particular base material due to its well established industrial manufacturing process, resulting in a high reproducibility of the electrical, mechanical and thermal quantities of the pellets. As a result, it is guaranteed that the influence of the metalization on the electrical properties is very well isolated and therefore comparable. A SEM cross-sectional image of both metalizations is given in figure D.14. The measurement results for silver metalized varactor are depicted in figure D.15.

At 13.56 MHz, the varactor shows a capacitive tunability of maximum 44.6 %, reducing the capacitance from 3.7 nF to 2.2 nF. The quality factor of 41.5 in unbiased state increases by 59 % to 66 in biased state. The acoustic resonances of the pellet are measured at 8.7 MHz, 14.6 MHz and 20.5 MHz in biased state, resulting in a static spacing of $\sim$ 5.9 MHz.

The characterization results of the copper metalized pellet are depicted in figure D.16. The varactor shows an unbiased capacitance of 3.5 nF and a tunability of maximum 36.6 %, reducing the capacitance to 2.2 nF in biased state at 13.56 MHz. A corresponding Q-factor of 50 is obtained in unbiased state, increasing to 70.5 in biased state by 40 %. Acoustic activity is measured at 8.7 MHz, 14.6 MHz and 20.4 MHz in biased state, resulting in a static spacing of $\sim$ 5.9 MHz. The characterization results of both metalizations are very well comparable. The slightly decreased tunability of the copper metalized pellet is attributable to a decreased temperature of 48 °C during the measurement. In regard to Q-factor, the silver metalized pellet shows a 17 % decrease in unbiased state and 6 % in biased state, indicating a similar electrical conductivity compared to the copper paste. Drawback of the

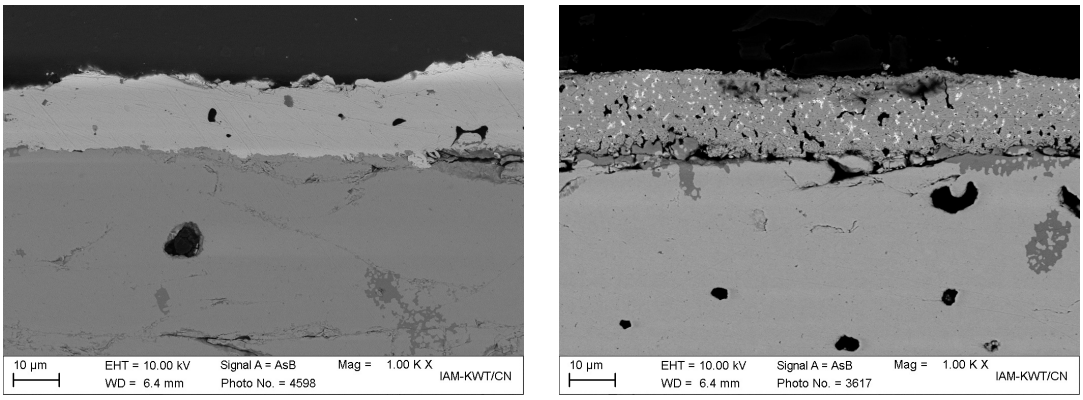

Figure D.14: SEM cross-sectional image of the silver (left) and copper (right) based metalizations applied to a class 2 dielectric based varactor pellet.

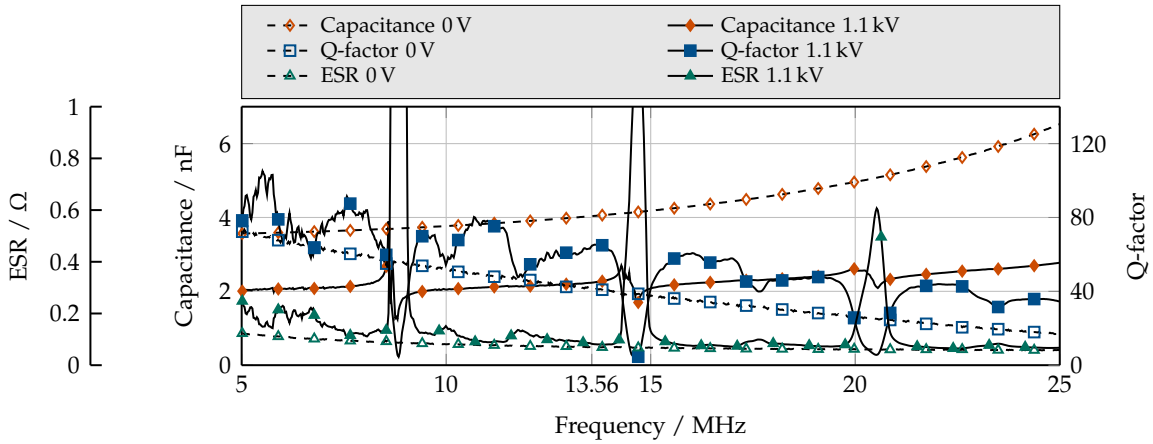

Figure D.15: C, Q and ESR of a BST based bulk ceramic disk varactor with silver metalization at 50 °C.

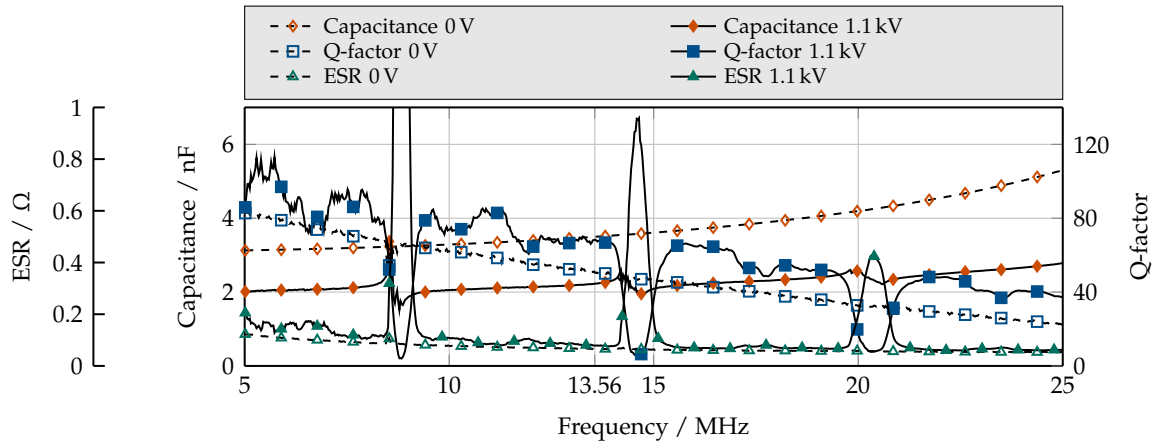

Figure D.16: C, Q and ESR of a BST based bulk ceramic disk varactor with copper metalization at 50 °C.

performed characterization is the overall low Q-factor of both samples, attributed to the utilized base material. The measurement results are dominated by the losses of the dielectric, which mask the losses of the metalization. In this particular case, the choice of metalization paste does not affect the Q-factor of the obtained disk varactors. However, when applied to a low loss bulk ceramic dielectric, metalization losses may become dominant and mainly impact the Q-factor of the pellets.

D.2 Acoustical Evaluation

D.2.1 Impact of Mechanical Parameters on the Acoustical Behavior

One indirectly accessible parameter, which is impacting the acoustical behavior of a bulk ceramic disk varactor, is the density ρ of the pellet. It can be altered by the manufacturing process and in particular, the sintering temperature and duration, see section 5.1.2 and [116]. From an electrical point of view, the highest possible density and lowest possible porosity of the pellet is desirable, as the probability for partial discharges due to the high DC biasing field strength in pores and irregularities is decreased. The sintering temperature and duration are defined prior to the large scale manufacturing process and tailored to a particular composition and amount of basic ingredients. As a result, the material development process for a certain set of electrical and mechanical parameters can be lengthy. In addition, it is possible that the developed manufacturing process deviates from its predefined parameters over time, resulting in altered electrical and mechanical properties of the obtained bulk ceramic. Therefore, a $\pm$ 20 % parameter variation is performed on the density of a bulk

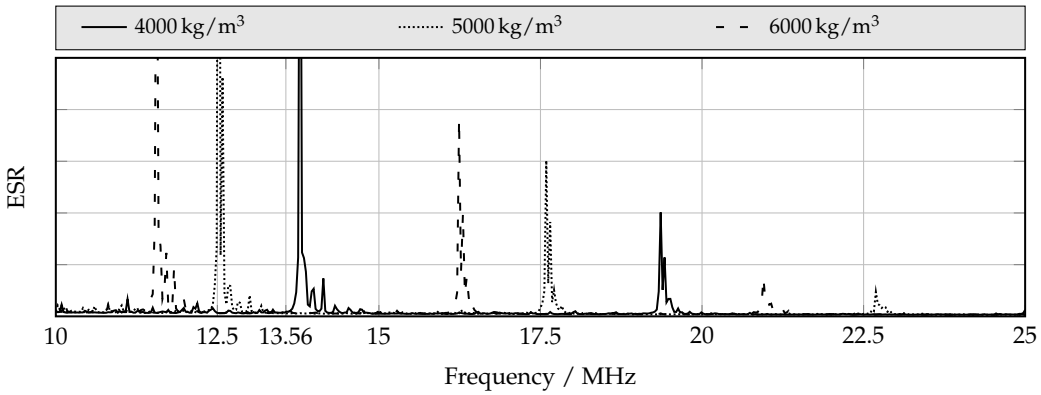

Figure D.17: Simulated impedance spectrum for ±20 % variation on norm density ρ of 5000 kg/m^3 and an elastic compliance s_{33} of 8.57 TPa^{-1}.

ceramic pellet, to evaluate its impact on the acoustical behavior. The average density for a $Ba_{0,7}Sr_{0,3}TiO_3$ based ceramic disk varactor with 0.5 % manganese is 5000 kg/m^3. The simulation is performed with the model depicted in figure 5.1. The result of the simulation in regard to ESR is depicted in figure D.17.

With increasing density, the acoustic resonances are shifted towards lower frequencies. The reason for this is the decreasing sound velocity with increasing density according to:

$$c^{(a)} = \sqrt{\frac{E_{\mathrm{lo}}^{(m)}}{\rho}} \tag{D.1}$$

with Young's modulus $E_{\mathrm{lo}}^{(m)}$ in longitudinal direction [117]. A reduction of ESR at the acoustic resonance is visible with decreasing density, as a result of the increasing mechanical Q-factor of the system:

$$Q^{(m)} = \frac{\sqrt{m \cdot B}}{D^{(m)}} \tag{D.2}$$

with mass m, spring constant B and mechanical dampening factor $D^{(m)}$. The mechanical Q-factor is defined as the ratio of stored kinetic energy to dissipated energy [15]. In conclusion, as an increased density is favorable in electrical regard, it proves to be unfavorable in an acoustical regard. A 20 % deviation of the pellets density results in a 11 % shift in frequency. Overall, density is verified as a critical parameter to the acoustical behavior of bulk ceramic disk varactors. However, the applied parameter variation of 20 % can be assumed as a worst case scenario.

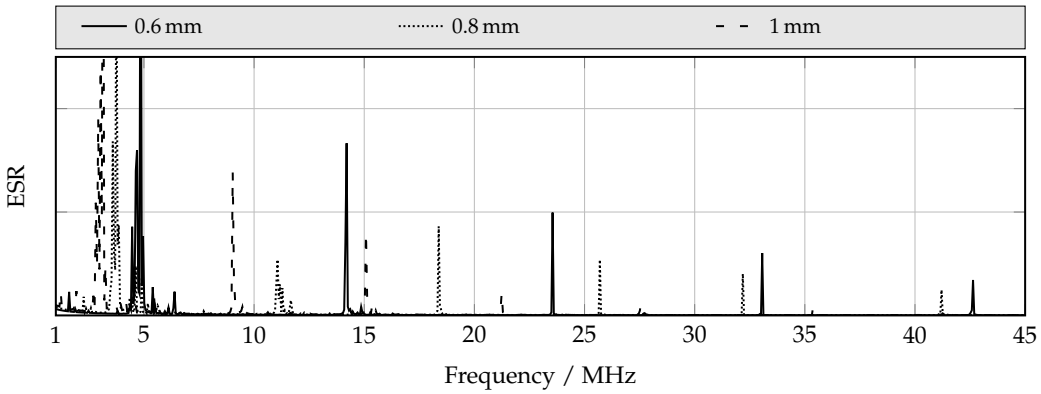

Figure D.18: Simulated impedance spectrum for several BST thicknesses.

D.2.2 Impact of Geometrical Parameters on the Acoustical Behavior

As well as the density, the geometrical dimensions of the disk varactor impact its acoustical behavior. In contrast to the density, however, they are accessible to the design process in more simple way. Therefore, they can be used to compensate for an unfavorable location of the resonances due to less accessible parameters of the pellet, such as density or elastic compliance. To evaluate the impact of each geometrical parameter a piezoelectric simulation is set up and the results are verified with measurements on specifically manufactured disk varactors. Altered geometrical parameters include the BST thickness, electrode thickness and diameter. The pellet diameter is not subject to change, as it is predefined by the required capacitance range for the application. In the scope of this work, the bulk ceramic pellets are employed on a CBIVM. Thereby, due to the mechanical constraints, the vibration capabilities of the pellet are altered. As a result, a varied acoustical behavior of the pellets can be assumed. To verify the assumption, a pellet is mechanically loaded with brass weights, soldered single sided and double sided to the metalization, simulating altered mechanical constraints. The basic model used for the simulation is depicted in figure 5.1. The thickness of a $BaTiO_3$ based, Y5U specified ceramic is altered in the range of 0.6 mm to 1 mm. The results of the simulation and measurement for different BST thickness are depicted in figure D.18. In figure D.19, measurement data is presented with an extended frequency range from 1 MHz to 45 MHz.

Simulation and measurement results are in good agreement. The change in thickness of the pellet results in a significant variation of the acoustic resonance locations. From the simulated and measured ESR spectrum in the range from 10 MHz to 25 MHz no decisive trend between thickness and location of the resonances is visible. Therefore a filtered measurement from 1 MHz to 45 MHz is added, see figure D.19. Filtering of the data is necessary as it is loaded with heavy noise in the lower frequencies as a result of the ESR hitting the lower limit of the measurement capabilities of the impedance analyzer. A moving average filter with a length of 10 is used to suppress the noise. The data shows a first acoustic

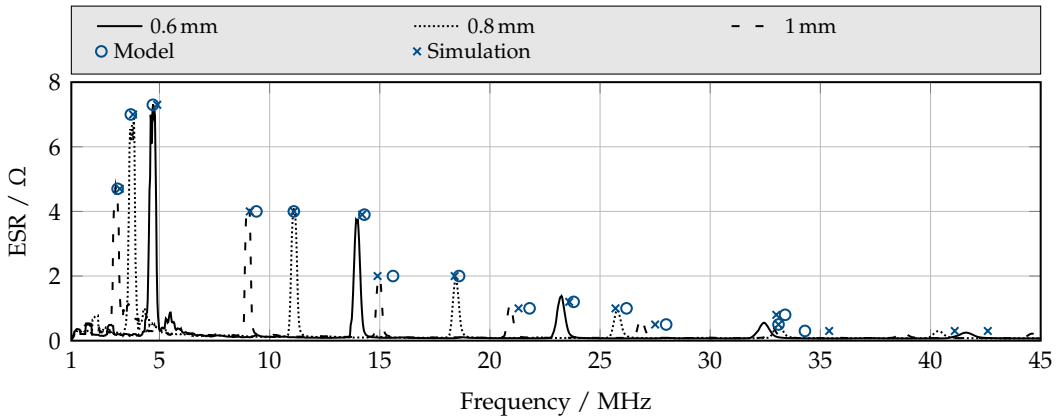

Figure D.19: Measured impedance spectrum for several BST thicknesses. Marked are the resonances obtained from the acoustic model and piezoelectric simulation in section 5.1.1.

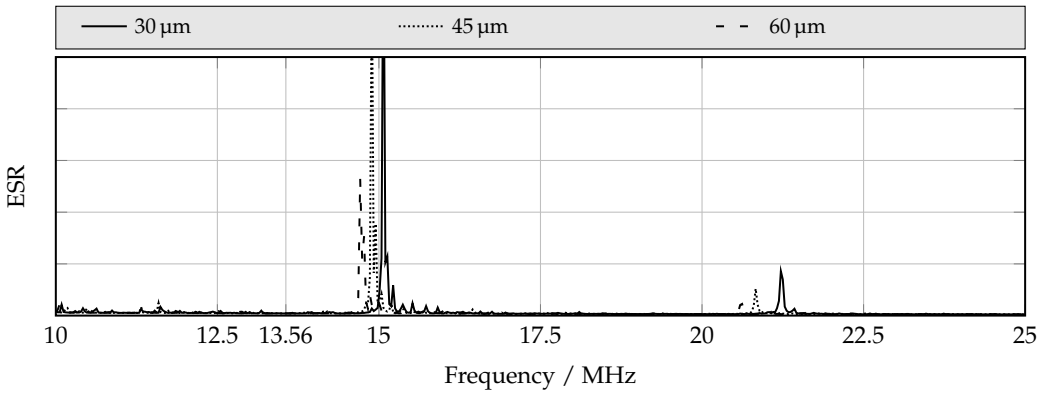

Figure D.20: Simulated impedance spectrum for several electrode thicknesses. Electrode diameters of 11 mm and 10 mm are chosen for the top and bottom electrode.

resonance of the pellet with a thickness of 1 mm at 2.9 MHz, followed by the 0.8 mm pellet at 3.9 MHz and 0.6 mm pellet at 4.9 MHz. A static gap between resonances of 6.2 MHz, 7.3 MHz and 9 MHz is obtained for the 1 mm, 0.8 mm and 0.6 mm pellet, respectively. With increasing resonance frequency, all resonances lose in ESR magnitude.

The simulation results for a variation of the electrode thickness in a range of 30 µm to 60 µm are depicted in figure D.20. The results indicate a shift of the resonance locations towards lower frequencies with increasing electrode thickness. A reduction in ESR is observed with increasing thickness, attributable to the increased mass of the top and bottom electrode, resulting a higher mechanical loading which is known to damp acoustic resonances, see section 4.2.1. A similar result is conceivable with an increase in metalization density. In conclusion, with the electrode thickness a parameter is identified, possibly improving the acoustical behavior of a pellet by damping acoustical resonances.

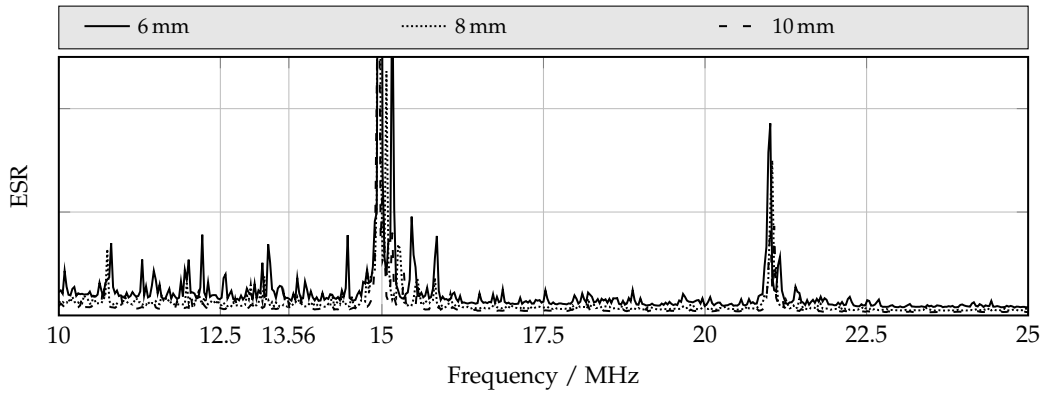

Figure D.21: Simulated impedance spectrum for several electrode diameters of the smaller electrode. The larger electrode always has a diameter of 11 mm.

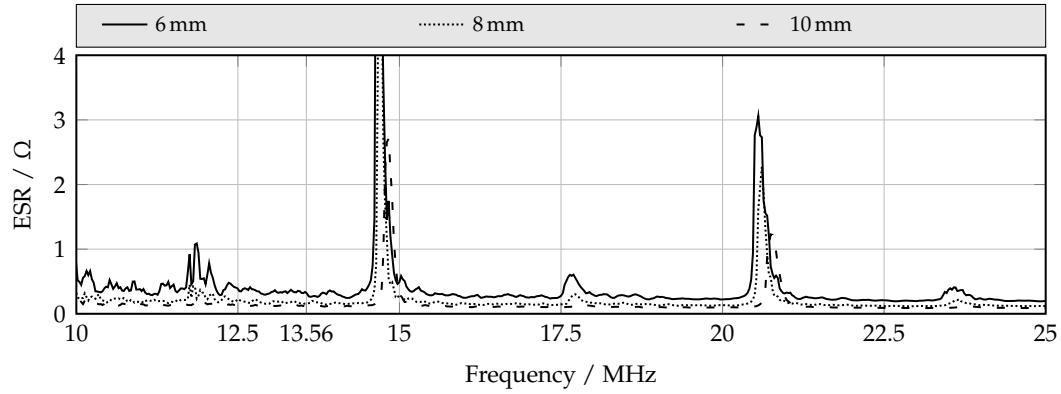

Figure D.22: Measured impedance spectrum for several electrode diameters of the smaller electrode. The larger electrode always has a diameter of 11 mm.

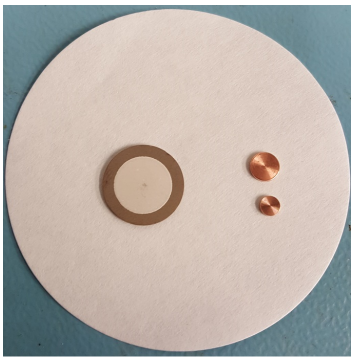

(a) 3D view of the piezoelectric pellet model utilized to estimate the acoustic behavior.

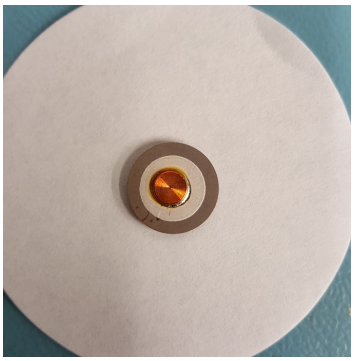

(b) 2D cut plane view of the pellet model.

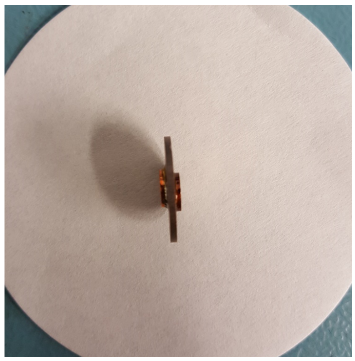

(c) 2D cut plane view of the pellet model.

Figure D.23: Fundamental bulk ceramic disk varactor model utilized for the piezoelectric simulations.

The electrode diameter is evaluated with an acoustic simulation and a verification measurement on a class 2 dielectric based disk varactor. The electrode diameter is altered in a range from 6 mm to 10 mm. The simulation and measurement results are depicted in figure D.21 and figure D.22, respectively. Simulation and measurement result are in good agreement in regard to the main resonances. Intermediate resonances, visible in the measurement are not included in the simulation result. This issue is further investigated in the next subsection. The electrode diameter impact on the location of the acoustic resonances is negligible. In the simulation, as well as the measurement, the resonances are shifted by less than 200 kHz towards higher frequencies with increasing electrode diameter. As a result, it is identified as a possible parameter for adjusting the disk varactor zero-bias capacitance without influencing its acoustical behavior. To evaluate the influence of integrating the varactors on a PCB on the acoustical behavior, the pellets mechanical degrees of freedom are restricted in longitudinal direction of the acoustic wave. For that, brass weights are soldered to the metalization of the pellet, see figure D.23. The applied brass weight type has a diameter of 6 mm and a thickness of 1 mm, resulting in a total mass of 0.25 g. The ESR spectrum of the pellet with a single brass weight applied to one side is obtained, as well as the spectrum of the pellet loaded with a brass weight on each side. The result of the measurement is depicted in figure D.24.

The measurement results generally agree with the simulation results evaluating the impact of the electrode thickness on the acoustical behavior depicted in figure D.20, both mechanically loading the disk varactor. In regard to electrode thickness, a not negligible impact on the acoustical behavior is obtained in the simulation, by a relocation of the resonances towards higher frequencies with decreasing electrode thickness. The measurement results for the loaded and unloaded pellet, depicted in figure D.24, show a slight relocation of the acoustical resonances towards higher frequencies, however, load induced broadening

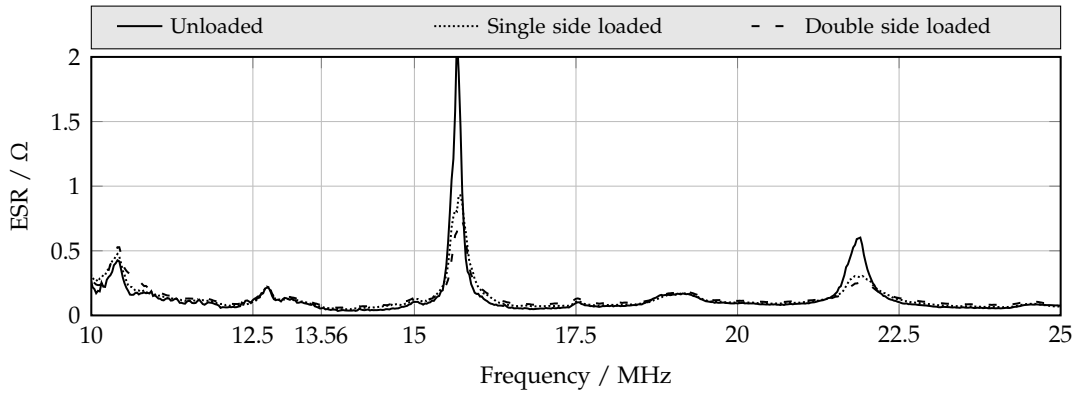

Figure D.24: Measured impedance spectrum of a mechanically unloaded, single side loaded and double side loaded bulk ceramic varactor pellet. The pellets base materials is 0.5 % manganese co-doped $Ba_{0,7}Sr_{0,3}TiO_3$ sintered at 1360 °C.

of the resonance peaks masks the effect largely. A significant decrease in ESR amplitude with increased loading is obtained, in full agreement with the simulation and the presented theory in section 4.2.1. The lower than expected relocation of the resonances is considered beneficial for integrating the bulk ceramic pellets with a mechanically constraining PCB. If this was not the case, the bulk ceramic disk varactors acoustical behavior had to be adjusted for the implementation on a PCB, making the design process significantly more complex.

Symbols and Abbreviations

χ_e	Electrical susceptibility
Δ	Laplace operator
Γ	Reflection coefficient
γ	3rd Townsend coefficient
λ	Wave length
μ_0	Magnetic vacuum permeability
∇	Nabla operator
ν	Poisson ratio
ω	Angular frequency
ω_0	Resonance frequency
φ	Electrical potential
Φ_0, Φ_{+-}	Energy to reorient a single dipole, Energy to reorient a dipole from + to - and vice versa
Ψ	Helmholtz free energy
ρ	Density
$\sigma^{(e)}$	Electrical conductivity
$\sigma^{(m)}$	Mechanical stress
τ	Tunability
Al_2O_3	Alumina
$BaSrTiO_3$	Barium strontium titanate (BST)

$BaTiO_3$	Barium titanate
B_2O_3	Boron trioxide
H_3BO_3	Boric acid
$SrTiO_3$	Strontium titanate
$\tan\delta$	Electrical loss factor
$\varepsilon^{(m)}$	Mechanical strain
ε_0	Electrical vacuum permittivity
ε_r	Electrical relative permittivity
A	Area
A, B	Gas specific constants
a^T	Electrostriction coefficient at constant temperature
B	Spring constant
b	Friction coefficient
C	Capacitance
$c^{(a)}$	Sound velocity
d	Piezoelectric coupling factor
$D, \vec{D}$	Electrical flux density
$D^{(m)}$	Mechanical dampening factor
e	Apparent piezoelectric coupling factor (from electrostriction)
$E, \vec{E}$	Electrical field strength
$E^{(m)}$	Young's modulus
$E_C, \vec{E}_C$	Coercive field strength
f	Frequency
$F, \vec{F}$	Force

G	Gibbs free energy
g	Piezoelectric stress, gap width
J	Electrical current density
$k, \vec{k}$	Circular wave number, wave vector
k_b	Boltzmann constant
L, l	Length, distance between plates in a parallel plate capacitor
m	Mass
N, N_+, N_-	Number of (total/positive/negative) cells
p	Gas pressure
$P, \vec{P}$	Electrical polarization
p_0	Dipole moment
$P_\mathrm{R}, \vec{P}_\mathrm{R}$	Reminiscent polarization
$P_s, \vec{P}_s$	Saturation polarization
Q	Electrical quality factor
q	Electrical charge
$r, \vec{r}$	Displacement
S	Entropy
S	Sensitivity of the LC transient measurement circuit
s	Elastic compliance
s_i	Dipole direction
T	Temperature
t	Time
T_C	Curie temperature
U	Inner energy

V	Volume
v	Propagation/phase velocity
v_{par}	Particle velocity
Z_{ac}	Acoustic impedance
AlN	Aluminium nitrid
CBIVM	Circuit board integrated bulk ceramic disk varactor module
LTCC	Low temperature cofired ceramic
MIM	Metal-insulator-metal
ZnO	Zinc oxide

Bibliography

[1] R. Hagelauer et al. *Informatik-Handbuch*. 1999.

[2] Intel. *Intel XMM 7560 modem*. Technical report. Intel, 2017.

[3] K. J. Kanarik et al. "Overview of atomic layer etching in the semiconductor industry". In: *Journal of Vacuum Science & Technology A* (2015). DOI: 10.1116/1.4913379.

[4] A. Goodyear and M. Cooke. "Atomic layer etching in close-to-conventional plasma etch tools". In: *Journal of Vacuum Science & Technology A: Vacuum, Surfaces, and Films* (2017). DOI: 10.1116/1.4972393.

[5] N. R. Johnson et al. "Thermal atomic layer etching of crystalline aluminum nitride using sequential, self-limiting hydrogen fluoride and Sn(acac)2 reactions and enhancement by H2 and Ar plasmas". In: *Journal of Vacuum Science & Technology A: Vacuum, Surfaces, and Films* (2016). DOI: 10.1116/1.4959779.

[6] S. D. Sherpa, P. L. G. Ventzek, and A. Ranjan. "Quasiatomic layer etching of silicon nitride with independent control of directionality and selectivity". In: *Journal of Vacuum Science & Technology A: Vacuum, Surfaces, and Films* (2017). DOI: 10.1116/1.4993133.

[7] A. Ranjan and S. D. Sherpa. "New frontiers of atomic layer etching". In: *Advanced Etch Technology for Nanopatterning VII*. SPIE, 2018. DOI: 10.1117/12.2284662.

[8] M. Moisan and M. R. Wertheimer. "Comparison of microwave and r.f. plasmas: fundamentals and applications". In: *Surface and Coatings Technology* (1993). DOI: 10.1016/0257-8972(93)90047-r.

[9] Panasonic. *Dry Etching System - Panasonic Dry Etching Device Suited for The Next Generation Bonding of 3D Lamination, MEMS, High Aspect and Micro Fabrication, and Device Processing of Difficult Etching Materials.* Technical report. Panasonic, 2008.

[10] A. Wiens. "Tunable Ferroelectric Matching Networks implemented into High Power RF Amplifiers for High Dynamic and Wideband Efficiency". PhD thesis. Technische Uninversität Darmstadt, 2017.

[11] S. Gevorgian. *Ferroelectrics in Microwave Devices, Circuits and Systems: Physics, Modeling, Fabrication and Measurements*. Engineering Materials and Processes. Springer, 2009.

[12] A. Ioachim et al. "Barium strontium titanate-based perovskite materials for microwave applications". In: *Progress in Solid State Chemistry* (2007). DOI: 10.1016/j.progsolidstchem.2007.01.017.

[13] H. Maune. "Design und Optimierung hochlinearer ferroelektrischer Varaktoren für steuerbare Hochfrequenz-Leistungsverstärker". PhD thesis. Technische Universität Darmstadt, 2011.

[14] C. Kohler. "Anorganische Barium-Strontium-Titanat-Komposite für die Hochfrequenztechnik : Material- und Bauteilentwicklung". Dissertation, Technische Universität Darmstadt, 2016. PhD thesis. Aachen: Technische Uninversität Darmstadt, 2016.

[15] J. W. Jewett and R. A. Serway. *Physics for Scientists and Engineers with Modern Physics*. Thomson Brooks/Cole, 2008.

[16] R. E. Newnham. *Properties of Materials: Anisotropy, Symmetry, Structure*. OUP Oxford, 2004.

[17] D. M. Pozar. *Microwave Engineering*. Wiley, 2004.

[18] P. A. Tipler and G. Mosca. *Physik für Wissenschaftler und Ingenieure*. Spektrum Akademischer Verlag, Heidelberg, 2012.

[19] K. Bethe. "Über das Mikrowellenverhalten Nichtlinearer Dielektrika". In: *Philips Res. Rep.* (1970).

[20] R. Waser, U. Böttger, and S. Tiedke. *Polar Oxides*. Wiley-VCH Verlag GmbH & Co. KGaA, 2004. DOI: 10.1002/3527604650.

[21] Vishay. *Ceramic Disk, RFI and Safety Capacitors*. Technical report. Vishay, 2015.

[22] CalRamic Technologies LLC. *The effect of temperature and voltage changes on high voltage ceramic capacitors*. Technical report. CalRamic Technologies LLC, 2014.

[23] H. Jaffe. "Piezoelectric Ceramics". In: *Journal of the American Ceramic Society* (1958). DOI: 10.1111/j.1151-2916.1958.tb12903.x.

[24] B. Jaffe, W. R. Cook, and H.L.Jaffe. *Piezoelectric Ceramics*. New York: Academic Press, 1971.

[25] A. F. Devonshire. "Theory of ferroelectrics". In: *Advances in Physics* (1954). DOI: 10.1080/00018735400101173.

[26] F. Li et al. "Electrostrictive effect in ferroelectrics: An alternative approach to improve piezoelectricity". In: *Applied Physics Reviews* (2014). DOI: 10.1063/1.4861260.

[27] M. Oshiki and E. Fukada. "Inverse piezoelectric effect and electrostrictive effect in polarized poly(vinylidene fluoride) films". In: *Journal of Materials Science* (1975). DOI: 10.1007/bf00541025.

[28] R. E. Newnham et al. "Electrostriction: Nonlinear Electromechanical Coupling in Solid Dielectrics". In: *The Journal of Physical Chemistry* (1997). DOI: 10.1021/jp971522c.

[29] S. Eury et al. "Converse electrostriction in polymers and composites". In: *Materials Chemistry and Physics* (1999). DOI: 10.1016/s0254-0584(99)00107-8.

[30] V. Sundar and R. E. Newnham. "Converse method measurements of electrostriction coefficients in low-K dielectrics". In: *Materials Research Bulletin* (1996). DOI: 10.1016/s0025-5408(96)00035-9.

[31] K. Uchino. *Ferroelectric Devices 2nd Edition*. Boca Raton: CRC Press, 2009.

[32] Y. Zheng. "Tunable Multiband Ferroelectric Devices". In: *Lecture Notes in Electrical Engineering*. Springer Berlin Heidelberg, 2013. DOI: 10.1007/978-3-642-35780-0_5.

[33] Z. Nazarchuk, V. Skalskyi, and O. Serhiyenko. *Acoustic Emission, Methodology and Application*. Springer, 2017.

[34] S. Tappe, U. Böttger, and R. Waser. "Electrostrictive resonances in (Ba0.7Sr0.3)TiO3 thin filmsat microwave frequencies". In: *Applied Physics Letters* (2004). DOI: 10.1063/1.1775880.

[35] M. Sazegar. "Phasedarray-Antennen mit integrierten Phasenschiebern auf ferroelektrischen Dickschichten". PhD thesis. Aachen: Technische Uninversität Darmstadt, 2013.

[36] J.-H. Jeon. "Effect of SrTiO3 concentration and sintering temperature on microstructure and dielectric constant of Ba1-xSrxTiO3". In: *Journal of the European Ceramic Society* (2004). DOI: 10.1016/s0955-2219(03)00385-6.

[37] O. G. Vendik et al. "Ferroelectric tuning of planar and bulk microwave devices". In: *Journal of Superconductivity* (1999). DOI: 10.1023/a:1007797131173.

[38] Z. Song et al. "Effect of grain size on the energy storage properties of (Ba0.4Sr0.6)TiO3 paraelectric ceramics". In: *Journal of the European Ceramic Society* (2014). DOI: 10.1016/j.jeurceramsoc.2013.11.039.

[39] M. H. Frey and D. A. Payne. "Grain-size effect on structure and phase transformations for barium titanate". In: *Physical Review B* (1996). DOI: 10.1103/physrevb.54.3158.

[40] W. Menesklou et al. "Nonlinear ceramics for tunable microwave devices part I: materials properties and processing". In: *Microsystem Technologies* (2011). DOI: 10.1007/s00542-011-1277-z.

[41] B. Su and T. W. Button. "Interactions between barium strontium titanate (BST) thick films and alumina substrates". In: *Journal of the European Ceramic Society* (2001). DOI: 10.1016/s0955-2219(01)00362-4.

[42] B. Su et al. "Dielectric and microwave properties of barium strontium titanate (BST) thick films on alumina substrates". In: *Journal of the European Ceramic Society* (2003). DOI: 10.1016/s0955-2219(03)00171-7.

[43] X. Zhou et al. "Correlation of the microstructure and microwave properties of Ba0.6Sr0.4TiO3 thick-films". In: *Journal of the European Ceramic Society* (2012). DOI: 10.1016/j.jeurceramsoc.2012.06.021.

[44] A. Küchler. *Hochspannungstechnik*. Springer Berlin Heidelberg, 2009. DOI: 10.1007/978-3-540-78413-5.

[45] T. Tick et al. “Screen printed low-sintering-temperature barium strontium titanate (BST) thick films”. In: *Journal of the European Ceramic Society* (2008). DOI: 10.1016/j.jeurceramsoc.2007.08.008.

[46] Y. Zeng et al. “Effects of B2O3-Li2O additions on the dielectric properties of screen printing Ba0.6Sr0.4TiO3 thick films”. In: *physica status solidi (a)* (2011). DOI: 10.1002/pssa.201127276.

[47] M. Zhang et al. “Low-Temperature Sintering (Ba0.6Sr0.4)TiO3Thick Film Prepared by Screen Printing”. In: *International Journal of Applied Ceramic Technology* (2009). DOI: 10.1111/j.1744-7402.2008.02265.x.

[48] C. Kohler et al. “Effects of ZnO-B2O3Addition on the Microstructure and Microwave Properties of Low-Temperature Sintered Barium Strontium Titanate (BST) Thick Films”. In: *International Journal of Applied Ceramic Technology* (2013). DOI: 10.1111/ijac.12116.

[49] C. Kohler et al. “Fully Screen-Printed Tunable Microwave Components Based on Optimized Barium Strontium Titanate Thick Films”. In: *International Journal of Applied Ceramic Technology* (2014). DOI: 10.1111/ijac.12276.

[50] G. T. Furukawa et al. “Thermal properties of aluminum oxide from 0 to 1200 K”. In: *Journal of Research of the National Bureau of Standards* (1956). DOI: 10.6028/jres.057.008.

[51] A. F. Júnior and D. J. Shanafield. “Thermal conductivity of polycrystalline aluminum nitride (AlN) ceramics”. In: *Cerâmica* (2004). DOI: 10.1590/s0366-69132004000300012.

[52] J. Ho, T. R. Jow, and S. Boggs. “Historical introduction to capacitor technology”. In: *IEEE Electrical Insulation Magazine* (2010). DOI: 10.1109/mei.2010.5383924.

[53] D. Kind and H. Kärner. *High-Voltage Insulation Technology*. Vieweg + Teubner Verlag, 1985. DOI: 10.1007/978-3-663-14090-0.

[54] R. Arora and W. Mosch. *High Voltage and Electrical Insulation Engineering*. John Wiley & Sons, Inc., 2011. DOI: 10.1002/9780470947906.

[55] V. V. Terzija and H.-J. Koglin. “On the Modeling of Long Arc in Still Air and Arc Resistance Calculation”. In: *IEEE Transactions on Power Delivery* (2004). DOI: 10.1109/tpwrd.2004.829912.

[56] P. G. Slade. *The Vacuum Interrupter: Theory, Design, and Application*. CRC Press, 2007.

[57] H.-J. Lippmann. *Schalten im Vakuum*. Vde Verlag GmbH, 2003.

[58] R. V. Latham. *High Voltage Vacuum Insulation: Basic Concepts and Technological Practice*. Academic Press, 1995.

[59] K. Mishra et al. “Conditioning technique for high power RF vacuum transmission line components using multipactor plasma”. In: *Journal of Physics: Conference Series* (2010). DOI: 10.1088/1742-6596/208/1/012017.

[60] M. Tioursi. "Conditioning phenonena in N2, SF6 and air". In: *11th International Symposium on High-Voltage Engineering (ISH 99)*. IEE, 1999. DOI: 10.1049/cp:19990737.

[61] S. Grzybowski, J. Thompson, and E. Kuffel. "Electric Surface Strength and Surface Deterioration of Thermoplastic Insulators in Vacuum". In: *IEEE Transactions on Electrical Insulation* (1983). DOI: 10.1109/tei.1983.298617.

[62] T. Psotta. "Konditionierungsverhalten von Hochspannungsvakuumanordnungen bei inhomogener Feldverteilung". PhD thesis. Technische Uninversität Darmstadt, 2017.

[63] P. H. Moon. "The Theory of Thermal Breakdown of Solid Dielectrics". In: *Transactions of the American Institute of Electrical Engineers* (1931). DOI: 10.1109/t-aiee.1931.5055909.

[64] V. Fock. "Zur Wärmetheorie des elektrischen Durchschlages". In: *Archiv für Elektrotechnik* (1927). DOI: 10.1007/bf01656306.

[65] Agilent Technologies. *Agilent Technologies Impedance Measurement Handbook*. 2006.

[66] Keysight Technologies. *E4991B Impedance Analyzer 1MHz to 500MHz / 1GHz / 3GHz*. Technical report. Keysight Technologies, 2016.

[67] U. Böttger. "Dielectric Properties of Polar Oxides". In: *Polar Oxides*. Wiley-VCH Verlag GmbH & Co. KGaA, 2005. DOI: 10.1002/3527604650.ch1.

[68] A. B. Kozyrev et al. "Response time and power handling capability of tunable microwave devices using ferroelectric films". In: *Integrated Ferroelectrics* (1998). DOI: 10.1080/10584589808208053.

[69] Rohde und Schwarz. *Allgemeine Messtechnik - Netzwerkanalysatoren*. Technical report. Rohde und Schwarz, 2007.

[70] M. Hirayama, K. Ino, and T. Ohmi. "Analysis of RF plasma using electrical equivalent circuit". In: *Proceedings of International Symposium on Semiconductor Manufacturing*. IEEE, 1995. DOI: 10.1109/issm.1995.524408.

[71] J. Hopwood. "Review of inductively coupled plasmas for plasma processing". In: *Plasma Sources Science and Technology* (1992). DOI: 10.1088/0963-0252/1/2/006.

[72] Orionfans. *Product Selector Guide*. Technical report. Orion Fans, 2015.

[73] J. R. Crump. "A heat transfer textbook". In: *AIChE Journal* (1981). DOI: 10.1002/aic.690270427.

[74] R. Gou et al. *Morphotropic Phase Boundary Perovskites, High Strain Piezoelectrics, and Dielectric Ceramics*. John Wiley & Sons, Inc., 2006. DOI: 10.1002/9781118380802.

[75] W. D. Nix. "Mechanical properties of thin films". In: *Metallurgical Transactions A* (1989). DOI: 10.1007/bf02666659.

[76] J. Y. Fu et al. "Experimental studies of the converse flexoelectric effect induced by inhomogeneous electric field in a barium strontium titanate composition". In: *Journal of Applied Physics* (2006). DOI: 10.1063/1.2219990.

[77] N. M. White and J. D. Turner. "Thick-film sensors: past, present and future". In: *Measurement Science and Technology* (1997). DOI: 10.1088/0957-0233/8/1/002.

[78] A. C. Dent et al. "Effective elastic properties for unpoled barium titanate". In: *Journal of the European Ceramic Society* (2007). DOI: 10.1016/j.jeurceramsoc.2007.02.031.

[79] Heraeus. *Technical Data Sheet - Thick Film Materials, Conductors, C8729*. Technical report. Heraeus, 2017.

[80] H. Abomostafa and M. Ellamey. "Studying the mechanical properties of barium strontium titanate ceramics by an ultrasonic pulse echo technique". In: *Journal of Ovonic Research* (2018).

[81] X. Zhou et al. "Characterization of metal (Fe, Co, Ni, Cu) and fluorine codoped barium strontium titanate thick-films for microwave applications". In: *Journal of Electroceramics* (2010). DOI: 10.1007/s10832-009-9580-0.

[82] X. Zhu, J. D. Phillips, and A. Mortazawi. "A DC Voltage Dependant Switchable Thin Film Bulk Wave Acoustic Resonator Using Ferroelectric Thin Film". In: *2007 IEEE/MTT-S International Microwave Symposium*. IEEE, 2007. DOI: 10.1109/mwsym.2007.380009.

[83] H. Fink et al. "Conditioning of Series Vacuum Interrupters (VIs) for Medium Voltage by Applying High-Frequency (HF) Current to Increase the Dielectric Strength of VIs". In: *IEEE Transactions on Plasma Science* (2007). DOI: 10.1109/tps.2007.901922.

[84] H. Yang et al. "A high efficiency conditioning method of vacuum interrupters by high frequency voltage impulses". In: *2012 25th International Symposium on Discharges and Electrical Insulation in Vacuum (ISDEIV)*. IEEE, 2012. DOI: 10.1109/deiv.2012.6412451.

[85] D. C. Faircloth. *Technological Aspects: High Voltage*. 2014. DOI: 10.5170/cern-2013-007.381.

[86] M. Budde and M. Kurrat. "Dielectric investigations on micro discharge currents and conditioning behaviour of vacuum gaps". In: *2006 International Symposium on Discharges and Electrical Insulation in Vacuum*. 2006. DOI: 10.1109/deiv.2006.357230.

[87] H. Okubo, N. Hayakawa, and A. Matsushita. "The relationship between partial discharge current pulse waveforms and physical mechanisms". In: *IEEE Electrical Insulation Magazine* (2002). DOI: 10.1109/mei.2002.1014966.

[88] B. Heil. "Untersuchungen zur Hochfrequenzkonditionierung von Vakuumschaltkammern". PhD thesis. RWTH Aachen, 2006.

[89] K. M. Lakin, G. R. Kline, and K. T. McCarron. "High-Q microwave acoustic resonators and filters". In: *IEEE Transactions on Microwave Theory and Techniques* (1993). DOI: 10.1109/22.260698.

[90] L. Reindl et al. "Theory and application of passive SAW radio transponders as sensors". In: *IEEE Transactions on Ultrasonics, Ferroelectrics and Frequency Control* (1998). DOI: 10.1109/58.726455.

[91] R. Baersch and A. Kuechler. "Beanspruchungen und elektrisches Verhalten von Isoliersystemen bei Gleich- und Mischfeldbeanspruchungen". In: *Isolierstoffsysteme bei Gleich- und Mischfeldbeanspruchung* (2010).

[92] K. D. Schomann. "Zum elektrischen Durchschlag von keramischem Bariumtitanat und Barium-Strontium-Titanat". In: *Archiv fuer Elektrotechnik* (1974). DOI: 10.1007/bf01496740.

[93] A. Giere et al. "Characterization of Acoustic Effects in Ferroelectric Thin-Films for Microwave Components". In: *Frequenz* (2008). DOI: 10.1515/freq.2008.62.3-4.52.

[94] M. A. Ramirez et al. "Elastic modulus and hardness of CaTiO3, CaCu3Ti4O12 and CaTiO3/CaCu3Ti4O12 mixture". In: *Materials Letters* (2010). DOI: 10.1016/j.matlet.2010.02.058.

[95] S.-J. L. Kang. *Sintering: Densification, Grain Growth and Microstructure*. Elsevier Science, 2004.

[96] R. L. Coble. "A Model for Boundary Diffusion Controlled Creep in Polycrystalline Materials". In: *Journal of Applied Physics* (1963). DOI: 10.1063/1.1702656.

[97] X.-H. Wang et al. "The grain size effect on dielectric properties of BaTiO3 based ceramics". In: *Materials Science and Engineering: B* (2003). DOI: 10.1016/s0921-5107(02)00520-2.

[98] S.-H. Yoon et al. "Effect of the Liquid-Phase Characteristic on the Microstructures and Dielectric Properties of Donor- (Niobium) and Acceptor- (Magnesium) Doped Barium Titanate". In: *Journal of the American Ceramic Society* (2003). DOI: 10.1111/j.1151-2916.2003.tb03282.x.

[99] E. E. Helgee and A. Isacsson. "Scattering of flexural acoustic phonons at grain boundaries in graphene". In: *Physical Review B* (2014). DOI: 10.1103/physrevb.90.045416.

[100] K. Wohak. "Näherungsweise Berechnung der Induktivität von Dünnschichtbahnen". In: *Frequenz* (1969). DOI: 10.1515/freq.1969.23.12.359.

[101] R. C. Smith et al. "A Free Energy Model for Hysteresis in Ferroelectric Materials". In: *Journal of Intelligent Material Systems and Structures* (2003). DOI: 10.1177/1045389X03038841.

[102] D. ter Haar. *Elements of Stastical Mechanics*. 3rd Edition. Butterworth-Heinemann, 1995.

[103] S. P. Joshi. "Non-linear constitutive relations for piezoceramic materials". In: *Smart Materials and Structures* (1992). DOI: 10.1088/0964-1726/1/1/012.

[104] Keysight Technologies. *Applying Error Correction to Vector Network Analyzer Measurements*. Technical report. Keysight Technologies, 2018.

[105] A. Friederich et al. *Barium Strontium Titanat Dickschichten für steuerbare Mikrowellenkomponenten: Prozesseinflüsse und Gefüge-Eigenschaftbeziehungen*. 2012. DOI: 10.13140/2.1.1845.6643.

[106] C. Weil. "Passiv steuerbare Mikrowellenphasenschieber auf Basis nichtlinearer Dielektrika". PhD thesis. Technische Universität Darmstadt, 2003.

[107] S. Gevorgian, A. Vorobiev, and T. Lewin. "dc field and temperature dependent acoustic resonances in parallel-plate capacitors based on SrTiO3 and Ba0.25Sr0.75TiO3 films: Experiment and modeling". In: *Journal of Applied Physics* (2006). DOI: 10.1063/1.2209727. eprint: http://dx.doi.org/10.1063/1.2209727.

[108] K.-I. Sakayori et al. "Curie Temperature ofBaTiO3". In: *Japanese Journal of Applied Physics* (1995). DOI: 10.1143/jjap.34.5443.

[109] T.-G. In, S. Baik, and S. Kim. "Leakage current of Al- or Nb-doped Ba0.5Sr0.5TiO3 thin films by rf magnetron sputtering". In: *Journal of Materials Research* (1998). DOI: 10.1557/jmr.1998.0139.

[110] Y. T. Kim and C. W. Lee. "Advantages of RuOxBottom Electrode in the Dielectric and Leakage Characteristics of (Ba,Sr)TiO3Capacitor". In: *Japanese Journal of Applied Physics* (1996). DOI: 10.1143/jjap.35.6153.

[111] M. W. Cole, P. C. Joshi, and M. H. Ervin. "La doped Ba1-xSrxTiO3 thin films for tunable device applications". In: *Journal of Applied Physics* (2001). DOI: 10.1063/1.1366656.

[112] S. Y. Wang et al. "Influence of Ce doping on leakage current in Ba0.5Sr0.5TiO3 films". In: *Journal of Physics D: Applied Physics* (2005). DOI: 10.1088/0022-3727/38/13/025.

[113] P. C. Joshi and M. W. Cole. "Mg-doped Ba0.6Sr0.4TiO3 thin films for tunable microwave applications". In: *Applied Physics Letters* (2000). DOI: 10.1063/1.126953.

[114] F. Feher. *Elemente der Siebenten Gruppe*. 2013.

[115] P. Panek et al. "The New Copper Composite of Pastes for Si Solar Cells Front Electrode Application". In: *Energy Procedia* (2016). DOI: 10.1016/j.egypro.2016.07.108.

[116] H. J. Hwang and K. Niihara. "Perovskite-type BaTiO3 ceramics containing particulate SiC: Part II Microstructure and mechanical properties". In: *Journal of Materials Science* (1998). DOI: 10.1023/a:1004365006839.

[117] G. Mavko, T. Mukerji, and J. Dvorkin. *The Rock Physics Handbook: Tools for Seismic Analysis of Porous Media*. Cambridge University Press, 2003.

Own Contributions

First Author

[1] D. Kienemund et al. “Temperature dependence of a tunable phase shifter based on inkjet printing technology”. In: *2015 German Microwave Conference*. IEEE, 2015. DOI: 10.1109/gemic.2015.7107775.

[2] D. Kienemund et al. “A fully-printed MIM varactor for high power application”. In: *2016 46th European Microwave Conference (EuMC)*. IEEE, 2016. DOI: 10.1109/eumc.2016.7824420.

[3] D. Kienemund et al. “Acoustical behavior of fully-printed, BST MIM varactor modules in high power matching circuits”. In: *2018 IEEE/MTT-S International Microwave Symposium - IMS*. IEEE, 2018. DOI: 10.1109/mwsym.2018.8439171.

[4] D. Kienemund et al. “Design and demonstration of acoustically optimized, fully-printed, BST MIM varactors for high power matching circuits”. In: *International Journal of Microwave and Wireless Technologies* (2018). DOI: 10.1017/s1759078718000387.

[5] D. Kienemund et al. “A fully-printed, BST MIM varactor for low ISM-band matching networks up to 1000 W”. In: *2017 47th European Microwave Conference (EuMC)*. IEEE, 2017. DOI: 10.23919/eumc.2017.8231015.

[6] D. Kienemund et al. “Suppression of acoustic resonances in fully-printed, BST thick film varactors utilizing double MIM structures”. In: *2018 48th European Microwave Conference (EuMC)*. IEEE, 2018. DOI: 10.23919/eumc.2018.8541497.

[7] D. Kienemund et al. “Low loss, fully-printed, ferroelectric varactors for high-power impedance matching at low ISM band frequency”. In: *International Journal of Microwave and Wireless Technologies* (2019). DOI: 10.1017/s1759078719000643.

Second Author

[1] A. Wiens et al. “Tunable in-package impedance matching for high power transistors based on printed ceramics”. In: *2015 European Microwave Conference (EuMC)*. 2015. DOI: 10.1109/EuMC.2015.7345993.

[2] H. Maune et al. “Ferroelectrics for tunable high-power applications”. In: *2018 IEEE MTT-S International Microwave Workshop Series on Advanced Materials and Processes for RF and THz Applications (IMWS-AMP)*. IEEE, 2018. DOI: 10.1109/imws-amp.2018.8457141.

[3] M. Nikfalazar et al. “Frequency extension of the fully printed phase shifter by paste composite optimization”. In: *2015 German Microwave Conference*. 2015. DOI: 10.1109/GEMIC.2015.7107774.

[4] S. Preis et al. “Discrete RF-power MIM BST thick-film varactors”. In: *2015 European Microwave Conference (EuMC)*. 2015. DOI: 10.1109/EuMC.2015.7345919.

[5] S. Preis et al. “Thick-film MIM BST varactors for GaN power amplifiers with discrete dynamic load modulation”. In: *2017 IEEE MTT-S International Microwave Symposium (IMS)*. 2017. DOI: 10.1109/MWSYM.2017.8059097.

[6] D. Walk et al. “Characterization and modeling of epitaxially grown BST on a conducting oxide electrode”. In: *2018 48th European Microwave Conference (EuMC)*. IEEE, 2018. DOI: 10.23919/eumc.2018.8541771.

[7] D. Walk et al. “Characterization and deembedding of negative series inductance in on-wafer measurements of thin-film all-oxide varactors”. In: *IEEE Microwave and Wireless Components Letters* (2019). DOI: 10.1109/lmwc.2019.2897901.

[8] A. Wiens et al. “Tunable impedance matching networks on printed ceramics for output matching of RF-power transistors”. In: *2014 44th European Microwave Conference*. 2014. DOI: 10.1109/EuMC.2014.6986479.

[9] D. Walk et al. “All-oxide thin film varactor: From test structure to SMD component”. In: *2019 49th European Microwave Conference (EuMC)*. IEEE, 2019.

[10] H. Maune et al. “Recent development in ferroelectric functional materials”. In: *2019 IEEE/MTT-S International Microwave Symposium - IMS*. 2019.

Patents

- „Variable Capacitor for RF Power Applications“, Thomas Fink, Mike Abrecht, Walter Bigler, Daniel Kienemund, Holger Maune, Rolf Jakoby, Nicole Bohn, Kevin Häuser, Joachim R. Binder, TUD: 2018-63, Unpublished patent application, submitted in March 2019

Supervised Work

- „Tunable Diplexer with Wideband Antenna for Reconfigurable Up- and Downlink of a Satellite Commmunication System at CIS Band “, Master Thesis, Masha Rasteh, 2015

- „Suppression Techniques for Acoustic Resonances in Ferroelectric Multilayer Varactors for High-Power Matching Circuits “, Master Thesis, Sanjay Shankaranarayana Sastry, 2017

Curriculum Vitae

Personal Data

Name: Daniel Markus Kienemund

Date of birth: 18. November 1985

Place of birth: Stuttgart, Deutschland

Education and Profession

1996–2005 – Konrad-Adenauer-Gymnasium, Meckenheim (Abitur)

2005–2013 – Study of Electrical Engineering
Rheinisch-Westfälische Technische Hochschule (RWTH), Aachen (Diploma)

since 2014 – Research Associate at the Institute for Microwave Engineering and Photonics,
Technische Universität Darmstadt

Darmstadt, 03.05.2019